

**MODELLING, SIMULATION AND ANALYSIS OF LOW-COST DIRECT
TORQUE CONTROL OF PMSM USING HALL-EFFECT SENSORS**

A Thesis

by

SALIH BARIS OZTURK

Submitted to the Office of Graduate Studies of
Texas A&M University
in partial fulfillment of the requirements for the degree of

MASTER OF SCIENCE

December 2005

Major Subject: Electrical Engineering

**MODELLING, SIMULATION AND ANALYSIS OF LOW-COST DIRECT
TORQUE CONTROL OF PMSM USING HALL-EFFECT SENSORS**

A Thesis

by

SALIH BARIS OZTURK

Submitted to the Office of Graduate Studies of
Texas A&M University
in partial fulfillment of the requirements for the degree of

MASTER OF SCIENCE

Approved by:

Chair of Committee,	Hamid A. Toliyat
Committee Members,	Prasat N. Enjeti
	S. P. Bhattacharyya
	Reza Langari
Head of Department,	Costas N. Georghiades

December 2005

Major Subject: Electrical Engineering

ABSTRACT

Modelling, Simulation and Analysis of Low-Cost Direct Torque Control
of PMSM Using Hall-Effect Sensors. (December 2005)
Salih Baris Ozturk, B.S., Istanbul Technical University
Chair of Advisory Committee: Dr. Hamid A. Toliyat

This thesis focuses on the development of a novel Direct Torque Control (DTC) scheme for permanent magnet (PM) synchronous motors (surface and interior types) in the constant torque region with the help of cost-effective hall-effect sensors. This method requires no DC-link sensing, which is a mandatory matter in the conventional DTC drives, therefore it reduces the cost of a conventional DTC of a permanent magnet (PM) synchronous motor and also removes common problems including; resistance change effect, low speed and integration drift. Conventional DTC drives require at least one DC-link voltage sensor (or two on the motor terminals) and two current sensors because of the necessary estimation of position, speed, torque, and stator flux in the stationary reference frame.

Unlike the conventional DTC drive, the proposed method uses the rotor reference frame because the rotor position is provided by the three hall-effect sensors and does not require expensive voltage sensors. Moreover, the proposed algorithm takes the acceleration and deceleration of the motor and torque disturbances into account to improve the speed and torque responses.

The basic theory of operation for the proposed topology is presented. A mathematical model for the proposed DTC of the PMSM topology is developed. A simulation program written in MATLAB/SIMULINK[®] is used to verify the basic operation (performance) of the proposed topology. The mathematical model is capable of simulating the steady-state, as well as dynamic response even under heavy load conditions (e.g. transient load torque at ramp up). It is believed that the proposed system

offers a reliable and low-cost solution for the emerging market of DTC for PMSM drives.

Finally the proposed drive, considering the constant torque region operation, is applied to the agitation part of a laundry washing machine (operating in constant torque region) for speed performance comparison with the current low-cost agitation cycle speed control technique used by washing machine companies around the world.

To my mother and father.

ACKNOWLEDGMENTS

There is a numerous amount of people I need to thank for their advice, help, assistance and encouragement throughout the completion of this thesis.

First of all, I would like to thank my advisor, Dr. Hamid A. Toliyat, for his support, continuous help, patience, understanding and willingness throughout the period of the research to which this thesis relates. Moreover, spending his precious time with me is appreciated far more than I have words to express. I am very grateful to work with such a knowledgeable and insightful professor. To me he is more than a professor; he is like a father caring for his students during their education. Before pursuing graduate education in the USA I spent a great amount of time finding a good school, and more importantly a quality professor to work with. Even before working with Dr. Toliyat I realized that the person who you work with is more important than the prestige at the university in which you attend.

I would also like to thank the members of my graduate study committee, Dr. Prasad Enjeti, Dr. S.P. Bhattacharyya, and Dr. Reza Langari for accepting my request to be a part of the committee.

I would like to extend my gratitude to my fellow colleagues in the Advanced Electric Machine and Power Electronics Laboratory: our lab manager Dr. Peyman Niazi, Dr. Leila Parsa, Dr. M.S. Madani, Dr. Namhun Kim, Dr. Mesuod Haji, Dr. Sang-Shin Kwak, Dr. Mehdi Abolhassani, Bilal Akin, Steven Campbell, Salman Talebi, Rahul Khopkar, and Sheab Ahmed. I cherish their friendship and the good memories I have had with them since my arrival at Texas A&M University.

Also, I would like to thank to the people who are not participants of our lab but who are my close friends and mentors who helped, guided, assisted and advised me during the completion of this thesis: Onur Ekinici, David Tarbell, Ms. Mina Rahimian, Dr. Farhad Ashrafzadeh, Peyman Asadi, Sanjey Tomati, Neeraj Shidore, Steve Welch, Burak Kelleci, Guven Yapici, Murat Yapici, Cansin Evrenosoglu, Ali Buendia, Kalyan Vadakkevedu, Leonardo Palma and many others whom I could not mention here.

I would also like to acknowledge the Electrical Engineering department staff at Texas A&M University: Ms. Tammy Carda, Ms. Linda Currin, Ms. Gayle Travis and many others for providing an enjoyable and educational atmosphere.

Last but not least, I would like to thank my parents for their patience and endless financial, and more importantly, moral support throughout my life. First, I am very grateful to my dad for giving me the opportunity to study abroad to earn a good education. Secondly, I am very grateful to my mother for her patience which gave me a glimpse of how strong she is. Even though they do not show their emotion when I talk to them, I can sense how much they miss me when I am away from them. No matter how far away from home I am, they are always there to support and assist me. Finally, to my parents, no words can express my gratitude for you and all the things you sacrifice for me.

TABLE OF CONTENTS

	Page
ABSTRACT	iii
ACKNOWLEDGMENTS.....	vi
TABLE OF CONTENTS	viii
LIST OF FIGURES.....	xi
LIST OF TABLES	xxii
CHAPTER	
I INTRODUCTION.....	1
1.1 Principles of DC Brush Motors and Their Problems	1
1.2 Mathematical Model of the DC Brush Motor	6
1.3 AC Motors and Their Trend.....	10
1.4 Thesis Outline	12
II BASIC OPERATIONAL PRINCIPLES OF PERMANENT MAGNET SYNCHRONOUS AND BRUSHLESS DC MOTORS	14
2.1 Permanent Magnet Synchronous Motors (PMSMs)	14
2.1.1 Mathematical Model of PMSM.....	20
2.2 Introduction to Brushless DC (BLDC) Motors	36
2.2.1 Mathematical Model of BLDC Motor	39
2.3 Mechanical Structure of Permanent Magnet AC Motors (PMSM and BLDC)	45
2.4 Advantages and Disadvantages of PMSM and BLDC Motors	49
2.5 Torque Production Comparison of PMSM and BLDC Motors	53
2.6 Control Principles of the BLDC Motor.....	55
2.7 Control Principles of the PM Synchronous Motor.....	62
III MEASUREMENTS OF THE PM SPINDLE MOTOR PARAMETERS	67
3.1 Introduction	67
3.2 Principles of Self-Commissioning with Identification	68
3.3 Resistance and dq-axis Synchronous Inductance Measurements.....	69
3.4 Measurement of the Back-EMF Constant and Rotor Flux Linkage	79
3.5 Load Angle Measurement	81

CHAPTER	Page
IV	OPEN-LOOP SIMULINK® MODEL OF THE PM SPINDLE MOTOR 88
4.1	Principles of PMSM Open-Loop Control 88
4.2	Building Open-Loop Steady and Transient-State Models 90
4.3	Power Factor and Efficiency Calculations in Open-Loop Matlab/Simulink® Model 97
V	CONVENTIONAL DIRECT TORQUE CONTROL (DTC) OPERATION OF PMSM DRIVE 99
5.1	Introduction and Literature Review 99
5.2	Principles of Conventional DTC of PMSM Drive 107
5.2.1	Torque Control Strategy in DTC of PMSM Drive..... 108
5.2.2	Flux Control Strategy in DTC of PMSM Drive..... 112
5.2.3	Voltage Vector Selection in DTC of PMSM Drive 107
5.3	Control Strategy of DTC of PMSM Drive 120
VI	PROPOSED DIRECT TORQUE CONTROL (DTC) OPERATION OF PMSM DRIVE 124
6.1	Introduction and Principles of the Proposed DTC Drive 124
6.2	Position and Speed Estimation Method with Low Resolution Position Sensor 130
VII	AGITATION CYCLE SPEED CONTROL OF VERTICAL-AXIS LAUNDRY MACHINE..... 135
7.1	Modern Washing Machines: Top Loaded (Vertical-axis) and Front Loaded (Horizontal-axis) Washine Machines 135
7.2	Introduction to Speed Control of a BLDC Spindle Motor (48 Pole/ 36 Slot) in the Agitation Cycle of a Washing Machine 136
7.3	Agitate Washer Controller Model in SIMPLORER® 138
VIII	EXPERIMENTAL AND SIMULATION ANALYSIS 148
8.1	Open-Loop Simulation vs. Experimental Results 148
8.1.1	Open-Loop Steady-State and Transient Analysis (Simulation)..... 148
8.1.2	Open-Loop Steady-State and Transient Analysis (Experiment)..... 152
8.1.3	System Configuration for Electrical Parameters Measurements..... 154
8.1.4	The M-Test 4.0 Software 156
8.1.5	Curve Testing 157
8.2	Experimental vs. Simulation Results (Commercial Agitation Control). 158
8.2.1	Complete Agitation Speed Control Analysis (Steady-State) .. 159

CHAPTER	Page
8.2.2 Complete Agitation Speed Control Analysis (Transient and Steady-States).....	169
8.2.3 Simulation Results of the Proposed DTC Method Used in Agitation Cycle Speed Control	176
8.2.3.1 Transient and Steady-State Response Under Load Condition.....	181
8.2.3.2 Effects of Stator Resistance Variation in Conventional DTC with Encoder.....	195
8.2.3.3 Drift Problem Occurs in Conventional DTC Scheme	209
8.2.3.4 Overview of the Offset Error Occured in the Proposed DTC Scheme	213
8.2.3.5 Overview of the Rotor Flux Linkage Error Occured in the Proposed DTC Scheme	218
IX SUMMARY AND FUTURE WORK.....	224
9.1 Summary of the Work and Conclusion.....	224
9.2 Future Work	225
REFERENCES	227
APPENDIX A	232
VITA	237

LIST OF FIGURES

FIGURE	Page
1.1. Basic model of a DC brush motor	2
1.2. Fundamental operation of a DC brush motor (Step 1).....	4
1.3. Fundamental operation of a DC brush motor (Step 2).....	5
1.4. Fundamental operation of a DC brush motor (Step 3).....	6
1.5. Electrical circuit model of a separately excited DC brush motor (transient-state).....	7
1.6. Electrical circuit model of a separately excited DC brush motor (steady-state)	8
2.1. Two-pole three phase surface mounted PMSM.	22
2.2. Q-axis leading d-axis and the rotor angle represented as θ_r	26
2.3. Q-axis leading d-axis and the rotor angle represented as θ	28
2.4. Line-to-line back-EMF (E_{ab}), phase back-EMFs, phase current waveforms and hall-effect position sensor signals for a BLDC motor	38
2.5. Equivalent circuit of the BLDC drive (R, L and back-EMF).....	40
2.6. Simplified equivalent circuit of the BLDC drive (R, (L-M) and back-EMF).....	42
2.7. Cross sectional view of four pole surface-mounted PM rotor ($L_d = L_q$)	46
2.8. Cross sectional view of four pole interior-mounted PM rotor ($L_d \neq L_q$).....	47
2.9. Ideal BLDC operation	55
2.10. PMSM controlled as BLDC	55
2.11. Voltage Source Inverter (VSI) PMAC drive.....	55

FIGURE	Page
2.12. Voltage Source Inverter (VSI) BLDC drive	56
2.13. A typical current-controlled BLDC motor drive with position feedback	59
2.14. Six possible switching sequences for a three-phase BLDC motor.....	60
2.15. PWM current regulation for BLDC motor [8]	61
2.16. Basic phasor diagram for PMSM [8]	63
2.17. Basic block diagram for high-performance torque control for PMSM [8]	64
2.18. Basic block diagram for high-performance torque control for PMSM [8]	65
2.19. Basic block diagram for high-performance torque control for PMSM [8]	65
3.1. Vector phasor diagram for non-salient PMSM	72
3.2. Measurement of phase resistance and inductance.....	74
3.3. Phase A voltage waveform and hall-effect signal of the same phase	82
3.4. Rotor magnet representation along with hall-effect signals.....	83
3.5. Phase A voltage waveform and hall-effect signal with jittering effect	83
3.6. Experimental vs. simulated load angle (deg.) at 20 Hz (No-load).....	85
3.7. Experimental vs. simulated load angle (deg.) at 40 Hz (No-load).....	86
3.8. Experimental vs. simulated load angle (deg.) at 40 Hz (Load).....	86
3.9. Possible vector representation of PMSM	87
4.1. Basic open-loop block diagram of PMSM	89
4.2. Overall open-loop control block diagram of PMSM in SIMULINK®	91

FIGURE	Page
4.3. Abc to stationary and stationary to dq rotor reference frame transformation block	91
4.4. Rotor reference frame and stationary reference frame coordinate representation	92
4.5. Dq rotor reference frame to stationary and stationary to abc transformation block	93
4.6. Steady state dq-axis rotor reference frame motor model	94
4.7. Rotor ref. frame, synchronous ref. frame, and stationary ref. frame representation as vectors	96
5.1. Eight possible voltage space vectors obtained from VSI	100
5.2. Circular trajectory of stator flux linkage in the stationary DQ-plane	101
5.3. Phasor diagram of a non-salient pole synchronous machine in the motoring mode	108
5.4. Electrical circuit diagram of a non-salient synchronous machine at constant frequency (speed)	109
5.5. Rotor and stator flux linkage space vectors (rotor flux is lagging stator flux)	112
5.6. Incremental stator flux linkage space vector representation in the DQ-plane	112
5.7. Representation of direct and indirect components of the stator flux linkage vector	114
5.8. Voltage Source Inverter (VSI) connected to the R-L load	116
5.9. Voltage vector selection when the stator flux vector is located in sector i ..	117
5.10. Basic block diagram of DTC of PMSM	120
6.1. Hall-effect sensor placement shown in DQ stationary reference frame	125

FIGURE	Page
6.2. Representation of the rotor and stator flux linkages both in the synchronous dq and stationary DQ-planes	127
6.3. Block diagram of the proposed DTC of PMSM	129
6.4. Speed and position estimation using low-resolution position sensor	131
6.5. Representation of acceleration and speed at the sectors and at the hall-effect sensors, respectively	134
7.1. Simple flowchart of the commercial agitation speed control [57]	138
7.2. Reference speed profile for the agitation speed control in a washing machine	139
7.3. Detailed flowchart of the simple agitation speed control of a washing machine [58]	140
7.4. PWM increment during the ramp time [58]	143
7.5. Speed response during ramp up when PWM is incremented at every T_p time [58]	144
7.6. Ideal speed profile of the agitation speed control [58]	146
7.7. Typical practical speed response of the agitation speed control [58]	147
8.1. Efficiency, power factor, motor current (Phase A), and motor speed versus applied load torque (open-loop exp. and sim.) at 100 rpm with $V / f \approx 2$	150
8.2. Dynamic speed response of exp. and sim. when $V / f = 18/15$ (0-37.5 rpm)	151
8.3. Dynamic speed response of exp. and sim. when $V / f = 1$ (0-37.5 rpm)	151
8.4. Torque response of PMSM when it is supplied by quasi-square wave currents	152

FIGURE	Page
8.5. Efficiency, power factor, motor current (Phase A), and motor speed versus applied load torque (experimental, open-loop) at 100 rpm with $V / f \approx 2$	154
8.6. Basic block diagram of overall system for efficiency measurements	155
8.7. Overall system configuration	156
8.8. Sample curve test	158
8.9. Graphical representation of the sample curve test	158
8.10. Input current of the single phase diode rectifier at 10 N·m of load torque..	159
8.11. Input current to the single phase diode rectifier (experiment) at 10 N·m of load torque (100 rpm).....	160
8.12. Voltage source obtained from the wall plug	161
8.13. DC-link voltage of the VSI at 10 N·m of load torque (100 rpm)	162
8.14. Steady-state load torque and plateau speeds (experiment and simulation) at 10 N·m of load torque (100 rpm)	163
8.15. Steady-state electromagnetic torque (simulation) at 10 N·m of load torque (100 rpm).....	164
8.16. Block diagram of the overall commercialized agitation washer control with the trapezoidal voltage waveform and efficiency calculation and measurement.....	165
8.17. Experimental three-phase motor phase currents at 10 N·m of load torque (100 rpm).....	166
8.18. Simulated three-phase motor phase currents at 10 N·m of load torque (100 rpm).....	167
8.19. Exp. PF., eff., and sim. PF., eff. vs. torque at 10 N·m (100 rpm).....	167
8.20. Block diagram of the overall commercialized agitation washer control with trapezoidal voltage waveform	168

FIGURE	Page
8.21. Experimental and simulation speed response (transient and steady-state) at no-load.....	170
8.22. Experimental and simulation speed response (transient and steady-state) at 5 N·m of load torque.....	171
8.23. Experimental and simulation speed response (transient and steady-state) at no-load (0.7 second ramp time).....	172
8.24. Rotor position obtained in simulation	173
8.25. Steady-state SIMPLORER [®] model of the agitation speed control	174
8.26. SIMPLORER [®] model of commercialized overall agitation speed control system (transient+steady-state).....	175
8.27. Agitation speed control test-bed.....	176
8.28. Load torque (T_L), T_{emref} , T_{emest} , and T_{emact} at a 0.35 second ramp time when the PI integrator initial value is 7 N·m.....	182
8.29. λ_s^* (Reference Stator Flux), λ_{s_est} and λ_{s_act} at a 0.35 second ramp time when the PI integrator initial value is 7 N·m.....	183
8.30. λ_{sD} and λ_{sQ} circular trajectory at a 0.35 second ramp time when the PI integrator initial value is 7 N·m	183
8.31. Load torque (T_L), T_{emref} , T_{emest} , and T_{emact} at a 0.35 second ramp time when the PI integrator initial value is 8.5 N·m.....	184
8.32. λ_s^* (Reference Stator Flux), λ_{s_est} and λ_{s_act} at a 0.35 second ramp time when the PI integrator initial value is 8.5 N·m.....	185
8.33. λ_{sD} and λ_{sQ} circular trajectory at a 0.35 second ramp time when the PI integrator initial value is 8.5 N·m	186
8.34. Phase-A current (i_{as}), i_{dqact} , and i_{dqrest} when a 0.35 second ramp time is used when the PI integrator initial value is 7 N·m.....	187

FIGURE	Page
8.35. Phase-A current (i_{as}), $i_{dq_{ract}}$, and $i_{dq_{rest}}$ when a 0.35 second ramp time is used when the PI integrator initial value is 8.5 N·m.....	188
8.36. Reference and actual speed, speed error (ref-act), actual and estimated position when a 0.35 second ramp time is used when the PI integrator initial value is 7 N·m	189
8.37. Reference and actual speed, speed error (ref-act), and actual and estimated position when a 0.35 second ramp time is used when the PI integrator initial value is 8.5 N·m.....	190
8.38. T_{emref} , T_{emest} , and T_{emact} at a 0.6125 second ramp time when the PI integrator initial value is 7 N·m	191
8.39. λ_s^* (reference stator flux), λ_{s_est} and λ_{s_act} at 0.6125 second ramp time when PI integrator initial value is 7 N·m.....	192
8.40. λ_{sD} (X axis) and λ_{sQ} (Y axis) circular trajectory at a 0.6125 second ramp time when the PI integrator initial value is 7 N·m.....	193
8.41. Phase-A current (i_{as}), $i_{dq_{ract}}$, and $i_{dq_{rest}}$ when a 0.6125 second ramp time is used when the PI integrator initial value is 7 N·m.....	194
8.42. Reference and actual speeds, speed error (ref-act), and actual and estimated positions when a 0.6125 second ramp time is used when the PI integrator initial value is 7 N·m.....	195
8.43. Reference and actual speeds, actual position, and three phase currents when a 0.35 second ramp time is used (no initial torque, just ramp rate is added). Stator resistance change effect is not applied.....	196
8.44. T_{emref} , T_{emest} , and $Flux_{est}$ at a 0.35 second ramp time. Stator resistance change effect is not applied.....	197

FIGURE	Page
8.45. Load torque (TL), T_{emref} , T_{emest} , T_{emact} , and estimated stator flux linkage under step stator resistance change ($1.5x R_s$) at 0 second when ramp time is 0.35 second when the initial integrator value of the PI is chosen as 7 N·m.....	198
8.46. Reference and actual speeds, actual position, and three phase currents when a 0.35 second ramp time is used (no initial torque, just ramp rate is added). Stator resistance is increased by $1.5x R_s$ at 0 second	199
8.47. Reference and actual speeds, speed error (ref-act), actual position, and three phase currents when a 0.35 second ramp time is used (no initial torque, just ramp rate is added). Stator resistance is increased by $1.5x R_s$ at 0.675 second	200
8.48. T_{emref} , T_{emest} , and $Flux_{est}$ at a 0.35 second ramp time. Stator resistance is increased by $1.5x R_s$ at 0.675 second	201
8.49. T_{emest} , T_{emact} , $Flux_{est}$, $Flux_{act}$, estimated and real rotor positions with a 0.35 second ramp time. Stator resistance is increased by $1.5x R_s$ at 0.675 second.....	202
8.50. T_{emest} , T_{emact} , $Flux_{est}$, $Flux_{act}$, estimated and real rotor positions with a 0.35 second ramp time. Stator resistance is increased by $1.5x R_s$ at 0.35/2 second ($V_{dc} = 370$ V).....	203
8.51. Reference and actual speeds, and three phase currents when a 0.35 second ramp time is used (no initial torque, just ramp rate is added). Stator resistance is increased by $1.5x R_s$ at 0.35/2 second ($V_{dc} = 370$ V)	204
8.52. T_{emest} , T_{emact} , and $Flux_{est}$ with a 0.35 second ramp time. Stator resistance is increased by $1.5x R_s$ at 0.35/2 second ($V_{dc} = 370$ V).....	205
8.53. Estimated λ_{sD} (X axis) and λ_{sQ} (Y axis) circular trajectory with a 0.35 second ramp time. Stator resistance is increased by $1.5x R_s$ at 0.675 second (kp=9, ki=3).....	206

FIGURE	Page
8.54. Estimated λ_{sD} (X axis) and λ_{sQ} (Y axis) circular trajectory with a 0.35 second ramp time. Stator resistance is increased by $1.5x R_s$ at 0.35/2 second (kp=9, ki=3).....	207
8.55. Actual λ_{sD} (X axis) and λ_{sQ} (Y axis) circular trajectory with a 0.35 second ramp time. Stator resistance is increased by $1.5x R_s$ at 0.35/2 second (stopped at 0.28 s.)	208
8.56. Actual λ_{sD} (X axis) and λ_{sQ} (Y axis) circular trajectory with a 0.35 second ramp time. Stator resistance is increased by $1.5x R_s$ at 0.675 second (stopped at 0.28 s.)	209
8.57. Reference and actual speeds, actual position, and three phase currents when a 0.35 second ramp time is used (no initial torque, just ramp rate is added. A 0.1 A current offset is added to the D- and Q-axes currents in the SRF ($V_{dc} = 370$ V).....	211
8.58. Load torque (TL), T_{emref} , T_{emact} , $Flux_{est}$, and actual stator flux linkage. A 0.1 A offset occurs on the D- and Q-axes currents in the SRF when the ramp time is 0.35 second.....	212
8.59. Estimated λ_{sD} (X axis) and λ_{sQ} (Y axis) circular trajectory with a 0.35 second ramp time. A 0.1 A offset is included in the D- and Q-axes currents in the SRF ($V_{dc} = 370$ V). (kp=9, ki=3)	213
8.60. Reference and actual speeds, speed error (ref-act), estimated and actual positions when a 0.35 second ramp time is used (7.5 N·m. initial torque is used in the PI's integrator with appropriate ramp rate). A 0.1 A offset is included in the d- and q-axes currents in the RRF ($V_{dc} = 370$ V) ...	214
8.61. Phase-A current (i_{as}), i_{dqact} , and i_{dqrest} when a 0.35 second ramp time is used with a PI integrator initial value of 7.5 N·m. A 0.1 A offset is include to the d- and q-axes currents in the RRF ($V_{dc} = 370$ V).....	215

FIGURE	Page
8.62. Load torque (TL), T_{emref} , T_{emest} , and T_{emact} . A 0.1 A offset occurs on d- and q-axes currents in the RRF when ramp time is 0.35 second ($V_{dc} = 370$ V).....	216
8.63. $Flux_{ref}$, $Flux_{est}$, $Flux_{actual}$ when a 0.35 second ramp time is used with a PI integrator initial value of 7.5 N·m. A 0.1 A offset is included in the d- and q-axes currents in the RRF ($V_{dc} = 370$ V).....	217
8.64. Estimated λ_{sD} (X axis) and λ_{sQ} (Y axis) circular trajectory at a 0.35 second ramp time with a PI integrator initial value of 7.5 N·m. A 0.1 A offset is included in the d- and q-axes currents in the RRF ($V_{dc} = 370$ V). (kp=9, ki=3).....	218
8.65. Reference and actual speeds, speed error (ref-act), estimated and actual positions when a 0.35 second ramp time is used (7 N·m. initial torque is used in the PI's integrator with appropriate ramp rate). $0.7x \lambda_r$ is used at 0.35/2 sec. in the motor model ($V_{dc} = 370$ V). (kp=9, ki=3)	219
8.66. Phase-A current (i_{as}), $i_{dqgract}$, and i_{dqrest} when a 0.35 second ramp time is used with a PI integrator initial value of 7 N·m. $0.7x \lambda_r$ is used at 0.35/2 second in the motor model ($V_{dc} = 370$ V). (kp=9, ki=3).....	220
8.67. Load torque (TL), T_{emref} , T_{emest} , and T_{emact} . $0.7x \lambda_r$ is used at 0.35/2 second in the motor model ($V_{dc} = 370$ V). (kp=9, ki=3).....	221
8.68. $Flux_{ref}$, $Flux_{est}$, $Flux_{actual}$ when a 0.35 second ramp time is used with a PI integrator initial value of 7 N·m. $0.7x \lambda_r$ is used at 0.35/2 second in the motor model ($V_{dc} = 370$ V). (kp=9, ki=3).....	222
8.69. Estimated λ_{sD} (X axis) and λ_{sQ} (Y axis) circular trajectory at a 0.35 second ramp time with a PI integrator initial value of 7 N·m. $0.7x \lambda_r$ is used 0.35/2 second in the motor model ($V_{dc} = 370$ V). (kp=9, ki=3)	223

FIGURE	Page
A-1. Specifications of the Fujitsu MB907462A microcontroller.....	234
A-2. Theoretical background of active power, apparent power, power factor and connection of the power analyzer to the load (motor).....	236
A-3. MATLAB/SIMULINK [®] model of the proposed DTC	237

LIST OF TABLES

TABLE		Page
3.1	Measurements of Self-Resistance and Self-Inductance	76
3.2	Measurements of Line-to-Neutral Back-EMF for Each Phase (0-50 rpm)	81
5.1	Switching Table.....	118

CHAPTER I

INTRODUCTION

1.1. Principles of DC Brush Motors and Their Problems

DC motors have been the most widespread choice for use in high performance systems. The main reason for their popularity is the ability to control their torque and flux easily and independently. In DC brush machines, the field excitation that provides the magnetizing current is occasionally provided by an external source, in which case the machine is said to be separately excited. In particular, the separately excited DC motor has been used mainly for applications where there was a requirement for fast response and four-quadrant operation with high performance near zero speed.

Generally in DC brush motors, flux is controlled by manipulating field winding current and torque by changing the armature winding current. The trade-off is less rugged motor construction, which requires frequent maintenance and an eventual replacement of the brushes and commutators. It also precludes the use of a DC motor in hazardous environments where sparking is not permitted. Moreover, there is a potential drop called ‘contact potential difference’, associated with this arrangement, and is usually in the range of 1-1.5 V, leading to a drop in the effective input voltage.

The well-known DC brush motor, like any other rotating machine, has a stator and rotor (as shown in Fig. 1.1). On the stator (stationary part), there is a magnetic field which can be provided either by permanent magnets or by excited field windings on the stator poles. On the rotor, the main components are the armature winding, armature core, a mechanical switch called commutator which rotates, and a rotor shaft. The commutator

This thesis follows the style and format of *IEEE Transactions on Industry Applications*.

segments are insulated from one another and from the clamp holding them. In addition to that brushes, the stationary external components of the rotor, together with the commutator act not only as rotary contacts between the coils of the rotating armature and the stationary external circuit, but also as a switch to commutate the current to the external DC circuit so that it remains unidirectional even though the individual coil voltages are alternating.

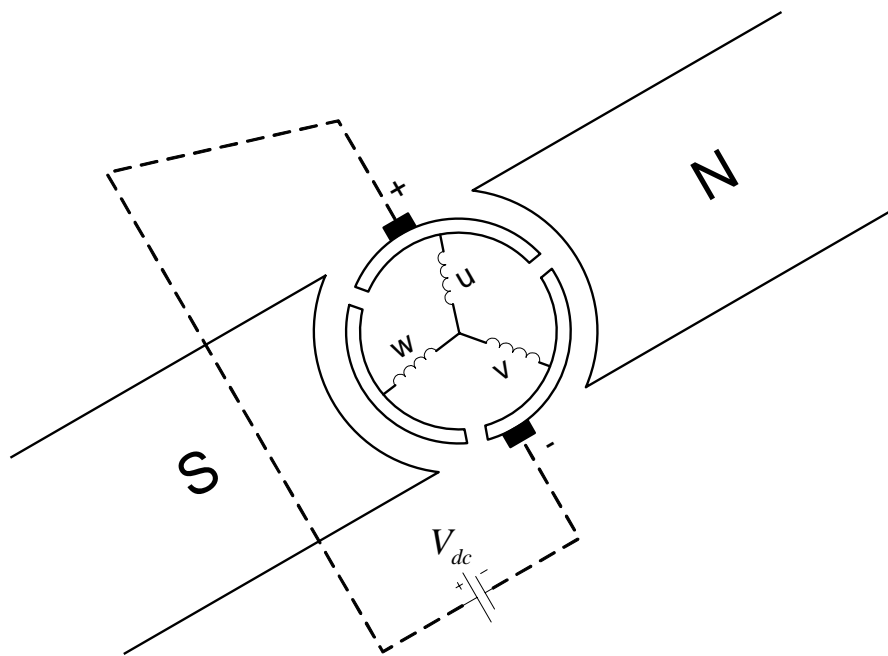


Fig. 1.1. Basic model of a DC brush motor.

The maximum torque is produced when the magnetic field of the stator and the rotor are perpendicular to each other (can be seen in Figs. 1.2 through 1.4, hypothetically). The commutator makes it possible for the rotor and stator magnetic fields to always be perpendicular. The commutation thus plays a very important part in the operation of the DC brush motor. It causes the current through the loop to reverse at the instant when unlike poles are facing each other. This causes a reversal in the polarity of the field, changing attractive magnetic force into a repulsive one causing the loop to continue to rotate.

When applying a voltage at the brushes, current flows through two of the coils. This current interacts with the magnetic field of the permanent magnet and produces torque. This torque causes to move. When the motor moves the brushes will switch to a different coil automatically causing the rotor to turn further. If the voltage (armature) is increased it will turn faster and if the magnetic field of permanent magnet is higher then it will produce more torque.

Since the back-EMF generated in the coil is short-circuited by the brush, a large current flows causing sparking at the interface of the commutator and the brushes, as well as causing heating and the production of braking torque. In order to minimize this problem, commutation is carried out in the magnetic field crossover region. Even after taking these measures, because of the distortion of the effective magnetic flux due to the armature reaction, some back-EMF is still generated in the coils in the magnetic filed crossover region. It is desirable to minimize the crossover region in order to maximize the utilization of the motor [1].

In general DC motors, the applied voltage (EMF) is never going to be greater than back-EMF. The difference between the applied EMF (voltage) and back-EMF is always such that current can flow in the conductor and produce motion.

Fundamental operation of the DC motor is explained from Figs. 1.2 through 1.4 as follows:

The direction of current flow from the DC voltage source in the figures is based on electron theory in which current flows from the negative terminal of a source of electricity to the positive terminal. On the contrary, the older convention supposes that current flows from positive terminal of a source of electricity through to the negative terminal [2].

The coil's pole pair positioning, shown in the figures, is decided by using Fleming's left hand rule for generators. If a coil resides in a magnetic field and the current and rotation of the coil are known, then direction of the magnetic field for the coil can be found easily by using Fleming's left hand rule. This rule states that if the thumb and the first and middle fingers of the left hand are perpendicular to one another,

with the first and middle fingers pointing in the flux direction and the thumb pointing in the direction of motion of the conductor, the middle finger will point in the direction in which the current flows [2].

With the loop in Fig. 1.2, the current flowing through the coil makes the top of the loop a north pole and the underside a south pole. This is found by applying the left-hand rule under the assumption of the back-EMF (direction) is opposite of the direction of current flow which is provided by DC voltage source [2].

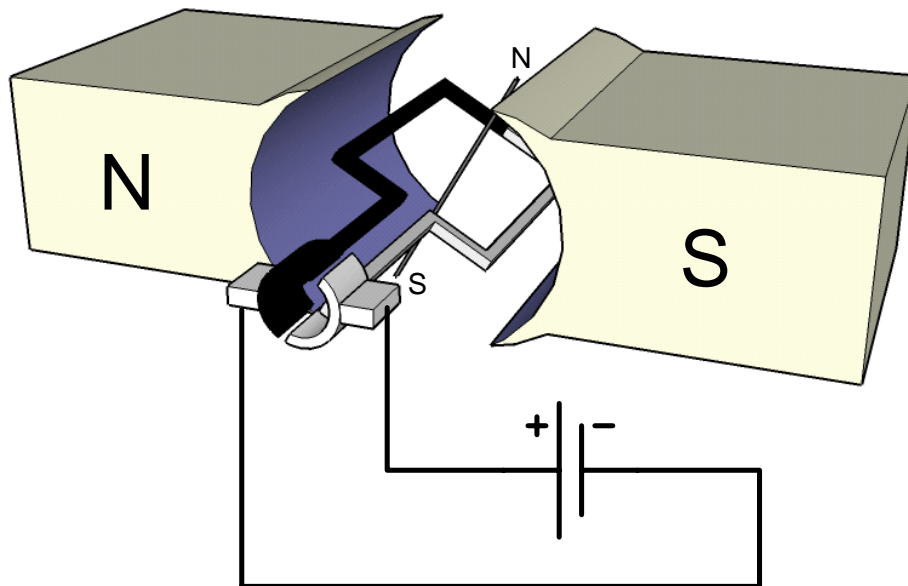


Fig. 1.2. Fundamental operation of a DC brush motor (Step 1).

The magnetic poles of the loop will be repelled by the like poles and attracted by the corresponding opposite poles of the field. The coil will therefore rotate clockwise, attempting to bring the unlike poles together.

When the loop has rotated through 90 degrees, shown in Fig. 1.3, commutation takes place, and the current through the loop reverses its direction. As a result, the magnetic field generated by the loop is reversed. Now, like poles face each other which means that they repel each other and the loop continues to rotate in an attempt to bring unlike poles together [2].

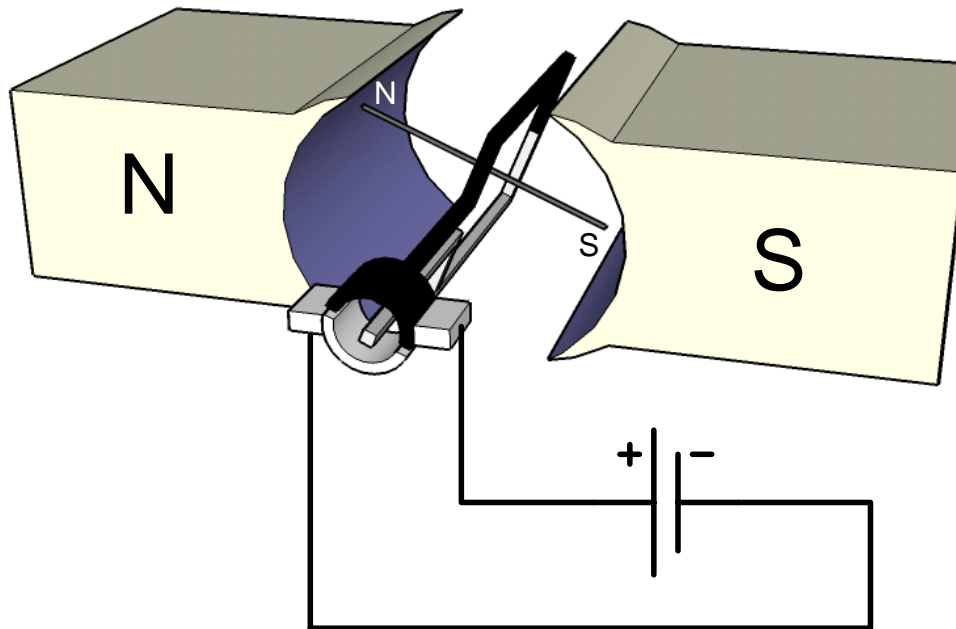


Fig. 1.3. Fundamental operation of a DC brush motor (Step 2).

Fig. 1.4 shows the loop position after being rotated 180 degrees from Fig. 1.3. Now the situation is the same as when the loop was back in the position shown in Fig. 1.3. Commutation takes place once again, and the loop continues to rotate. In this very basic DC brush motor example, two commutator segments used with one coil loop for simplicity. Having a small number of commutator segments in DC brush motor causes torque ripples. As the number of segments increases, the torque fluctuation produced by commutation is greatly reduced. In a practical machine, for example, one might have as many as 60 segments, and the variation of the load angle between stator magnetic flux and rotor flux would only vary ± 3 degrees, with a fluctuation of less than 1 percent. Thus, the DC brush motor can produce a nearly constant torque [3].

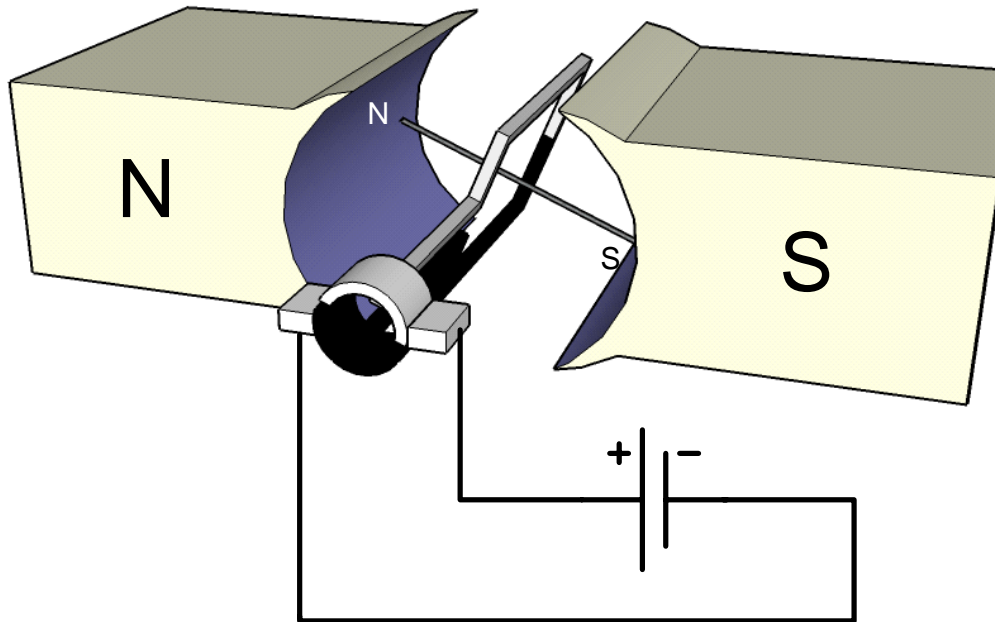


Fig. 1.4. Fundamental operation of a DC brush motor (Step 3).

1.2. Mathematical Model of the DC Brush Motor

Fig. 1.5 depicts the electrical circuit model of a separately excited DC motor. The field excitation is shown as a voltage, V_f , which generates a field current, I_f , that flows through a variable resistor (which permits adjustment of the field excitation,) R_f , and through the field coil, L_f . The armature circuit, on the other hand, consists of a back-emf, E_b , an armature resistance, R_a , and an armature voltage, V_a .

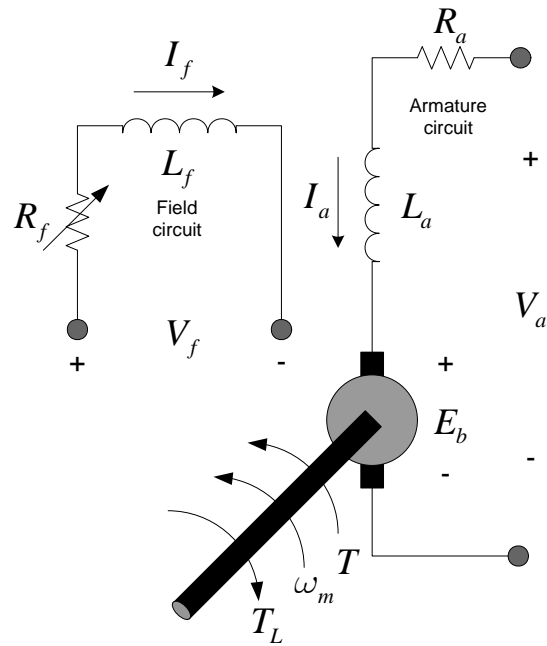


Fig. 1.5. Electrical circuit model of a separately excited DC brush motor (transient-state).

In the motor mode, $V_a > E_b$, armature current, I_a , flows into the machine. Thus, according to the circuit model of Fig. 1.6, the operation of a DC brush motor at steady-state, considering the inductance terms as zero, is described by the following equation:

$$V_a = R_a I_a + E_b \quad (\text{armature circuit at steady-state}) \quad (1.1)$$

$$I_f = \frac{V_f}{R_f} \quad (\text{field circuit at steady-state}) \quad (1.2)$$

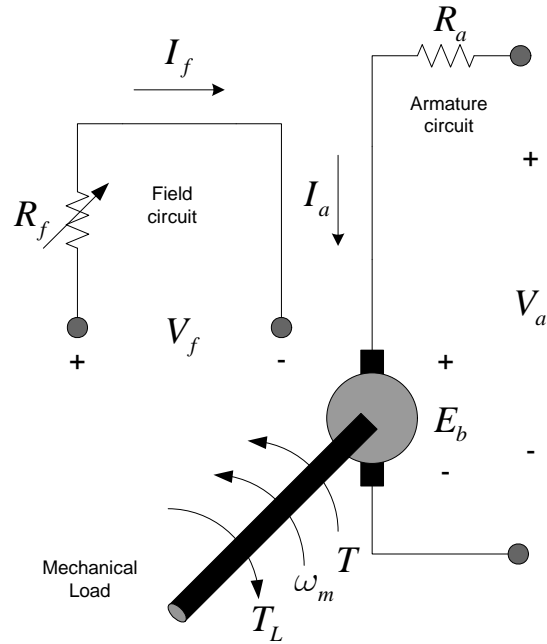


Fig. 1.6. Electrical circuit model of a separately excited DC brush motor (steady-state).

The equations describing the dynamic behavior of a separately excited DC brush motor, as its circuit model in Fig. 1.5 depicts, are as follows:

$$V_a(t) = R_a I_a(t) + L_a \frac{dI_a(t)}{dt} + E_b(t) \quad (\text{Armature circuit at transient-state}) \quad (1.3)$$

$$V_f(t) = R_f I_f(t) + L_f \frac{dI_f(t)}{dt} \quad (\text{Field circuit at transient-state}) \quad (1.4)$$

The torque developed by the motor can be written as follows:

$$T_{em}(t) = T_L + B\omega_m(t) + J \frac{d\omega_m(t)}{dt} \quad (1.5)$$

In that equation, the total moment of inertia is represented by J such that the motor is assumed to be rigidly connected to an inertial load. Friction losses in the load are represented by a viscous friction coefficient by B , and load torque is represented by T_L , which is typically either constant or some function of speed, ω_m . Using these

conventions, the electromechanical (developed) torque of the DC brush motor can be written as follows:

Since the electromechanical torque is related to the armature and field currents by (1.6), (1.5) and (1.6) they are coupled to each other. This coupling may be expressed as follows:

$$T_{em}(t) = k_T \phi I_a(t) \quad (1.6)$$

where k_T is called the torque constant and is related to the geometry and magnetic properties of the structure.

Rotation of the armature conductors in the field generated by field excitation causes a back-EMF, E_b , in a direction that opposes the rotation of the armature. This back-EMF is given by the expression:

$$E_b = k_a \phi \omega_m \quad (1.7)$$

where k_a is called the armature constant which is related to the geometry and magnetic properties of the structure (like k_T does). The constants k_a and k_T in (1.6) and (1.7) are related to geometry factors, such as the dimension of the rotor, the number of turns in the armature winding, and the properties of materials, such as the permeability of the magnetic materials.

The mechanical generated output power P_m is given by:

$$P_m = \omega_m T_{em} = \omega_m k_T \phi I_a \quad (1.8)$$

where ω_m is the mechanical speed in rad/s.

The electric power dissipated by the motor is given by the product of the back-EMF and the armature current which is shown as follows:

$$P_e = E_b I_a \quad (1.9)$$

The ideal energy-conversion case, $P_m = P_e$, k_T will equal k_a .

If the angular speed is denoted as rad/s, then k_a can be expressed as:

$$k_a = \frac{pN}{2\pi M} \quad (1.10)$$

where p is the number of magnetic poles, N is the number of conductors per coil and M is the number of parallel paths in armature winding.

Furthermore, (1.6) can be substituted into (1.5) which yields the following equation:

$$k_T \phi I_a(t) = T_L + b\omega_m(t) + J \frac{d\omega_m(t)}{dt} \quad (1.11)$$

In the case of separately excited DC brush motors as shown in Fig. 1.6, the field flux is established by a separate field excitation, therefore the flux equation can be written as follows:

$$\phi = \frac{N_f}{R} I_f = k_f I_f \quad (1.12)$$

where N_f is the number of turns in the field coil, R is the reluctance of the field circuit and I_f is the field current.

1.3. AC Motors and Their Trends

Unlike DC brush motors, AC motors such as Permanent Magnet AC motors (PMSM, and BLDC motors), and Induction Motors (IM) are more rugged meaning that they have lower weight and inertia than DC motors. The main advantage of AC motors over DC motors is that they do not require an electrical connection between the stationary and rotating parts of the motor. Therefore, they do not need any mechanical commutator and brush, leading to the fact that they are maintenance free motors. They also have higher efficiency than DC motors and a high overload capability.

All of the advantages listed above label AC motors as being more robust, quite cheaper, and less prone to failure at high speeds. Furthermore, they can work in explosive or corrosive environments because they don't produce sparks.

All the advantages outlined above show that AC motors are the perfect choice for electrical to mechanical conversion. Usually mechanical energy is required not at a constant speeds but variable speeds. Variable speed control for AC drives is not a trivial matter. The only way of producing variable speeds AC drives is by supplying the motor with a variable amplitude and frequency three phase source.

Variable frequency changes the motor speed because the rotor speed depends on the speed of the stator magnetic field which rotates at the same frequency of the applied voltage. For example, the higher the frequency of the applied voltage the higher the speed. A variable voltage is required because as the motor impedance reduces at low frequencies the current has to be limited by means of reducing the supply voltage [4].

Before the days of power electronics and advanced control techniques, such as vector control and direct torque control AC motors have traditionally been unsuitable for variable speed applications. This is due to the torque and flux within the motor being coupled, which means that any change in one will affect the other.

In the early times, very limited speed control of induction motors was achieved by switching the three-stator windings from delta connection to star connection, allowing the voltage at the motor windings to be reduced. If a motor has more than three stator windings, then pole changing is possible, but only allows for certain discrete speeds. Moreover, a motor with several stator windings is more expensive than a conventional three phase motor. This speed control method is costly and inefficient [5].

Another alternative way of speed control is achieved by using wound rotor induction motor, where the rotor winding ends are connected to slip rings. This type of motor however, negates the natural advantages of conventional induction motors and it also introduces additional losses by connecting some impedance in series with the stator windings of the induction motor. This results in very poor performance [5].

At the time the above mentioned methods were being used for induction motor speed control, DC brush motors were already being used for adjustable speed drives with good speed and torque performance [5].

The goal was to achieve an adjustable speed drive with good speed characteristics compared to the DC brush motor. Even after discovering of the AC asynchronous motor, also named induction motor, in 1883 by Tesla, more than six decades later of invention of DC brush motors, capability of adjustable speed drives for induction motors is not as easy as DC brush motors.

Speed control for DC motors is easy to achieve. The speed is controlled by applied voltage; e.g. the higher the voltage the higher the speed. Torque is controlled by armature current; e.g. the higher the current the higher the torque. In addition, DC brush motor drives are not only permitted four quadrant operations but also provided with wide power ranges.

Recent advances in the development of fast semiconductor switches and cost-effective DSPs and micro-processors have opened a new era for the adjustable speed drive. These developments have helped the field of motor drives by shifting complicated hardware control structures onto software based advanced control algorithms. The result is a considerable improvement in cost while providing better performance of the overall drive system. The emergence of effective control techniques such as vector and direct torque control, via DSPs and microprocessors allow independent control of torque and flux in an AC motor, resulting in achievement of linear torque characteristics resembling those of DC motors.

1.4. Thesis Outline

This thesis is mainly organized as follows: First, the modeling and analysis of the simple low-cost BLDC motor speed control on a laundry washing machine during the agitation part of a washing cycle using Ansoft\SIMPLORER[®] is presented and compared

with the experimental ones for verification of the simulation model. To accomplish this, motor parameters are measured to be used in the simulation platforms without considering the saturation and temperature effects on the measured parameters.

Second, open-loop, steady-state and transient MATLAB/SIMULINK[®] models are built in the dq-axis rotor reference frame. Also, to verify the open-loop simulation models, open-loop, steady-state and transient test-beds are built. Open-loop experimental tests are conducted under no-load and load conditions using a three phase AC power source and results are discussed.

Third, the theoretical basis behind the simple low-cost speed control of a BLDC motor is explained and the steady-state simulation model is built in SIMPLORER[®] for comparison with the experimental results.

Fourth, overall transient and steady-state speed control of the agitation cycle in a laundry washing machine is modeled in SIMPLORER[®] and verified with the experimental tests under no-load and load conditions.

As a final goal, the proposed direct torque control of the PMSM method is developed in MATLAB/SIMULINK[®] using the rotor reference frame with the help of cheap hall-effect sensors without using any DC-link voltage sensing. This method is then applied to the agitation cycle of washing machine speed control system for the speed performance comparison of both methods.

The suggested method over current techniques is tested under heavy transient load conditions resembling real washing machine load characteristics. Possible disadvantages that may be observed in the proposed method are also considered, such as offset and the rotor flux linkage amplitude change effect which occurs when temperature increases on the machine. Advantages of the proposed speed control over current methods are discussed and the results are compared.

CHAPTER II

BASIC OPERATIONAL PRINCIPLES OF PERMANENT MAGNET SYNCHRONOUS AND BRUSHLESS DC MOTORS

2.1. Permanent Magnet Synchronous Motors (PMSMs)

Recent availability of high energy-density permanent magnet (PM) materials at competitive prices, continuing breakthroughs and reduction in cost of powerful fast digital signal processors (DSPs) and micro-controllers combined with the remarkable advances in semiconductor switches and modern control technologies have opened up new possibilities for permanent magnet brushless motor drives in order to meet competitive worldwide market demands [1].

The popularity of PMSMs comes from their desirable features [4]:

- High efficiency
- High torque to inertia ratio
- High torque to inertia ratio
- High torque to volume ratio
- High air gap flux density
- High power factor
- High acceleration and deceleration rates
- Lower maintenance cost
- Simplicity and ruggedness
- Compact structure
- Linear response in the effective input voltage

However, the higher initial cost, operating temperature limitations, and danger of demagnetization mainly due to the presence of permanent magnets can be restrictive for some applications.

In permanent magnet (PM) synchronous motors, permanent magnets are mounted inside or outside of the rotor. Unlike DC brush motors, every brushless DC (so called BLDC) and permanent magnet synchronous motor requires a “drive” to supply commutated current. This is obtained by pulse width modulation of the DC bus using a DC-to-AC inverter attached to the motor windings. The windings must be synchronized with the rotor position by using position sensors or through sensorless position estimation techniques. By energizing specific windings in the stator, based on the position of the rotor, a rotating magnetic field is generated. In permanent magnet ac motors with sinusoidal current excitation (so called PMSM), all the phases of the stator windings carry current at any instant, but in permanent magnet AC motors with quasi-square wave current excitation (BLDC), which will be discussed in more detail later, only two of the three stator windings are energized in each commutation sequence [1].

In both motors, currents are switched in a predetermined sequence and hence the permanent magnets that provide a constant magnetic field on the rotor follow the rotating stator magnetic field at a constant speed. This speed is dependent on the applied frequency and pole number of the motor. Since the switching frequency is derived from the rotor, the motor cannot lose its synchronism. The current is always switched before the permanent magnets catch up, therefore the speed of the motor is directly proportional to the current switching rate [5].

Recent developments in the area of semiconductor switches and cost-effective DSPs and micro-processors have opened a new era for the adjustable speed motor drives. Such advances in the motor related sub-areas have helped the field of motor drives by replacing complicated hardware structures with software based control algorithms. The result is considerable improvement in cost while providing better performance of the overall drive system [6].

Vector control techniques, including direct torque control incorporating fast DSPs and micro-processors, have made the application of induction motor, synchronous motor, recently developed PMSM, and BLDC motor drives possible for high performance applications where traditionally only DC brush motor drives were applied.

In the past, such control techniques would have not been possible because of complex hardware and software requirement to solve the sophisticated algorithms. However with the recent advances in the field of power electronics, microprocessor, and DSPs this phenomenon is solved.

Like DC brush motors, torque control in AC motors is achieved by controlling the motor currents. However, unlike DC brush motor, in AC motors both the phase angle and the modulus of the current has to be controlled, in other words the current vector should be controlled. That is why the term “vector control” is used for AC motors. In DC brush motors the field flux and armature MMF are coupled, whereas in AC motors the rotor flux and the spatial angle of the armature MMF requires external control. Without this type of control, the spatial angle between various fields in the AC motor will vary with the load and cause unwanted oscillating dynamic response. With vector control of AC motors, the torque and flux producing current components are decoupled resembling a DC brush motor, the transient response characteristics are similar to those of a separately excited DC motor, and the system will adapt to any load disturbances and/or reference value variations as fast as a brushed-DC motor [4].

The primitive version of the PMAC motor is the wound-rotor synchronous motor which has an electrically excited rotor winding which carries a DC current providing a constant rotor flux. It also usually has a three-phase stator winding which is similar to the stator of induction motors.

The synchronous motor is a constant-speed motor which always rotates at synchronous speed depending on the frequency of the supply voltage and the number of poles. The permanent magnet synchronous motor is a kind of synchronous motor if its electrically excited field windings are replaced by permanent magnets which provide a constant rotor magnetic field.

The main advantages of using permanent magnets over field excitation circuit used by conventional synchronous motors are given below [4]:

- Elimination of slip-rings and extra DC voltage supply.
- No rotor copper losses generated in the field windings of wound-field synchronous motor.
- Higher efficiency because of fewer losses.
- Since there is no circuit creating heat on the rotor, cooling of the motor just through the stator in which the copper and iron losses are observed is more easily achieved.
- Reduction of machine size because of high efficiency.
- Different size and different arrangements of permanent magnets on the rotor will lead to have wide variety of machine characteristics.

PMAC motors have gained more popularity especially after the advent of high performance rare-earth permanent magnets, like samarium cobalt and neodymium-boron iron which surpass the conventional magnetic material in DC brush and induction motors and are becoming more and more attractive for industrial applications.

The positive specific characteristics of PMAC motors explained above make them highly attractive candidates for several classes of drive applications, such as in servo-drives containing motors with a low to mid power range, robotic applications, motion control system, aerospace actuators, low integral-hp industrial drives, fiber spinning and so on. Also high power rating PMAC motors have been built, for example, for ship propulsion drives up to 1 MW. Recently two major sectors of consumer market are starting to pay more attention to the PM motor drive due to its features [7].

PMAC motors have many advantages over DC brush motors and induction motors. Most of these are summarized as [1]:

- High dynamic response
- High efficiency providing reduction in machine size
- Long operating life
- Noiseless operation

- High power factor
- High power to weight ratio; considered the best comparing to other available electric motors
- High torque to inertia ratio; providing quick acceleration and deceleration for short time
- High torque to volume ratio
- High air-gap flux density
- Higher speed ranges
- Better speed versus torque characteristics
- Lower maintenance cost
- Simplicity and ruggedness
- Compact design
- Linear response
- Controlled torque at zero speed

Compared to IMs, PMSMs have some advantages, such as higher efficiency in steady-state, and operate constantly at synchronous speed. They do not have losses due to the slip which occurs when the rotor rotates at a slightly slower speed than the stator because the process of electromagnetic induction requires relative motion called “slip” between the rotor conductors and the stator rotating field that is special to IM operation. The slip makes the induction motor asynchronous, meaning that the rotor speed is no longer exactly proportional to the supply frequency [1].

In IMs, stator current has both magnetizing and torque-producing currents. On the other hand, in PMSMs there is no need to supply magnetizing current through the stator for constant air-gap flux. Since the permanent magnet generates constant flux in the rotor, only the stator current is needed for torque production. For the same output, the PMSM will operate at a higher power factor and will be more efficient than the IM [1].

Finally, since the magnetizing is provided from the rotor circuit by permanent magnets instead of the stator, the motor can be built with a large air gap without losing

performance. According to the above results, the PMSM has a higher efficiency, torque to ampere rating, effective power factor and power density when compared with an IM. Combining these factors, small PM synchronous motors are suitable for certain high performance applications such as robotics and aerospace actuators in which there is a need for high torque/inertia ratio [1].

Induction machine drives have been widely used in industry. Squirrel-cage induction machines have become popular drive motors due to their simple, rugged structure, ease of maintenance, and low cost. In pumps, fans, and general-purpose drive systems, they have been a major choice. In servo applications, permanent magnet (PM) machine drives are more popular due to their high output torque performance. They are also actively used in high-speed applications, not only as motors/starters but also as generators, as in the flywheel energy storage system (FEES), electric vehicle (EV), and industrial turbo-generator system (ITG) [7].

The smaller the motor, the more preferable it is to use permanent magnet synchronous motors. As motor size increases the cost of the magnetics increases as well making large PMACs cost ineffective. There is no actual “breakpoint” under which PMSMs outperform induction motors, but the 1-10 kW range is a good estimate of where they do [8].

As compared with induction and conventional wound-rotor synchronous motors (WRSM), PMSMs have certain advantages over both motors, including the fact that there is no field winding on the rotor as compared to the WRSM, therefore there are no attendant copper losses. Moreover, there is no circuit in the rotor but only in the stator where heat can be removed more easily [1].

Compared with conventional WRSMs, elimination of the field coil, DC supply, and slip rings result in a much simpler motor. In a PMSM, there is no field excitation control. The control is provided by just stator excitation control. Field weakening is possible by applying a negative direct axis current in the stator to oppose the rotor magnet flux [1].

Elimination of the need for separate field excitation results in smaller overall size such that for the same field strength the diameter of a PMSM is considerably smaller than its wound field counterpart, providing substantial savings in both size and weight.

2.1.1. Mathematical Model of PMSM

In a permanent magnet synchronous motor (PMSM) where the inductances vary as a function of the rotor angle, the two-phase (d-q) equivalent circuit model is a perfect solution to analyze the multiphase machines because of its simplicity and intuition. Conventionally, a two-phase equivalent circuit model instead of complex three-phase model has been used to analyze reluctance synchronous machines [9]. This theory is now applied in the analysis of other types of motors including PM synchronous motors, induction motors etc.

In this section, an equivalent two-phase circuit model of a three-phase PM synchronous machine (interior and surface mount) is derived in order to clarify the concept of the transformation (Park) and the relation between three-phase quantities and their equivalent two-phase quantities.

Throughout the derivation of the two-phase (d-q) mathematical model of PMSM, the following assumptions are made [6]:

- Stator windings produce sinusoidal MMF distribution. Space harmonics in the air-gap are neglected.
- Air-gap reluctance has a constant component as well as a sinusoidal varying component.
- Balanced three-phase sinusoidal supply voltage is considered.
- Eddy current and hysteresis effects are neglected.
- Presence of damper windings is not considered; PM synchronous motors used today rarely have that kind of configuration.

Comparing a primitive version of a PMSM with wound-rotor synchronous motor, the stator of a PMSM has windings similar to those of the conventional wound-rotor

synchronous motor which is generally three-phase, Y-connected, and sinusoidally distributed. However, on the rotor side instead of the electrical-circuit seen in the wound-rotor synchronous motor, constant rotor flux (λ_r) provided by the permanent magnet in/on the rotor should be considered in the d-q model of a PMSM.

The space vector form of the stator voltage equation in the stationary reference frame is given as:

$$\vec{v}_s = r_s \vec{i}_s + \frac{d\vec{\lambda}_s}{dt} \quad (2.1)$$

where, r_s , \vec{v}_s , \vec{i}_s , and $\vec{\lambda}_s$ are the resistance of the stator winding, complex space vectors of the three phase stator voltages, currents, and flux linkages, all expressed in the stationary reference frame fixed to the stator, respectively. They are defined as:

$$\begin{aligned} \vec{v}_s &= \frac{2}{3} [v_{sa}(t) + av_{sb}(t) + a^2v_{sc}(t)] \\ \vec{i}_s &= \frac{2}{3} [i_{sa}(t) + ai_{sb}(t) + a^2i_{sc}(t)] \\ \vec{\lambda}_s &= \frac{2}{3} [\lambda_{sa}(t) + a\lambda_{sb}(t) + a^2\lambda_{sc}(t)] \end{aligned} \quad (2.2)$$

The resultant voltage, current, and flux linkage space vectors shown in (2.2) for the stator are calculated by multiplying instantaneous phase values by the stator winding orientations in which the stator reference axis for the a-phase is chosen to the direction of maximum MMF. Reference axes for the b- and c- stator frames are chosen 120° and 240° (electrical degree) ahead of the a-axis, respectively. Fig. 2.1 illustrates a conceptual cross-sectional view of a three-phase, two-pole surface PM synchronous motor along with the two-phase d-q rotating reference frame.

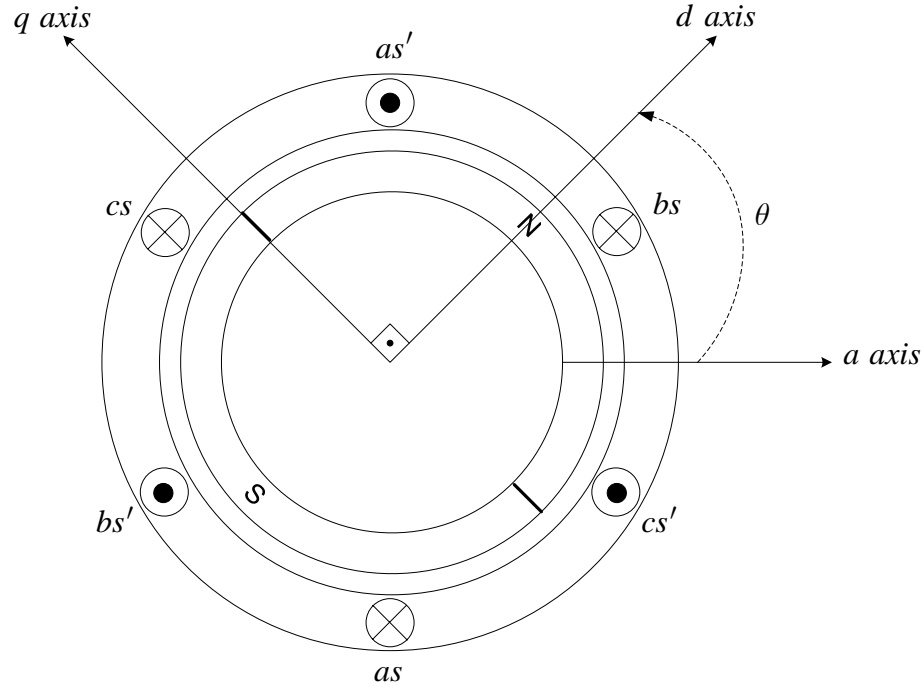


Fig. 2.1. Two-pole three phase surface mounted PMSM.

Symbols used in (2.2) are explained in detail below:

a , and a^2 are spatial operators for orientation of the stator windings; $a = e^{j2\pi/3}$,
 $a^2 = e^{j4\pi/3}$.

v_{sa} , v_{sb} , and v_{sc} are the values of stator instantaneous phase voltages.

i_{sa} , i_{sb} , and i_{sc} are the values of stator instantaneous phase currents.

λ_{sa} , λ_{sb} , and λ_{sc} are the stator flux linkages and are given by:

$$\begin{aligned}\lambda_{sa} &= L_{aa}i_a + L_{ab}i_b + L_{ac}i_c + \lambda_{ra} \\ \lambda_{sb} &= L_{ab}i_a + L_{bb}i_b + L_{bc}i_c + \lambda_{rb} \\ \lambda_{sc} &= L_{ac}i_a + L_{bc}i_b + L_{cc}i_c + \lambda_{rc}\end{aligned}\tag{2.3}$$

where

L_{aa} , L_{bb} , and L_{cc} are the self-inductances of the stator a-phase, b-phase, and c-phase respectively.

L_{ab} , L_{bc} , and L_{ac} are the mutual inductances between the a- and b-phases, b- and c-phases, and a- and c-phases, respectively.

λ_{ra} , λ_{rb} , and λ_{rc} are the flux linkages that change depending on the rotor angle established in the stator a, b, and c phase windings, respectively, due to the presence of the permanent magnet on the rotor. They are expressed as:

$$\begin{aligned}\lambda_{ra} &= \lambda_r \cos \theta \\ \lambda_{rb} &= \lambda_r \cos(\theta - 120^\circ) \\ \lambda_{rc} &= \lambda_r \cos(\theta + 120^\circ)\end{aligned}\tag{2.4}$$

In (2.4), λ_r represents the peak flux linkage due to the permanent magnet. It is often referred to as the back-EMF constant, k_e .

It can be seen in Fig. 2.1 that the direction of permanent magnet flux is chosen as the d-axis, while the q-axis is 90° ahead of the d-axis. The symbol, θ , represents the angle of the q-axis with respect to the a-axis.

Note that in the flux linkage equations, inductances are the functions of the rotor angle, θ . Self-inductance of the stator a-phase winding, L_{aa} , including leakage inductance and a- and b-phase mutual inductance, $L_{ab} = L_{ba}$, have the form:

$$\begin{aligned}L_{aa} &= L_{ls} + L_0 - L_{ms} \cos(2\theta) \\ L_{ab} = L_{ba} &= -\frac{1}{2}L_0 - L_{ms} \cos(2\theta - \frac{2\pi}{3})\end{aligned}\tag{2.5}$$

where

L_{ls} is the leakage inductance of the stator winding due to the armature leakage flux.

L_0 is the average inductance; due to the space fundamental air-gap flux;

$$L_0 = \frac{1}{2}(L_q + L_d),$$

L_{ms} is the inductance fluctuation (saliency); due to the rotor position dependent on flux; $L_{ms} = \frac{1}{2}(L_d - L_q)$.

For mutual inductance, $L_{ab} = L_{ba}$, in the above equation, a $-(1/2)$ coefficient appears due to the fact that stator phases are displaced by 120° , and $\cos(120^\circ) = -1/2$.

Similar to that of L_{aa} , but with θ replaced by $(\theta - \frac{2\pi}{3})$ and $(\theta - \frac{4\pi}{3})$, b-phase and c-phase self-inductances, L_{bb} and L_{cc} can also be obtained, respectively.

Also, a similar expression for L_{bc} and L_{ac} can be provided by replacing θ in (2.5) with $(\theta - \frac{2\pi}{3})$ and $(\theta - \frac{4\pi}{3})$, respectively.

All stator inductances are represented in matrix form below:

$$L_{ss} = \begin{bmatrix} L_{ls} + L_0 - L_{ms} \cos 2\theta & -\frac{1}{2}L_0 - L_{ms} \cos 2(\theta - \frac{\pi}{3}) & -\frac{1}{2}L_0 - L_{ms} \cos 2(\theta + \frac{\pi}{3}) \\ -\frac{1}{2}L_0 - L_{ms} \cos 2(\theta - \frac{\pi}{3}) & L_{ls} + L_0 - L_{ms} \cos 2(\theta - \frac{2\pi}{3}) & -\frac{1}{2}L_0 - L_{ms} \cos 2(\theta - \pi) \\ -\frac{1}{2}L_0 - L_{ms} \cos 2(\theta + \frac{\pi}{3}) & -\frac{1}{2}L_0 - L_{ms} \cos 2(\theta + \pi) & L_{ls} + L_0 - L_{ms} \cos 2(\theta + \frac{2\pi}{3}) \end{bmatrix} \quad (2.6)$$

It is evident from (2.6) that the elements of L_{ss} are a function of the rotor angle which varies with time at the rate of the speed of rotation of the rotor [10].

Under a three-phase balanced system with no rotor damping circuit and knowing the flux linkages, stator currents, and resistances of the motor, the electrical three-phase dynamic equation in terms of phase variables can be arranged in matrix form similar to that of (2.1) written as:

$$[v_s] = [r_s][i_s] + \frac{d}{dt}[\Lambda_s] \quad (2.7)$$

where,

$$\begin{aligned}
[v_s] &= [v_{sa}, v_{sb}, v_{sc}]^t \\
[i_s] &= [i_{sa}, i_{sb}, i_{sc}]^t \\
[r_s] &= \text{diag}[r_a, r_b, r_c]^t \\
[\Lambda_s] &= [\lambda_{sa}, \lambda_{sb}, \lambda_{sc}]^t
\end{aligned} \tag{2.8}$$

In (2.7), $[v_s]$, $[i_s]$, and $[\Lambda_s]$ refer to the three-phase applied voltages, three-phase stator currents, and three-phase stator flux linkages in matrix forms as shown in (2.8), respectively. Furthermore, $[r_s]$ is the diagonal matrix in which under balanced three-phase conditions, all phase resistances are equal to each other and represented as a constant, $r_s = r_a = r_b = r_c$, not in matrix form.

The matrix representation of the flux linkages of the three-phase stator windings can also be expressed with using equations (2.4), (2.6) and (2.8) as

$$[\Lambda_s] = L_{ss}[i_s] + [\Lambda_r] \tag{2.9}$$

where, L_{ss} is the stator inductance matrix varying with rotor angle.

$[\Lambda_r]$ is the flux linkage matrix due to permanent magnet; $[\Lambda_r] = [\lambda_{ra}, \lambda_{rb}, \lambda_{rc}]^t$

As it was discussed before, L_{ss} has time-dependent coefficients which present computational difficulty when (2.1) is being used to solve for the phase quantities directly. To obtain the phase currents from the flux linkages, the inverse of the time-varying inductance matrix will have to be computed at every time step. The computation of the inverse at every time step is time-consuming and could produce numerical stability problems [10].

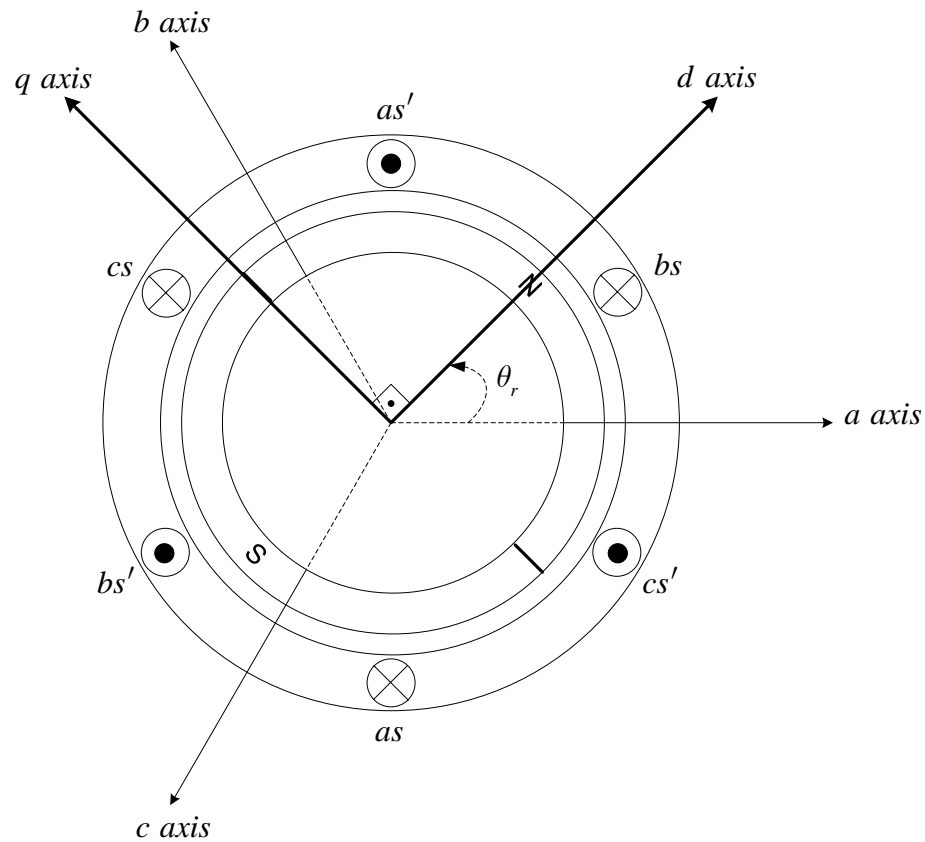


Fig. 2.2. Q-axis leading d-axis and the rotor angle represented as θ_r .

To remove the time-varying quantities in voltages, currents, flux linkages and phase inductances, stator quantities are transformed to a d-q rotating reference frame. This results in the voltages, currents, flux linkages, part of the flux linkages equation and inductance equations having time-invariant coefficients. In the idealized machine, the rotor windings are already along the q- and d-axes, only the stator winding quantities need transformation from three-phase quantities to the two-phase d-q rotor rotating reference frame quantities. To do so, Park's Transformation is used to transform the stator quantities of an AC machine onto a d-q reference frame that is fixed to the rotor, with the positive d-axis aligned with the magnetic axis of the rotor which has a permanent magnet in PMSMs. The positive q-axis is defined as leading the positive d-axis by $\pi/2$ in the original Park's Transformation, as shown in Fig. 2.2. The original Park's Transformation equation is of the form:

$$[f_{dq0}] = [T_{dq0}(\theta_r)][f_{abc}] \quad (2.10)$$

where the d-q transformation matrix is defined as:

$$[T_{dq0}(\theta_r)] = \frac{2}{3} \begin{bmatrix} \cos \theta_r & \cos(\theta_r - \frac{2\pi}{3}) & \cos(\theta_r + \frac{2\pi}{3}) \\ -\sin \theta_r & -\sin(\theta_r - \frac{2\pi}{3}) & -\sin(\theta_r + \frac{2\pi}{3}) \\ \frac{1}{2} & \frac{1}{2} & \frac{1}{2} \end{bmatrix} \quad (2.11)$$

and its inverse is given by

$$[T_{dq0}(\theta_r)]^{-1} = \begin{bmatrix} \cos \theta_r & -\sin \theta_r & 1 \\ \cos(\theta_r - \frac{2\pi}{3}) & -\sin(\theta_r - \frac{2\pi}{3}) & 1 \\ \cos(\theta_r + \frac{2\pi}{3}) & -\sin(\theta_r + \frac{2\pi}{3}) & 1 \end{bmatrix} \quad (2.12)$$

In Fig. 2.2, if the d-q axis is turned $\pi/2$ radian degrees clock wise (CW), the q-d transformation is obtained which is still considered a Park's Transformation as shown in Fig. 2.3. In the q-d transformation, the q-axis still leads the d-axis but angle representation is changed such that now θ is the rotor angle between the q-axis and a-axis which is chosen as a 0° reference for simplicity. Q-d transformation is used to analyze the self and mutual inductances because of the ease of calculation. θ_r is considered as the actual rotor position (generally it can be obtained by using an encoder or similar position sensors) with respect to the a-axis which is used in the original Park's Transformation matrix, $[T_{dq0}(\theta_r)]$, but the angle depicted in Fig. 2.3, θ , which is between the q-axis and a-axis in q-d transformation does not represent the real rotor position. Therefore, the d-axis should be considered as a reference for measuring the real rotor angle with respect to 0° position selected as the a-axis in general. Eventually, the d- and q- axis synchronous inductances will be independent of the rotor position so that either of the transformations will give the same result.

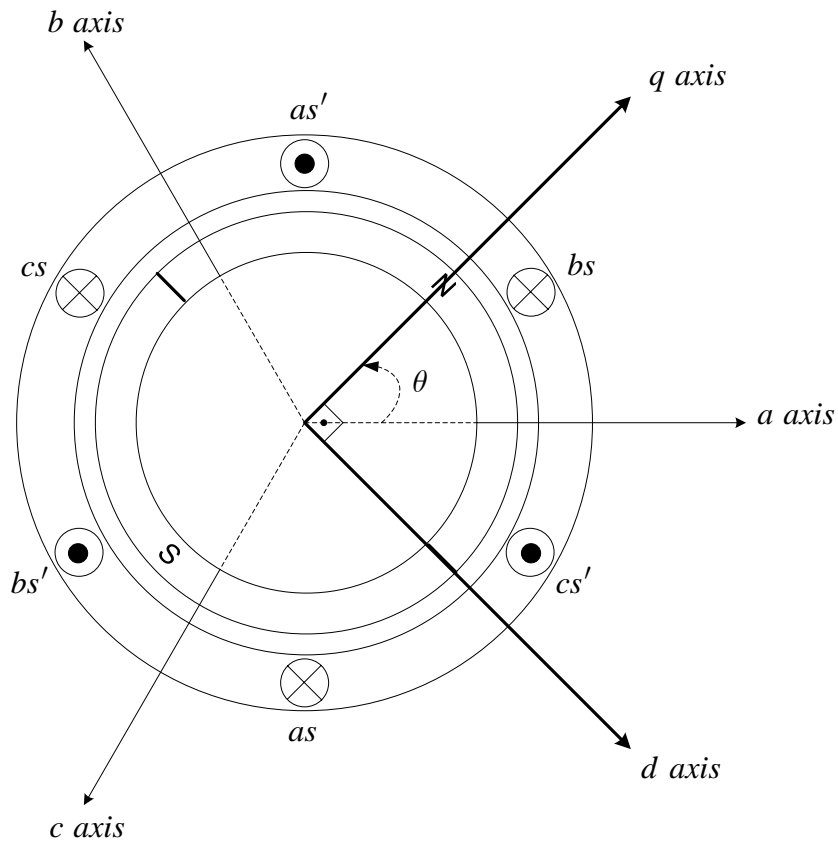


Fig. 2.3. Q-axis leading d-axis and the rotor angle represented as θ .

The Park's Transformation which has a d-q reference is of the form:

$$[f_{dq0}] = [T_{dq0}(\theta_r)][f_{abc}] \quad (2.13)$$

where f represents either a voltage, a current or a flux linkage; $[f_{qd0}] = [f_q, f_d, f_0]^t$,

$$[f_{abc}] = [f_a, f_b, f_c]^t.$$

The q-d transformation matrix is obtained as

$$[T_{qd0}(\theta)] = \frac{2}{3} \begin{bmatrix} \cos \theta & \cos(\theta - \frac{2\pi}{3}) & \cos(\theta + \frac{2\pi}{3}) \\ \sin \theta & \sin(\theta - \frac{2\pi}{3}) & \sin(\theta + \frac{2\pi}{3}) \\ \frac{1}{2} & \frac{1}{2} & \frac{1}{2} \end{bmatrix} \quad (2.14)$$

And the inverse of the above transformation matrix is given by

$$[T_{qd0}(\theta)]^{-1} = \begin{bmatrix} \cos \theta & \sin \theta & 1 \\ \cos(\theta - \frac{2\pi}{3}) & \sin(\theta - \frac{2\pi}{3}) & 1 \\ \cos(\theta + \frac{2\pi}{3}) & \sin(\theta + \frac{2\pi}{3}) & 1 \end{bmatrix} \quad (2.15)$$

Basically, if the rotor position θ is known, the above matrix transforms the variables of the stator reference frame to the one fixed to the rotor as shown in (2.13).

The relationship between θ and θ_r can be expressed with the help of Figs. 2.2 and 2.3 as

$$\theta = \theta_r + \frac{\pi}{2} \quad (2.16)$$

Equation (2.16) depicts that the actual rotor position, θ_r , is 90° (electrical degree) behind θ . If the q-d transformation matrix, $[T_{qd0}(\theta)]$, is used as a transformation matrix, the above description should be taken into account for deriving the q-d voltage equations of a PMSM.

If θ_r is known, the above formula can be substituted into the q-d transformation matrix $[T_{qd0}(\theta)]$ with the help of some trigonometric reduction equations shown below:

$$\begin{aligned} \cos(\theta_r + \frac{\pi}{2}) &= -\sin \theta_r \\ \sin(\theta_r + \frac{\pi}{2}) &= \cos \theta_r \end{aligned} \quad (2.17)$$

As a consequence of these manipulations, it has been observed that $[T_{qd0}(\theta)]$ and $[T_{dq0}(\theta_r)]$ are basically the same, except for the ordering of the d and q variables. One might say that $[T_{dq0}(\theta_r)]$ is more useful if no additional modification is wanted for assigning the actual rotor position, θ_r , as shown in Fig. 2.1.

Since L_{ss} is analyzed according to the q-d rotating reference frame, the corresponding relationship between flux linkages, $[\Lambda_{qd0}]$, the q-d axis currents, $[i_{qd0}]$, and the time-invariant q-d axis inductances, $[L_{qd0}]$, can be obtained by transforming only the stator quantities, that is:

$$[\Lambda_{qd0}] = [T_{qd0}(\theta)] L_{ss} [T_{qd0}(\theta)]^{-1} [i_{qd0}] + [T_{qd0}(\theta)] [\Lambda_r] \quad (2.18)$$

where term $[T_{qd0}(\theta)] L_{ss} [T_{qd0}(\theta)]^{-1}$ is the transformation matrix which transforms the phase inductance matrix, L_{ss} , into the q-d axis synchronous inductance matrix, $[L_{qd0}]$. If the above description is applied to (2.18) then it can be shortened to:

$$[\Lambda_{qd0}] = [L_{qd0}] [i_{qd0}] \quad (2.19)$$

by

$$\begin{aligned} [\Lambda_{qd0}] &= [\lambda_q, \lambda_d, \lambda_0]^T \\ [L_{qd0}] &= [L_q \ L_d \ L_0] \\ [i_{qd0}] &= [i_q, i_d, i_0]^T \end{aligned} \quad (2.20)$$

After simplifying the right hand side of (2.18), the rotor angle, θ_r , independent q-d axis flux linkages, λ_q and λ_d , synchronous inductances, L_q and L_d , and currents, i_q and i_d are obtained as follows:

$$\begin{aligned} \lambda_q &= \left(L_{ls} + \frac{3}{2} (L_0 - L_{ms}) \right) i_q = L_q i_q \\ \lambda_d &= \left(L_{ls} + \frac{3}{2} (L_0 + L_{ms}) \right) i_d + \lambda_r = L_d i_d + \lambda_r \\ \lambda_0 &= L_s i_0 \quad (\text{zero in balanced systems}) \end{aligned} \quad (2.21)$$

where

$$\begin{aligned} L_q &= L_{ls} + L_{mq} \\ L_d &= L_{ls} + L_{md} \end{aligned} \quad (2.22)$$

In equation (2.22), L_{mq} and L_{md} are the common mutual inductances on the d-axis and q-axis circuits, respectively. Traditionally, the sums, $(L_{ls} + L_{mq})$ and $(L_{ls} + L_{md})$, are referred as the q-axis and d-axis synchronous inductances, respectively.

Flux linkages in (2.20) can also be written as:

$$\begin{bmatrix} \Lambda_{qd0} \end{bmatrix} = \begin{bmatrix} \lambda_q \\ \lambda_d \\ \lambda_0 \end{bmatrix} \quad (2.23)$$

On the contrary, flux linkages using the original Park's Transformation is differ from the above representation, $[\Lambda_{dq0}] = [\lambda_d, \lambda_q, \lambda_0]^t$. The only difference between $[\Lambda_{qd0}]$ and $[\Lambda_{dq0}]$ is the order of λ_q and λ_d . When λ_q and λ_d are known either $[\Lambda_{qd0}]$ or $[\Lambda_{dq0}]$ can be constructed easily. Once their components are known the transfer between each flux linkage matrix is easy.

So that (2.18) could have been written also as follows:

$$[\Lambda_{dq0}] = [T_{dq0}(\theta_r)] L_{ss} [T_{dq0}(\theta_r)]^{-1} [i_{dq0}] + [T_{dq0}(\theta_r)] [\Lambda_r] \quad (2.24)$$

To collect the correct result out of the above equation, the rotor angle, θ , in the inductance matrix, L_{ss} , should be in the form of θ_r to be used in (2.24) by (2.16). After computing the above formula, the stator d-q axis flux linkages, λ_q and λ_d , will be the same as provided by (2.18). Results of the derivation of d-q axis stator flux linkages are given in (2.21).

The following part is the derivation of the d-q axis motor voltages of PMSM:

Equations (2.7) and (2.14) are the starting point. First, the original d-q Park's Transformation $[T_{dq0}(\theta_r)]$ is applied to the stator quantities shown in (2.7). This is given by:

$$\begin{aligned} [v_{dq0}] &= [T_{dq0}(\theta_r)][v_s] \\ [i_{dq0}] &= [T_{dq0}(\theta_r)][i_s] \\ [\Lambda_{dq0}] &= [T_{dq0}(\theta_r)][\Lambda_s] \end{aligned} \quad (2.25)$$

where

$$[v_{dq0}] = [v_d, v_q, v_0]^t \quad (2.26)$$

When the three-phase system is symmetrical and the voltages form a balanced three-phase set of *abc* sequences, the sum of the set is zero, hence the third components of the d-q quantities in (2.25) are zero, e.g. $v_0 = 0$.

If (2.25) is substituted into (2.7), then the stator voltage equation is written in d-q coordinates as:

$$[v_{dq0}] = [T_{dq0}(\theta_r)][r_s][T_{dq0}(\theta_r)]^{-1}[i_{dq0}] + [T_{dq0}(\theta_r)]p[T_{dq0}(\theta_r)]^{-1}[\Lambda_{dq0}] \quad (2.27)$$

where, p is the differential operation, $p = \frac{d}{dt}$.

In a three-phase balanced system, all the phase resistances are equal, $r_s = r_a = r_b = r_c$, such that the resistive drop term in the above equation reduces to

$$[T_{dq0}(\theta_r)][r_s][T_{dq0}(\theta_r)]^{-1}[i_{dq0}] = r_s [i_{dq0}] \quad (2.28)$$

The second term having a derivative part in (2.27) can be expanded as:

$$[T_{dq0}(\theta_r)]p[T_{dq0}(\theta_r)]^{-1}[\Lambda_{dq0}] = [T_{dq0}(\theta_r)] \left\{ \left(p[T_{dq0}(\theta_r)]^{-1} \right) [\Lambda_{dq0}] + [T_{dq0}(\theta_r)]^{-1} p[\Lambda_{dq0}] \right\} \quad (2.29)$$

Further manipulations lead us to:

$$\begin{aligned} [T_{dq0}(\theta_r)] p [T_{dq0}(\theta_r)]^{-1} [\Lambda_{dq0}] &= [T_{dq0}(\theta_r)] p [T_{dq0}(\theta_r)]^{-1} [\Lambda_{dq0}] + [T_{dq0}(\theta_r)] [T_{dq0}(\theta_r)]^{-1} p [\Lambda_{dq0}] \end{aligned} \quad (2.30)$$

And finally,

$$[T_{dq0}(\theta_r)] p [T_{dq0}(\theta_r)]^{-1} [\Lambda_{dq0}] = [T_{dq0}(\theta_r)] \left(p [T_{dq0}(\theta_r)]^{-1} \right) [\Lambda_{dq0}] + p [\Lambda_{dq0}] \quad (2.31)$$

where, the term $[T_{dq0}(\theta_r)] \left(p [T_{dq0}(\theta_r)]^{-1} \right)$ is simplified as follows:

First, taking the derivative of (2.12), we get:

$$p [T_{dq0}(\theta_r)]^{-1} = \omega_r \begin{bmatrix} -\sin \theta_r & -\cos \theta_r & 0 \\ -\sin(\theta_r - \frac{2\pi}{3}) & -\cos(\theta_r - \frac{2\pi}{3}) & 0 \\ -\sin(\theta_r + \frac{2\pi}{3}) & -\cos(\theta_r + \frac{2\pi}{3}) & 0 \end{bmatrix} \quad (2.32)$$

where, ω_r is the rotor angular speed in electrical radians/sec, $\omega_r = \frac{d\theta_r}{dt}$. Multiplying equations (2.11) and (2.32), we obtain:

$$[T_{dq0}(\theta_r)] \left(p [T_{dq0}(\theta_r)]^{-1} \right) = \omega_r \frac{2}{3} \begin{bmatrix} T_{11} & T_{12} & 0 \\ T_{21} & T_{21} & 0 \\ T_{31} & T_{32} & 0 \end{bmatrix} \quad (2.33)$$

where the elements of the matrix are written and manipulated by using some trigonometric reduction equations. The results are given below [1]:

$$\begin{aligned}
T_{11} &= -\cos \theta_r \sin \theta_r - \cos\left(\theta_r - \frac{2\pi}{3}\right) \sin\left(\theta_r - \frac{2\pi}{3}\right) - \cos\left(\theta_r + \frac{2\pi}{3}\right) \sin\left(\theta_r + \frac{2\pi}{3}\right) = 0 \\
T_{12} &= -\cos^2 \theta_r - \cos^2\left(\theta_r - \frac{2\pi}{3}\right) - \cos^2\left(\theta_r + \frac{2\pi}{3}\right) = -\frac{3}{2} \\
T_{21} &= \sin^2 \theta_r + \sin^2\left(\theta_r - \frac{2\pi}{3}\right) + \sin^2\left(\theta_r + \frac{2\pi}{3}\right) = \frac{3}{2} \\
T_{22} &= \sin \theta_r \cos \theta_r + \sin\left(\theta_r - \frac{2\pi}{3}\right) \cos\left(\theta_r - \frac{2\pi}{3}\right) + \sin\left(\theta_r + \frac{2\pi}{3}\right) \cos\left(\theta_r + \frac{2\pi}{3}\right) = 0 \\
T_{31} &= -\frac{1}{2} \left\{ \sin \theta_r + \sin\left(\theta_r - \frac{2\pi}{3}\right) + \sin\left(\theta_r + \frac{2\pi}{3}\right) \right\} = 0 \\
T_{32} &= -\frac{1}{2} \left\{ \cos \theta_r + \cos\left(\theta_r - \frac{2\pi}{3}\right) + \cos\left(\theta_r + \frac{2\pi}{3}\right) \right\} = 0
\end{aligned} \tag{2.34}$$

Putting all the elements obtained in (2.34) into (2.33), we get:

$$\left[T_{dq0}(\theta_r) \right] \left(p \left[T_{dq0}(\theta_r) \right]^{-1} \right) = \omega \frac{2}{3} \begin{bmatrix} 0 & -\frac{3}{2} & 0 \\ \frac{3}{2} & 0 & 0 \\ 0 & 0 & 0 \end{bmatrix} \tag{2.35}$$

More simplification leads us to:

$$\left[T_{dq0}(\theta_r) \right] \left(p \left[T_{dq0}(\theta_r) \right]^{-1} \right) = \omega \begin{bmatrix} 0 & -1 & 0 \\ 1 & 0 & 0 \\ 0 & 0 & 0 \end{bmatrix} \tag{2.36}$$

Equations (2.31) and (2.36) yield the following result, written in expanded matrix form:

$$\begin{bmatrix} v_d \\ v_q \\ v_0 \end{bmatrix} = r_s \begin{bmatrix} i_d \\ i_q \\ i_0 \end{bmatrix} + \omega_r \begin{bmatrix} 0 & -1 & 0 \\ 1 & 0 & 0 \\ 0 & 0 & 0 \end{bmatrix} \begin{bmatrix} \lambda_d \\ \lambda_q \\ \lambda_0 \end{bmatrix} + p \begin{bmatrix} \lambda_d \\ \lambda_q \\ \lambda_0 \end{bmatrix} \tag{2.37}$$

The above matrix can be arranged in equation form shown below:

$$\begin{aligned}
v_d &= r_s i_d - \omega_r \lambda_q + p \lambda_d \\
&= r_s i_d - \omega_r L_q i_q + L_d p i_d \\
&= (r_s + L_d p) i_d - \omega_r L_q i_q
\end{aligned} \tag{2.38}$$

Similarly,

$$\begin{aligned}
v_q &= r_s i_q + \omega_r \lambda_d + p \lambda_q \\
&= r_s i_q + \omega_r L_d i_d + \omega_r \lambda_r + L_q p i_q \\
&= (r_s + L_q p) i_q + \omega_r (L_d i_d + \lambda_r)
\end{aligned} \tag{2.39}$$

Equations (2.38) and (2.39) can be put together to form the famous d-q voltage model for the PMSM in matrix form. This is given in below:

$$\begin{bmatrix} v_d \\ v_q \end{bmatrix} = \begin{bmatrix} r_s + L_d p & -L_q \omega_r \\ L_d \omega_r & r_s + L_q p \end{bmatrix} \begin{bmatrix} i_d \\ i_q \end{bmatrix} + \lambda_r \omega_r \begin{bmatrix} 0 \\ 1 \end{bmatrix} \tag{2.40}$$

To obtain the d-q reference frame electromechanical torque, T_{em} , and the instantaneous input power P_{in} are used. Details are as follows:

Total input power P_{in} into the machine can be represented as

$$P_{in} = v_{sa} i_{sa} + v_{sb} i_{sb} + v_{sc} i_{sc} \tag{2.41}$$

When the stator phase quantities are transformed to the rotor d-q reference frame that rotates at a speed of $\omega_r = d\theta_r / dt$, (2.41) becomes:

$$P_{in} = \frac{3}{2} (v_q i_q + v_d i_d) \tag{2.42}$$

where the zero sequence quantities are neglected. Using (2.42), the mechanical output power P_{out} can be obtained by replacing v_d and v_q with the associated speed voltages as

$$P_{out} = \frac{3}{2} (-\omega_r \lambda_q i_d + \omega_r \lambda_d i_q) \tag{2.43}$$

For a P-pole machine, $\omega_r = (P/2)\omega_{rm}$, where ω_{rm} is the mechanical rotor speed in radians/sec, produced electromechanical torque T_{em} is derived when the output power P_{out} is divided by the mechanical speed ω_{rm} , which is given as:

$$\begin{aligned} T_{em} &= \frac{3}{2} \frac{P}{2} (\lambda_d i_q - \lambda_q i_d) \\ &= \frac{3}{2} \frac{P}{2} ((L_d - L_q) i_q i_d + \lambda_r i_q) \end{aligned} \quad (2.44)$$

It is apparent from the above equation that the produced torque is composed of two distinct mechanisms. The first term corresponds to “reluctance torque” due to the saliency (difference in the d-axis and q-axis reluctance or inductance), while the second term corresponds to the “excitation torque” occurring between i_q and the permanent magnet λ_r [10].

2.2. Introduction to Brushless DC (BLDC) Motors

Brushless DC (BLDC) motors contain most of the characteristics of PMAC motors, explained in Section 2.1.1. They are generally designed as surface-mount motors with concentrated windings on the stator. With the appropriate placement of the permanent magnet on the rotor, a trapezoidal back-EMF shape is obtained.

As compared to a conventional DC brush motor, brushless DC (BLDC) motors are DC brush motors turned inside out, so that the field is on the rotor and the armature is on the stator. As explained before, field excitation of BLDC motor is provided by a permanent magnet and commutation is achieved electronically instead of using mechanical commutators and brushes.

One of the main characteristics of the BLDC motor is that it is a modified PMSM such that the back-EMF is trapezoidal instead of being sinusoidal. To achieve smooth torque production, quasi-square wave currents are applied to the stator phases when the

corresponding back-EMFs have a flat constant portion (approximately 120 degrees like the currents). The “commutation region” of the back-EMF of a BLDC motor should be as small as possible. On the other hand, when driven by a Current Source Inverter that region should not be extremely narrow making it difficult to commute a phase of the motor.

Each phase of a BLDC motor is energized by a digital controller in a sequence. The energization is synchronized with the rotor position in order to produce constant torque, therefore, it is important to know the rotor position in order to understand which winding will be energized following the energizing sequence. One alternative way to sense the position of the rotor is by using an optical position sensor. Optical position sensors consist of phototransistors (sensitive to light), revolving shutters and a light source. The output of an optical position sensor is usually a logic signal. This is especially useful when unipolar switching is used to drive a BLDC motor [5].

The most common method of sensing in a BLDC motor is using hall-effect position sensors. For a brushless DC (BLDC) motor with a trapezoidal back-EMF, it is sufficient to get position information that is updated at each 60 degree electrical interval. The position information is used then by the microcontroller/DSP to decide the triggering of inverter switches. Generally, three hall-effect sensors are used for a three phase motor, (they will be named as Hall-A, Hall-B, and Hall-C each with 120 degree lag with respect to the previous sensor), to determine the position of the rotor magnetic field.

Hall-effect sensors are generally embedded into the stator on the non-driving end of the motor. According to the corresponding “Hall Effect Theory”, named after E.H. Hall who discovered it in 1879, whenever the rotor magnetic poles pass near the hall-effect sensors, a high or low signal will be generated indicating when the N (north) or S (south) pole is passing near the sensors. In general, the North Pole signal corresponds to “1” and the South Pole to “0” [11]. In motors not having a neutral accessibility each hall-effect sensor output signal is synchronized with the corresponding line-to-line back-EMF for alignment easiness. For example in Fig. 2.4

Hall-A is aligned with $E_{ab} = E_a - E_b$ and so forth and so on. This means that the output of each hall-effect sensor is actually leading the zero crossing of the corresponding phase of each back-EMF by 30 electrical degrees.

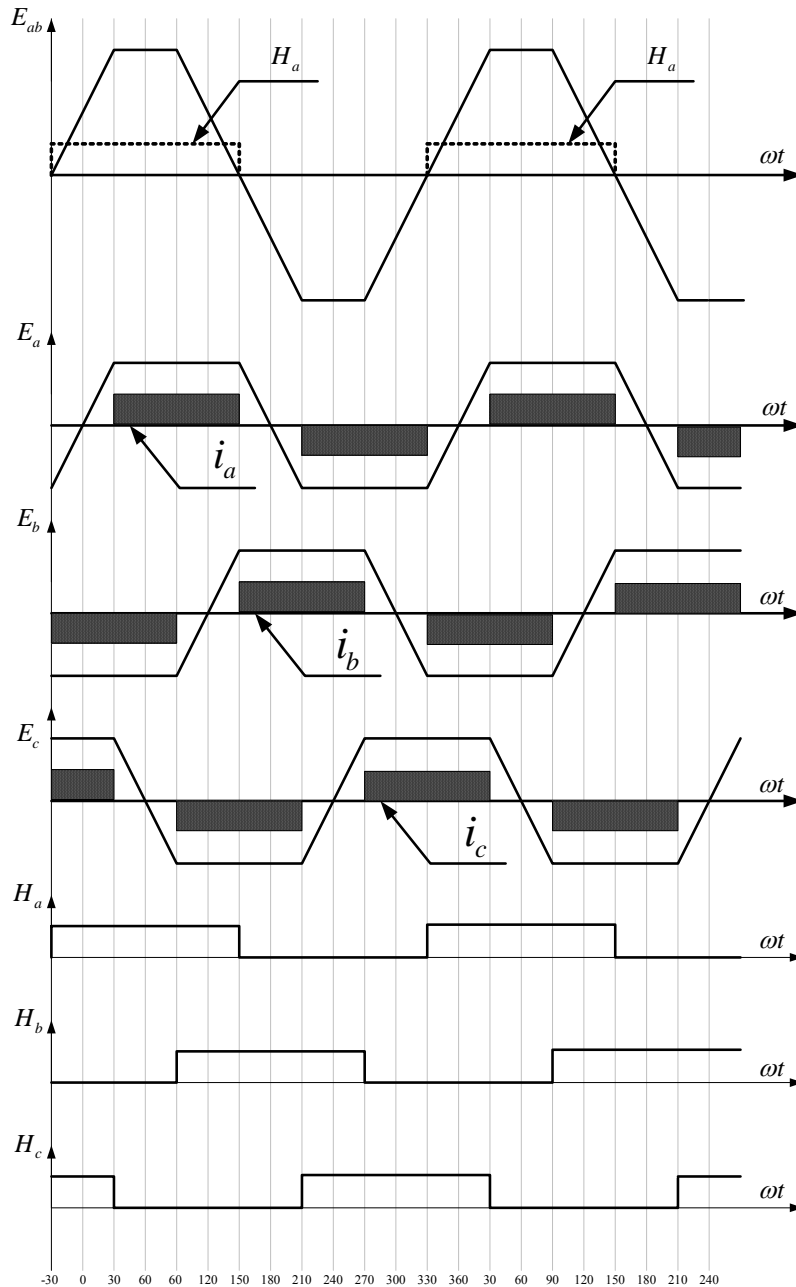


Fig. 2.4. Line-to-line back-EMF (E_{ab}), phase back-EMFs, phase current waveforms and hall-effect position sensor signals for a BLDC motor [3].

For example, as illustrated in the digital output of Fig. 2.4, H_a is leading E_a by 30 degrees. In motors that have neutral access, each of the hall-effect sensor signals can represent the corresponding phase back-EMF. Alignment can then be easily achieved since there is a neutral connection available to observe the phase back-EMF waveforms to be used for the alignment process.

The motor that is used in this thesis, a 48 pole 36 slot PMSM, has that kind of luxury such that its hall-effect signals are aligned with the corresponding phase back-EMF voltages. Fig. 2.4 shows an example of the hall-effect sensor signals with respect to the corresponding line-to-line back-EMF voltages and phase currents. For example, to know the starting point of the phase A current, the digital output of H_a alone is not sufficient; additionally the falling edge signal of H_c is needed to trigger the switch T1 (T6 is still on) [5].

As a consequence, when the hall-effect signals generate a logic of "1 0 0", " $H_a H_b H_c$ ", respectively, T1 is turned on while T6 still conducts to energize the phase A current shown in Fig. 2.4. By observation, the logic high of a hall-effect position sensor is maintained for 180 electrical degrees. This can be a significant disadvantage, since timers may have to be used in order to reduce the switching times to 120 electrical degrees (two-thirds of the hall-effect position sensor output high of 180 electrical degrees) [5].

2.2.1. Mathematical Model of BLDC Motor

In general, the analysis of a BLDC motor is conducted in phase variables due to its non-sinusoidal back-EMF and current. Fig. 2.5 shows the equivalent circuit of a BLDC motor and a power inverter. The analysis of the BLDC motor drive is based on the following assumptions for simplification [6]:

- The motor is not saturated,
- The motor windings have a constant resistance, self inductance, and mutual inductance. The resistance and inductance of all phases are identical,
- All three phases have an identical back-EMF shape,
- Power semiconductor devices in the inverter are ideal,
- Iron losses are negligible,
- Eddy current and hysteresis effects are neglected.

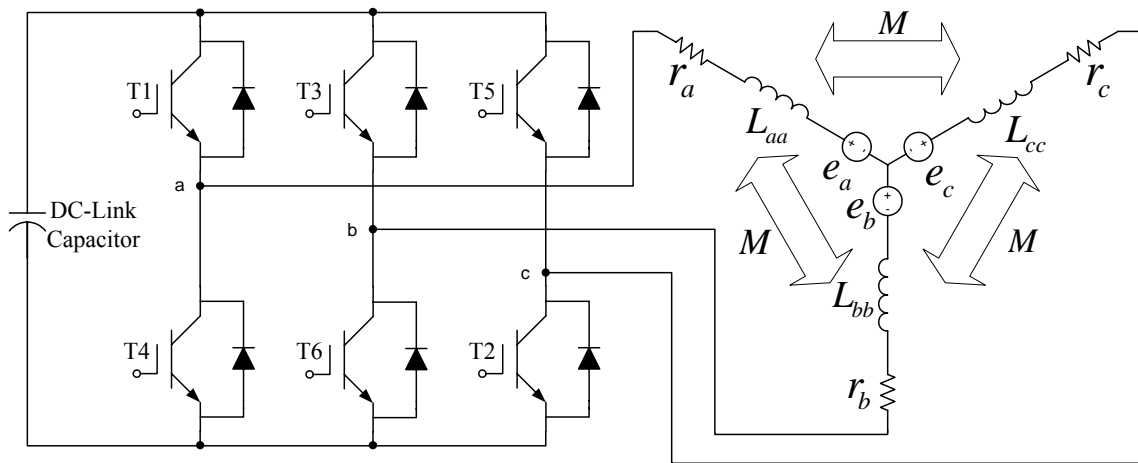


Fig. 2.5. Equivalent circuit of the BLDC drive (R, L and back-EMF) [3].

The model of a BLDC motor consisting of three phases, as shown in Fig. 2.5, is explained by the following series of equations. Since there is no neutral used, the system is wye connected, thus the sum of the three phase currents must add up to zero, i.e.

$$\begin{aligned} i_{sa} + i_{sb} + i_{sc} &= 0 \\ i_{sa} + i_{sb} &= -i_{sc} \end{aligned} \quad (2.45)$$

Under the above assumptions and referring to Fig. 2.5, a three-phase BLDC motor mathematical model can be represented by the following equation in matrix form:

$$\begin{bmatrix} v_{sa} \\ v_{sb} \\ v_{sc} \end{bmatrix} = \begin{bmatrix} r_a & 0 & 0 \\ 0 & r_b & 0 \\ 0 & 0 & r_c \end{bmatrix} \begin{bmatrix} i_{sa} \\ i_{sb} \\ i_{sc} \end{bmatrix} + \frac{d}{dt} \begin{bmatrix} L_{aa} & L_{ba} & L_{ca} \\ L_{ab} & L_{bb} & L_{cb} \\ L_{ac} & L_{bc} & L_{cc} \end{bmatrix} \begin{bmatrix} i_{sa} \\ i_{sb} \\ i_{sc} \end{bmatrix} + \begin{bmatrix} e_a \\ e_b \\ e_c \end{bmatrix} \quad (2.46)$$

If the rotor has a surface-mounted design, which is generally the case for today's BLDC motors, there is no saliency such that the stator self inductances are independent of the rotor position, hence:

$$L_{aa} = L_{bb} = L_{cc} = L \quad (2.47)$$

Again with no saliency all mutual inductances will have the same form such that,

$$L_{ab} = L_{ba} = L_{bc} = L_{cb} = L_{ca} = L_{ac} = M \quad (2.48)$$

Also, under balanced three-phase condition all the phase resistances are equal, such that:

$$r_s = r_a = r_b = r_c \quad (2.49)$$

Equations (2.47-2.49) are substituted into (2.46), giving the following reduced matrix form,

$$\begin{bmatrix} v_{sa} \\ v_{sb} \\ v_{sc} \end{bmatrix} = \begin{bmatrix} r_s & 0 & 0 \\ 0 & r_s & 0 \\ 0 & 0 & r_s \end{bmatrix} \begin{bmatrix} i_{sa} \\ i_{sb} \\ i_{sc} \end{bmatrix} + \begin{bmatrix} L & M & M \\ M & L & M \\ M & M & L \end{bmatrix} \frac{d}{dt} \begin{bmatrix} i_{sa} \\ i_{sb} \\ i_{sc} \end{bmatrix} + \begin{bmatrix} e_a \\ e_b \\ e_c \end{bmatrix} \quad (2.50)$$

Using the concept of (2.47), the inductance matrix above is simplified and the resultant matrix form is given by:

$$\begin{bmatrix} v_{sa} \\ v_{sb} \\ v_{sc} \end{bmatrix} = \begin{bmatrix} r_s & 0 & 0 \\ 0 & r_s & 0 \\ 0 & 0 & r_s \end{bmatrix} \begin{bmatrix} i_{sa} \\ i_{sb} \\ i_{sc} \end{bmatrix} + \begin{bmatrix} L-M & 0 & 0 \\ 0 & L-M & 0 \\ 0 & 0 & L-M \end{bmatrix} \frac{d}{dt} \begin{bmatrix} i_{sa} \\ i_{sb} \\ i_{sc} \end{bmatrix} + \begin{bmatrix} e_a \\ e_b \\ e_c \end{bmatrix} \quad (2.51)$$

where the back-EMF waveforms e_a , e_b and e_c are trapezoidal in nature and can be represented by either Fourier Series or Laplace Transforms.

After rearranging the equations, the model of the BLDC motor depicted in Fig. 2.5 is reduced to Fig. 2.6 which resembles (2.51).

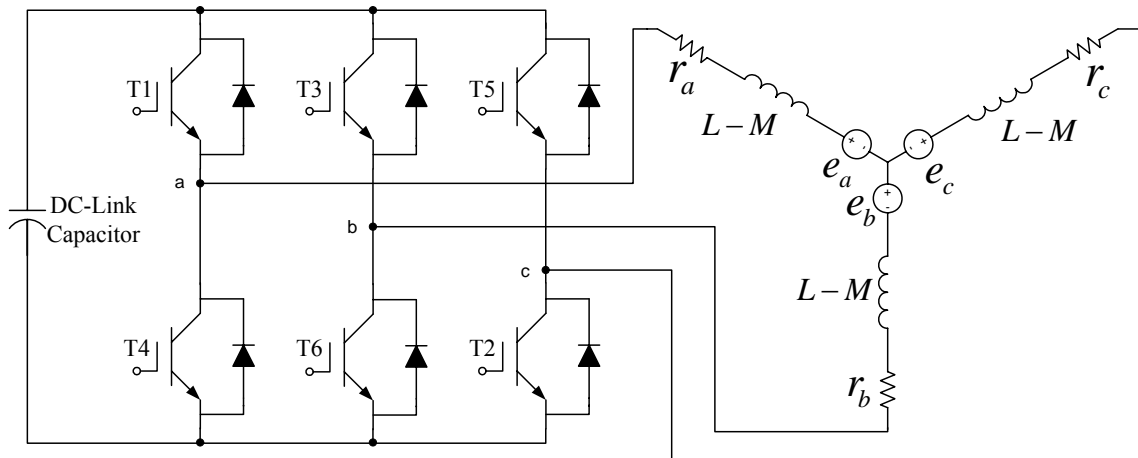


Fig. 2.6. Simplified equivalent circuit of the BLDC drive (R , $(L-M)$ and back-EMF).

The electromechanical torque is expressed as

$$T_{em} = \frac{e_a i_a + e_b i_b + e_c i_c}{\omega_m} :$$

where

e_a is the phase-to-neutral back-EMF of phase A in volts,

e_b is the phase-to-neutral back-EMF of phase B in volts,

e_c is the phase-to-neutral back-EMF of phase C in volts,

i_{sa} is the stator current in phase A in ampere,

i_{sb} is the stator current in phase B in ampere,

i_{sc} is the stator current in phase C in ampere, and

ω_m is the rotor angular velocity in mechanical radian/sec; $\omega_{re} = (P/2)\omega_m$,

P is the number of poles,

ω_{re} is the rotor angular velocity in electrical radian/sec.

The Laplace domain representation of the BLDC motor model will lead us to construct the block diagram of the overall BLDC motor system easily. Since the back-EMF waveforms are periodic, they can be represented by a periodic function [5].

The voltage equation of a BLDC motor, which is the same as brush DC motor model, can be depicted in the time domain by substituting (2.51) in (2.52) shown below:

$$v(t) = r_a i_a(t) + k_e \omega_{rm}(t) + L_a \frac{di_a(t)}{dt} \quad (2.52)$$

where

$v(t)$ is the supply voltage (line-to-neutral) in volts,

i_a is the armature current in ampere,

L_a is the armature inductance; $L_a = L - M$,

$k_e \omega_{rm}(t)$ is the line-to-neutral back-EMF, shown as E ,

k_e is the back-EMF constant in Vs/rad.

The Laplace form of (2.52) is given as:

$$I_a(s) = \frac{V(s) - k_e \Omega_{rm}}{r_a + sL_a} \quad (2.53)$$

By using the following equations, the transient model of a BLDC motor can be obtained as illustrated in Fig. 2.5.

If the current term is put aside in (2.52), we obtain

$$\frac{di_a(t)}{dt} = \frac{v(t)}{L_a} - \frac{r_a}{L_a} i_a(t) - \frac{E(t)}{L_a} \quad (2.54)$$

where $E(t) = k_e \omega_{rm}$ is the periodic back-EMF which is a function of the rotor angle.

The relation between the electrical power, P_e , and the mechanical power, P_m , is:

$$P_e = E i_a = P_m = T_{em} \omega_{rm} \quad (2.55)$$

The electromechanical torque, T_{em} , is linearly proportional to the armature current i_a , i.e.

$$T_{em} = k_T i_a \quad (2.56)$$

where k_T is the torque constant. Equation (2.55) can then be substituted into (2.56) yielding:

$$T_{em} = \frac{E}{\omega_{rm}} i_a, \quad (2.57)$$

such that for the ideal motor with no saturation, resistance, or voltage-drops in the controller:

$$k_t = \frac{E}{\omega_{rm}} = \frac{k_e \omega_{rm}}{\omega_r} \approx k_e \quad (2.58)$$

Provided that k_T and k_e are in consistent units (such as Nm/A and Vs/rad), it can be seen from the derivations above that the ideal squarewave brushless DC (BLDC) motor has the same basic energy-conversion equation as the DC commutator motor.

The motion equation is:

$$T_{em}(t) = T_L(t) + J \frac{d\omega_{rm}}{dt} + B\omega_{rm} \quad (2.59)$$

where, T_L , J , and B stand for load torque, inertia and friction, respectively.

The motion equation can be expressed in Laplace form as:

$$\Omega_{rm} = \frac{T_{em} - T_L}{(B + sJ)} \quad (2.60)$$

Equation (2.56) can also be expressed in Laplace form as:

$$T_{em} = \frac{k_T(V(s) - k_e\Omega_{rm})}{r_a + sL_a} \quad (2.61)$$

2.3. Mechanical Structure of Permanent Magnet AC Motors

There are mainly two types of PMAC motor construction which are based on the way magnets are mounted on the rotor and the shape of the back-EMF waveform that was explained briefly above. In case where the magnets are mounted on the rotor surface, the PMAC motor is called surface-mounted. If the magnets are buried inside the rotor then it is called an interior-mounted motor. The back-EMF waveform can be either sinusoidal or trapezoidal as expressed above. Detailed information about the PMAC motor construction is as follows:

1) Surface-mounted PMAC Motor:

The typical design of this type of PMAC motor is shown in Fig. 2.7. Its name implies that the magnets are placed on the surface of the rotor. Doing so makes the mounting of the magnets on the rotor easier and less costly. Moreover, skewed poles can be easily magnetized on the round rotor to minimize cogging torque. Since the magnets are located on the rotor surface, the machine has a large effective air-gap, which makes the effects of saliency negligible (thus the direct-axis magnetizing inductance is equal to the quadrature-axis magnetizing inductance, $L_{md} = L_{mq} + L_m$).

Furthermore, because of the large air-gap, synchronous inductance ($L_s = L_{sl} + L_m$) is small and therefore the effects of armature reaction are negligible. A further consequence of the large air-gap is that the electrical time constant of the stator winding is small. One problem with this type of design is that during high-speed operation magnets can detach from the rotor [4].

There could be various shapes of magnets for surface-mounted PMAC motor. Bar-shaped and circumferential segments with angles up to 90 degrees and thickness of a few millimeters are available. Radially magnetized circumferential segments produce a smoother air-gap flux density and less torque ripples [4].

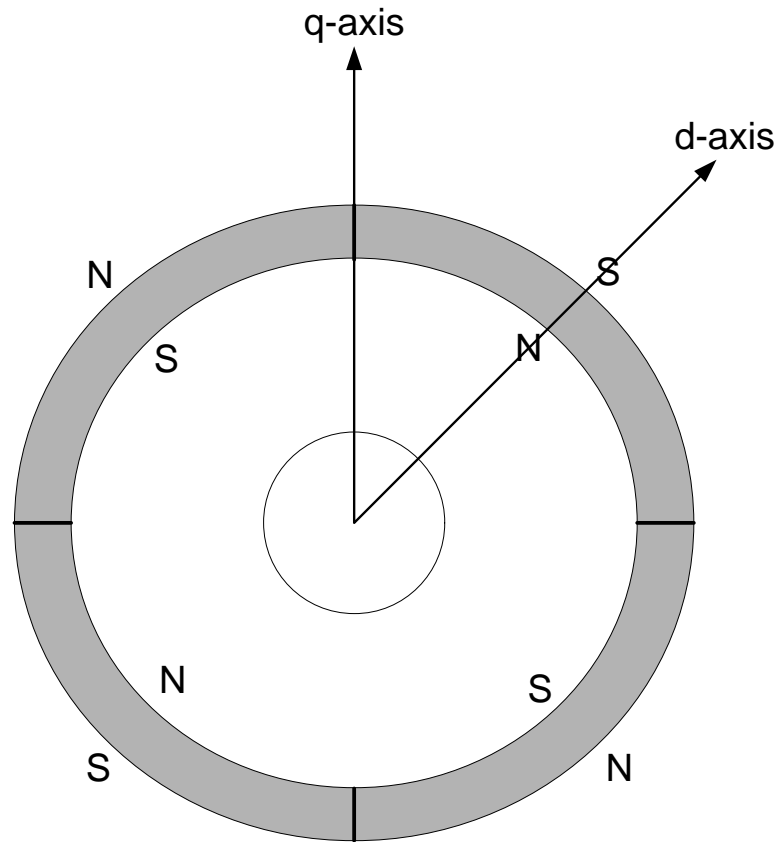


Fig. 2.7. Cross sectional view of four pole surface-mounted PM rotor ($L_d = L_q$).

2) Interior-mounted PMAC Motor:

The typical construction of this type of PMAC motor is shown in Fig. 2.8. Each permanent magnet is mounted inside the rotor core rather than being bonded on the rotor surface; the motor not only provides mechanically robust and rugged construction, but also has possibility of increasing its torque capability. This type of PMAC motor can be used for high-speed applications since the magnets are physically contained and protected. By designing a rotor magnetic circuit such that the synchronous inductances vary as a function of rotor angle, the reluctance torque can be produced in addition to the excitation torque (which is the multiplication of q-axis current and the rotor flux linkage due to permanent magnet) [4].

The reluctance torque is generated by this kind of motor because each magnet is buried and covered by a steel pole piece. This significantly changes the magnetic behavior of the machine since, via these iron pole pieces, high-permeance paths are created which are between two consecutive magnet poles as shown in Fig. 2.8. This path is considered as the quadrature axis in which its inductance is higher than the inductance measured through the direct axis (also shown in Fig 2.8). One can say that the q-axis is leading the d-axis by 90 electrical degrees, thus there are saliency effects which significantly alter the torque production mechanism of the machine [4].

As described in Section 2.1.1, in addition to the excitation there is a reluctance torque which is due to the difference in the d- and q-axes inductances, the so called saliency. This class of interior PM (IPM) synchronous motors can be considered as a combination of the reluctance synchronous motor and the surfaced-mounted PM synchronous motor. Currently, it is very popular in industrial and military applications for providing high power density and high efficiency compared to other types of electric motors [6].

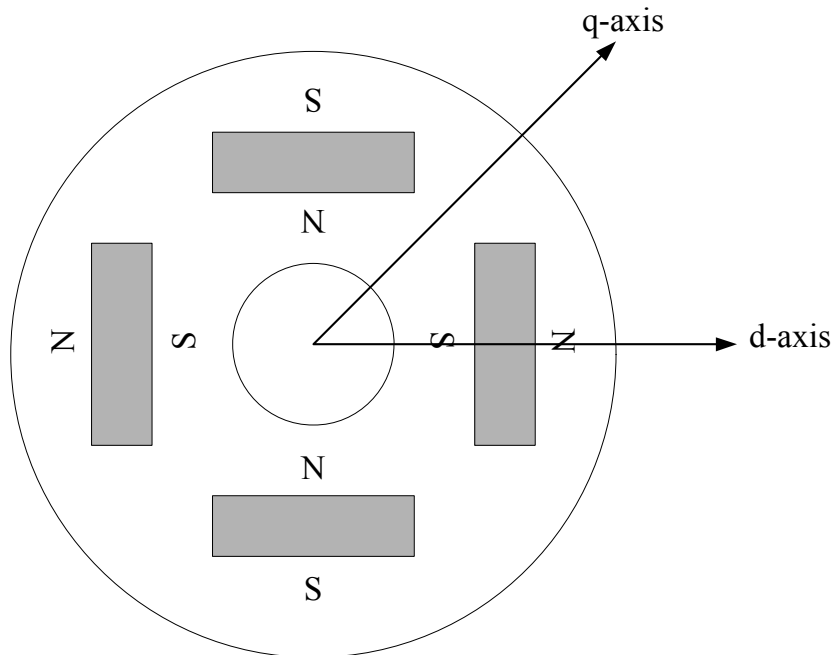


Fig. 2.8. Cross sectional view of four pole interior-mounted PM rotor ($L_d \neq L_q$).

Another classification for PMAC motors is based on the shape of the back-EMF generated (either as trapezoidal or sinusoidal). These back-EMF waveforms can be obtained by a generator test in which open-circuit voltages are induced in the stator windings due to the permanent magnets which show the characteristics of the back-EMF [6].

If the flux distribution and back-EMF shapes are trapezoidal then this type of motor is called a brushless DC (BLDC) motor, whereas if the shape of back-EMF waveform is sinusoidal then this is considered a PM synchronous motor (PMSM). More details about these types of PMAC motors are discussed in below:

3) PMAC Motors with Sinusoidal Shape Back-EMF:

For the PMAC motor with a sinusoidal back-EMF, the so called PMSM, all three stator phases are excited at one instant of time providing quasi-sinusoidal current flow through the stator windings. Since all of the stator phases are excited simultaneously, the torque per ampere ration is higher than PMAC motors with a trapezoidal shape back-EMF.

In this type of PMAC motor, stator conductors are sinusoidally distributed for each phase to achieve a sinusoidal current waveform. Also, permanent magnets are arranged such that they generate a sinusoidal flux distribution in the air-gap. With the interaction of sinusoidal current and sinusoidal flux, and because of the lack of a commutation scheme like BLDC motors, ripple free torque is generated.

The commutation in PMSM motors is not going to be as harsh as the BLDC motor which is fed by square wave currents. The condition in which a change of cycle of square wave currents occurs, huge torque ripples are generated. On the other hand, for the sinewave condition there is a smooth transition from one cycle to another.

The construction of this type of PMAC motor is more expensive than BLDC motors. Additionally, PMSM drives use continuous motor position feedback to feed the motor with sinusoidal voltage or current. Due to this reason, expensive position sensors

(>100\$) like the resolver or encoder are necessary, which increases the overall cost of the motor drive system.

Unlike the BLDC trapezoidal shape back-EMF motors, the working principle of a PMAC motor with a sinusoidal back-EMF is very similar to the AC synchronous motor, therefore it can be analyzed with a phasor diagram.

4) PMAC Motors with Trapezoidal Shape Back-EMF:

The stator currents of a BLDC motor are quasi-square wave with 120 electrical-degree conduction periods. Magnetic flux distribution in the air-gap is rectangular. When the phase currents are timed approximately with the constant part of the back-EMF a constant torque is generated. These rectangular current-fed motors have concentrated windings on the stator. Unlike the PMSM which needs continuous position sensing, PMAC motors with trapezoidal shape back-EMFs (BLDC), require sensing only at every 60 electrical-degree period for commutation of the phase currents. As a result, six commutation points are required for one electrical cycle [6].

Basically, in each commutation point, the switching cycle is changed. By doing so, there is no need to have a high resolution position sensor such as an absolute or incremental encoder or resolver. In this case, a very simple and cheap (<1\$) hall-effect sensor would be appropriate enough. During these commutation intervals, however torque ripples occur. Minimizing the torque ripples is an on-going research topic that is not in the scope of this thesis.

2.4. Advantages and Disadvantages of PMAC Motors

The following are some of the most common advantages of PMAC motors over other electric motors available on the market:

- PMAC motors are high efficient motors. PMSM and BLDC motors, are considered the most efficient of all electric motors. There is an absence of

a rotor circuit, instead of which permanent magnets on the rotor are used for the excitation (generating constant rotor magnetic field). These magnets consume almost no power whatsoever, so copper losses are negligible at the rotor level unlike AC induction and synchronous motors. Also, the friction is lower and the durability is higher, since there are no mechanical commutators and brushes to wear out. All of these characteristics of PMAC motors put them into the top spot of the high efficiency category [6].

- Recent advances in high-energy density magnets, such as samarium cobalt and Neodymium Iron Boron (NdFeB), have allowed achievement of very high flux densities in the PMAC motors. These magnets provide providing high torques and allow for the motors to be built smaller and lighter [6].
- One category of PMAC motors, BLDC motors, can be controlled with a closed-loop system as simple that is as a DC brush motor because the control variables are easily accessible and constant throughout the operation of the motor. PMSM, on the other hand, has an open-loop control capability unlike BLDC motors in which its closed-loop control is not as easy as the BLDC motor, but is similar to the induction motors. PMSM drives need advanced control techniques, such as vector control and direct torque control, just like AC induction motors [6].
- In PMAC motors, there is no rotor circuit available, reducing losses. The only heat is produced on the stator, which is easier to cool than the rotor because the stator is static and is located on the outer part of the motor [6].
- PMAC motors have low maintenance, great longevity and reliability. Without brushes and mechanical commutators, regular maintenance is greatly reduced and risks such as sparking in explosive or corrosive environments like oil field etc are eliminated. The longevity of the motor

is mainly based on the winding insulation and bearings (like other electric motors), and the life-length of the magnet [6].

- There is no noise generated with the commutation because it is achieved electronically, not mechanically. The converter switching frequency is high enough so that the noise created by the harmonics is not audible [6].

PMAC motors also have some inherent disadvantages just like any other electrical machine. These are summarized in the following:

- Magnet cost is the most important issue in PMAC motors. Rare-earth magnets such as samarium-cobalt and neodymium boron iron are especially costly. Neodymium boron iron is the most powerful, but is the most expensive. If the initial cost is a major issue in applications where PMSM motors would be used, then the cost of higher energy density magnets prohibits their use in those kinds of applications [6].
- Very large opposing magneto motive forces (MMF) and high temperature can demagnetized the magnets. Although the critical demagnetization force is different for each magnet material, extra caution must be taken to cool the motor, especially if it is built compact [6].
- For surface-mounted PMAC motors, high speed operation is limited or not possible because the mechanical construction of the rotor. The rotor is not suitable to handle huge centrifugal forces at high speed. The magnets are adhered onto the rotor. This type of assembly is not strong and compact enough not to hold the magnets under high speed circumstances. On the other hand, interior-mounted PMAC motors have the capability to run at high speeds with no problem on the rotor side because the magnets are buried inside the rotor, but demagnetization still is an important factor in those types of motors [6].
- There is a limitation in the range of the constant power region, especially for surface-mounted PMAC motors. In the constant power region, the so called “flux weakening” region, the flux of the rotor is weakened to

extend the speed torque curve as far as possible. Surface-mounted PMAC motors have no saliency so that flux generation current does not appear in the torque equation to weaken it. Interior-mounted PMAC motors have the saliency effect causing the d-axis (direct axis) current to be weakened which extends the speed versus torque curve and eventually the constant power region (flux weakening region). PMAC motors with trapezoidal shape back-EMFs (BLDC motor) are incapable of achieving a maximum speed greater than twice the base speed [6].

- Because there is a constant energy on the rotor due to the permanent magnets, PMAC motors present a major risk in case of short circuit failures in the inverter. If any short circuit happens in the inverter during the operation of the motor, the rotor constantly induces an electromotive force in the short-circuited windings causing a very large current to flow through those windings. This produces large torque which tends to block the rotor. For vehicle applications, the danger of blocking one or several wheels of a vehicle is not acceptable [6].

2.5. Torque Production Comparison of PMSM and BLDC Motors

The torque productions are for each motor compared in the following paragraphs, assuming the same copper loss.

The BLDC motor has a high torque density in low and medium speeds but is not suitable for extended high-speed operation because of its limited flux weakening capability. Also, in BLDC operation with a rectangular current wave shape, torque pulsation occurs at the 6th harmonic of the fundamental frequency.

The following equations show the torque density difference between BLDC motors and PMSMs in the constant torque region (the PMSM has superiority in the flux-weakening region over the BLDC motor):

Assume I_{ps} and I_p are the peak values of the stator currents in the PMSM and BLDC machines, respectively. The rms values of these currents are:

$$I_{sy} = \frac{I_{ps}}{\sqrt{2}} \quad (2.62)$$

$$I_d = \frac{I_p \sqrt{2}}{\sqrt{3}} \quad (2.63)$$

Equating the copper losses and substituting for the currents in terms of their peak currents gives:

$$3I_{sy}^2 R_s = 3I_d^2 R_s \quad (2.64)$$

Therefore,

$$I_p = \frac{\sqrt{3}}{2} I_{ps} \quad (2.65)$$

The ratio of output torque is obtained from these relationships as follows:

$$\frac{BLDC_Torque}{PMSM_Torque} = \frac{(2xE_p x I_p) / \omega}{\left(3x \frac{E_p}{\sqrt{2}} x \frac{I_{ps}}{\sqrt{2}}\right) / \omega} = 1.1547 \quad (2.66)$$

The above result shows that the BLDC motor has approximately a 15.5% greater torque compared to the PMSM in the constant torque region [12]. A PMAC with a sinusoidal back-EMF (PMSM) can be operated as a BLDC. In ideal commutation, the current is conducting 120 electrical degrees with its center aligned with the peak point of the back-EMF, as shown in Fig. 2.9. On the other hand, a brushless DC motor can also be operated as a PM synchronous motor as depicted in Fig. 2.10, but this type of control creates more torque ripples. The motor used in this thesis, a 48 pole 36 slot exterior rotor pancake type PMSM, generates a sinusoidal back-EMF.

In this thesis, the proposed method discussed regulates the motor speed using a control scheme similar to typical BLDC motor control scheme without current regulation with the help of three cost-effective hall-effect sensors. Since the motor is surface-mounted and generates sinusoidal back-EMF, it is considered as surface-mounted PMSM. Vector control techniques can be used so that a relatively ripple-free average torque is obtained.

As a consequence, if the torque ripple is not a big deal, a simple trapezoidal current control scheme (BLDC type), instead of a complicated sinusoidal current control scheme (PMSM type), can be a simple, cost-effective and quite efficient solution for washing machine speed control applications.

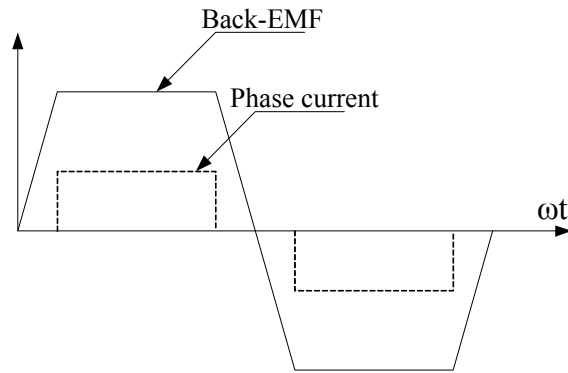


Fig. 2.9. Ideal BLDC operation.

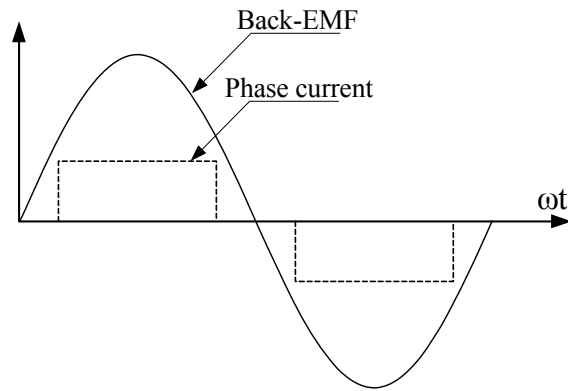


Fig. 2.10. PMSM controlled as BLDC.

2.6. Control Principles of the BLDC Motor

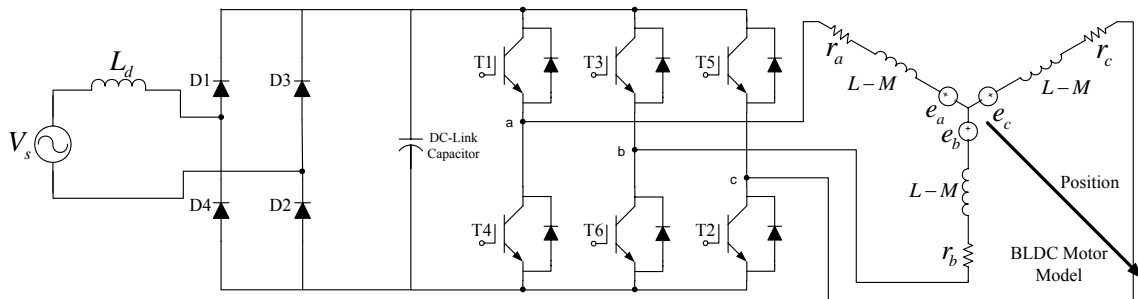


Fig. 2.11. Voltage Source Inverter (VSI) PMAC drive [13].

Almost all home appliances operate on a single-phase input supply. Fig. 2.11 illustrates the circuit configuration of a widely used PMAC motor drive in low-cost applications, such as washing machine control. This configuration is commonly used today in both BLDC and PM synchronous motor (PMSM) drives. The only differences between the drives are the control methods used and the choice of position sensing if no sensorless technique is used. The BLDC motor drive which is represented in Fig. 2.12 consists of an uncontrolled diode rectifier converting single phase AC to DC, a DC-link electromagnetic capacitor for energy storage, and a Voltage Source Inverter (VSI). The DC-link energy is distributed using the part of VSI, made up of IGBTs or MOSFETs, based on PWM scheme. That is why this type of drive is also called a “PWM inverter PMAC motor drive.” [13]

There are various types of PWM techniques which can be used in AC motor drives. The main goal is to reduce the harmonic content to a minimum and achieve the best utilization of the DC bus. Also, an expensive EMI filter is inevitable at the input to comply with various utility interface regulations. When a sensorless technique is not used, one of the necessary components of a BLDC drive is a position sensor. Either a hall-effect sensor or an optical shutter arrangement is used along with some sort of microcontroller/microprocessor or Digital Signal Processor (DSP) to control the VSI. Although snubbers are not shown, in practical applications they are necessary to protect the switches from voltage spikes generated by switching [14].

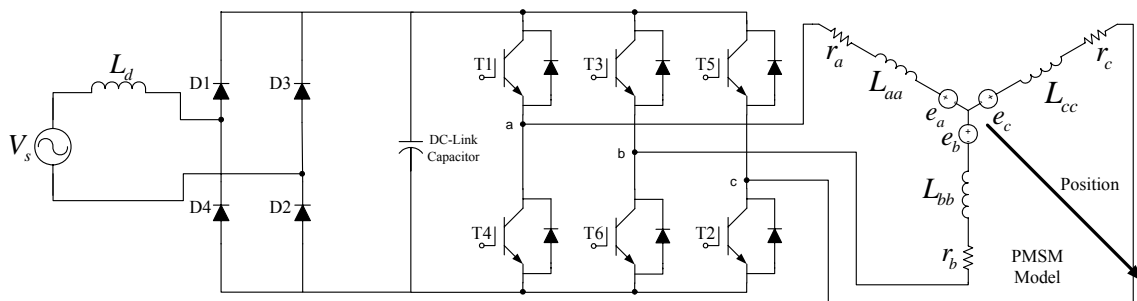


Fig. 2.12. Voltage Source Inverter (VSI) BLDC drive.

A profile for each phase of the BLDC motor with respect to the corresponding back-EMFs as a function of the rotor position is shown in Fig 2.4. At each rotor position, the constant current multiplies with the constant part of the back-EMF to give torque; hence the sum of the products of a phase back-EMF and the corresponding phase current is constant such that this result produces constant torque which is represented in (2.52). The desired current profile is achieved by supplying the BLDC motor from either a VSI or a Current Source Inverter (CSI) which is not discussed here. When using a VSI, the desired current profile is achieved by controlling the switching of the transistors [14]. At any given time, only two of the six switches are conducting. This means that only two phases are conducting at any instant and the third one is floating. In other words, as current enters one of the three phases and leaves through the other and there is no current flowing in the third phase. Having no current in the third phase helps in sensing the back-EMF for a sensorless control of BLDC motor.

The convention of negative and positive current schemes represented in this thesis is as follows the current entering any phase of a motor is assigned as a positive sign, and the current that is leaving any phase of a motor is assigned as a negative sign. Therefore, the upper switches of the inverter, namely, T1, T3 and T5, carry a current (flowing into the motor) which is assigned as a positive sign. The lower switches of the inverter, namely, T2, T4 and T6, carry a negative current (flowing out from the motor). In order to properly operate this motor, it is necessary to synchronize the phase currents with the corresponding phase back-EMFs. This is achieved by the use of hall-effect position sensors which detect the position of the rotor magnetic field, and hence the position of the rotor shaft. In conclusion, a motor with synchronized switching produces an average positive torque.

As seen in Fig. 2.4, each phase current conducts and turns off in a definite sequence. For both the positive and negative cycles on the same phase there is 120 electrical degrees of conduction and 60 electrical degrees of turn off. The current commutation from one phase to the other corresponding to a particular state of the back-EMF is synchronized by the hall-effect sensors such that for every 60 electrical

degrees of rotation one of the hall-effect sensors changes state. Given this, it takes six steps to complete an electrical cycle. Basically, for every 60 electrical degrees, the phase current switching should update.

One electrical cycle, however, may not correspond to a complete mechanical revolution of the rotor. The number of electrical cycles to be repeated to complete a mechanical rotation is determined by the rotor pole pairs. For each rotor pole pairs, one electrical cycle must be completed. The number of electrical cycles/rotations is then equal to the number of rotor pole pairs.

A typical closed-loop block diagram of a brushless DC (BLDC) motor drive system with phase current control is shown in Fig. 2.13. Similar to DC brush motors, BLDC motors with electronic commutation can operate from a DC voltage source and the speed can be adjusted by varying supply voltages. Higher voltage means higher speed. This can be achieved by rectification of a variable voltage transformer output or by using a thyristor bridge in which the DC bus voltage is a function of the firing angle of the thyristor bridge. Instead of varying supply voltage, variable speed operation can also be realized from a constant bus voltage. Fig. 2.11 represents a typical configuration of this phenomenon in which power semiconductor switches are used not only to commutate but also to control the motor terminal voltage via the PWM (Pulse Width Modulation) technique.

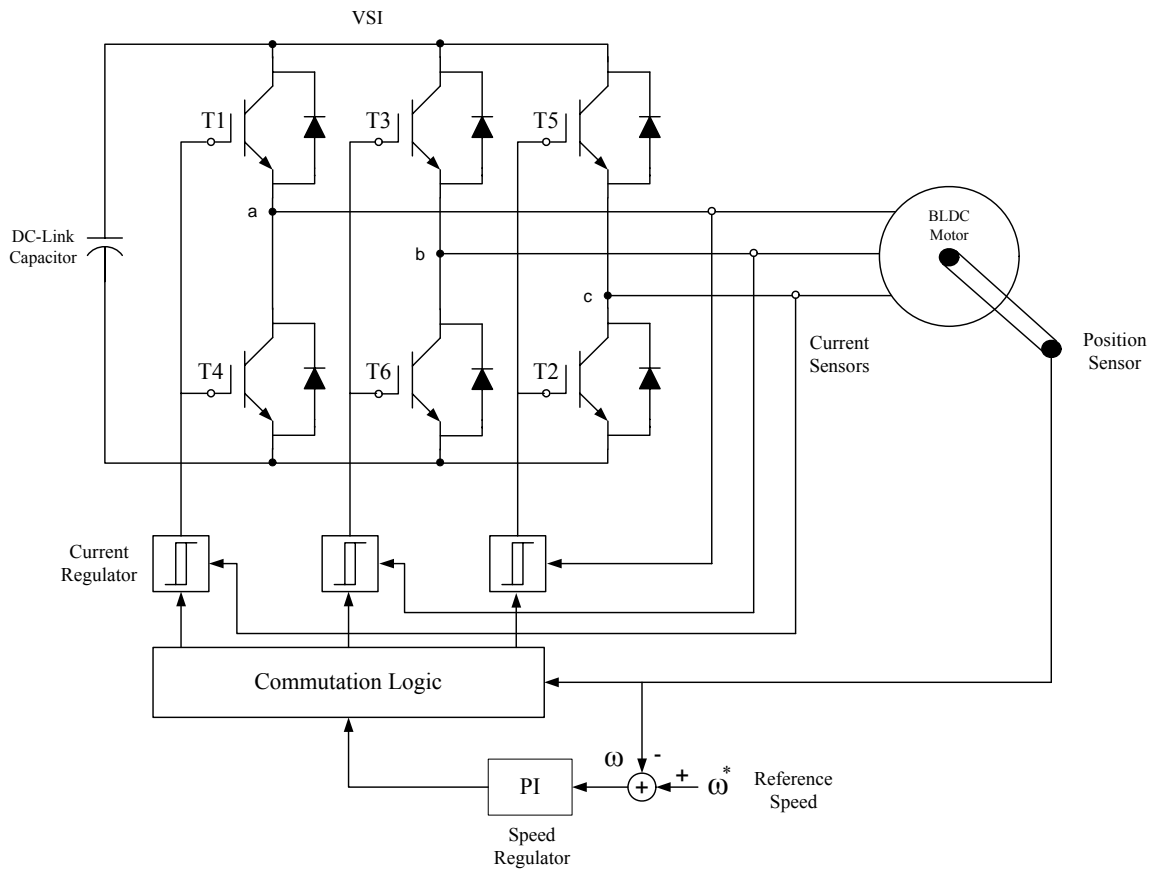


Fig. 2.13. A typical current-controlled BLDC motor drive with position feedback [7].

PWM generates a fixed frequency (usually 2 kHz – 30 kHz) voltage pulse whose on-time duration can be controlled. As a rule of thumb, the PWM frequency should be at least 10 times that of the maximum frequency of the motor. When the duty cycle of the PWM signal is varied within sequences, the average voltage supplied to the stator changes, thus the motor speed will change. If the duty cycle is higher, the motor will turn faster; if it is smaller the motor will slower. Another advantage of having PWM is that if the DC bus voltage is much higher than the motor rated voltage, the motor can be controlled by limiting the percentage of the PWM duty cycle corresponding to that of the motors rated voltage. This adds flexibility to the controller to hook up motors with different rated voltages can be connected to the drive and be utilized at the rated voltage by controlling the PWM duty cycle [14].

Since the brushless DC motor is highly inductive, the motor current produced from the switched voltage will be almost identical to that of a fixed voltage source whose magnitude is the average of the switched voltage waveform. Although PWM control is now very popular in drives, variable bus voltage control is still used in some applications where dynamic performance is not important [14].

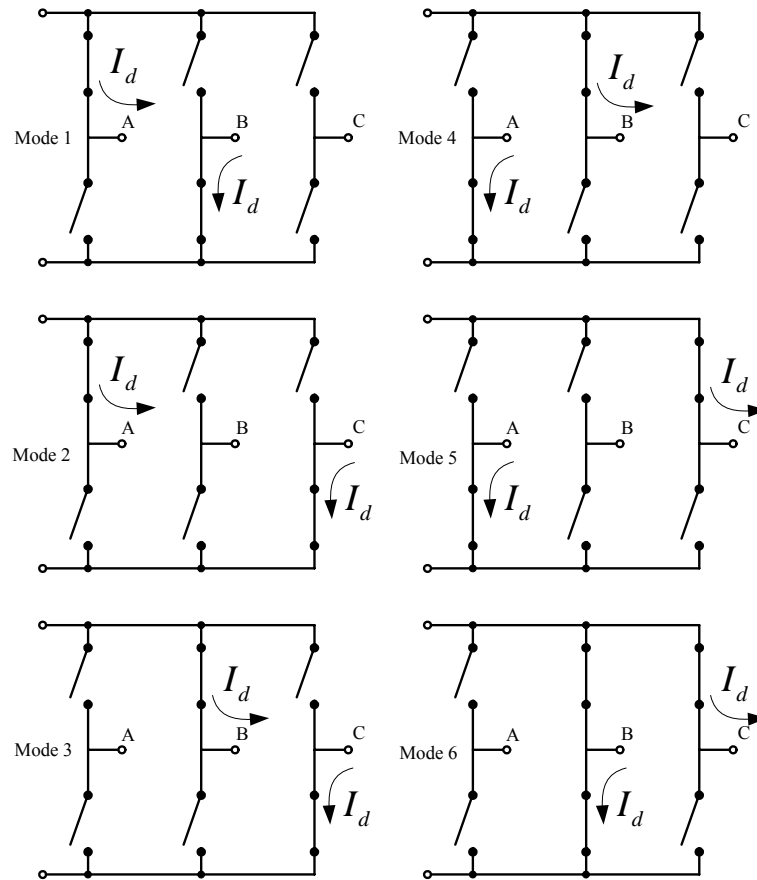


Fig. 2.14. Six possible switching sequences for a three-phase BLDC motor [15].

There are six possible switching modes in the inverter for a three-phase BLDC motor, illustrated in Fig. 2.14. The power circuit of the electronic controller is a switchmode circuit. The only means of controlling such a circuit is to control the timing of the gate signals that turn the power transistors on and off.

According to the quasi-squarewave current condition (120 electrical degrees) in BLDC motors, only two inverter switches (one in the upper inverter bank and one in the lower) are conducting at any instant, as shown in Fig.2.14. If the motor is connected in wye, this means that the inverter input current, I_d , is only flowing through two of the three motor phases in series at all times. Only a single current sensor in the DC-link is sufficient to accomplish the current regulation of the current, I_d , which flows through two phases. With the help of three hall-effect sensors, the position of all the three phase currents can be known so that the proper switches are turned on/off using the PWM current control mode through hysteresis current controllers [15].

For instance, when the currents (equal in magnitude) tend to exceed the hysteresis band, both switches are turned off at the same instant to initiate current feedback through the diodes. Finally, each phase current is regulated and synchronized with the corresponding back-EMF to achieve desired torque and speed characteristics.

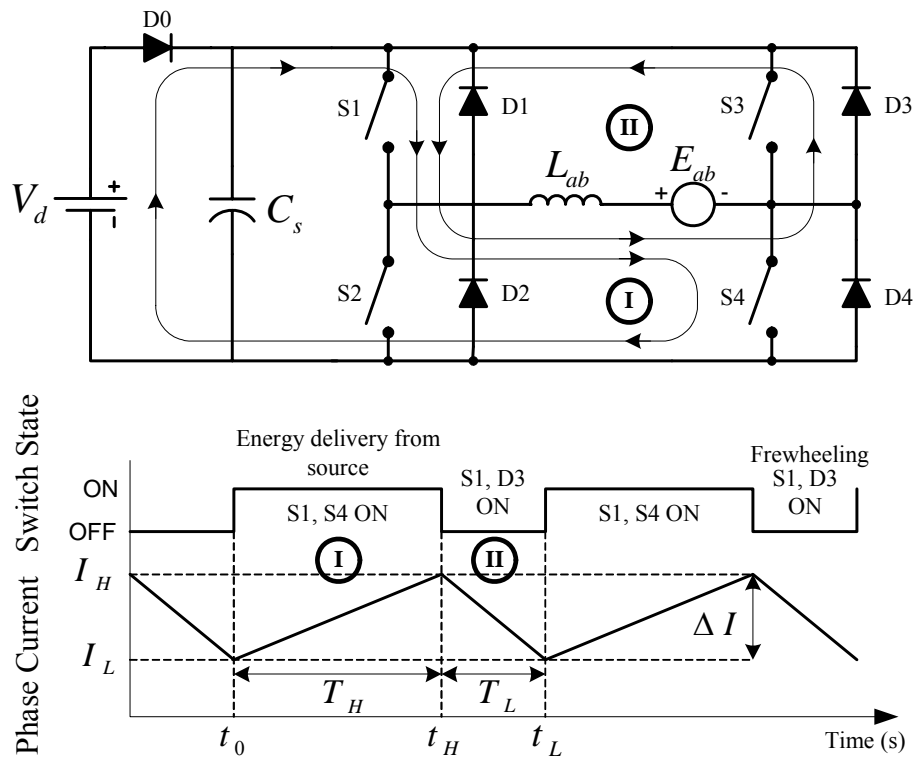


Fig. 2.15. PWM current regulation for BLDC motor [15].

Current regulation for motoring action, using the inverter switches corresponding to mode 1 (switches S1 and S6 are turned on) from Fig. 2.14, is shown in Fig. 2.15. When switches S1 and S6 are turned on, current I_d flows through phase A and B. For this system, line-to-line inductance $L_{ab} = 2(L - M)$ and line-to-line back-EMF $E_{ab} = E_a - E_b$ are used (displayed in Fig. 2.15) instead of phase to neutral values. Resistance drops are neglected.

When the applied source V_d is bigger than the back-EMF voltage, E_{ab} , current flows through the motor when switches S1 and S6 are turned on; otherwise if V_d is less than E_{ab} , then current might flow from the motor. If one of the switches in Fig. 2.15 is turned off (let's say S6) then current decays due to the back-EMF and it flows through diode D3 and switch S1 (loop II), short-circuiting the motor terminals. This is called freewheeling. The amplitude of the phase current is regulated by controlling the duty cycle of the switch S6 (chopping) such that ΔI is kept at a constant minimum value.

The simple BLDC drive is a current-regulated drive in which there is only one current reference signal that is used for all six pairings of the transistors. As it can be seen in Fig. 2.13, the current reference signal is derived from the speed error signal, which represents the difference between the desired speed and the actual speed. The control system for the BLDC motor shown in Fig. 2.13 has three hall-effect sensors for position sensing along with three hysteresis current regulators. Its simple version is explained above, for each phase, and the PI speed regulators are combined together to form the fundamental speed control scheme of a three-phase BLDC motor [16].

2.7. Control Principle of the PM Synchronous Motor

In the three-phase PMSM control, more sophisticated control such as vector or direct torque control techniques are required because all the three phases are conducting at the same time unlike BLDC motor control. A sinewave drive generates less than 1%

torque ripple as compared to a squarewave drive (BLDC drive), but this is only true when both the back-EMF and phase current have sinusoidal waveforms. Because current in each phase is a sinusoidal function of rotor position, separate PWM control for each individual phase currents is required.

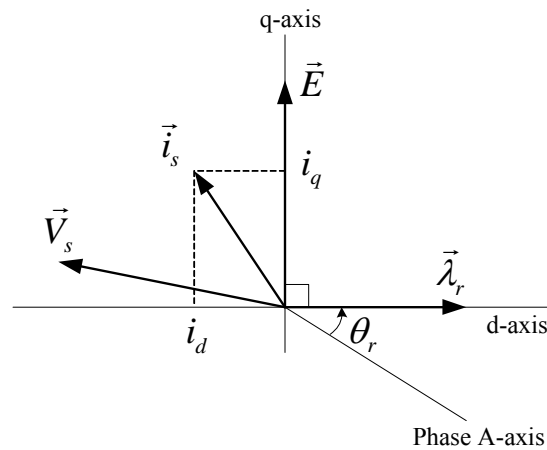


Fig. 2.16. Basic phasor diagram for PMSM [15].

Vector control, or field-oriented control, for all sinewave drives is fundamentally based on the two-axis theory and the phasor diagram shown in Fig. 2.16. Vector control is appropriate for sinewave motors in which torque is produced by the interaction of the fundamental flux and the fundamental ampere-conductor distribution. There are several different ways of creating a two-axis system but generally the method operates with the d- and q- axis current phasor components, i_d and i_q , which may be defined in a variety of reference frames such as rotor or fixed to the stator. To determine i_d and i_q from the instantaneous line currents, a reference frame transformation, such as Park's Transformation shown in Fig. 2.11, is used [15].

Referring to the instantaneous phasor diagram in Fig. 2.16, responsive current regulation plus self-synchronization make it possible to place the instantaneous current phasor \vec{i}_s anywhere within dq-axis rotor reference frame under the limitation of maximum current and regulator saturation constraints. Independent control of the

orthogonal current components i_d and i_q is the simplest known way to control the output torque for PMSMs, shown in (2.44) [15].

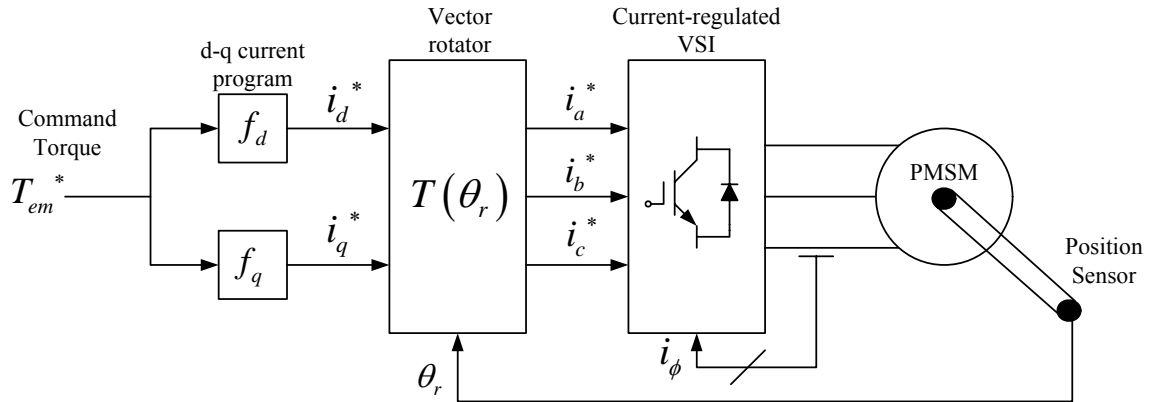


Fig. 2.17. Basic block diagram for high-performance torque control for PMSM [15].

The baseline for implementing this type of high-performance torque control for sinusoidal PMAC motors (PMSM) is shown in Fig. 2.17. An incoming torque command, T_{em}^* , is extracted into the d- and q-axis currents by using (2.44). These are shown as the f_d and f_q function blocks in Fig. 2.17. These current commands, i_d and i_q , in the dq-axis rotor reference frame are DC quantities for a constant torque command. To apply sinewave currents to the motor, these quantities are then transformed into the instantaneous sinusoidal current commands (I_a , I_b , and I_c) for the individual stator phases using the rotor angle feedback (θ_r) and the inverse reference frame transformation matrix $[T_{dq0}(\theta_r)]^{-1}$ as in (2.12).

Commonly, the f_d and f_q functions map the torque command into the dq-axis current component commands, i_d and i_q , so that the maximum torque per ampere operation is achieved providing maximized operating efficiency. There are two different current phasor, \vec{i}_s , trajectories that lie in the synchronously rotating dq-axis:

1) Maximum torque-per-amp trajectory for non-salient (surface-mounted) PMSM which is represented in Fig. 2.18.

2) Maximum torque-per-amp trajectory for salient (interior-mounted) PMSM (so called IPMSM) which is plotted in Fig. 2.19.

As it can be seen in Fig. 2.18, torque-per-amp in a non-salient PMAC machine is maximized by setting i_d to zero regardless of the torque value, so that the sinusoidal phase currents are always exactly in phase (or 180 degrees out of phase) with the sinusoidal back-EMF voltages.

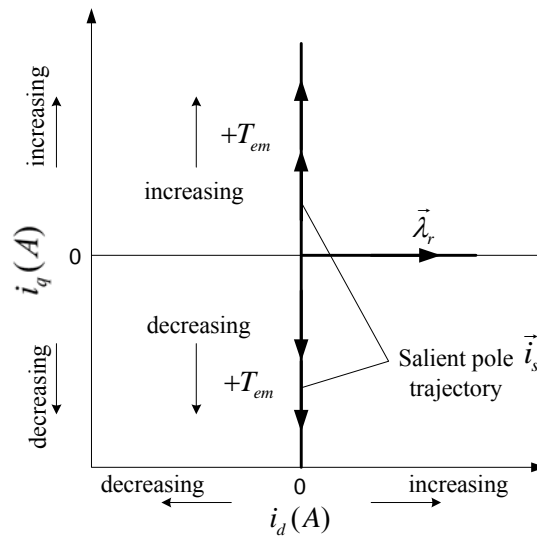


Fig. 2.18. Basic block diagram for high-performance torque control for PMSM [15].

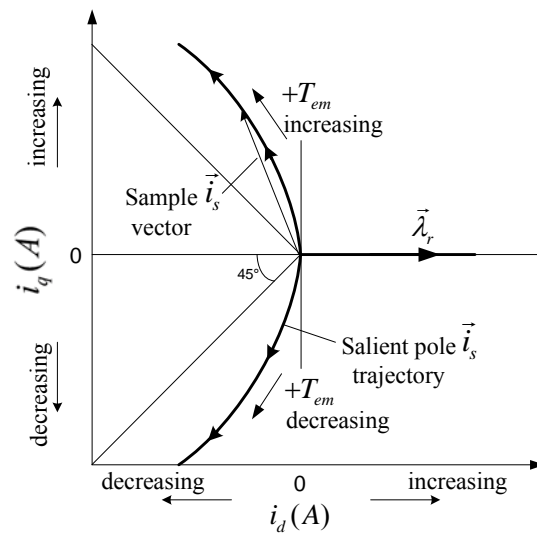


Fig. 2.19. Basic block diagram for high-performance torque control for PMSM [15].

This phenomenon resembles the BLDC motor control that is described in Section 2.11. The idea of creating a positive torque is by aligning the phase currents with the corresponding back-EMF such as in surface-mounted PMSM control. As a consequence, there is a similarity between surface-mounted PMSM control and BLDC motor control. In contrast, the maximum torque-per-amp is achieved for salient PMAC machines (interior-mounted PMSM) by changing both i_d and i_q by using the f_d and f_q mapping functions obtained with respect to torque values [15].

CHAPTER III

MEASUREMENT OF THE PM SPINDLE MOTOR PARAMETERS

3.1. Introduction

All instantaneous torque-controlled drives (vector drives, direct-torque-controlled drives) use various machine parameters. Motor parameters must be considered carefully in order to facilitate a proper simulation platform to resemble the real system. The main objective of this chapter is to show how to measure the necessary motor parameters used in the simulations. There are many techniques which can be used for the identification of the PMSM parameters without direct measurement; the most useful one is called self-commissioning with identification which will be discussed briefly in Section 3.5, but this technique is not used in this thesis.

Temperature rise is a very difficult parameter to calculate unless the thermal time constant has been measured. Under heavy load conditions temperature rises and all the parameters that are measured change proportional to the temperature, however, in this thesis temperature change effect will not be considered on the motor parameters in the simulations.

Because the motor used in the thesis is a high torque, low speed, 48 pole, outer rotor and inner stator PMSM and the operational speed of the agitation control is between 0 and 100 rpm (which is less than the base speed (~150 rpm) of the motor). It is assumed that the motor will not go through the field-weakening region where the saturation effects on the dq-axis synchronous inductances must be taken into account. To model the real motor in the simulations the following parameters should be measured:

- Resistance (R_s) and phase inductance (L_{sa} : Phase A self-inductance)
- Back-EMF constant (k_e)

3.2. Principles of Self-Commissioning with Identification

In many industrial applications, the AC machine and converter are sold by separate manufacturers and the parameters of the AC machine are not known. Prior to starting the variable-speed drive system, however, some machine parameters have to be known. Although the name-plate of the machine can be used for this purpose, in many applications this does not yield accurate information on the parameters required. In general, extensive testing of the machine and tuning of the controller is required, but this can be expensive and time-consuming and requires specially trained equipment (which also increases the costs).

It is possible to obtain various machine parameters and to tune the controllers by an automated process during a self-commissioning stage. It is important to note that various modern industrial drives now incorporate self-commissioning techniques. For example, in a permanent magnet synchronous machine the required electrical parameters such as stator resistance and dq-axis synchronous inductances can be obtained from on-line measurements of the stator currents and/or stator voltages when the machine is at standstill while the inverter in the drive is utilized to generate the signals required for the parameter estimation. [16]

In self-commissioning with identification, various test signals (step signals, ramp signals, etc.) are applied to the machine and the responses are measured. It is also possible to use the name-plate of the motor and other data to ensure that the machine will not be destroyed during the tests. It is also a goal to use a minimum number of sensors. Currents are always measured in every drive to ensure safe operation of semiconductor switches, even when a sensorless technique is being used. However, it is not desirable to use too many sensors. Additional voltage and/or speed sensors should be avoided in self-commissioning systems [16].

There are basically two types of Self-commissioning with identification.

- 1) Off-line identification: Test signals are applied to the motor and the response data is measured. This is used to identify the parameters. However, it is a disadvantage that parameter variations are not considered,

since these can only appear during the normal operation of the drive. When this approach is used it is also a goal not to produce torque [16].

- 2) On-line identification: In this case, initial pre-computed controller parameter values are required. Measurements are made during the operation of the drive and motor and controller parameters are continuously estimated, and the controller is continuously adapted. This approach imposes high computation burdens [16].

3.3. Resistance and dq-axis Synchronous Inductance Measurements

The phase resistance of the motor is measured by a HP 4284A Precision LCR Meter (20 Hz ~ 1 MHz) at two different frequencies (20 Hz and 400 Hz). This is because when the frequency is increased resistance also increases due to the skin effect. Other than the RLC meter, precision ohmmeters or multimeters can also be used for the measurement of the phase resistance. For our purpose, an RCL meter will give more accurate results than the rest of the methods because the test frequency can be adjusted relative to our needs. Because the operation speed range of the tested motor is between 0 and 100 rpm (0 Hz to 40 Hz), the test frequency is set to 20 Hz in the RLC meter which is equal to the average value of the speed range of agitating cycle. On the other hand, a test conducted with the frequency 400 Hz in the phase resistance measurement is conducted because it could be used in future high speed PMSM washing machine applications. At high speed (high frequency) the resistance will change due to skin effect.

In this thesis work, a dq-axis model (SIMPLORER[®] has a built-in model of PMSM) of the motor in simulation platforms (MATLAB/SIMULINK[®] and SIMPLORER[®]) is built because the tested motor generates a sinusoidal back-EMF. This ensures that the dq-axis model is applicable even if the motor is supplied by squarewave currents like a BLDC motor. Knowing the phase resistance, R_s , therefore is important in

the dq-axis motor model. The wye connected motor has a neutral access, so the measurement of the resistance is done between the phase and neutral point as shown in Fig. 3.1. If the three-phase wye connected motor does not have a neutral access then the only way of measuring the phase resistance is by measuring the line-to-line resistance, R_{LL} , and dividing it by 2. Consequently, the line-to-line resistance, R_{LL} , is two times the phase resistance, R_s , when the motor is three-phase symmetrical.

Usually in three-phase motors, the windings are connected in wye fashion and there is no neutral point to access. Therefore for those types of motors the inductance measurement is conducted between two phases (line-to-line inductance) which is given by

$$L_{LL} = L_{sa} + L_{sb} - 2M_{ab} = 2(L - M) \quad (3.1)$$

where $L_{sa} = L_{sb} = L$ is the phase self-inductance, (Phase A and Phase B self inductances are equal under the three-phase symmetrical system) and M_{ab} is the mutual inductance between Phase A and Phase B.

In the above equation, the line-to-line inductance of Phase A and B is represented. Under symmetrical systems, ($L_{sa} = L_{sb} = L_{sc} = L$ and $M_{ab} = M_{ac} = M_{bc} = M$) the above equation can be applicable to the other remaining phases and the resultant line-to-line inductance for the corresponding two phases will be always be equal to $2(L - M)$.

In our case, the motor has a neutral access such that each phase inductance can be measured between phase and neutral point by the HP 4284A Precision LCR Meter (20 Hz ~ 1 MHz) at both 20 Hz and 400 Hz test frequencies. The test level is chosen as 1 V which is generally chosen as a common test level for motor inductance measurements.

In sinewave PMSM drives generating sinusoidal back-EMFs, the parameters of interest are the per-phase resistance, R_s , and the per-phase synchronous inductance, L_s , (both of which are employed in constructing the phasor diagram which is the main tool

for analyzing sinewave operation are necessary). Accordingly, the appropriate methods for measuring synchronous inductance should be used. The synchronous inductance incorporates the self and mutual inductances in a way that correctly represents their effects with a sinewave drive [16].

As mentioned in the previous chapter, phase inductance is represented in (2.5). In this case, the q-axis in dq-plane is chosen as a reference for the rotor position θ with respect to the a-axis as shown in Fig. 2.3. This is done because deriving the phase inductance is easier if the q-axis is taken as a reference for the rotor position, θ . In general motor drives, the d-axis is the reference to represent the rotor position with respect to the a-axis as shown in Fig. 2.2. If the rotor position, θ , is rewritten incorporating the real rotor position, θ_r , in (2.5), then new phase inductance when the d-axis is chosen as a reference point for the rotor position, θ_r , is obtained as:

$$L_{sa} = L_{sl} + L_0 + L_{ms} \cos 2\theta_r \quad (\text{H}) \quad (3.2)$$

The above equation demonstrates the self-inductance of Phase A. The only difference between (3.2) and (2.5) is that the sign of L_{ms} is now positive because the dq-axis is turned 90 electrical degrees CCW, and θ_r now represents the angle between the d-axis and the a-axis (the a-axis is the 0 degree reference).

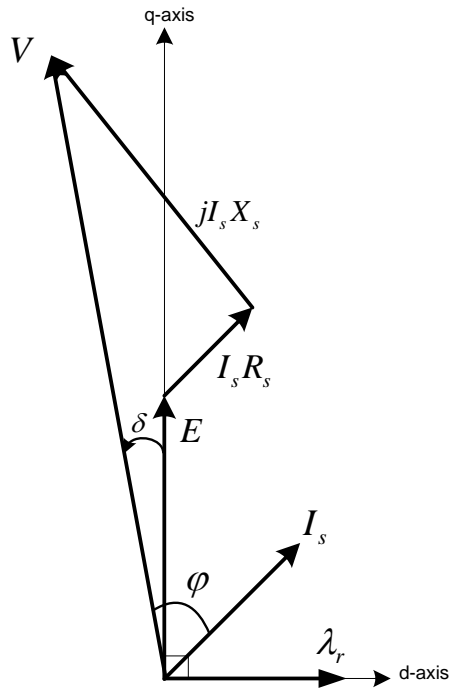


Fig. 3.1. Vector phasor diagram for non-salient PMSM.

The synchronous inductance can be measured by several methods such as a short-circuit generating test for non-salient machines and a lock-rotor test by using the RLC meter as shown in Fig. 3.2. In this thesis the later one is used for simplicity because the first method requires an additional motor that needs to be coupled so that generation is possible. In the short-circuit generating test the motor is driven at a low speed with all the phases shorted together. The current in one phase, or preferably in all three, is measured. If a non-salient motor is wye connected in steady-state with balanced sinusoidal phase currents, the operation can be represented by the phasor diagram shown in Fig. 3.1, and then its voltage equation can be written as:

$$\mathbf{V} = \mathbf{E} + (R_s + j\omega L_s)\mathbf{I} \quad (3.3)$$

where \mathbf{V} , \mathbf{E} and \mathbf{I} are represented in bold showing that they are vectors and rotate in the dq-plane. ω is the synchronous speed in rad/sec, \mathbf{V} is the applied voltage phasor, \mathbf{E} is the back-EMF phasor and \mathbf{I} is the current phasor. In a sinewave permanent magnet

synchronous machine, the d-axis and q-axis synchronous inductances are equal; $L_{ds} = L_{qs} = L_s$. The voltage, back-EMF and the current phasors are described below:

The terminal voltage phasor is given by

$$\mathbf{V} = V_{ds} + jV_{qs} \quad (3.4)$$

And the current phasor is:

$$\mathbf{I} = I_{ds} + jI_{qs} \quad (3.5)$$

The d-axis is chosen as the real, or reference axis. The open-circuit voltage phasor, (the back-EMF phasor) is aligned with the q-axis in the phasor diagram since it leads the flux-linkage by 90 electrical degrees. It can be written as:

$$\mathbf{E} = jE_{qs} = j\omega\lambda_r \quad (3.6)$$

where λ_r is the RMS phase flux-linkage due to the magnet.

The current I_d flows in the short-circuited motor which is equal to (3.7) when $V = 0$ and if the resistance is neglected in (3.3), then:

$$\omega L_s = \frac{E}{I_{sc}} \quad (3.7)$$

where E is the value of the open-circuit voltage per phase at the same speed. Caution should be taken during the short-circuit test because the short-circuit current may be much larger than the rated current, and may be sufficient enough to partially demagnetize the magnet. Also, short-circuit connection should not be applied suddenly while the machine is running; first it should be connected while the machine is stationary and then the machine should be brought to the desired test value slowly. The reason is that a sudden short-circuit produces a higher transient current with DC-offsets that might demagnetize the magnets [17].

The first method explained above is only applicable in the non-salient motors. For salient motors, the short-circuit generation test will help to measure only the d-axis synchronous inductance. Other tests should be conducted to get the q-axis inductance.

Together it is a time-consuming and complicated method. The second technique used in this thesis to measure the synchronous inductance is an easy solution as compared to the first method which is explained below:

According to Fig. 3.2, self-resistance, R_s , and self-inductance, L_{sa} , are measured by the LCR meter for two different frequency levels (20 Hz and 400 Hz) as discussed before. Because the self-inductance and mutual inductance are dependent of the rotor position, the rotor dependent terms in (3.2) should be eliminated. To achieve this, the rotor magnetic flux (d-axis) is aligned (locked) with the a-axis. The alignment is obtained by applying a DC power supply between Phase A and the neutral access of the motor which is also illustrated in Fig. 3.2. The above condition should be considered when the motor has saliency, meaning that the d- and q- axis inductances are not equal such that the self and mutual inductances are dependent on the rotor position. In our case, the motor (non-salient = surface-mounted PMSM) has very little saliency so that the saliency effect can be neglected. Actually, from the above conclusion, to measure the d- and q-axis synchronous inductances for surface-mounted PMSMs there is no need to align the magnet flux with the known reference axis (a-axis). The saliency effect coefficient, L_{ms} , in the self and mutual inductance equations will be zero for non-salient motors.

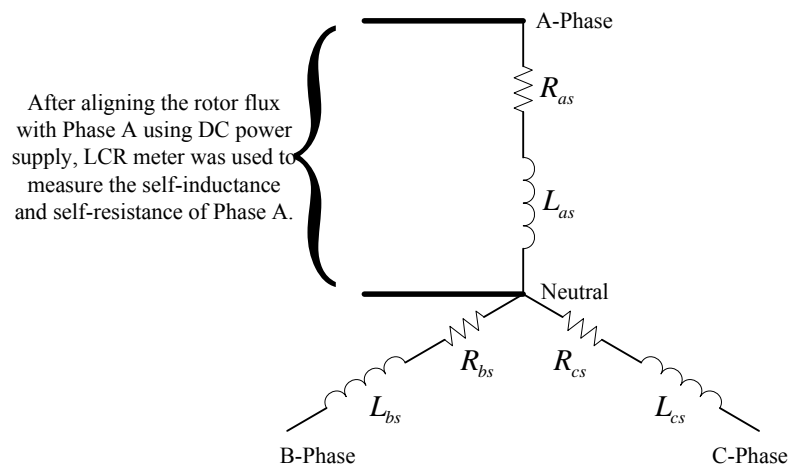


Fig. 3.2. Measurement of phase resistance and inductance.

When the rotor magnetic flux (d-axis) is aligned with the a-axis then θ_r in (3.2) becomes zero and the self-inductance of Phase A can be written as

$$L_{sa} = L_{sl} + L_0 + L_{ms} \quad (3.8)$$

where L_{ms} is the dq-axis synchronous inductance variation. Since $L_{ms} = \frac{L_d - L_q}{2}$ in surface-mounted motors and L_{sl} are equal to zero, then in steady-state L_{sa} can be shorten to:

$$L_{sa} = L_0 + L_{ms} \quad (3.9)$$

When $L_{ms} = 0$ then (3.9) can be reduced farther to:

$$L_{sa} = L_0 \quad (3.10)$$

From the simplified self-inductance above a relationship is found between the d- and q-axis synchronous inductances. It is obtained as follows:

$$\begin{aligned} L_{ds} &= L_{md} + L_{ls} \\ L_{qs} &= L_{mq} + L_{ls} \end{aligned} \quad (3.11)$$

where L_{sl} is chosen as zero under steady-state conditions and the d- and q-axis synchronous inductances are equal to their corresponding magnetizing values L_{md} and L_{mq} , respectively as shown below:

$$L_{md} = \frac{3}{2}(L_0 + L_{ms}) = L_{ds} \quad (3.12)$$

$$L_{mq} = \frac{3}{2}(L_0 - L_{ms}) = L_{qs} \quad (3.13)$$

If $L_{ms} = 0$ is placed in (3.12) and (3.13), we obtain

$$L_{md} = L_{mq} = L_{ds} = L_{qs} = \frac{3}{2}L_0 \quad (3.14)$$

If (3.10) is substituted into (3.14), then the d-axis synchronous inductance relationship with the a-axis self-inductance can be gathered as:

$$L_{ds} = L_{qs} = \frac{3}{2}L_0 = \frac{3}{2}L_{sa} \quad (3.15)$$

Self-resistance and self-inductance measurements of the 36 slot/48 pole spindle motor at 20 Hz and 400 Hz are given in Table I below:

TABLE I
MEASUREMENTS OF SELF-RESISTANCE AND SELF-INDUCTANCE

Ω (ohm) @ 20 Hz (test level 1V)	mH @ 20 Hz (test level 1V)
$R_{as} : 16.285 \quad \Omega$	$L_{aa} : 62.09 \quad \text{mH}$
$R_{bs} : 16.31 \quad \Omega$	$L_{bb} : 62.04 \quad \text{mH}$
$R_{cs} : 16.3345 \quad \Omega$	$L_{cc} : 61.10 \quad \text{mH}$
$R_{savg20Hz} : 16.30983 \quad \Omega$	$L_{savg20Hz} : 61.7433 \quad \text{mH}$
Ω (ohm) @ 400 Hz (test level 1V)	mH @ 400 Hz (test level 1V)
$R_{as} : 21.11 \quad \Omega$	$L_{aa} : 61.72 \quad \text{mH}$
$R_{bs} : 21.2115 \quad \Omega$	$L_{bb} : 62.10 \quad \text{mH}$
$R_{cs} : 21.10 \quad \Omega$	$L_{cc} : 61.86 \quad \text{mH}$
$R_{savg400Hz} : 21.1405 \quad \Omega$	$L_{savg400Hz} : 61.8933 \quad \text{mH}$

As a result of the measurements of the three-phase self-resistances and self-inductances of the tested motor, the following conclusions are obtained about the average self-resistance and self-inductance of the motor to be used in simulation platforms (MATLAB/SIMULINK[®] and SIMPLORER[®]):

$$R_{avg_self} : \underline{16.30983} \quad \Omega \text{ (chosen from 20 Hz test)}$$

$$L_{avg_self} : \underline{61.8183} \quad \text{mH (chosen from average of 20 Hz and 400 Hz tests)}$$

The synchronous inductance of the motor is obtained using (3.13) and the above average value of the self-inductance from above as:

$$L_s = L_{ds} = L_{qs} = \frac{3}{2} L_{sa} = \frac{3}{2} 61.8183 = 92.72745 \text{ mH}$$

Although using the LCR meter is an easy way to measure the line-to-line and line-to-neutral (if the motor has a neutral access) inductances, LCR meters generally use a test frequency on the order of 1 kHz with very low currents, so the measured inductance may differ appreciably from the correct value which corresponds to a lower frequency and much higher currents. A complete experimental analysis of the inductances requires DC inductance measurements using, for example, the Prescott bridge described by Jones [17], which can be modified to permit inductances to be measured with varying levels of bias to demagnetizing stator MMF or quadrature-axis stator MMF [17].

It is a good idea to take inductance measurements at several rotor positions. Unless there are some problems with the magnets in the motor, there should be very little inductance variation observed as the rotor rotates in a surface-mounted PMSM (our test motor is a surface-mounted PMSM). On the other hand, interior-mounted PMSMs have a saliency such that inductances vary greatly with the rotor position. When the d-axis inductance is measured by a locked-rotor test in an interior-mounted PMSM the q-axis synchronous inductance can be measured if the rotor is rotated 90 mechanical degrees CCW or CW from the d-axis. The rotor could have been brought to the 90 degree electrical position when the a-axis is chosen as a reference, but if the motor is a high pole motor such as our test motor, rotating the motor 90 electrical degrees from the reference position is more difficult than rotating it 90 mechanical degrees.

To get the synchronous inductance of the tested motor more precisely another method can be performed which does not eliminate the leakage inductance in the calculations. This technique is applicable if the motor has a neutral access. In this thesis, this method is not implemented, but the theory behind it will be explained in below:

To find the leakage inductance, L_{sl} , a line-to-line inductance measurement should be performed corresponding equation is given by:

$$L_{LL} = L_{sa} + L_{sb} - 2M_{ab} \quad (3.16)$$

where M_{ab} is the mutual inductance between Phase A and Phase B. If the system is symmetrical then all the self-inductances are equal, ($L_{sa} = L_{sb} = L_{sc} = L$), therefore the line-to-line inductance can be summarized as:

$$L_{LL} = 2(L - M_{ab}) \quad (3.17)$$

If the line-to-line inductance is measured between Phase A and Phase B and the self-inductance measurement result, which is obtained from the previous experiment for Phase A is placed into (3.17), then the mutual inductance, M_{ab} , between Phase A and Phase B can be found easily.

$$M_{ab} = -\frac{1}{2}L_0 + L_{ms} \cos 2\theta_r \quad (3.18)$$

Because the dq-axes inductances are the same, the saliency coefficient for mutual inductances will also be equal to zero and the final mutual inductance equation, without the L_{ms} term, can be shown as:

$$M_{ab} = -\frac{1}{2}L_0 \quad (3.19)$$

The self-inductance of Phase A without the L_{ms} term and including leakage inductance is written as:

$$L_{sa} = L_{sl} + L_0 \quad (3.20)$$

Knowing M_{ab} and putting it in (3.19), L_0 is obtained. If L_0 is then substituted in (3.20), then L_{sl} can be found because L_{sa} was known previously from the LCR meter result which includes the leakage inductance effect also.

If the d- and q-axis inductances, L_{sd} and L_{sq} , in (3.12) and (3.13) are re-written including the known leakage inductance, then we obtain:

$$L_{ds} = L_{md} + L_{ls} = \frac{3}{2}(L_0 + L_{ms}) + L_{ls} \quad (3.21)$$

$$L_{ds} = L_{mq} + L_{ls} = \frac{3}{2}(L_0 - L_{ms}) + L_{ls} \quad (3.22)$$

where all the components in the above equations are known so that the d- and q-axis inductances, L_{sd} and L_{sq} , can be precisely found.

3.4. Measurement of the Back-EMF Constant (k_e) and PM Flux Linkage (λ_r)

To calculate the rotor flux linkage, λ_r , which is the line-to-neutral peak rotor flux linkage amplitude value, first the back-EMF constant, k_e , is measured. This done by the generator test in which the tested motor is coupled to a DC motor and it is driven through the shaft by the DC motor at a constant mechanical speed, ω_{rm} . The flux linkage of the permanent magnet, λ_r , and the peak value of back-EMF constant, k_e , can then be easily obtained by measuring the no load line-to-neutral peak voltage (back-EMF, E_{anpk}) of the motor while it is driven by DC motor. The derivation of λ_r is given by:

$$E_{anpk} = \sqrt{2}k_e\omega_{re} = \sqrt{2}k_e 2\pi f_e \quad (3.23)$$

If the peak back-EMF constant, $\sqrt{2}k_e$, is replaced by the line-to-neutral peak rotor flux linkage value, λ_r , in (3.23), we obtain:

$$\frac{E_{anpk}}{\omega_{re}} = \lambda_r = \sqrt{2}k_e = 0.223256 \text{ Vrad / s} \quad (3.24)$$

where $\omega_{re} = \frac{P}{2}\omega_{rm}$; P is the number of poles and ω_{rm} is the mechanical speed in rad/sec.

When the motor has no neutral access, the measurement of the peak line-to-neutral back-EMF, E_{anpk} , is impossible. In this case, the following procedures need to be conducted to find the peak rotor flux amplitude, λ_r :

First, the line-to-line and line-to-neutral voltage relation is written as:

$$V_{ab} = \sqrt{3}V_{an} \quad (3.25)$$

The relationship between the rms and peak voltages can be expressed as:

$$V_{pk} = \sqrt{2}V_{rms} \quad (3.26)$$

The measured line-to-line rms value of the back-EMF is equal to:

$$E_{abrms} = k_e\omega_{re} \quad (3.27)$$

where k_e is the line-to-line back-EMF constant. From (3.25), the back-EMF is considered as a voltage, therefore:

$$E_{an} = \frac{E_{ab}}{\sqrt{3}} \quad (3.28)$$

The peak value of (3.27) is given by:

$$E_{abpk} = \sqrt{2}k_e\omega_{re} \quad (3.29)$$

If (3.29) is substituted into (3.28), we obtain:

$$E_{anpk} = \frac{\sqrt{2}k_e}{\sqrt{3}}\omega_{re} \quad (3.30)$$

Equation (3.30) is the placed into (3.24) and the following result is gathered.

$$\lambda_r = \frac{E_{anpk}}{\omega_{re}} = \sqrt{\frac{2}{3}} \frac{2}{P} \frac{E_{abpk}}{\omega_{rm}} = \frac{2}{\sqrt{3}} k_e \quad (3.31)$$

TABLE II
MEASUREMENTS OF LINE-TO-NEUTRAL BACK-EMF FOR EACH PHASE (0-50 RPM)

Ean (V-rms)	Ebn (V-rms)	Ecn (V-rms)	freq-Ea(Hz)	speed(RPM)
0	0	0	0	0
4.417	4.467	4.68	4.56	11.3
4.397	4.513	4.648	4.52	11.3
4.321	4.33	4.524	4.38	11.3
4.384	4.514	4.626	4.53	11.3
8.2	8.159	8.348	8.3	20.8
8.256	8.207	8.429	8.31	20.8
8.24	8.216	8.41	8.34	20.8
7.993	8.58	8.396	8.35	20.8
11.701	11.887	12.106	12.03	30.4
11.914	12.038	12.211	12.18	30.4
11.996	12.119	12.243	12.25	30.4
12.04	12.17	12.31	12.19	30.4
16.34	16.28	15.75	16.15	40.2
16.28	16.25	15.71	16.18	40.2
16.25	16.25	15.7	16.14	40.2
16.08	16.11	15.58	15.96	40.2
15.56	16.3	16.3	16.15	40.2
15.53	16.27	16.31	16.11	40.2
19.67	19.79	19.65	19.85	50
19.91	19.88	19.9	20.05	50
19.91	19.88	19.9	20.04	50
19.92	19.9	19.94	20.08	50

If the average value of the line-to-neutral back-EMF, $E_{anpkavg}$, found in Table II, is substituted into (3.23), then the average back-EMF constant, k_e , can be derived as:

$$k_e = 0.223256 \text{ Vrad/s}$$

3.5. Load Angle (δ) Measurement

Load angle measurement is performed in this thesis to validate the motor model in the simulations by making the motor model as similar to the real motor as possible.

Load angle, δ , is the angle between the back-EMF, E , and the input voltage of the same phase back-EMF, V , as shown in Fig. 3.1.

To measure the load angle, the following equipment is used:

- 1) Three-phase AC power source
- 2) LeCroy Digital Storage Oscilloscope (DSO)
- 3) Maxtrol Hysteresis Dynamometer (max torque is 11.3 lbs)
- 4) Hall-effect sensor mounted on the stator

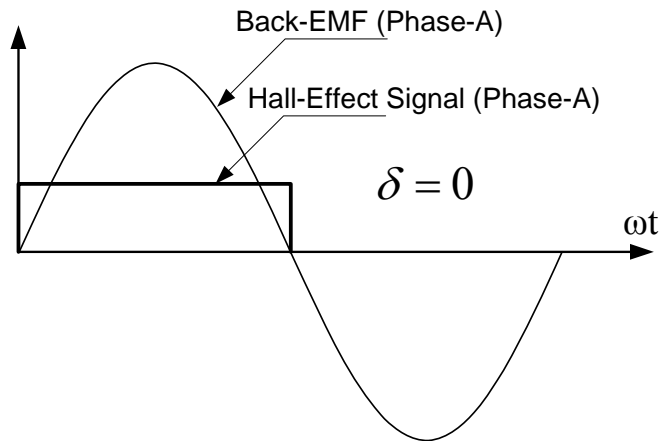


Fig. 3.3. Phase A voltage waveform and hall-effect signal of the same phase.

A load angle measurement is conducted for Phase A of the tested motor. It could have been performed for the other phases, but under symmetrical conditions the results would be the same. For the motor that it is used in this thesis, the line-to-neutral back-EMF is aligned with the corresponding hall-effect signal so that hall-effect sensor signals are used to get the back-EMF, E , position. The load angle will be the angle of back-EMF, E , with respect to the input voltage of the same phase back-EMF, V . A difficulty that exists though is reading the hall-effect signals on the oscilloscope efficiently. This is due to jittering in the hall-effect signals. The reason this jittering occurs is because of uneven distribution of the magnets on the rotor. Whenever the N pole is seen by the hall-effect sensor it generates a pulse, and when the S pole is seen the signal goes to zero. Fig. 3.4 shows an example of uneven distribution of the magnets causing jittering in the hall-effect signals:

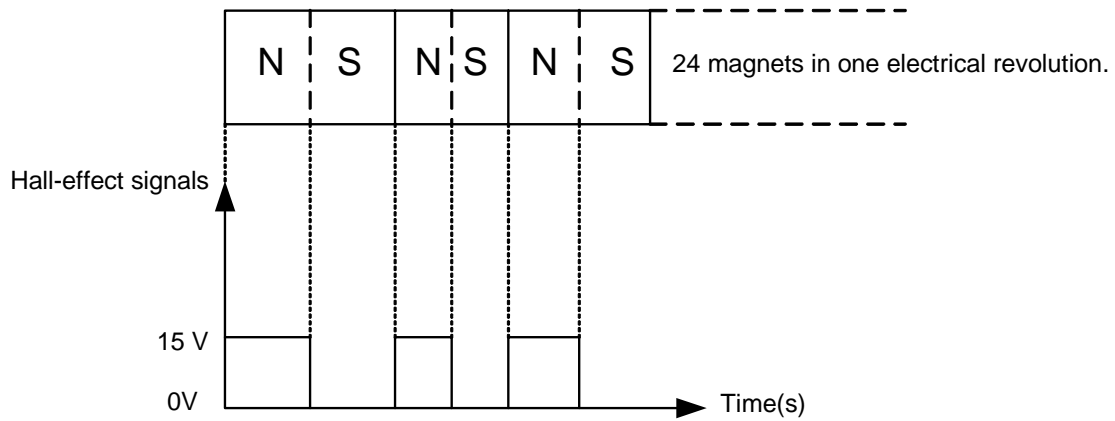


Fig. 3.4. Rotor magnet representation along with hall-effect signals.

From the above figure, it can be observed that uneven distribution of the magnets alters the width of the hall-effect signals and causes jittering in the running motor as mimicked in the graph below:

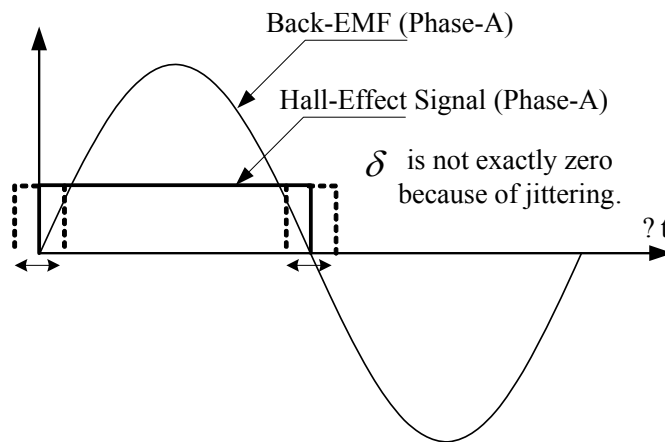


Fig. 3.5. Phase A voltage waveform and hall-effect signal with jittering effect.

As it can be seen in Fig. 3.5, uneven distribution of the magnets on the rotor causes shaking back and forth in hall-effect signals creating difficulty in reading those signals on the oscilloscope. To overcome the jittering problem (not %100), The LeCroy DSO is used to average 20 pulses of the hall-effect signal for Phase A, H_a .

There are two different ways of measuring the load angle which are explained below:

- 1) The motor is started and operated in open-loop by a three-phase AC power supply. When V/f control is used starting from $V/f = 1$ (20 Vrms) up to 2 (40 Vrms) for a reference test frequency at 20 Hz, when operating frequency is chosen as 40 Hz (100 rpm) using $V/f \approx 1$ (40 Vrms) created an unbalance operation of the motor such that over 30 Hz the motor oscillates a lot (very unbalanced current is observed after 25-30 Hz with $V/f \approx 1$). To diminish the oscillation, the motor should have had a higher current flow through them over the 25-30 Hz frequencies. In this case $V/f \approx 2$ is chosen which means there is an 80 Vrms input sine wave applied to handle up to 10 N·m of load torque at 100 rpm (40 Hz). $V/f \approx 2$ is chosen as our operating point for most of the tests to achieve less oscillation in the current, speed and torque response. The results for the 40 Hz test frequency under no-load but with an increased applied voltage condition is shown in Fig. 3.7.

The three-phase AC power supply is a programmable AC source such that various voltage and frequency levels as well as steps in either can be preset. For example, in the load test the motor is started at a low frequency, such as 12 Hz to 15 Hz, and then the frequency is automatically increased to the desired test level (20 Hz and 40 Hz).

The applied voltage, V , is then increased from 20 Vrms up to 40 Vrms for the first part of the load test (the second part starts from 70 Vrms and up to 90 Vrms). The voltage is incremented by 5 Vrms at the test frequency. At each increment the average of the hall-effect signal is read on the DSO. The DSO then calculates the load angle between the applied voltage and its corresponding hall-effect signal. When the applied voltage is increased, the load angle increases simultaneously, shown in the vector phasor diagram of the PMSM in Fig. 3.9. When the applied voltage, V_s , is increased, the current, I_s , also increases so that the V_s vector moves farther than corresponding back-EMF, thus the load angle

increases. Related results to the first measurement technique are shown in Figs. 3.6 and 3.7.

- 2) The above procedures are applied to the second part of the load test in which motor is started under open-loop conditions as discussed before up to a 40 Hz operating frequency with $V / f \approx 2$ (80 Vrms). When the motor reaches 40 Hz, a load torque is applied from zero up to 10 N·m by the dynamometer. The results are obtained as a graph shown in Fig. 3.8. When the motor is loaded, the current flows through the terminal conductors to the motor and the applied voltage deviates from the corresponding back-EMF so that the load angle is generated.

With the phase (radian) function and reasonable sweeping (25-100 sweeps), the load angle, δ , values are collected for various operation points and are shown in the figure below:

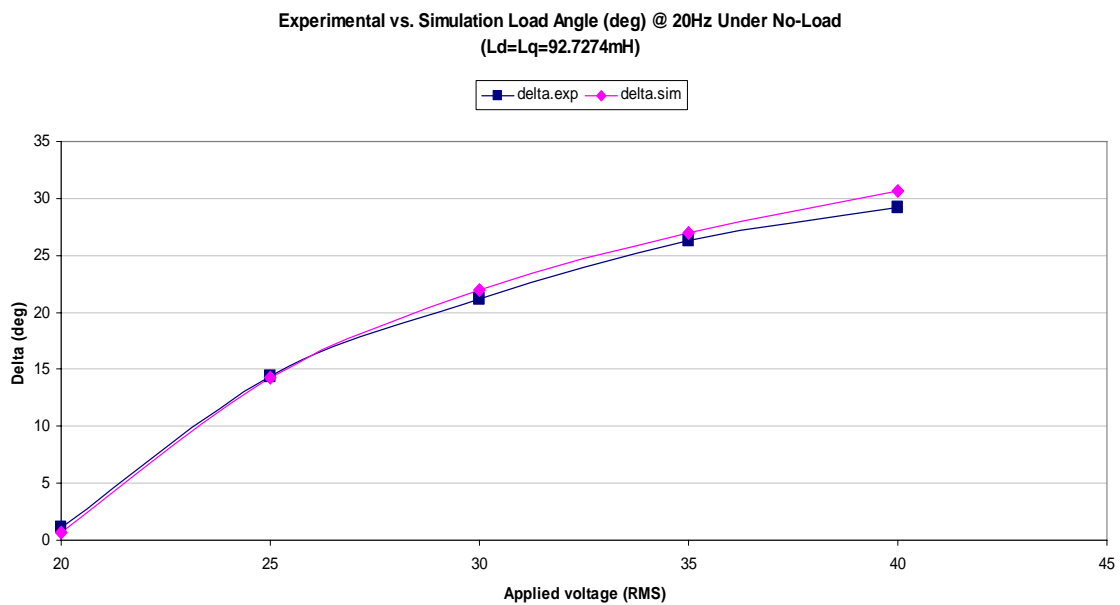


Fig. 3.6. Experimental vs. simulated load angle (deg.) at 20 Hz (No-load).

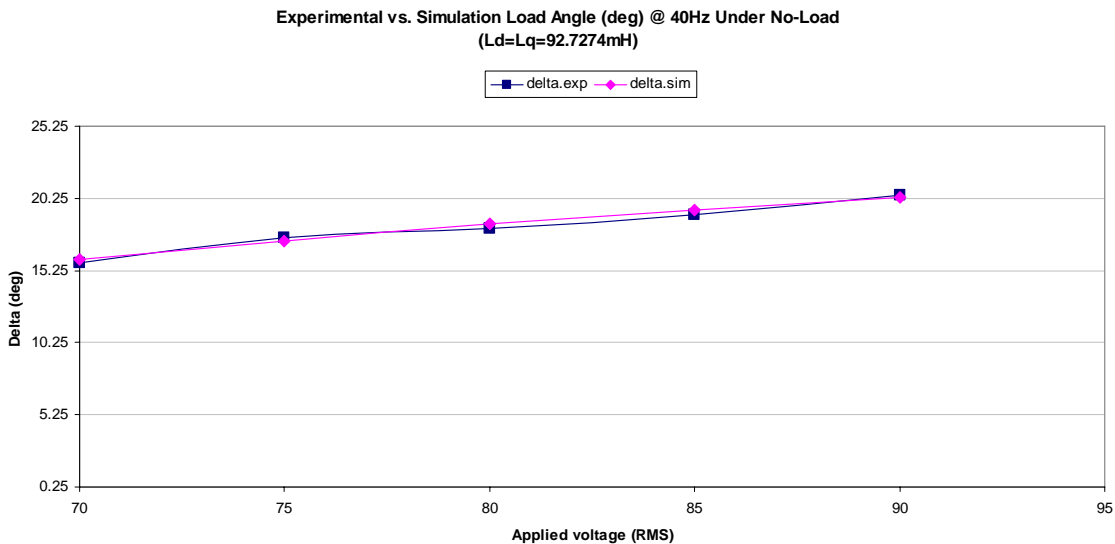


Fig. 3.7. Experimental vs. simulated load angle (deg.) at 40 Hz (No-load).

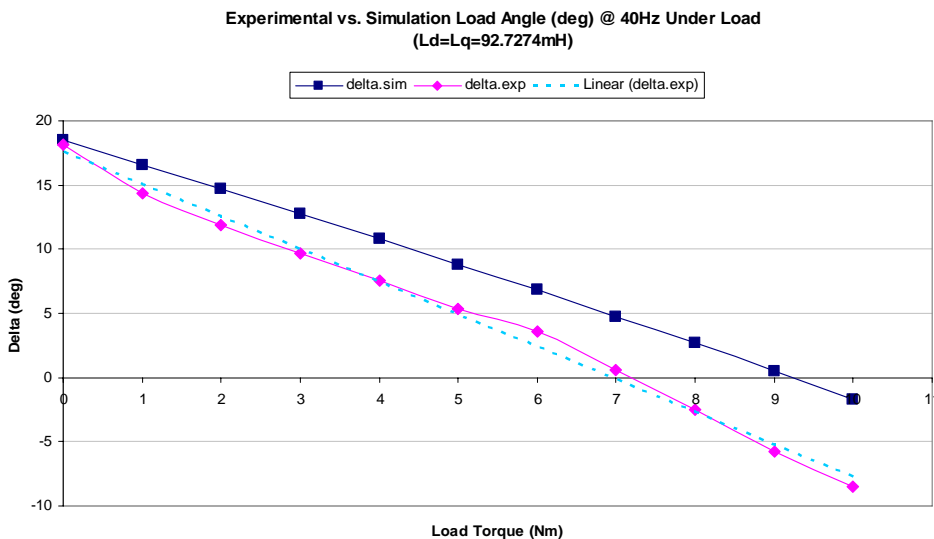


Fig. 3.8. Experimental vs. simulated load angle (deg.) at 40 Hz (Load).

The reason we compared the load angles of both the simulation and experiment is that for the same rms value of the motor current (I_s), the behavior of the overall system is different. This is because of the possible difference between the parameters of the

motor model and the real motor. The overall behavior of the PMSM system is shown in the graph below:

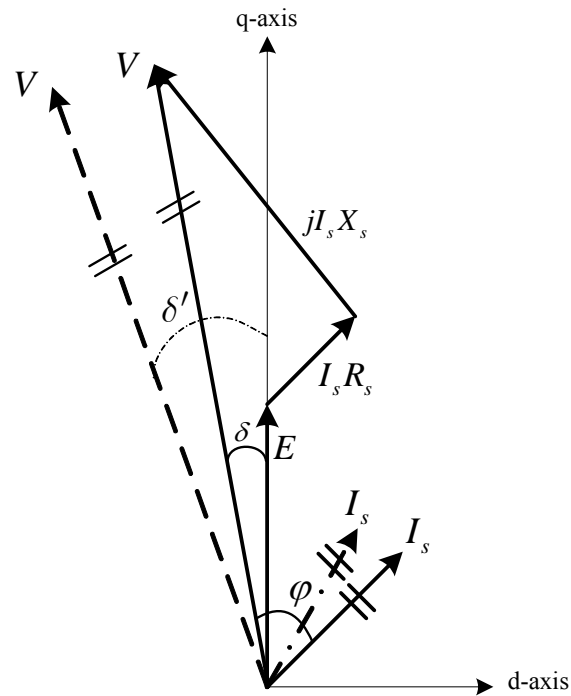


Fig. 3.9. Possible vector representation of PMSM.

It can be shown from Fig. 3.9 that even if the amplitude of I_s is same, the difference in position of I_s will affect the behavior of PMSM. That is why load angle values from both the simulation and the experiment are compared.

CHAPTER IV

OPEN-LOOP SIMULINK[®] MODEL OF THE PM SPINDLE MOTOR

4.1. Principles of PMSM Open-Loop Control

When the stator resistance, R_s , is neglected (near the motor base speed ω_b), the torque expression for non-salient (surface-mounted PMSM) is given in (5.7), referred to as (4.1):

$$T_{em} = 3 \left(\frac{P}{2} \right) \frac{|V_s| |E|}{\omega_e |X_s|} \sin \delta \quad (4.1)$$

where ω_e is the variable angular frequency, $2\pi f_e$, of the input AC supply to the motor, V_s is the rms AC supply voltage of the motor at frequency f_e and X_s is the synchronous reactance, $2\pi f_e L_s$, of the motor at the supply frequency.

Since the back-EMF, E , and the synchronous reactance, X_s , are proportional to the angular frequency ω_e , then the same maximum torque (when $\delta = 90^\circ$) is achieved if the $\frac{V_s}{\omega_e}$ or $\frac{V_s}{f_e}$ ratio is maintained constant at all speeds (frequencies) at a given load angle δ . This control method is very similar to the one used for induction motors. The above methodology used as an open-loop control for PMSM drives is valid when the motor speed is near the base speed (or base frequency). This is because near base speed the back-EMF of the motor, E , and supply voltage, V_s , are much larger than the voltage drop in the stator resistance. On the other hand, at low frequencies the voltage drop due to the stator resistance may not be negligible.

In open-loop control (V/f control) the speed of the motor is commanded by the input frequency f_e of the supply, and V_s is chosen such that at all speeds V/f is maintained constant so as not to strengthen the stator flux linkage more than its normal value. To implement the idea of V/f control, a sinusoidal PWM technique can be used. Sudden reference speed changes may cause load angle to exceed its limit $\delta (=90^\circ)$ as a precaution, a filter in the speed reference input may be used, as shown in Fig. 4.1. Generally, V_s is increased proportionally with f_e until base frequency is reached. Afterwards, the constant torque region ends and field weakening region, or constant power region, is started. In that region V_s is maintained constant at the base voltage, V_b , of the motor providing constant power. Above the base speed, ω_b , only the supply frequency f_e can be increased which weakens the stator flux linkage so that maximum torque is reduced according to (5.7).

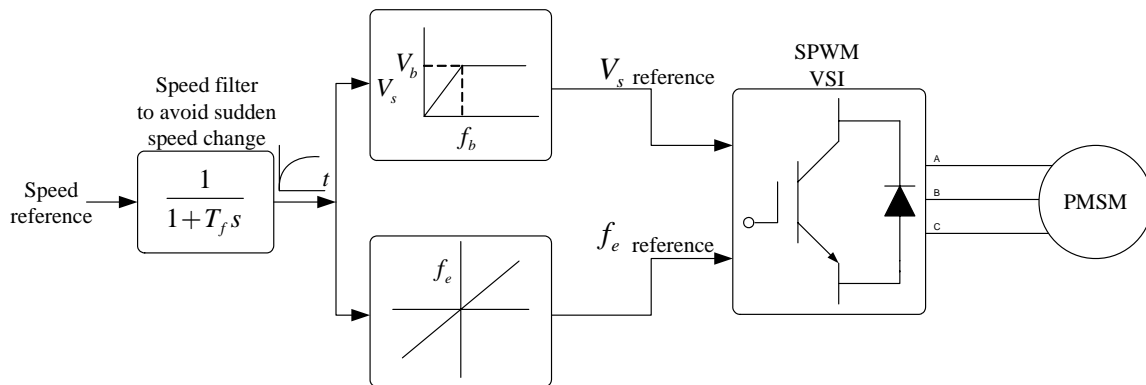


Fig. 4.1. Basic open-loop block diagram of PMSM.

4.2. Building Open-Loop Steady and Transient-State Models

Even though the conventional washing machine agitation speed control system is simulated in the SIMPLORER[®] platform, open-loop steady state and even transient controls are done in MATLAB/SIMULINK[®] because steady-state motor models are not provided in SIMPLORER[®]. The ones it provides are transient models, and modification of the models is not allowed. Therefore, relying on the convenience of SIMULINK[®], open-loop, steady-state and transient models are built in the MATLAB/SIMULINK[®] platform. The dq-rotor model equations used in the open-loop control of the PMSM are written again:

$$\begin{aligned} v_q &= (R_s + L_s p)i_q + \omega_r L_s i_d + \omega_r \lambda_r \\ v_d &= (R_s + L_s p)i_d - \omega_r L_s i_q \end{aligned} \quad (4.2)$$

where p is the derivative.

If the derivative terms are removed, the steady-state voltage equations in the rotor reference frame become:

$$\begin{aligned} v_q &= R_s i_q + \omega_r L_s i_d + \omega_r \lambda_r \\ v_d &= R_s i_d - \omega_r L_s i_q \end{aligned} \quad (4.3)$$

Fig. 4.2 is the block diagram of the overall open-loop PMSM drive system designed in MATLAB/SIMULINK[®]. In this figure, transformations are in the following order from left to right: abc reference frame to DQ -stationary reference frame transformation, DQ -stationary reference frame to dq-rotor reference frame transformation and finally dq-rotor reference frame to abc-frame transformation.

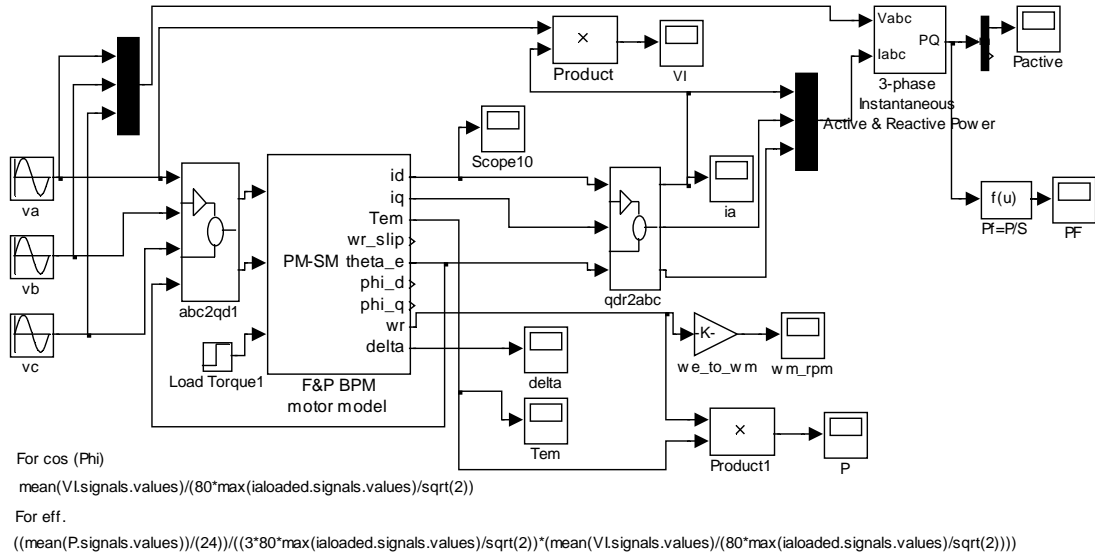


Fig. 4.2. Overall open-loop control block diagram of PMSM in SIMULINK®.

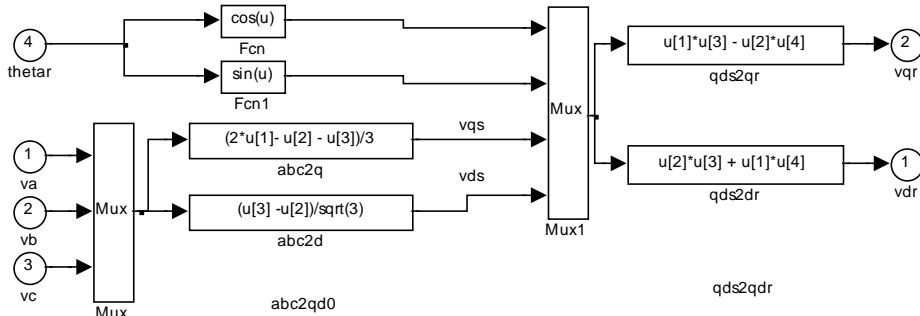


Fig. 4.3. Abc to stationary and stationary to dq rotor reference frame transformation block.

where v_{qs} and v_{ds} or v_{α} and v_{β} are the stationary reference frame voltages converted from the motors abc terminal voltages by using Clark's Transformation which are given by:

$$\begin{aligned}
 v_\alpha = v_{qs} &= \frac{(2v_a - v_b - v_c)}{3} \\
 v_\beta = v_{ds} &= \frac{(v_c - v_b)}{\sqrt{3}}
 \end{aligned}
 \tag{4.4}$$

From Fig. 4.3, the stationary to rotor reference frame voltage equations corresponding to the Park's Transformation under the assumption that the rotor angle representation is chosen between the rotor q-axis and the stationary q-axis, as shown in Fig. 4.4, are given by:

$$\begin{aligned}
 v_q &= v_q^s \cos \theta_r - v_d^s \sin \theta_r \\
 v_d &= v_q^s \sin \theta_r + v_d^s \cos \theta_r
 \end{aligned}
 \tag{4.5}$$

The coordinate representation of the stationary reference frame is shown in Fig. 4.4.

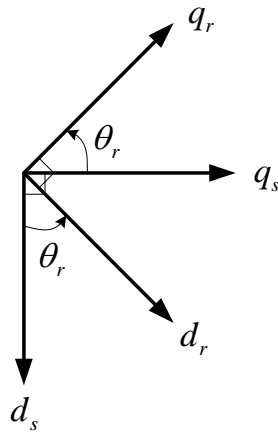


Fig. 4.4. Rotor reference frame and stationary reference frame coordinate representation.

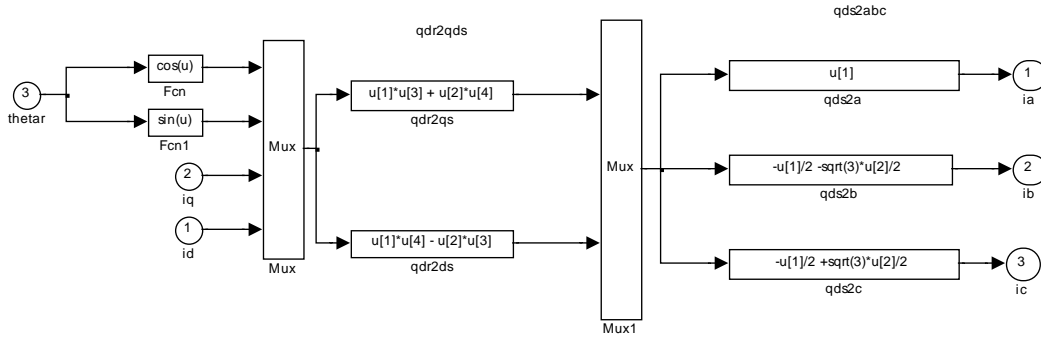


Fig. 4.5. Dq rotor reference frame to stationary and stationary to abc transformation block.

From Fig. 4.5, the rotor frame to stationary frame current equations corresponding to the inverse Park's Transformation, under the assumption that the rotor angle representation is chosen as between the rotor q-axis and the stationary q-axis as shown in Fig. 4.4, are given by:

$$\begin{aligned} i_q^s &= i_q \cos \theta_r + i_d \sin \theta_r \\ i_d^s &= i_d \cos \theta_r - i_q \sin \theta_r \end{aligned} \quad (4.6)$$

Again from Fig. 4.5, the stationary frame to the abc frame current transformation corresponding to the inverse Clark's Transformation can be expressed as:

$$\begin{aligned} i_a &= i_{qs} \\ i_b &= -\frac{1}{2} i_{qs} - \frac{\sqrt{3}}{2} i_{ds} \\ i_c &= -\frac{1}{2} i_{qs} + \frac{\sqrt{3}}{2} i_{ds} \end{aligned} \quad (4.7)$$

From Fig. 4.2, the inside of the PMSM model is presented in Fig. 4.6.

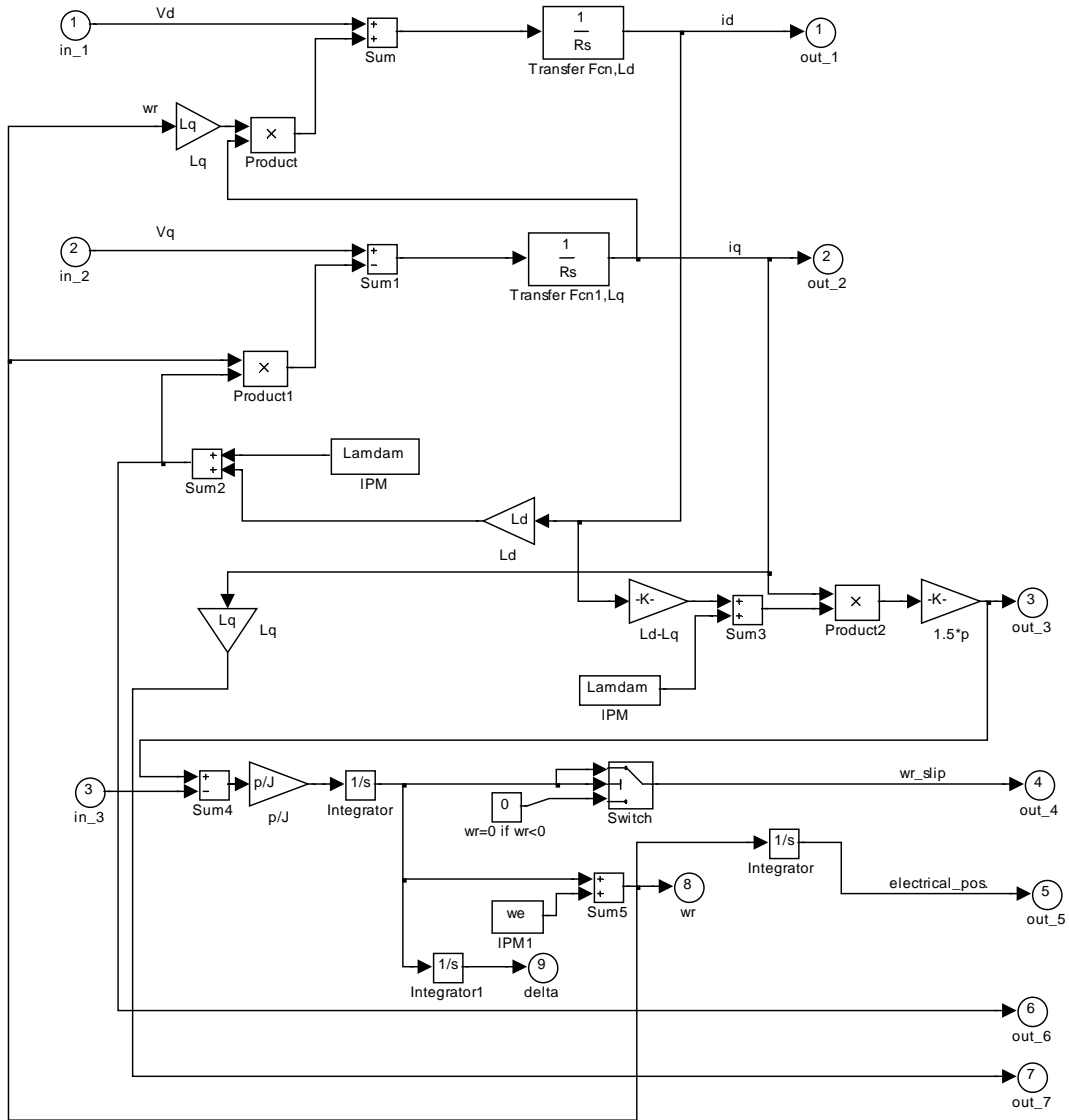


Fig. 4.6. Steady state dq-axis rotor reference frame motor model.

Equations for Fig. 4.6 can be summarized as:

$$\begin{aligned}
v_q &= R_s i_q + \omega_r L_d i_d + \omega_r \lambda_r \\
v_d &= R_s i_d - \omega_r L_q i_q
\end{aligned}
\tag{4.8}$$

$$T_{em} = \frac{3}{2} \frac{P}{2} (\lambda_i i_q + (L_d - L_q) i_q i_d)$$

$$T_{em} + T_{mech} - T_{damp} = \frac{2J}{P} \frac{d(\omega_r(t) - \omega_e)}{dt} = J \frac{d\omega_{rm}(t)}{dt}$$

where damping torque, T_{damp} , is assumed to be zero.

$$\begin{aligned}
\delta(t) &= \theta_r(t) - \theta_e(t) \\
&= \int_0^t \{\omega_r(t) - \omega_e\} dt + \theta_r(0) - \theta_e(0)
\end{aligned}
\tag{4.9}$$

$$\frac{d(\omega_r(t) - \omega_e)}{dt} = \frac{d\omega_r(t)}{dt}$$

$$\omega_r(t) - \omega_e = \frac{P}{2J} \int_0^t (T_{em} + T_{mech} - T_{damp}) dt$$

where $\theta_r(0) - \theta_e(0)$ is the initial value of the load angle, $\delta(0)$, also known as 'delto' in the simulation.

When the steady-state rotor speed is equal to the synchronous speed $\omega_r(t) = \omega_e$, δ (load angle) is constant and $\omega_{rslip} = 0$ ($\omega_r(t) - \omega_e = 0$). It is always better to get $\theta_e(0) = 0$. This is done by aligning the d-axis (synchronous reference frame) with the a-axis or stationary reference frame as shown in Fig. 4.7.

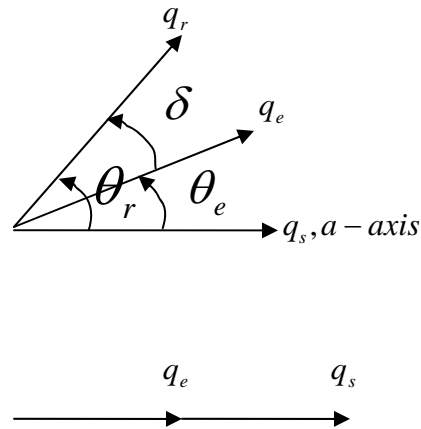


Fig. 4.7. Rotor ref. frame, synchronous ref. frame, and stationary ref. frame representation as vectors.

For ease the q_r -axis will also be aligned with the a-axis which makes the rotor initial position zero (we need to be aware of this in the experiment also). If the SIMULINK[®] open-loop control is used in the transient analysis, then the synchronous speed, ω_e , is chosen to be zero because the initial speed of the rotor is zero in the beginning of transient-state. In steady-state the desired speed is $2\pi \cdot 40$ electrical rad/s for 100 rpm (48 rotor poles). Additionally, (4.3) is used for designing the transient PMSM model instead of (4.2).

For the correct load angle in the SIMULINK[®] model, the ‘delto’ value in the motor model should be equal to $\pi/2$ for the following reason:

Let’s assume that the input voltage waveform is $V_a = V_m \cos(\omega_e t + \theta_e(0))$ (our input is a sine wave), which means $\theta_e(0) = 0$. If $\theta_e(0)$ is not zero (as with a sine wave excitation of $V_a = V_m \sin(\omega_e t)$ (like the model used in SIMULINK[®]) which equals $V_m \cos(\omega_e t - \pi/2)$ where $\theta_e(0) = -\pi/2$), the no-load steady-state value of δ will be $-\pi/2$ instead of zero, therefore ‘delto’ will be $\pi/2$ [10].

4.3. Power Factor and Efficiency Calculations in Open-Loop Matlab/Simulink®

Model

To verify that the simulated model is exactly like the real motor more characterization tests should be conducted, such as power factor and efficiency comparisons. These can be calculated in the MATLAB/SIMULINK® platform in two ways. One way is by using SIMULINK® internal power measurement blocks. The other way to obtain these is by using the MATLAB® workspace with the following equations:

$$PF = \cos \phi = \frac{\text{Real_Power}}{\text{Apparent_Power}} = \frac{P}{|S|} = \frac{V_{rms} I_{rms} \cos \phi}{V_{rms} I_{rms}}$$

$$P = \text{mean}(VI.\text{signals.values}) \quad (4.10)$$

$$S = V_{rms} I_{rms} = 80 \left(\frac{\max(\text{ia.signals.values})}{\sqrt{2}} \right)$$

where PF is the abbreviation for Power Factor, S is the apparent power, and 80 is the rms value of the applied sinewave voltage.

P is calculated by taking the average (mean function) of VI which is the product of v_a (phase A voltage) and i_a (phase A current). They are shown as the scope names in SIMULINK® shown in Fig. 4.2. Below is the derivation of the efficiency formula which is used in MATLAB®:

$$\eta = \frac{P_{out}}{P_{in}} = \frac{T_{em} \omega_m}{3V_{rms} I_{rms} \cos \phi}; \omega_e = \frac{P}{2} \omega_m \quad (4.11)$$

$$\eta = \frac{T_{em} \left(\frac{\omega_e}{P/2} \right)}{3V_{rms} I_{rms} \cos \phi}$$

where ϕ is the power factor angle between the motor voltage and current.

The formulas below are used to calculate the power factor and efficiency. They are used in MATLAB® workspace after the simulation ends:

Power Factor (PF):

$$\text{mean}(VI.\text{signals.values})/(80*\max(\text{ia.signals.values})/\text{sqrt}(2))$$

Motor Efficiency (Eff.):

$$\frac{((\text{mean}(P.\text{signals.values}))/24)/((3*80*\text{max}(\text{ia.signals.values})/\text{sqrt}(2))*\text{mean}(\text{VI.signals.values}))/80*\text{max}(\text{ia.signals.values})/\text{sqrt}(2))}{(3*80*\text{max}(\text{ia.signals.values})/\text{sqrt}(2))}$$

In open-loop steady-state control there is a transient in the beginning, so to have the real values data should be collected when transient passes, otherwise the transient will dramatically change the PF and eff. values. To do that, in the scope parameters the 'limit data points to last' description should be sufficient enough to pass and not include those transient effects. For example, 5000 points is chosen in the simulation and that was enough for the calculation of PF and eff. Once the simulation is run the signal values which are collected from the SIMULINK[®] scopes are run in the MATLAB[®] workspace using the equations above so that the PF and eff. values are obtained. Similarly, the SIMULINK[®] internal Power Measurement blocks can be used to calculate the PF and Active (Real) Power easily. With those results, the eff. block can also be built in SIMULINK[®], as given below:

$$\eta = \frac{P_{out}}{P_{in}} = \frac{\frac{P_e(scope)}{24}}{P_{active}} \quad (4.12)$$

where 24 is the pole pair number of the 48 pole PM spindle motor, $P_e(scope)$ is the electrical output power of the motor and P_{active} is the resultant active power part of the output of the built-in internal power block. If better power results are desired then they can be averaged out using 'mean (P.signals.values)', but it can only be done in the MATLAB[®] command screen.

CHAPTER V

CONVENTIONAL DIRECT TORQUE CONTROL (DTC)

OPERATION OF PMSM DRIVE

5.1. Introduction and Literature Review

Today there are basically two types of instantaneous electromagnetic torque-controlled AC drives used for high-performance applications: vector and direct torque control (DTC) drives. The most popular method, vector control was introduced more than 25 years ago in Germany by Hasse [18], Blaske [13], and Leonhard. The vector control method, also called Field Oriented Control (FOC) transforms the motor equations into a coordinate system that rotates in synchronism with the rotor flux vector. Under a constant rotor flux amplitude there is a linear relationship between the control variables and the torque. Transforming the AC motor equations into field coordinates makes the FOC method resemble the decoupled torque production in a separately excited DC motor. Over the years, FOC drives have achieved a high degree of maturity in a wide range of applications. They have established a substantial world wide market which continues to increase [6].

No later than 20 years ago, when there was still a trend toward standardization of control systems based on the FOC method, direct torque control was introduced in Japan by Takahashi and Nagochi [19] and also in Germany by Depenbrock [20], [21], [22]. Their innovative studies depart from the idea of coordinate transformation and the analogy with DC motor control. These innovators proposed a method that relies on a bang-bang control instead of a decoupling control which is the characteristic of vector control. Their technique (bang-bang control) works very well with the on-off operation of inverter semiconductor power devices.

After the innovation of the DTC method it has gained much momentum, but in areas of research. So far only one form of a DTC of AC drive has been marketed by an industrial company, but it is expected very soon that other manufacturers will come out with their own DTC drive products [2].

The basic concept behind the DTC of AC drive, as its name implies, is to control the electromagnetic torque and flux linkage directly and independently by the use of six or eight voltage space vectors found in lookup tables. The possible eight voltage space vectors used in DTC are shown in Fig. 5.1 [2].

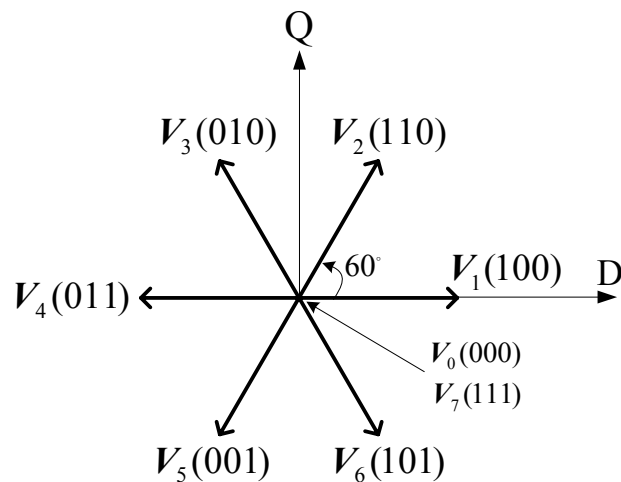


Fig. 5.1. Eight possible voltage space vectors obtained from VSI.

The typical DTC includes two hysteresis controllers, one for torque error correction and one for flux linkage error correction. The hysteresis flux controller makes the stator flux rotate in a circular fashion along the reference trajectory as shown in Fig. 5.2. The hysteresis torque controller tries to keep the motor torque within a pre-defined hysteresis band.

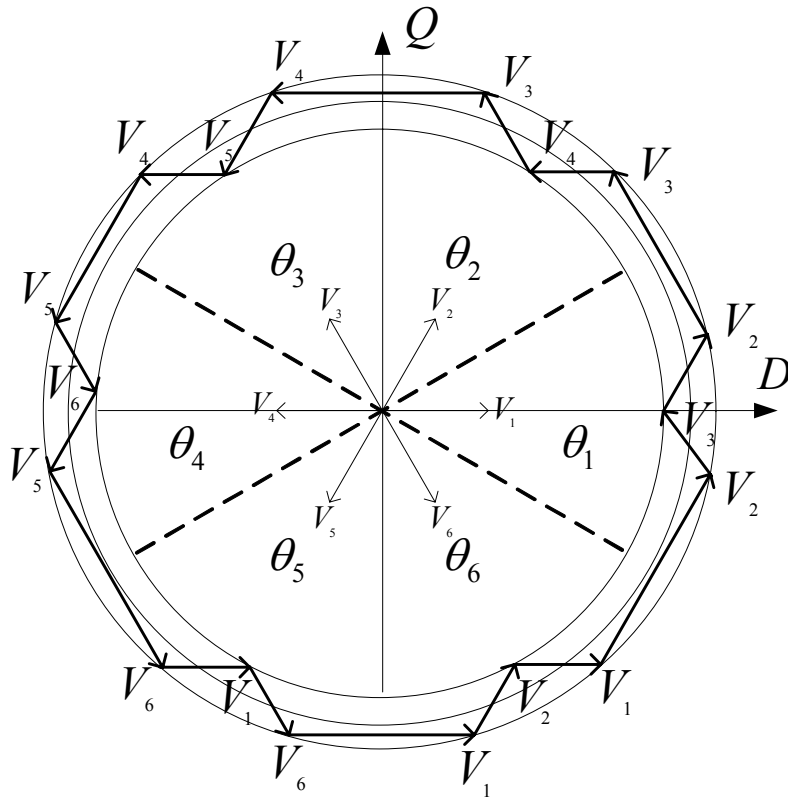


Fig. 5.2. Circular trajectory of stator flux linkage in the stationary DQ-plane.

At every sampling time the voltage vector selection block decides on one of the six possible inverter switching states (S_a , S_b , S_c) to be applied to the motor terminals. The possible outputs of the hysteresis controller and the possible number of switching states in the inverter are finite, so a look-up table can be constructed to choose the appropriate switching state of the inverter. This selection is a result of both the outputs of the hysteresis controllers and the sector of the stator flux vector in the circular trajectory.

There are many advantages of direct torque control over other high-performance torque control systems such as vector control. Some of these are summarized as follows:

- The only parameter that is required is stator resistance

- The switching commands of the inverter are derived from a look-up table, simplifying the control system and also decreasing the processing time unlike a PWM modulator used in vector control
- Instead of current control loops, stator flux linkage vector and torque estimation are required so that simple hysteresis controllers are used for torque and stator flux linkage control
- Vector transformation is not applied because stator quantities are enough to calculate the torque and stator flux linkage as feedback quantities to be compared with the reference values
- The rotor position, which is essential for torque control in a vector control scheme, is not required in DTC (for induction and synchronous reluctance motor DTC drives)

Once the initial position of the rotor magnetic flux problem is solved for PMSM drives by some initial rotor position estimation techniques or by bringing the rotor to the known position, DTC of the PMSM can be as attractive as DTC of an induction motor. It is also easier to implement and as cost-effective (no position sensor is required) when compared to vector controlled PMSM drives. The DTC scheme, as its name indicates, is focused on the control of the torque and the stator flux linkage of the motor, therefore, a faster torque response is achieved over vector control. Furthermore, due to the fact that DTC does not need current controller, the time delay caused by the current loop is eliminated.

Even though the DTC technique was originally proposed for the induction machine drive in the late 1980's, its concept has been extended to the other types of AC machine drives recently, such as switched reluctance and synchronous reluctance machines. In the late 90s, DTC techniques for the interior permanent magnet synchronous machine appeared, as reported in [23], [24].

Although there are several advantages of the DTC scheme over vector control, it still has a few drawbacks which are explained below:

- A major drawback of the DTC scheme is the high torque and stator flux linkage ripples. Since the switching state of the inverter is updated once every sampling time, the inverter keeps the same state until the outputs of each hysteresis controller changes states. As a result, large ripples in torque and stator flux linkage occur.
- The switching frequency varies with load torque, rotor speed and the bandwidth of the two hysteresis controllers.
- Stator flux estimation is achieved by integrating the difference between the input voltage and the voltage drop across the stator resistance (by the back-EMF integration as given in (5.9)). The applied voltage on the motor terminal can be obtained either by using a DC-link voltage sensor, or two voltage sensors connected to the any two phases of the motor terminals. For current sensing there should be two current sensors connected on any two phases of the motor terminals. Offset in the measurements of DC-link voltage and the stator currents might happen, because for current and voltage sensing, however, temperature sensitive devices, such as operational amplifiers, are normally used which can introduce an unwanted DC offset. This offset may introduce large drifts in the stator flux linkage computation (estimation) thus creating an error in torque estimation (torque is proportional to the flux value) which can make the system become unstable.
- The stator flux linkage estimation has a stator resistance, so any variation in the stator resistance introduces error in the stator flux linkage computation, especially at low frequencies. If the magnitude of the applied voltage and back-EMF are low, then any change in the resistance will greatly affect the integration of the back-EMF.
- Because of the constant energy provided from the permanent magnet on the rotor the rotor position of motor will not necessarily be zero at start up. To successfully start the motor under the DTC scheme from any

position (without locking the motor at a known position), the initial position of the rotor magnetic flux must be known. Once it is started properly, however, the complete DTC scheme does not explicitly require a position sensor.

From the time the DTC scheme was discovered for AC motor drives, it was always inferior to vector control because of the disadvantages associated with it. The goal is to bring this technology as close to the performance level of vector control and even exceed it while keeping its simple control strategy and cost-effectiveness. As a result, many papers have been presented by several researchers to minimize or overcome the drawbacks of the DTC scheme. Here are some of the works that have been done by researchers to overcome the drawbacks for the most recent AC drive technology using direct torque control:

- Recently, researchers have been working on the torque and flux ripple reduction, and fixing the switching frequency of the DTC system, as reported in [25]-[30]. Additionally, they came up with a multilevel inverter solution in which there are more voltage space vectors available to control the flux and torque. As a consequence, smoother torque can be obtained, as reported in [28] and [29], but by doing so, more power switches are required to achieve a lower ripple and an almost fixed switching frequency, which increases the system cost and complexity. In the literature, a modified DTC scheme with fixed switching frequency and low torque and flux ripple was introduced in [27] and [30]. With this design, however, two PI regulators are required to control the flux and torque and they need to be tuned properly. Very recently Rahman [31] proposed a method for torque and flux ripple reduction in interior permanent magnet synchronous machines under an almost fixed switching frequency without using any additional regulators. This method is a modified version of the previously discovered method for the induction machine by the authors in [32].

- Stator flux linkage estimation by the integration of the back-EMF should be reset regularly to reduce the effect of the DC offset error. There has been a few compensation techniques related to this phenomenon proposed in the literature [33]-[35] and [16]. Chapuis et al. [18] introduced a technique to eliminate the DC offset, but a constant level of DC offset is assumed which is usually not the case. In papers [33]-[35] and [16], low-pass filters (LPFs) have been introduced to estimate the stator flux linkage. In [33], a programmable cascaded LPF was proposed instead of the single-stage integrator to help decrease the DC offset error more than the single-stage integrator for induction motor drives. More recently, Rahman [36] has reached an approach like [33] with further investigation and implementation for the compensation of DC offset error in a direct controlled interior permanent magnet (IPM) synchronous motor drive. It has been claimed and proven with simulation and experimental results that programmable cascaded LPFs can also be adopted to replace the single-stage integrator and compensate for the effect of DC offsets in a direct-torque-controlled IPM synchronous motor drive, improving the performance of the drive.
- The voltage drop in the stator resistance is very large when the motor runs at low frequency such that any small deviations in stator resistance from the one used in the estimation of the stator flux linkage creates large errors between the reference and actual stator flux linkage vector. This also affects the torque estimation as well. Due to these errors, the drive can easily go unstable when operating at low speeds. The worst case scenario might happen at low speed under a very high load. A handful of researchers have recently pointed to the issue of stator resistance variation for the induction machine. For example, fuzzy and proportional-integral (PI) stator resistance estimators have been developed and compared for a DTC induction machine based on the error between the reference current

and the actual one by Mir et al. [37]. On the other hand, they did not show any detail on how to obtain the reference current for the stator resistance estimation. Additionally, some stability problems of the fuzzy estimator were observed when the torque reference value was small. As reported in [38], fuzzy logic based stator resistance observers are introduced for induction motor. Even though it is an open-loop controller based on fuzzy rules, the accuracy of estimating the stator resistance is about 5% and many fuzzy rules are necessary. This resulted in having to conduct handful numbers of extensive experiments to create the fuzzy rules resulting in difficulty in implementation. Lee and Krishnan [39] contributed a work related to the stator resistance estimation of the DTC induction motor drive by a PI regulator. An instability issue caused by the stator estimation error in the stator resistance, the mathematical relationships between stator current, torque and flux commands, and the machine parameters are also analyzed in their work. The stator configuration of all AC machines is almost the same, so the stator resistance variation problem still exists for permanent magnet synchronous motors. Rahman et al. [40] reported a method, for stator resistance estimation by PI regulation based on the error in flux linkage. It is claimed that any variation in the stator resistance of the PM synchronous machine will cause a change in the amplitude of the actual flux linkage. A PI controller works in parallel with the hysteresis flux controller of the DTC such that it tracks the stator resistance by eliminating the error in the command and the actual flux linkage. One problem with this method was that the rotor position was necessary to calculate the flux linkage. Later on the same author proposed a similar method but this time the PI stator resistance estimator was able to track the change of the stator resistance without requiring any position information.

- The back-EMF integration for the stator flux linkage calculation, which runs continuously, requires a knowledge of the initial stator flux position, $\lambda_{s|t=0}$, at start up. In order to start the motor without going in the wrong direction, assuming the stator current is zero at the start, only the rotor magnetic flux linkage should be considered as an initial flux linkage value in the integration formula. The next step is to find its position in the circular trajectory. The initial position of the rotor is not desired to be sensed by position sensors due to their cost and bulky characteristics, therefore some sort of initial position sensing methods are required for permanent magnet synchronous motor DTC applications. A number of works, [41]-[52], have been proposed recently for the detection of the initial rotor position estimation at standstill for different types of PM motors. Common problems of these methods include: most of them fail at standstill because the rotor magnet does not induce any voltage, so no information of the magnetization is available; position estimation is load dependent; excessive computation and hardware are required; instead of a simple voltage vector selection method used in the DTC scheme, those estimation techniques need one or more pulse width-modulation (PWM) current controllers. Recently, a better solution was introduced for the rotor position estimation. It is accomplished by applying high-frequency voltage to the motor, as reported in [50]-[52]. This approach is adapted to the DTC of interior permanent magnet motors for initial position estimation by Rahman et. al. [36].

5.2. Principles of Conventional DTC of PMSM Drive

The basic idea of direct torque control is to choose the appropriate stator voltage vector out of eight possible inverter states (according to the difference between the

reference and actual torque and flux linkage) so that the stator flux linkage vector rotates along the stator reference frame (DQ frame) trajectory and produces the desired torque. The torque control strategy in the direct torque control of a PM synchronous motor is explained in Section 5.2.1. The flux control is discussed following the torque control section.

5.2.1. Torque Control Strategy in DTC of PMSM Drive

Before going through the control principles of DTC for PMSMs, an expression for the torque as a function of the stator and rotor flux will be developed. The torque equation used for DTC of PMSM drives can be derived from the phasor diagram of conventional or permanent magnet synchronous motor shown in Fig. 5.3.

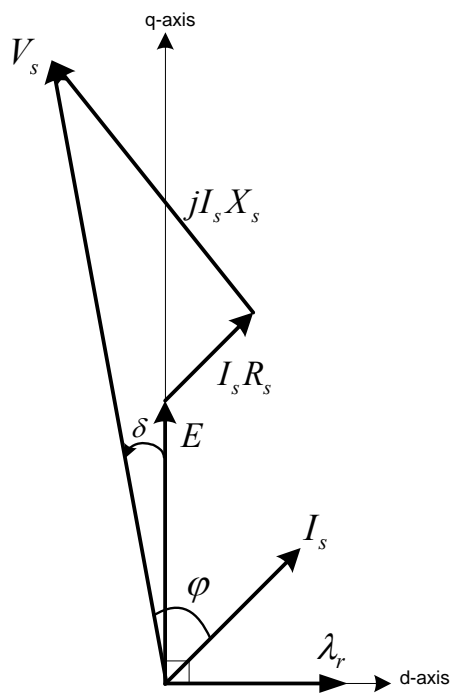


Fig. 5.3. Phasor diagram of a non-salient pole synchronous machine in the motoring mode.

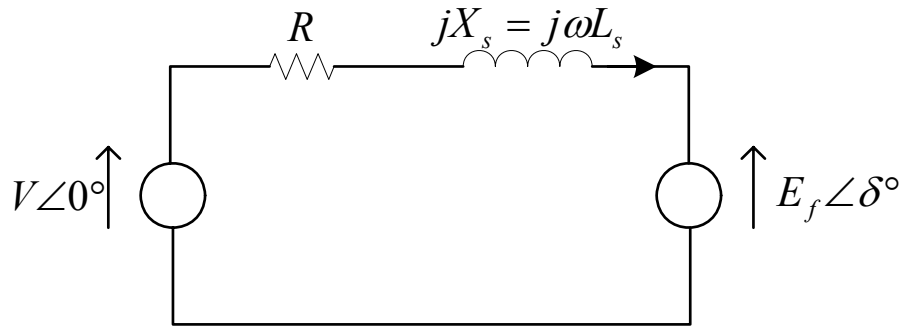


Fig. 5.4. Electrical circuit diagram of a non-salient synchronous machine at constant frequency (speed).

When the machine is loaded through the shaft, the motor will take real power. The rotor will then fall behind the stator rotating field. From the circuit diagram, shown in Fig. 5.4, the motor current expression can be written as:

$$I_s = \frac{V_s\angle 0 - E\angle \delta}{R_s + jX_s} = \frac{V_s\angle 0 - E\angle \delta}{|Z_s|\angle \varphi} \quad (5.1)$$

where $|Z_s| = \sqrt{R_s^2 + X_s^2}$, also $X_s = \omega_e L_s$

and $\varphi = \tan^{-1}\left(\frac{X_s}{R_s}\right)$

Assuming a reasonable speed such that the X_s term is higher than the resistance, R_s ,

such that R_s can be neglected, then $|Z_s| \approx X_s$ and $\varphi \approx \frac{\pi}{2}$. I_s can then be rewritten as:

$$I_s = \frac{V_s\angle 0}{X_s} - \frac{E\angle \delta - \frac{\pi}{2}}{X_s} \quad (5.2)$$

Such that the real part of I_s is:

$$\begin{aligned}\operatorname{Re}[I_s] &= I_s \cos \varphi = \frac{V_s}{X_s} \cos \left(-\frac{\pi}{2} \right) - \frac{E}{X_s} \cos \left(\delta - \frac{\pi}{2} \right) \\ &= -\frac{E}{X_s} \cos \left(\delta - \frac{\pi}{2} \right) = -\frac{E}{X_s} \sin \delta\end{aligned}\quad (5.3)$$

the developed power is given by:

$$P_i = 3V_s \operatorname{Re}[I_s] = 3V_s I_s \cos \varphi \quad (5.4)$$

Substituting (5.3) into (5.4) yields:

$$P_i = -3 \frac{V_s E}{X_s} \sin \delta \quad \text{Watts/phase} \quad (5.5)$$

This power is positive when δ negative, meaning that when the rotor field lags the stator field the machine is operating in the motoring region. When $\delta > 0$ the machine is operating in the generation region. The negative sign in (5.5) can be dropped, assuming that for motoring operation a negative δ is implied.

If the losses of the machine are ignored, the power P_i can be expressed as the shaft (output) power as well:

$$P_i = P_o = \frac{2}{P} \omega_e T_{em} \quad (5.6)$$

When combining (5.5) and (5.6), the magnitude of the developed torque for a non-salient synchronous motor (or surface-mounted permanent magnet synchronous motor) can be expressed as:

$$\begin{aligned}T_{em} &= 3 \left(\frac{P}{2} \right) \frac{|V_s|}{\omega_e} \frac{|E|}{|X_s|} \sin \delta \\ &= 3 \left(\frac{P}{2} \right) \frac{|\lambda_s| |\lambda_r|}{L_s} \sin \delta\end{aligned}\quad (5.7)$$

where δ is the torque angle between flux vectors λ_s and λ_r . If the rotor flux remains constant and the stator flux is changed incrementally by the stator voltage, V_s , then the torque variation, ΔT_{em} , expression can be written as:

$$\Delta T_{em} = 3 \left(\frac{P}{2} \right) \frac{|\lambda_s + \Delta \lambda_s| |\lambda_r|}{L_s} \sin \Delta \delta \quad (5.8)$$

where the bold terms in the above expressions indicate vectors.

As it can be seen from (5.8), if the load angle, δ , is increased then torque variation is increased. To increase the load angle, δ , the stator flux vector should turn faster than rotor flux vector. The rotor flux rotation depends on the mechanical speed of the rotor, so to decrease load angle, δ , the stator flux should turn slower than rotor flux. Therefore, according to the torque (5.7), the electromagnetic torque can be controlled effectively by controlling the amplitude and rotational speed of stator flux vector, λ_s . To achieve the above phenomenon, appropriate voltage vectors are applied to the motor terminals. For counter-clockwise operation, if the actual torque is smaller than the reference value, then the voltage vectors that keep the stator flux vector, λ_s , rotating in the same direction are selected. When the load angle, δ , between λ_s and λ_r increases the actual torque increases as well. Once the actual torque is greater than the reference value, the voltage vectors that keep stator flux vector, λ_s , rotating in the reverse direction are selected instead of the zero voltage vectors. At the same time, the load angle, δ , decreases thus the torque decreases. The reason the zero voltage vector is not chosen in the DTC of PMSM drives will be discussed later in this chapter. A more detailed look at the selection of the voltage vectors and their effect on torque and flux results will be discussed later as well. Referring back to the discussion above, however, torque is controlled via the stator flux rotation speed, as shown in Fig. 5.5. If the speed of the stator flux is high then faster torque response is achieved.

For a short interval of time, namely the sampling time, $T_s = \Delta t$, the stator flux linkage, λ_s , position and amplitude can be changed incrementally by applying the stator voltage vector, V_s . As discussed above, the position change of the stator flux linkage vector, λ_s , will affect the torque. The stator flux linkage of a PMSM that is depicted in the stationary reference frame is written as:

$$\lambda_s = \int (V_s - R_s i_s) dt \quad (5.9)$$

During the sampling interval time or switching interval, one out of the six voltage vectors is applied, and each voltage vector applied during the pre-defined sampling interval is constant, s (5.9) can be rewritten as:

$$\lambda_s = V_s t - R_s \int i_s dt + \lambda_{s|t=0} \quad (5.10)$$

where $\lambda_{s|t=0}$ is the initial stator flux linkage at the instant of switching, V_s is the measured stator voltage, i_s is the measured stator current, and R_s is the estimated stator resistance. When the stator term in stator flux estimation is removed implying that the end of the stator flux vector, λ_s , will move in the direction of the applied voltage vector, as shown in Fig. 5.6, we obtain:

$$V_s = \frac{d}{dt}(\lambda_s) \quad (5.11)$$

or

$$\Delta \lambda_s = V_s \Delta t \quad (5.12)$$

The goal of controlling the flux in DTC is to keep its amplitude within a pre-defined hysteresis band. By applying a required voltage vector stator flux linkage amplitude can be controlled. To select the voltage vectors for controlling the amplitude of the stator flux linkage the voltage plane is divided into six regions, as shown in Fig. 5.2.

In each region two adjacent voltage vectors, which give the minimum switching frequency, are selected to increase or decrease the amplitude of stator flux linkage, respectively. For example, according to the Table III, when the voltage vector V_2 is applied in Sector 1, then the amplitude of the stator flux increases when the flux vector rotates counter-clockwise. If V_3 is selected then stator flux linkage amplitude decreases. The stator flux incremental vectors corresponding to each of the six inverter voltage vectors are shown in Fig. 5.1.

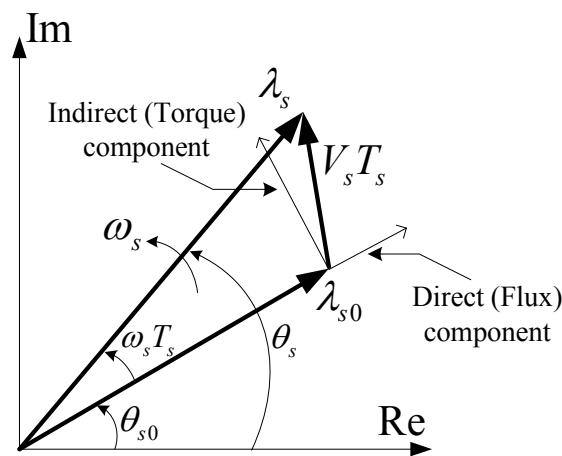


Fig. 5.7. Representation of direct and indirect components of the stator flux linkage vector [35].

Fig. 5.7 is a basic graph that shows how flux and torque can be changed as a function of the applied voltage vector. According to the figure, the direct component of applied voltage vector changes the amplitude of the stator flux linkage and the indirect component changes the flux rotation speed which changes the torque. If the torque needs to be changed abruptly then the flux does as well, so the closest voltage vector to the indirect component vector is applied. If torque change is not required, but flux amplitude is increased or decreased then the voltage vector closest to the direct component vector is chosen. Consequently, if both torque and flux are required to change then the appropriate resultant mid-way voltage vector between the indirect and direct components is applied [35]. It seems obvious from (5.9) that the stator flux linkage vector will stay at

its original position when zero voltage vectors $S_a(000)$ and $S_a(111)$ are applied. This is true for an induction motor since the stator flux linkage is uniquely determined by the stator voltage. On the other hand, in the DTC of a PMSM, the situation of applying the zero voltage vectors is not the same as in induction motors. This is because the stator flux linkage vector will change even when the zero voltage vectors are selected since the magnets rotate with the rotor. As a result, the zero voltage vectors are not used for controlling the stator flux linkage vector in a PMSM. In other words, the stator flux linkage should always be in motion with respect to the rotor flux linkage vector [24].

5.2.3. Voltage Vector Selection in DTC of PMSM Drive

As discussed before, the stator flux is controlled by properly selected voltage vectors, and as a result the torque by stator flux rotation. The higher the stator vector rotation speed the faster torque response is achieved.

The estimation of the stator flux linkage components described previously requires the stator terminal voltages. In a DTC scheme it is possible to reconstruct those voltages from the DC-link voltage, V_{dc} , and the switching states (S_a, S_b, S_c) of a six-step voltage-source inverter (VSI) rather than monitoring them from the motor terminals. The primary voltage vector, \mathbf{v}_s , is defined by the following equation:

$$\mathbf{v}_s = \frac{2}{3}(v_a + v_b e^{j(2/3)\pi} + v_c e^{j(4/3)\pi}) \quad (5.13)$$

where v_a , v_b , and v_c are the instantaneous values of the primary line-to-neutral voltages. When the primary windings are fed by an inverter, as shown in Fig. 5.8, the primary voltages v_a , v_b and v_c are determined by the status of the three switches, S_a , S_b , and S_c . If the switch is at state 0 that means the phase is connected to the negative and if it is at 1 it means that the phase is connected to the positive leg.

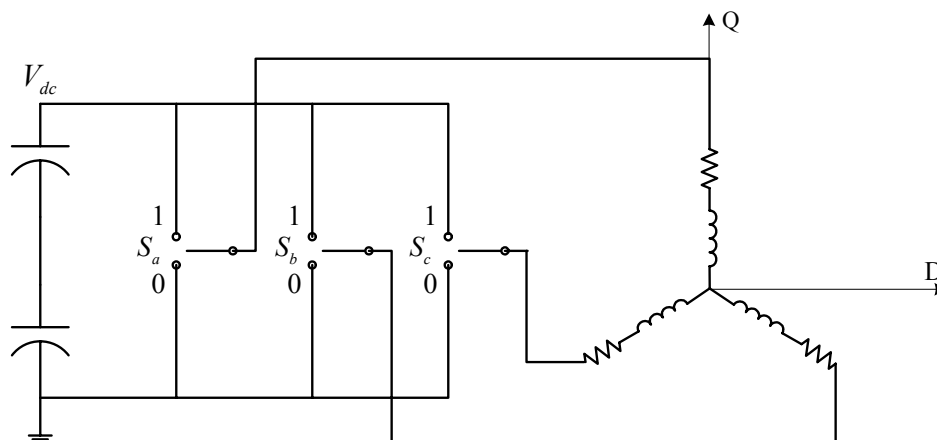


Fig. 5.8. Voltage source inverter (VSI) connected to the R-L load [19].

For example, v_a is connected to V_{dc} if S_a is one, otherwise v_a is connected to zero. This is similar for v_b and v_c . The voltage vectors that are obtained this way are shown in Fig. 5.1. There are six nonzero voltage vectors: $V_1(100)$, $V_2(110)$, ..., and $V_6(101)$ and two zero voltage vectors: $V_7(000)$ and $V_8(111)$. The six nonzero voltage vectors are 60° apart from each other as in Fig. 5.1.

The stator voltage space vector (expressed in the stationary reference frame) representing the eight voltage vectors can be shown by using the switching states and the DC-link voltage, V_{dc} , as:

$$\mathbf{v}_s(S_a, S_b, S_c) = \frac{2}{3} V_{dc} (S_a + S_b e^{j(2/3)\pi} + S_c e^{j(4/3)\pi}) \quad (5.14)$$

where V_{dc} is the DC-link voltage and the coefficient of $2/3$ is the coefficient comes from the Park's Transformation. Equation (5.14) can be derived by using the line-to-line voltages of the AC motor which can be expressed as: $v_{ab} = V_{dc}(S_a - S_b)$, $v_{bc} = V_{dc}(S_b - S_c)$, and $v_{ca} = V_{dc}(S_c - S_a)$. The stator phase voltages (line-to-neutral voltages) are required for (5.14). They can be obtained from the line-to-line voltages as $v_a = (v_{ab} - v_{ca})/3$, $v_b = (v_{bc} - v_{ab})/3$, and $v_c = (v_{ca} - v_{bc})/3$. If the line-to-line voltages

in terms of the DC-link voltage, V_{dc} , and switching states are substituted into the stator phase voltages it gives:

$$\begin{aligned} v_a &= \frac{1}{3}V_{dc}(2S_a - S_b - S_c) \\ v_b &= \frac{1}{3}V_{dc}(-S_a + 2S_b - S_c) \\ v_c &= \frac{1}{3}V_{dc}(-S_a - S_b + 2S_c) \end{aligned} \quad (5.15)$$

Equation (5.15) can be summarized by combining with (5.13) as:

$$\begin{aligned} v_a &= \text{Re}(\mathbf{v}_s) = \frac{1}{3}V_{dc}(2S_a - S_b - S_c) \\ v_b &= \text{Re}(\mathbf{v}_s) = \frac{1}{3}V_{dc}(-S_a + 2S_b - S_c) \\ v_c &= \text{Re}(\mathbf{v}_s) = \frac{1}{3}V_{dc}(-S_a - S_b + 2S_c) \end{aligned} \quad (5.16)$$

To determine the proper applied voltage vectors, information from the torque and flux hysteresis outputs, as well as stator flux vector position, are used so that circular stator flux vector trajectory is divided into six symmetrical sections according to the non zero voltage vectors as shown in Fig. 5.2.

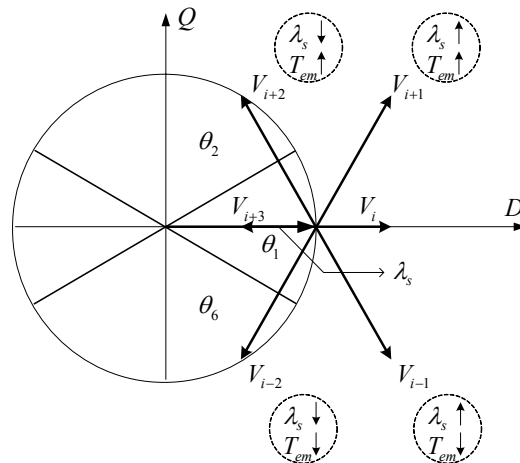


Fig. 5.9. Voltage vector selection when the stator flux vector is located in sector i [35].

According to Fig. 5.9, while the stator flux vector is situated in sector i , voltage vectors V_{i+1} and V_{i-1} have positive direct components, increasing the stator flux amplitude, and V_{i+2} and V_{i-2} have negative direct components, decreasing the stator flux amplitude. Moreover, V_{i+1} and V_{i+2} have positive indirect components, increasing the torque response, and V_{i-1} and V_{i-2} have negative indirect components, decreasing the torque response. In other words, applying V_{i+1} increases both torque and flux but applying V_{i-1} increases torque and decreases flux amplitude [35].

The switching table for controlling both the amplitude and rotating direction of the stator flux linkage is given in Table III.

TABLE III
SWITCHING TABLE

φ	τ	θ					
		$\theta(1)$	$\theta(2)$	$\theta(3)$	$\theta(4)$	$\theta(5)$	$\theta(6)$
$\varphi = 1$	$\tau = 1$	$\mathbf{V}_2(110)$	$\mathbf{V}_3(010)$	$\mathbf{V}_4(001)$	$\mathbf{V}_5(101)$	$\mathbf{V}_6(110)$	$\mathbf{V}_1(110)$
	$\tau = 0$	$\mathbf{V}_6(101)$	$\mathbf{V}_1(100)$	$\mathbf{V}_2(010)$	$\mathbf{V}_3(011)$	$\mathbf{V}_4(110)$	$\mathbf{V}_5(110)$
$\varphi = 0$	$\tau = 1$	$\mathbf{V}_3(010)$	$\mathbf{V}_4(011)$	$\mathbf{V}_5(101)$	$\mathbf{V}_6(100)$	$\mathbf{V}_1(110)$	$\mathbf{V}_2(110)$
	$\tau = 0$	$\mathbf{V}_5(001)$	$\mathbf{V}_6(101)$	$\mathbf{V}_1(110)$	$\mathbf{V}_2(010)$	$\mathbf{V}_3(110)$	$\mathbf{V}_4(110)$

The voltage vector plane is divided into six sectors so that each voltage vector divides each region into two equal parts. In each sector, four of the six non-zero voltage vectors may be used. Zero vectors are also allowed. All the possibilities can be tabulated into a switching table. The switching table presented by Rahman et al [24] is shown in Table III. The output of the torque hysteresis comparator is denoted as τ , the output of the flux hysteresis comparator as φ and the flux linkage sector is denoted as θ . The torque hysteresis comparator is a two valued comparator; $\tau = 0$ means that the actual value of the torque is above the reference and out of the hysteresis limit and $\tau = 1$ means that the actual value is below the reference and out of the hysteresis limit. The flux hysteresis comparator is a two valued comparator as well where $\varphi = 1$ means that the actual value of the flux linkage is below the reference and out of the hysteresis limit and $\varphi = 0$ means that the actual value of the flux linkage is above the reference and out of

the hysteresis limit. Rahman et al [24] have suggested that no zero vectors should be used with a PMSM. Instead, a non zero vector which decreases the absolute value of the torque is used. Their argument was that the application of a zero vector would make the change in torque subject to the rotor mechanical time constant which may be rather long compared to the electrical time constants of the system. This results in a slow change of the torque. This reasoning does not make sense, since in the original switching table the zero vectors are used when the torque is inside the torque hysteresis (i.e. when the torque is wanted to be kept as constant as possible). This indicates that the zero vector must be used. If the torque ripple needs to be kept as small as with the original switching table, a higher switching frequency must be used if the suggestion of [24] is obeyed [6].

We define φ and τ to be the outputs of the hysteresis controllers for flux and torque, respectively, and $\theta(1) - \theta(6)$ as the sector numbers to be used in defining the stator flux linkage positions. In Table III, if $\varphi = 1$, then the actual flux linkage is smaller than the reference value. On the other hand, if $\varphi = 0$, then the actual flux linkage is greater than the reference value. The same is true for the torque.

5.3. Control Strategy of DTC of PMSM

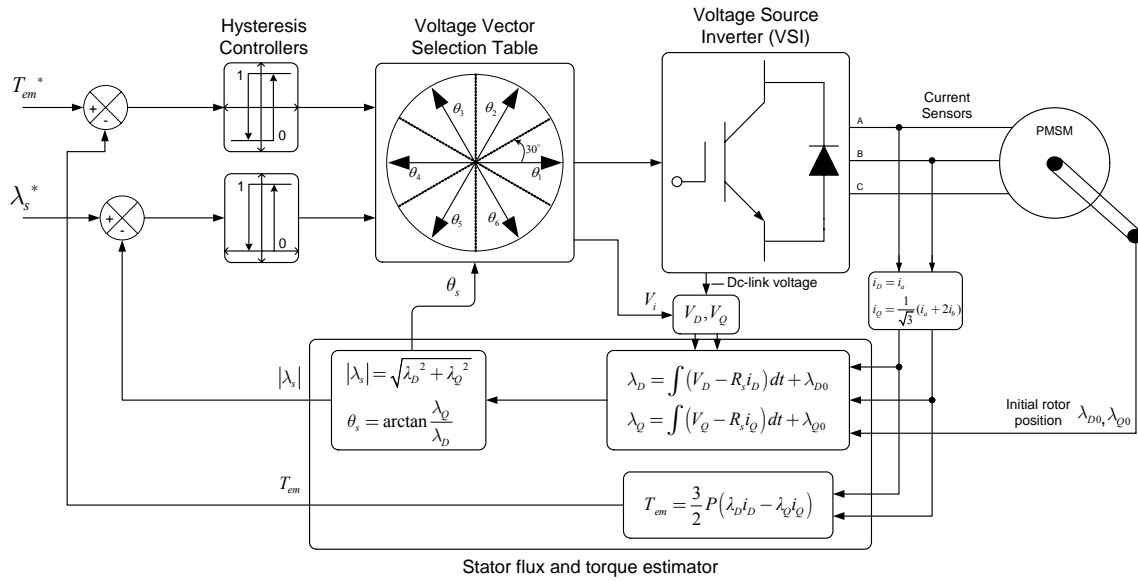


Fig. 5.10. Basic block diagram of DTC of PMSM.

Fig. 5.10 illustrates the schematic of the basic DTC controller for PMSM drives. The command stator flux, λ_s^* , and torque, T_{em}^* , magnitudes are compared with their respective estimated values. The errors are then processed through the two hysteresis comparators, one for flux and one for torque which operate independently of each other. The flux and torque controller are two-level comparators. The digital outputs of the flux controller have following logic:

$$d_\lambda = 1 \quad \text{for } |\lambda_s| < \lambda_s^* - H_\lambda \quad (5.17)$$

$$d_\lambda = 0 \quad \text{for } |\lambda_s| < \lambda_s^* + H_\lambda \quad (5.18)$$

where $2H_\lambda$ is the total hysteresis-band width of the flux comparator, and d_λ is the digital output of the flux comparator.

By applying the appropriate voltage vectors the actual flux vector, λ_s , is constrained within the hysteresis band and it tracks the command flux, λ_s^* , in a zigzag

path without exceeding the total hysteresis-band width. The torque controller has also two levels for the digital output, which have the following logic:

$$d_{T_{em}} = 1 \text{ for } T_{em} < T_{em}^* + H_{T_{em}} \quad (5.19)$$

$$d_{T_{em}} = 0 \text{ for } T_{em} < T_{em}^* - H_{T_{em}} \quad (5.20)$$

where $2H_{T_{em}}$ is the total hysteresis-band width of the torque comparator, and $d_{T_{em}}$ is the digital output of the torque comparator.

$$\begin{bmatrix} f_D \\ f_Q \\ f_0 \end{bmatrix} = \begin{bmatrix} 1 & -\frac{1}{2} & -\frac{1}{2} \\ 0 & -\frac{\sqrt{3}}{2} & \frac{\sqrt{3}}{2} \\ \frac{1}{2} & \frac{1}{2} & \frac{1}{2} \end{bmatrix} \begin{bmatrix} f_a \\ f_b \\ f_c \end{bmatrix} \quad (5.21)$$

Knowing the output of these comparators and the sector of the stator flux vector, the look-up table can be built such that it applies the appropriate voltage vectors via the inverter in a way to force the two variables to predefined trajectories. If the switching states of the inverter, the DC-link voltage of the inverter and two of the motor currents are known then the stator voltage and current vectors of the motor in the DQ stationary frame are obtained easily by a simple transformation. This transformation is called the Clarke transformation [19] (5.21) as shown in Fig. 5.10. The DQ frame voltage and current information can then be used to estimate the corresponding D-and Q-axes stator flux linkages, λ_D and λ_Q , which are given by:

$$\lambda_D(k) = \lambda_D(k-1) + \{v_D(k-1) - R_s \bar{i}_D(k)\} T_s \quad (5.22)$$

$$\lambda_Q(k) = \lambda_Q(k-1) + \{v_Q(k-1) - R_s \bar{i}_Q(k)\} T_s \quad (5.23)$$

where k and $k-1$ are present and previous sampling instants, respectively, v_D and v_Q are the stator voltages in DQ stationary reference frame, $\bar{i}_D(k) = (i_D(k-1) + i_D(k))/2$

and $\bar{i}_Q(k) = (i_Q(k-1) + i_Q(k))/2$ are the average values of stator currents, i_D and i_Q , derived from the present, $i_{DQ}(k)$, and previous, $i_{DQ}(k-1)$, sampling interval values of the stator currents, R_s is the stator resistance, and T_s is the sampling time. The stator flux linkage vector can be written as:

$$\lambda_s(k) = \sqrt{\lambda_D(k)^2 + \lambda_Q(k)^2} \angle \tan^{-1} \left(\frac{\lambda_Q(k)}{\lambda_D(k)} \right) \quad (5.24)$$

where $\sqrt{\lambda_D(k)^2 + \lambda_Q(k)^2}$ is the magnitude of the stator flux linkage vector and $\tan^{-1} \left(\frac{\lambda_Q(k)}{\lambda_D(k)} \right)$ is the angle of stator flux linkage vector with respect to the stationary

D-axis in DQ frame (or a-axis in abc frame). The developed stationary DQ reference frame electromagnetic torque in terms of the DQ frame stator flux linkages and currents is given by

$$T_{em}(k) = \frac{3}{2} P \{ \lambda_Q(k) i_D(k) - \lambda_D(k) i_Q(k) \} \quad (5.25)$$

where P is the number of pole pairs.

As it can be seen from (5.22) and (5.23) the stator resistance is the only machine parameter to be known in the flux, and consequently torque, estimation. Even though the stator is the direct parameter seen in (5.22) and (5.23), there is an indirect (hidden) motor parameter for DTC of PMSM drives. This parameter is the rotor flux magnitude which constructs the initial values of the D- and Q-axes stator fluxes. If the rotor flux vector, λ_r , is assumed to be aligned with the D-axis of the stationary reference frame, then $\lambda_D(k-1)$ equals the rotor flux amplitude $\sqrt{2}\lambda_r$. If the rotor magnetic flux, λ_r , resides on the D-axis (the rotor magnetic flux can be intentionally brought to the known position by applying the appropriate voltage vector for a certain amount of time), then the initial value of the Q-axis flux, $\lambda_Q(k-1)$, is considered to be zero, therefore there will not be any initial starting problem for the motor. On the other hand, if the rotor is in a position

other than the zero reference degree then both the $\lambda_d(k-1)$ and $\lambda_q(k-1)$ values should be known to start the motor properly in the correct direction without oscillation. Moreover, if the initial values of the DQ frame integrators are not estimated correctly then those incorrect initial flux values will be seen as DC components in the integration calculations of the DQ frame fluxes. This will cause the stator flux linkage space vector to drift away from the origin centered circular path and if they are not corrected quickly while motor is running then instability in the system will result quickly.

CHAPTER VI

PROPOSED DIRECT TORQUE CONTROL (DTC) OPERATION OF PMSM DRIVE

6.1. Introduction and Principles of the Proposed DTC Drive

In conventional DTC drives, there are some drawbacks, such as the DC drifts in the voltage and current measurements, wrong DQ-frame initial flux linkages being used or having resistance term exists in the estimation algorithm of the DQ stationary reference frame flux linkages [36]. These disadvantages of the basic DTC scheme are claimed to be eliminated by the proposed DTC technique.

Unlike the conventional DTC scheme which has a voltage model [24], the proposed method is based on the current model which is considered in the rotor coordinate system (rotor reference frame). By using the current model, the stator quantities need to be transferred to the rotor reference frame quantities (this is ensured by the position information). In this thesis, position information is provided by three cheap hall-effect sensors (1\$<) instead of bulky and expensive encoders or resolvers. One hall-effect sensor is mounted on the stator starting from the boundary of Sector 1 and 2, and the remaining two hall-effect sensors are placed 120 electrical degrees apart from each other in the counter-clockwise direction as shown in Fig. 6.1. The sector change of the stator flux linkage space vector on the trajectory can be easily determined by the help of the six hall-effect sensor signals that accompany one complete electrical cycle.

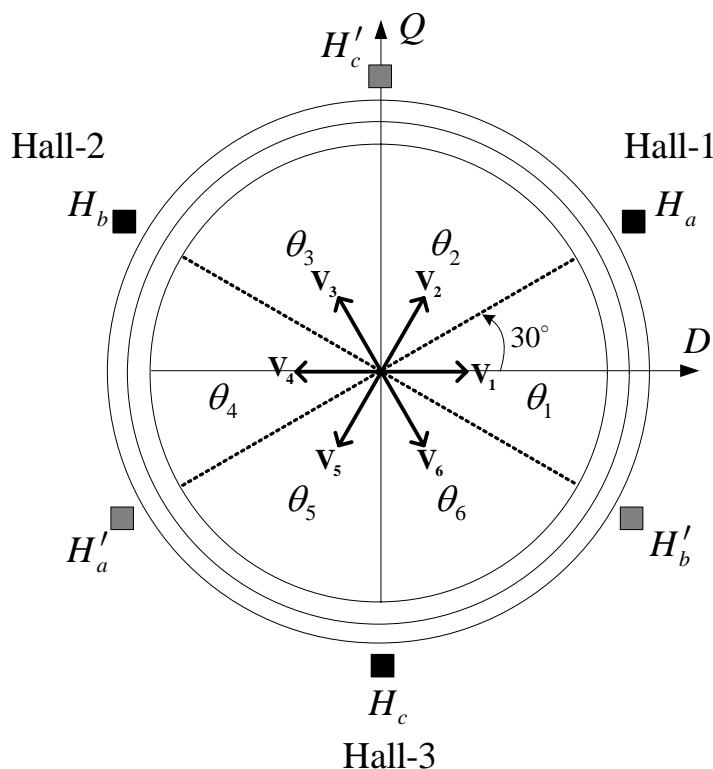


Fig. 6.1. Hall-effect sensor placement shown in DQ stationary reference frame.

The rotor reference frame stator flux linkages, λ_d and λ_q , (dq rotor reference frame) from the current model and torque equation are the key formulas in the proposed DTC drive shown in (2.21) and (2.44), respectively. Unlike conventional DTC drives which use stator reference frame currents, currents in (2.21) and (2.44) are represented in the rotor reference frame as discussed in Chapter II. In this case, continuous rotor position information is needed for use in the Park's Transformation because the Park's transformation is originally used in sinusoidal machines which need high resolution position feedback for the complex vector control algorithm. High-resolution position information can be obtained from an encoder or resolver generating high number of pulses, but in this thesis three hall-effect sensors assisted by a simplified observer are used to mimic the behavior of those expensive high-resolution position sensors. Usually hall-effect sensors are used in BLDC motor drives that have trapezoidal back-EMF. In BLDC motor drives, each phase current conducts 120 electrical degrees and their shapes

are like square waveforms and their power devices are switched every 60 electrical degrees to commutate the phase currents. The position sensor, therefore, has a resolution of only 60 electrical degrees, thus an inexpensive low-resolution position sensor, such as a hall-effect sensor, is suitable. On the other hand, in sinusoidal machines like PMSMs, high-performance current vector control cannot be achieved and the operating performance is inferior to the drive system which has low-resolution feedback position information. The detailed explanation of position and speed sensing used in the proposed DTC scheme by a simple observer assisted with three low-cost hall-effect sensors will be discussed in the next section.

Once the position is estimated by the three hall-effect sensors, the Park's Transformation is applied to the three phase abc frame currents that are measured to get the dq rotor reference frame currents. After that, the obtained dq rotor reference frame currents are placed in (2.21) to estimate the stator dq axes flux linkages. With this information, the stator flux linkage amplitude can be derived as:

$$|\lambda_s| = \sqrt{\lambda_d^2 + \lambda_q^2} \quad (6.1)$$

The stator flux linkage amplitude calculated from rotor reference frame quantities is exactly the same as the one found by using the stator reference frame fluxes λ_D and λ_Q as shown in Fig. 6.2.

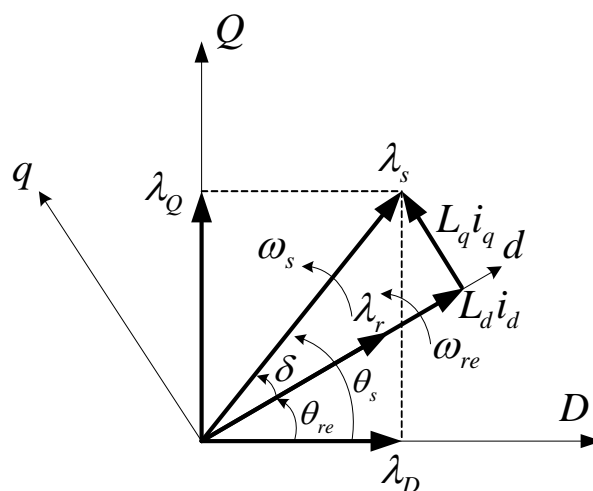


Fig. 6.2. Representation of the rotor and stator flux linkages both in the synchronous dq and stationary DQ-planes.

Although the stator flux linkage amplitude calculation in both the stator and rotor reference frames generates the same result, the exact position of the stator flux vector in the DQ frame cannot be applied to the rotor reference frame flux components by just using (5.27). The angle between the rotor reference frame q-axis flux and d-axis flux, which is a constant value due to the DC values of the synchronous frame currents equals to the load angle, δ , and the stator flux vector angle, θ_s , with respect to the D-axis, is given by:

$$\theta_s = \theta_r + \arctan\left(\frac{\lambda_q}{\lambda_d}\right) = \theta_r + \delta \quad (6.2)$$

With the proposed method, the initial flux errors which cause drift in the basic DTC scheme will not be added to the next calculations (integration). The only problem in flux calculations might happen at high current and high temperature. The rotor reference frame stator flux linkages possess d- and q-axes inductances along with a rotor magnetic flux linkage amplitude which is affected by an increase in temperature. Under magnetic saturation the q-axis inductance of an IPMSM varies and the d-axis inductance is affected by the armature reaction therefore the saturation model for various load

conditions should be developed such that inductance should be expressed taking into account magnetic saturation. Also, when the load is increased the amplitude of the rotor magnetic flux linkage is increased (due to temperature rise) therefore it is necessary to consider the change in the synchronous inductance ($L_s = L_d = L_q$ in surface-mounted PMSMs) because it is greatly affected due to magnetic saturation. Magnetic saturation and temperature effects are not included in the proposed system, but it should be considered and compensated for if there is high current and the operating points of the current reside in the saturation region of the motor.

Basic DTC is based on a voltage model which is plagued by the stator resistance error and the integration drift at low frequencies. On the other hand, the current model is affected by parameter detuning (due to magnetic saturation) and also by the position error, but it works pretty well from zero speed if a high-resolution position sensor such as an encoder is used. In the literature, a combination of the voltage and current model is proposed with a PI compensator such that the current model is predominant at low speeds while the voltage model takes over at high speeds. Applications of this combined method can be very costly due to the additional sensor (position). To make the overall system cheaper, the current model is suggested instead of the voltage model therefore only a very cheap position sensor is needed (hall-effect sensor). A complete block diagram of the proposed DTC scheme is given in Fig. 6.3. Because the motor used in this thesis is a high torque motor and in washing machine applications there is a certain limit for the capacity of the load (approximately known load torque) in the drum such that currents cannot bring the motor into the saturation region easily, thus inductance compensation can be ignored. In certain applications where very high currents bring the motor to the saturation region and temperature increases inside the motor are evident, the inductance and amplitude of the rotor flux linkage should be compensated.

6.2. Position and Speed Estimation Method with Low-Resolution Position Sensor

In permanent magnet synchronous motors (PMSMs) and for every other sinusoidal current controlled AC drive systems, in order to produce the sinusoidal current commands and control the current phase accurately, high resolution position information is essential. A high resolution position sensor such as an optical encoder with large pulses per revolution or a resolver is therefore usually used.

Since the current model is used for the proposed DTC of a PMSM drive, continuous rotor position information should be obtained. In this thesis, a low resolution position sensor which has an accuracy of only 60 electrical degrees is used instead of a high resolution sensor. Such low-resolution position feedback can be achieved by the processed signals from three cost-effective hall-effect sensors as shown in Fig. 6.1. One electrical cycle is divided into six intervals (representing the six sectors for the DTC scheme) of 60 electrical degrees by the processed signals H_a , H_b , and H_c . In this case, the absolute position with an accuracy of ± 30 electrical degrees (mid point of two consecutive hall-effect signals are chosen as a reference point) can be obtained, and as a result reverse rotation at starting never occurs. The hall-effect sensor has advantages such as smaller size and lower cost compared to an optical encoder or resolver. However, since the position updates occur at every 60 electrical degree interval, the necessary continuous position information for PMSM drives cannot be achieved by using just three hall-effect sensors like in BLDC drives. Knowing this, vector transformations (Park's and inverse Park's Transformations) and sinusoidal current drives cannot be achieved by using low-resolution position sensing. The main goal of this thesis is to estimate higher resolution position information from the rough position information obtained from the three hall-effect sensors. The method of obtaining the high-resolution position information from the three hall-effect sensor signals is explained using Fig. 6.4 as follows:

In Fig. 6.4, the actual positions, $\theta_{real}(j)$, corresponding to 0° , 60° , 120° , 180° , 240° , and 300° are obtained from the three hall-effect sensors at every 60 electrical degrees. The index pointer of the corresponding component is defined as j and $j-1$ is

$$\omega_{mt-\frac{1}{2}} = \frac{\omega_{t-\frac{1}{2}}}{P/2} \quad \text{in mechanical rad/sec} \quad (6.4)$$

where P is the pole numbers of the motor.

At each 60 electrical degree interval time the speed of the rotor including the average acceleration or deceleration rate can be defined as:

$$\omega_{est}(j,0) = \omega_{t-\frac{1}{2}} + a_{avg}(j-1) \frac{T_{hall}(j)}{2} \quad (6.5)$$

To resemble the high-resolution position sensing phenomenon, the rotor position and speed corresponding to the well-known Newton's motion law between two consecutive hall-effect signals can be estimated as follows:

$$\omega_{est}(j,k) = \omega_{est}(j,0) + a_{avg}(j-1)T_s \quad (6.6)$$

where T_s is the sampling time of the overall system.

At every 60 electrical degrees (hall-effect sensor signal observed) the average rotor acceleration or deceleration rate ($\dots a_{avg}(j-1), a_{avg}(j), \dots$) is calculated as:

$$a_{avg}(j) = \frac{\omega_{est}(j,0) - \omega_{est}((j-1),0)}{t_j - t_{j-1}} \quad \text{electrical rad/s}^2 \quad (6.7)$$

where t_{j-1} is the time at $((j-1),0)$ and t_j is the time at $(j,0)$ as shown in Fig. 6.4. The present estimated position between two consecutive hall-effect sensor signals, $\theta_{est}(j,k)$, when the acceleration or deceleration is ignored can be expressed as:

$$\theta_{est}(j,k) = \theta_{real}(j) + \theta_p(j,k) \quad (6.8)$$

where $\theta_p(j,k) = \omega_{avg}(j)kT_s$ denotes the incremental position added to the real position which is obtained from the hall-effect sensor. Replacing that into (6.8), we obtain:

$$\theta_{est}(j,k) = \theta_{real}(j) + \omega_{avg}(j)kT_s \quad (6.9)$$

Using angular velocity, $\omega_{est}(j, k)$, the present estimated position, $\theta_{est}(j, k)$, is calculated by adding the real position, $\theta_{real}(j)$, obtained from the hall-effect sensors to the estimated incremental position, $\theta_p(k)$, and also it is the angle rotated from the actual position to the present that is represented by:

$$\theta_{est}(j, k) = \theta_{real}(j) + \frac{1}{2} a_{avg}(j-1)(kT_s)^2 + \omega_{est}(j, k)kT_s \quad (6.10)$$

The real position, $\theta_{real}(j)$, can be expressed when $k = 0$ as:

$$\theta_{real}(j) = \theta_{est}(j, 0) \quad (6.11)$$

where k in the above equations is the index pointer representing the incremental value of the sampling time, T_s , starting at 0 incrementing by one.

Basically, in the above method position is collected from the hall-effect sensors and the average acceleration or deceleration rate of the rotor is calculated at every 60 electrical degrees interval. The estimated rotor position and the speed values between those intervals are obtained by using Newton's motion law equations given above. Fig. 6.5 depicts the acceleration and speed estimations in each sector and at the sector boundaries of the proposed DTC scheme, respectively. Because the acceleration or deceleration of the motor is included in the above position and speed estimation equations, the hesitation problems associated with step and ramp speed references under initial load condition are sufficiently improved.

Even though the rotor position is calculated from (6.10), it needs to be clarified that if the estimated rotor position is still within the assumed section. For example, if the rotor is assumed to be in the Sector 1, the condition that $330 \leq \theta_r \leq 30$ should be satisfied. The estimated rotor position is corrected when the limits exceeded for Sector 1. The correction logic that is used in the Sector 1 is given below [55]:

If $\theta_r < 330$, then $\theta_r = 330$;

If $\theta_r > 30$, then $\theta_r = 30$.

There are four major advantages associated with the proposed algorithm [55]:

CHAPTER VII

AGITATION PERIOD SPEED CONTROL OF VERTICAL-AXIS LAUNDRY MACHINE

7.1. Modern Washing Machines: Top Loaded (Vertical-axis) vs. Front Loaded (Horizontal-axis) Washing Machine

Contemporary washing machines are available in two main configurations: “top-loading” and “front-loading”. The “top-loading” design, the most popular in the US, Australia, and some parts of Europe, has the clothes placed in a vertically-mounted cylinder with a propeller-like agitator in the center of the bottom of the cylinder. The cloths are loaded at the top of the machine, which is covered with a hinged door. The “front-loading” design, the most popular in Europe (especially in UK), instead mounts the cylinder horizontally, that allows loading through a glass door at the front of machine. The cylinder is called the drum.

Tests comparing front-loading and top-loading machines have shown that, in general, front-loaders wash cloths more thoroughly, cause less wear, and use less water and energy than top-loaders. As a result of using less water, they require less detergent. They also allow a dryer to be mounted directly above the washer, which is impossible with a top-loader. On the other hand, top loaders complete washing much faster, tend to cost less for the same capacity machine, and allow clothes to be removed at intermediate stages of the cycle (for instance, if some clothes within a wash are not to be spun).

7.2. Introduction to Speed Control of a BLDC Spindle Motor (48 Pole/36 slot) in The Agitation Cycle of a Washing Machine

In a vertical-axis washing machine, agitation is supplied by the back-and-forth rotation of the cylinder (drum) and by gravity. The items are lifted up by paddles in the drum, and they are then dropped down to the bottom of the drum. This motion forces the water and detergent solution through the fabric. Although more infrequent, there is also a variant of the horizontal axis design that is loaded from the top, through a flop in the circumference of the drum. These machines usually have a shorter cylinder and are therefore smaller [56].

In the agitation part of a laundry washing cycle, the controller controls the power supplied to the motor using Pulse Width Modulation (PWM) in order to maintain motor speed in accordance with a predetermined speed profile. The agitation speed profile can be categorized into three sections [56]:

- (i) Ramp up from standstill to a desired plateau speed (steady-state speed), the so called “acceleration” or “ramp” region.
- (ii) Maintaining the plateau speed for a predetermined period of time. This section is called the “plateau” region.
- (iii) Removing the motor power by turning off the lower switches of three-phase inverter and coasting the motor towards zero speed. The end of plateau section is the start of the coast section. Once the speed of the motor drops to the predetermined reversal speed, which is usually defined as half of the reference plateau speed, motor will be reversed. If it is necessary, after reaching the reversal speed, the motor will be turned in reverse direction when the motor speed drops to zero. Consequently, the time between the end of plateau section and reversal speed is called the “coast” time and the time between the reversal speed and the zero speed in one stroke is called the “pause” time. Altogether the coast and pause time establish the “coast/pause” region of a stroke.

The combination of (i), (ii), and (iii) is the stroke time of the washing machine in the agitation cycle. At the end of each stroke, the motor direction is reversed. In each agitation stroke, the stroke time is controlled by adjusting the “coast” (pause time is constant) phase of each stroke in order to maintain consistent washing performance. Before starting the agitation washing cycle, all of the above phases (times) determined by the controller depending on the load condition are chosen using the information given on the washing machine panel by the customer. Only the ramp, plateau phases and pause times stay constant in every stroke. The “coast” phase is initiated, however, (after a predetermined period elapsed in the “plateau” phase) by starting a timer and allowing the motor to coast until the motor velocity (speed) drops to a predetermined reversal speed at which point the motor is reversed to begin the next agitation stroke. Several experiments have proven that the reversal speed should be chosen to be equal to the half of the plateau speed and can be adjusted depending on the load conditions (bunching, etc.). Reversal speed will be changed in accordance with the difference between the timer value when the velocity reaches the reversal speed and the predetermined timer value representing the total coast time. If the timer value is greater than the desired value or range of values then the predetermined value of the reversal speed will be increased. Alternatively, if the timer value is less than the desired value or range of value the reversal speed will be decreased. Eventually, the period of the coast phase of the next stroke should be closer to the desired period. The “coast/pause” phase is not going to be the main focus in this thesis work, instead the “ramp” and “plateau” phases will be the main subjects to be discussed. A simple flowchart of the agitation speed control is depicted in Fig. 7.1.

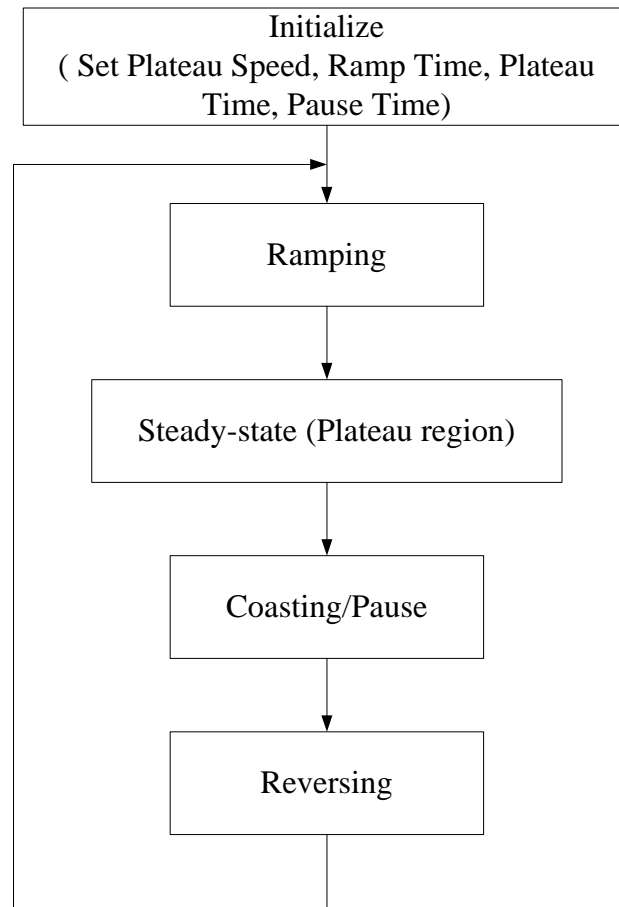


Fig. 7.1. Simple flowchart of the commercial agitation speed control [57].

7.3. Agitate Washer Controller Model in SIMPLORER[®]

A complete agitation washer controller is built in SIMPLORER[®]. Unlike a real-time microcontroller that uses interrupts and counters, the simulation will use time based logic for simplicity. Details are as follows:

As explained before, the agitator speed controller has ramp, plateau, coast and/or pause time sections in the reference speed profile which is shown in Fig. 7.2. Basically, the controller has four inputs. Those are: Plateau Speed (PS), Ramp Time (RT), Plateau Time (PT), and Pause Time (PaT). Coast Time (CT) is an input usually maintained at a

certain predefined time by the controller. In this thesis, the coast and pause sections are not modeled fully. They were discussed briefly in the previous section. Characteristics of each section will be explained. One positive complete cycle (stroke) is shown in the graph below. The negative cycle which has the same shape, but in reverse direction, is not shown here, the reverse rotation starts when the coast/pause section is over.

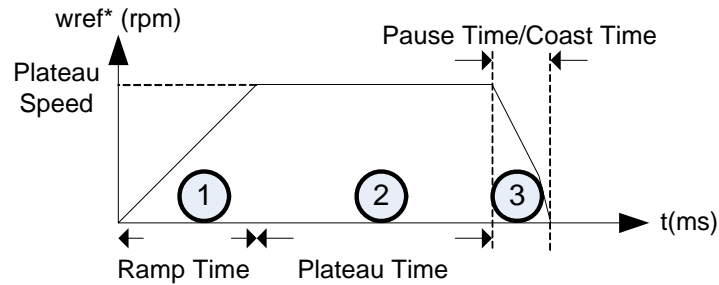


Fig. 7.2. Reference speed profile for the agitation speed control in a washing machine.

The operation of the agitation control in a laundry washing machine algorithm used in commercial washing machines is discussed below. A flowchart is provided detailing the operation of the simple agitation washing controller which is implemented in the simulation platform, SIMPLORER[®].

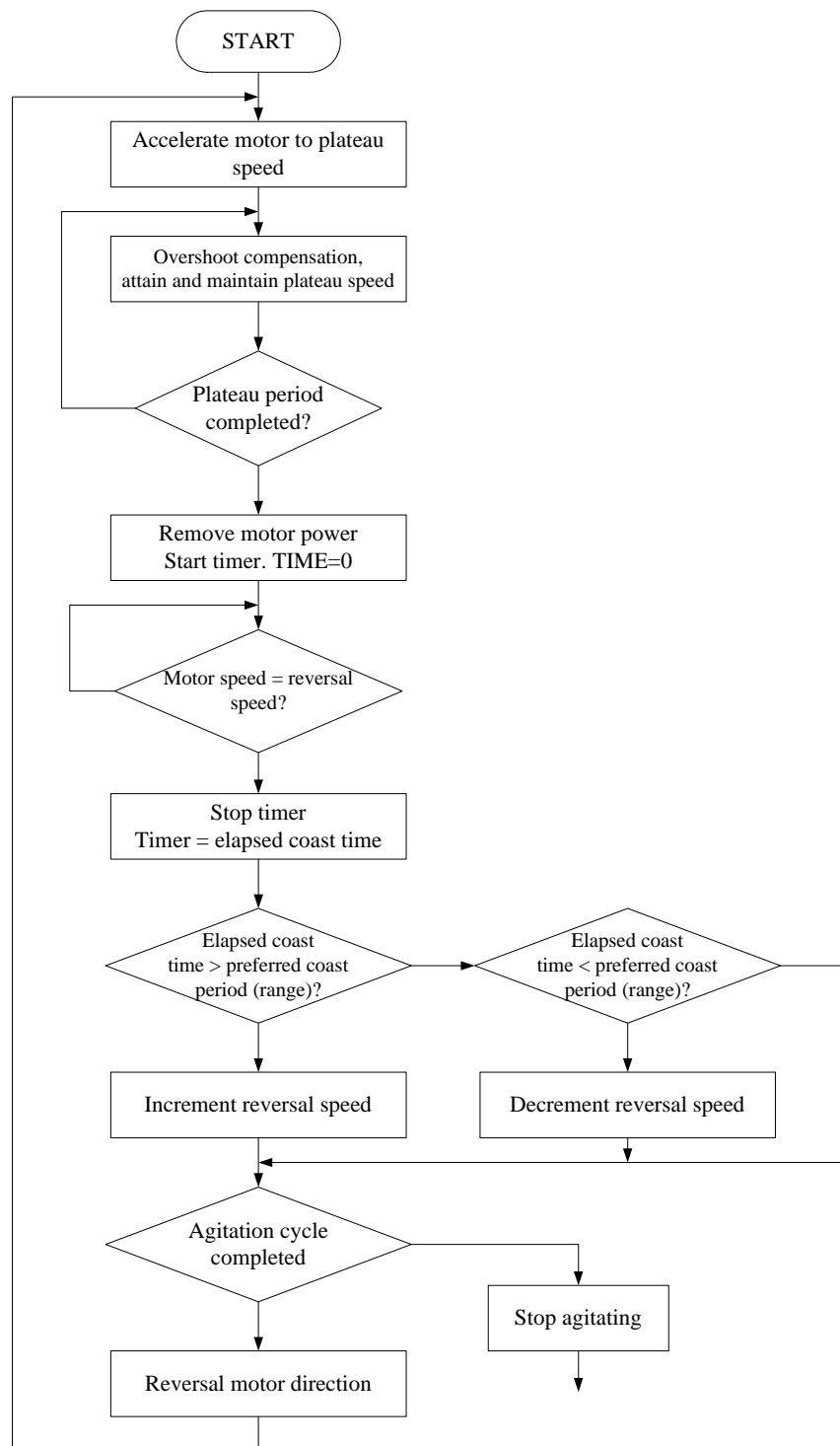


Fig.7.3. Detailed flowchart of the simple agitation speed control of a washing machine

[58].

Fig. 7.3 presents the instructions required to carry out the agitation phase of a washing cycle with a detail flowchart. Descriptions of that flowchart are as follows:

When the washing machine has completed a fib phase and the laundry load is floating (or submerged) in a suitable mixture of water and detergent, the motor is accelerated (ramped up) incrementally by increasing the PWM duty cycle starting at a minimum value up to plateau speed. More details about ramping up the motor to the desired plateau speed will be discussed later.

Due to the inertia of the drum and laundry load speed overshoot can occur, therefore an overshoot compensation algorithm is developed to bring the exceeded motor speed down to the desired plateau speed as quickly as possible. When the plateau speed is achieved after applying the overshoot compensation (if it is necessary) then the desired plateau speed is maintained till the predetermined “plateau” region is completed (by checking the motor controller timer). At the end of the plateau region the motor power is removed by turning off the lower side of the inverter switches. At the same time the motor timer is started from zero to determine the length of the coast section. While the coasting condition is continuing the reversal speed may be reached (which is assumed to be half of the plateau speed). As time elapses during this phase, the total coast region length is determined for use in the adaptation mechanism of the next strokes. The elapsed coast time is then compared with the predetermined coast time. If the measured coast time is greater than the desired coast period (or range of periods) then the controller increments the reversal speed to be used in the next stroke. If the measured coast time is less than the desired coast period the controller decrements the reversal speed for the next stroke. One stroke late adaptation algorithm is therefore established by controlling the coast time because if the reversal speed for the next cycle is higher than what was defined previously then the coast time will be shorter and vice versa, eventually causing a change in the length of the stroke time. If the pause time is defined as zero then the agitation reverses the motor and the same method is applied until the agitation phase of the washing cycle is completed. Agitation is then stopped and the control executes the next washing cycle. If, however the agitation phase is not yet

complete, then the motor direction is reversed and power is reapplied to the motor windings where the above described process is repeated until the end of the agitation phase [56].

1) Ramp-up Section:

As it is known in DC motor control, to increase the rotational speed of the motor the PWM duty cycle of the inverter outputs should be increased. To reduce the speed of the motor the duty cycle should be decreased, as a result it can be stated that the change in the duty cycle is proportional to the change in speed. The duty cycle of the PWM signal which is applied to the motor terminals by a VSI inverter is determined by the following equation:

$$duty_cycle(\%) = 100 / \left(\frac{PWM_{current}}{PWM_{max}} \right) \quad (7.1)$$

The ratio above determines the on time of the one PWM period (PWM frequency can be any value not less than 2 kHz). If $PWM_{current}$ becomes equal to PWM_{max} the full DC-link voltage will be applied to the motor terminals and maximum speed will be achieved. In starting, $PWM_{current}$ is chosen as small as possible to handle the light load. PWM_{max} is the key component to decide the resolution of the speed increment. If it is higher and the incremental rate of $PWM_{current}$ is small then a higher speed increment resolution is achieved, but if it is small and the $PWM_{current}$ incremental rate is bigger then a lower speed increment resolution is provided.

In ramping, the PWM rate is incremented till the end of ramp period. At that moment the speed is measured by the help of three hall-effect sensors which provide electrical signals indicative of the rotor position. These signals are then fed to the input of a microcontroller via an interface circuit. According to the resultant speed feedback, $PWM_{current}$ (along with the duty cycle) is adjusted up or down depending on whether the measured speed is too low or too high.

As several tests show, regardless of how fast the agitation period is, it is possible to have any ramp period from (e.g. 80 ms – 400 ms) for a better speed profile with less overshoot under heavy laundry load conditions. The ramp time also depends on the wash profile; if it is very gentle then soft agitation is desired therefore a longer ramp up time is preferred and vice versa.

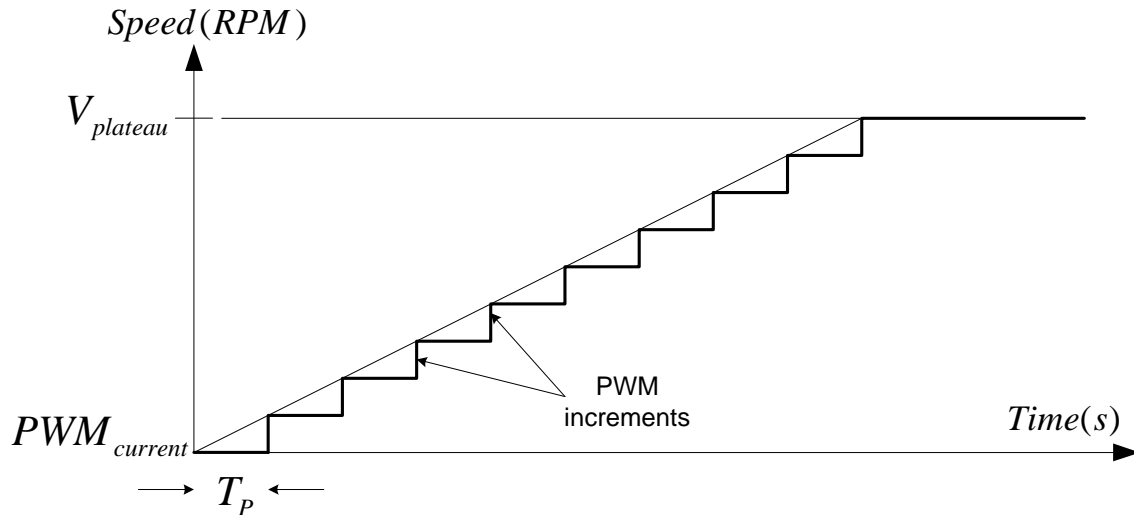


Fig. 7.4. PWM increment during the ramp time [58].

$PWM_{current}$ is incremented at every T_p (sampling time of the $PWM_{current}$ in ramping) as shown in Fig. 7.4 in a series of incremental steps, therefore the speed of the motor gradually increases because the PWM increment occurs at every time interval T_p as shown in Fig. 7.5.

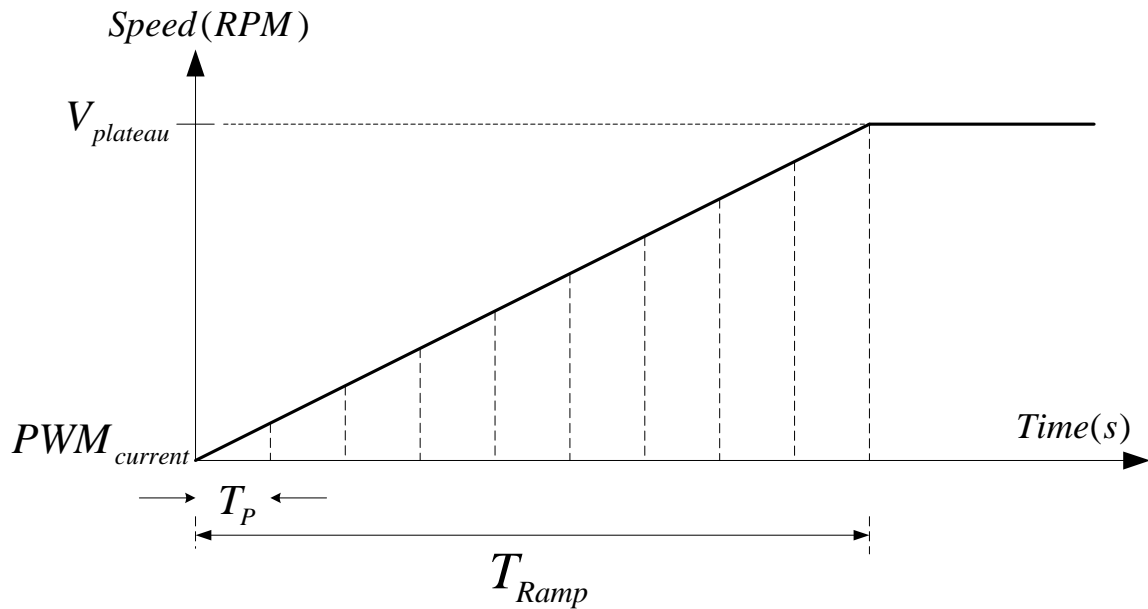


Fig. 7.5. Speed response during ramp up when PWM is incremented at every T_p time [58].

In Fig. 7.4 the angular speed is shown diagrammatically as increasing in discrete steps. Each step corresponds to an increase in $PWM_{current}$ which also increases the duty cycle of the PWM signal. The smaller T_p is the more $PWM_{current}$ is incremented therefore more power is supplied to the motor. All the above descriptions given about ramping up are summarized as follows: $PWM_{current}$ is started at a certain number which can handle the light laundry load at starting and a certain increment step value is chosen (e.g. 16) such that the step time, T_p , (also known as the sampling time) of $PWM_{current}$ can be found if the ramp time is known by the following formula:

$$T_p = \frac{Ramp_Time}{STEPS} \quad (7.2)$$

At every sampling time the $PWM_{current}$ value is incremented by a certain predetermined amount until the speed reaches the desired plateau speed in the predetermined ramp time. If the actual speed is less than what is necessary then ramp

adjustment is used starting from the very next stroke. The ramp adjustment algorithm is a mandatory tool in agitation control. For example, the load on the motor can not always be the same due to varying wash loads, and it is not possible to predetermine the number of incremental steps in order to obtain the correct speed within the ramp time.

A small amount of power (i.e. a small duty cycle value) is enough to start accelerating the motor to the desired plateau speed during the ramp time when there is a very light load on the machine. With a heavy load more power (larger duty cycle value) will be required. The amount of power that can be supplied to accelerate the motor to the desired plateau speed in the predetermined ramp time is proportional to the rate of increase of the incremental steps. The number of steps is initially preset to a minimum setting so that no adjustment is needed for very light loads. Let's say a machine has a very light load and 6 incremental steps are necessary to accelerate the motor to a desired plateau speed in a predetermined ramp time (e.g. 100 ms). On the other hand with a heavy load 62 steps might be required to reach the same speed in same amount of time (100 ms). The software therefore needs to adjust the number of steps to attain the desired speed at a desired interval time. This is performed when the speed is first time monitored at the end of the ramp time at every stroke. If the measured speed at the end of the ramp period is found to be under the desired plateau speed then the number of steps is incremented, thus the value of $PWM_{current}$ increases, and hence the torque of the motor increases [58].

2) Plateau Section:

Ideally, in the plateau region, a constant speed is maintained for a desired predetermined plateau time period. This is the case when there is no heavy load (too much laundry load) on the motor, but at extremely heavy loads a normal agitate controller cannot maintain the speed at the desired plateau speed due to torque constraints on the motor. There is a need for overshoot control in the plateau region to ensure the speed maintains an ideal profile at heavy loads, as shown in Fig. 7.6.

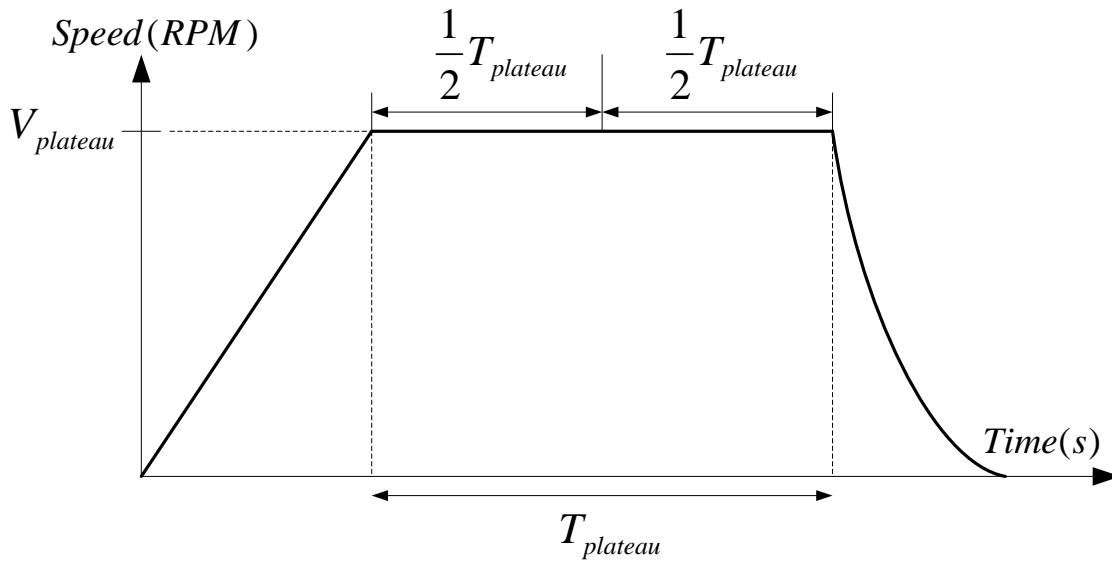


Fig. 7.6. Ideal speed profile of the agitation speed control [58].

Under very heavy loads the actual profile digresses from the desired speed profile as shown in Fig. 7.7. Several experiments show that the load condition of the motor during the plateau region is not its heaviest until approximately half way through the plateau region. If the load in the drum is increased, then the tail end of the plateau region begins to diverge $\frac{3}{4}$ of the way through the plateau region, hence the best point to measure the speed and determine when to add or subtract compensation is at the mid point of the plateau region as illustrated in Fig. 7.7 [58].

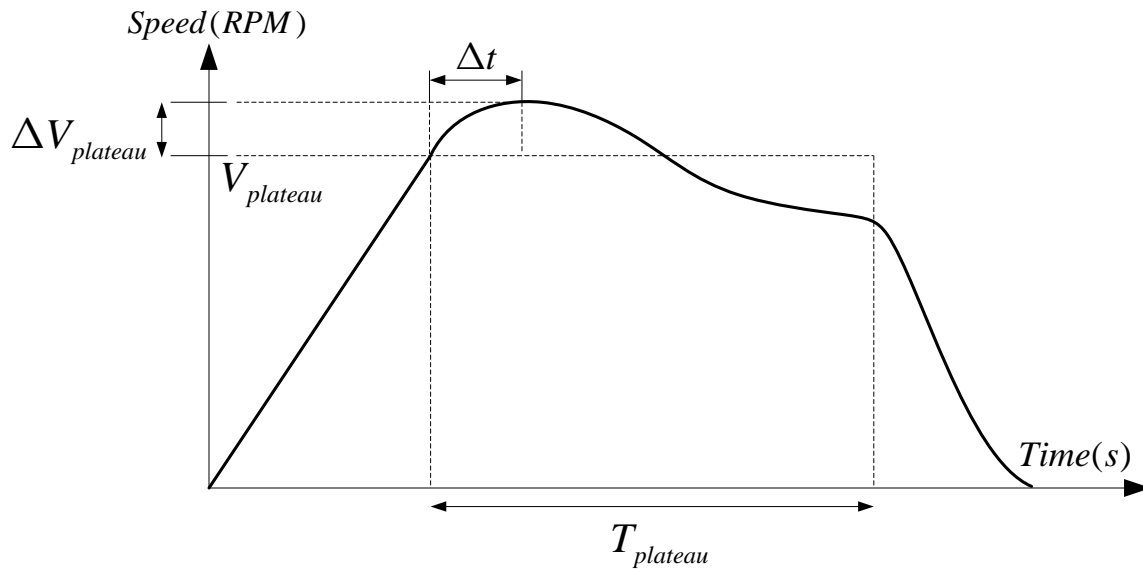


Fig. 7.7. Typical practical speed response of the agitation speed control [58].

If the measuring point indicates a speed that is under the desired plateau speed then on the next stroke cycle at the end of the ramp period the software will increase the plateau speed by an error received from the compensation algorithm, $\Delta V_{plateau}$, for a predetermined time, Δt , as seen in Fig. 7.7. As the load increases, the compensation should also increase. The first parameter that is increased is the overshoot time, Δt . This is increased until either the speed has reached a desired value at the measuring point (mid point of the plateau region) or Δt is equal to the plateau time [58].

If Δt is equal to the plateau time and the speed at the measuring mid point is still under the desired speed due to very heavy load, then the overshoot speed, $\Delta V_{plateau}$, is increased until a predetermined limit is reached or the speed at the measuring mid point is acquired [58].

If the maximum compensation limit has occurred but actual speed measured at the mid point of the plateau region is still under the desired plateau speed due to heavy load condition, however, then the ramp rate is increased by increasing the number of steps, as explained above, in relation to the acceleration ramp control.

CHAPTER VIII

EXPERIMENTAL AND SIMULATION ANALYSIS

8.1. Open-Loop Simulation vs. Experimental Results

In this section of Chapter VIII, before going into the detailed discussion of the simulation and experimental results of the commercialized agitation cycle speed control, an open-loop steady-state and transient-state simulation and experimental results will be given and those results discussed and compared. The experimental setup of the open-loop control system is explained in detail. Important motor parameters such as efficiency and power factor, are measured in both the simulation and experiment. Open-loop analysis and suggested measurement methods of those motor parameters are explained in detail.

8.1.1. Open-Loop Steady-State and Transient Analysis (Simulation)

Open-loop (V/f control) MATLAB/SIMULINK[®] simulations have been conducted to verify and compare the performance of the simulated 48 pole PMSM with the real model. All the open-loop steady-state and transient state simulations are carried out using the default variable-step ode45 (Dormand-Prince) algorithm. The maximum step size, relative tolerance and absolute tolerance are all set to 1e-3. Several parameters such as power factor, efficiency, rms motor phase current, and load angle are simulated at a 100 rpm (40 Hz) steady-state operating speed to compare with the experimental results to verify how close the simulated motor model is to the real motor. A three-phase AC voltage source is used to implement the open-loop V/f control in the simulation of the PMSM.

The PMSM cannot be started at reasonable high constant frequencies, such as 40 Hz, which is used in our tests, so in the simulations the initial speed is selected as 40 Hz (100 rpm) instead of 0 Hz to overcome this problem. The V/f ratio is set to 2, meaning an 80 Vrms sinewave signal with 40 Hz frequency will be generated. By choosing $V/f \approx 2$, a good speed result (no pulsation) and better current shapes (close to pure sinusoidal and less oscillation) are obtained, and the results of efficiency, power factor, rms motor phase current (Phase A) and motor speed versus load torque are displayed in Fig. 8.1 in comparison with the experiments. It is observed that the simulation results are very close to the experiments, especially at low load torque values since the parameter change effect is not considered in the simulations when the load torque increases up to 10 N·m a discrepancy occurs at high temperature (rotor flux linkage amplitude and resistance are affected by temperature change). If the saturation level of the motor is reached and exceeded then the synchronous inductance value will also alter.

A transient analysis is performed to observe the starting performance of the simulated model in comparison with the experimental results; basically this test has been done to verify the inertia and other torque effective components such as friction and windage load etc. on the transient conditions. From Figs. 8.2 and 8.3, it can be seen that the simulation speed response to the step input is faster than the experimental result. Having a transient response in open-loop is quite challenging due to the lack of position information to synchronize the rotor field with stator rotating field at start up. If the transient is less than 0.4 second both responses converge and reach the steady-state speed. To start the motor properly in both simulation and experimental transient tests, the zero initial position is selected as the reference point. Any position can be chosen as a reference, but since the input voltage is a sinewave, starting the motor from the zero position generates less torque pulsation. In general, the zero reference position is the position when the rotor flux is aligned with the Phase A axis. In practice, if the neutral access is available then enough DC voltage is applied between Phase A and the neutral point to enable the rotor to stay aligned with the Phase A axis. If the neutral is not

available then Phase B and C are short-circuited, so when DC voltage is applied between Phase A and the short-circuited Phase B and C the same zero position alignment will be achieved.

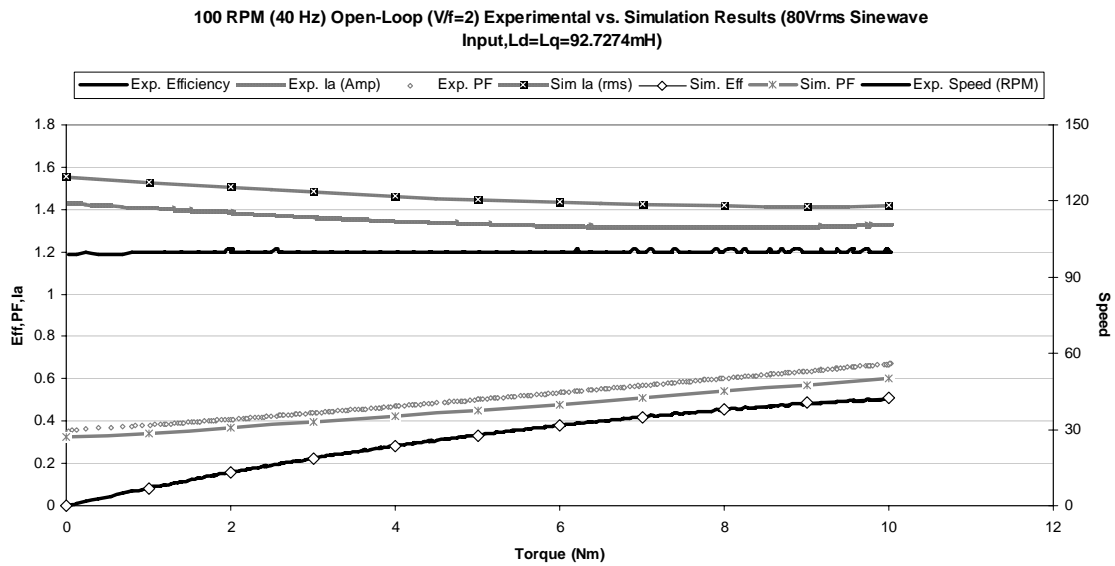


Fig. 8.1. Efficiency, power factor, motor current (Phase A), and motor speed versus applied load torque (open-loop exp. and sim.) at 100 rpm with $V/f \approx 2$.

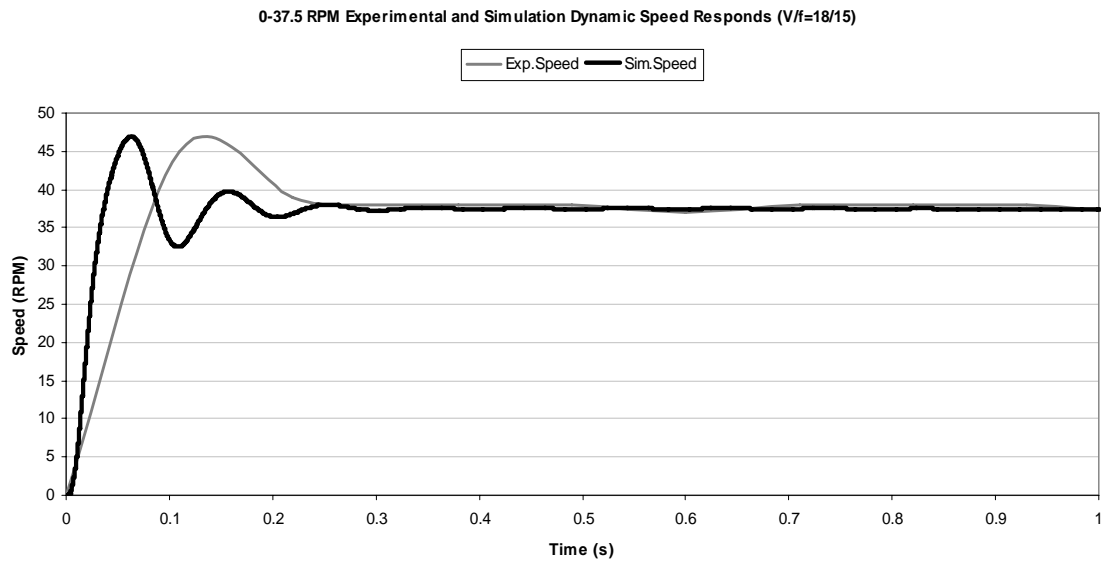


Fig. 8.2. Dynamic speed response of exp. and sim. when $V / f = 18/15$ (0-37.5 rpm).

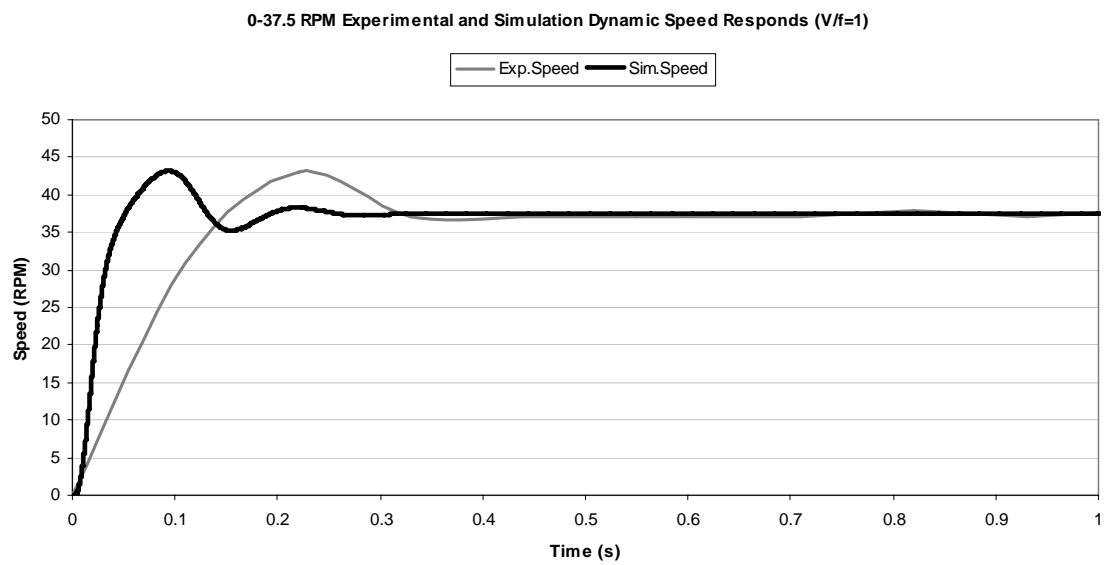


Fig. 8.3. Dynamic speed response of exp. and sim. when $V / f = 1$ (0-37.5 rpm).

8.1.2. Open-Loop Steady-State and Transient Analysis (Experiment)

Experimental tests have been conducted on a 325 V_{dc} PM synchronous machine (sinusoidal back-EMF) with 48 rotor poles. Even though the agitation control algorithm generates squarewave currents to control the motor, in an open-loop test the sinewave input voltages are used to get better performance on the measurements of the efficiency, power factor, load torque, and rms phase current of the motor. Since the current is rectangular in agitation control, but the back-EMF of the machine is sinusoidal, the resultant torque (electromagnetic torque) is not smooth. Fig. 8.4 shows the electromagnetic torque of a PMSM having a sinusoidal back-EMF when it is driven with square-wave currents.

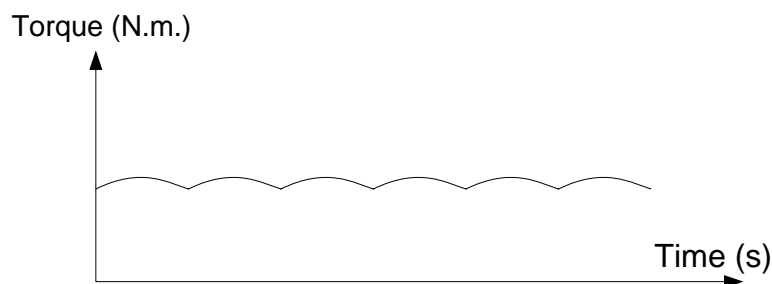


Fig. 8.4. Torque response of PMSM when it is supplied by quasi-square wave currents.

In the open-loop transient test, the rotor is locked with the zero position as explained above and a three phase programmable AC voltage source is connected to the motor terminals. The minimum frequency available from the power source, 12 Hz, is chosen such that the V/f ratio will be around 1. With this V/f ratio the rms value of the sinusoidal voltage becomes 12 V_{rms} . Additionally, a second test for transient analysis is performed with $V/f \approx 18/12$. During this test, a dynamometer controller (DSP600) is used so the speed response can be stored in the M-TEST 4.0[®] software and saved as a Microsoft[®] Excel spreadsheet as shown in Figs. 8.2 and 8.3.

The open-loop efficiency calculation, explained in Chapter IV, which is done in MATLAB/SIMULINK[®] shows an agreement with the actual measurement provided by the Magtrol Power Analyzer Model 6530, as shown in Fig. 8.1. Measurements of real

power, power factor, efficiency, motor voltages and currents, etc. are obtained in the M-TEST 4.0[®] software which communicates with the power analyzer through the GPIB cable. Other necessary equipment for measuring the above parameters include a Magtrol Hysteresis Dynamometer (Model HD-800-6N), a Magtrol DSP6000 Dynamometer Controller interconnected with the Magtrol Hysteresis Dynamometer and the M-TEST 4.0[®] software. The software sends the load torque information to the Magtrol Hysteresis Dynamometer through the Dynamometer Controller and depending on the control configuration (either closed or open-loop (if curve test is selected in the M-TEST 4.0[®] software, then the dynamometer controller will control the values assigned in the software in a close-loop fashion) the load torque value is controlled by the Dynamometer Controller. Communication between the M-TEST 4.0[®] software and the dynamometer controller is achieved through the GPIB cable. The results of the measured and calculated parameters which are processed in the power analyzer are sent back to the M-TEST 4.0[®] software to be read. Fig. 8.5 shows the measured experimental efficiency, power factor, rms motor phase current and motor speed versus applied load torque when the curve test is used. More detail about curve test will be given later in this chapter.

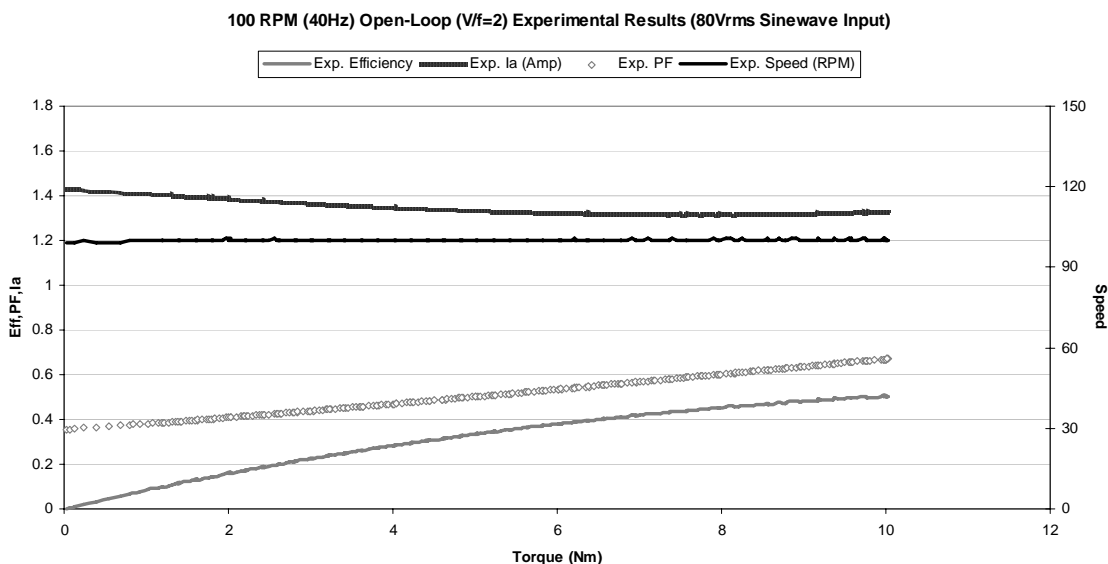


Fig. 8.5. Efficiency, power factor, motor current (Phase A), and motor speed versus applied load torque (experimental, open-loop) at 100 rpm with $V / f \approx 2$.

8.1.3. System Configuration for Electrical Parameters Measurements

A Magtrol Hysteresis Dynamometer provides motor loading with Magtrol Programmable Dynamometer Controller (DSP6000) acting as the interface between the personal computer running M-TEST 4.0[®]. The Hysteresis Dynamometer and motor electrical parameters are measured or used to determine load points by a Magtrol Power Analyzer. A three-phase Power Analyzer Data Acquisition system is configured such that it can obtain data on each individual phase and/or their sum which is used in the chosen parameters (amps, volts, input watts and power factor).

The interface between the computer and the electronic instrumentation is provided by the National Instruments[™] PCI-GPIB card when using a DSP6000.

Basic block diagram of overall system for efficiency measurements is represented in Fig. 8.6. Fig. 8.7 illustrates the configuration of the overall measurement system including one additional power analyzer (magtrol model 6550). There are two reasons for having an additional power analyzer: The first reason is to measure the input

active power of the single phase supply source so that the overall system efficiency can be easily calculated. The overall efficiency is represented as η_1 in the same figure. Efficiency loss in the power converter can be calculated by using the efficiency of the three-phase inverter measured by power analyzer model 6530 when the motor is driven by the agitation washer controller. To achieve that, one of the power analyzers (model 6550) measures the active power which goes to the single phase rectifier from the single phase supply while the other (model 6530) measures the active power which goes to the motor provided by three-phase inverter. The output power generated by motor is the same when those measurements are taken place. A detailed system connection is given in Fig. 8.7.

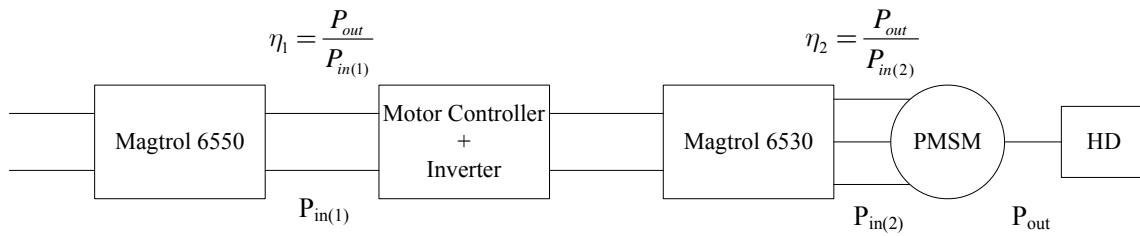


Fig. 8.6. Basic block diagram of overall system for efficiency measurements.

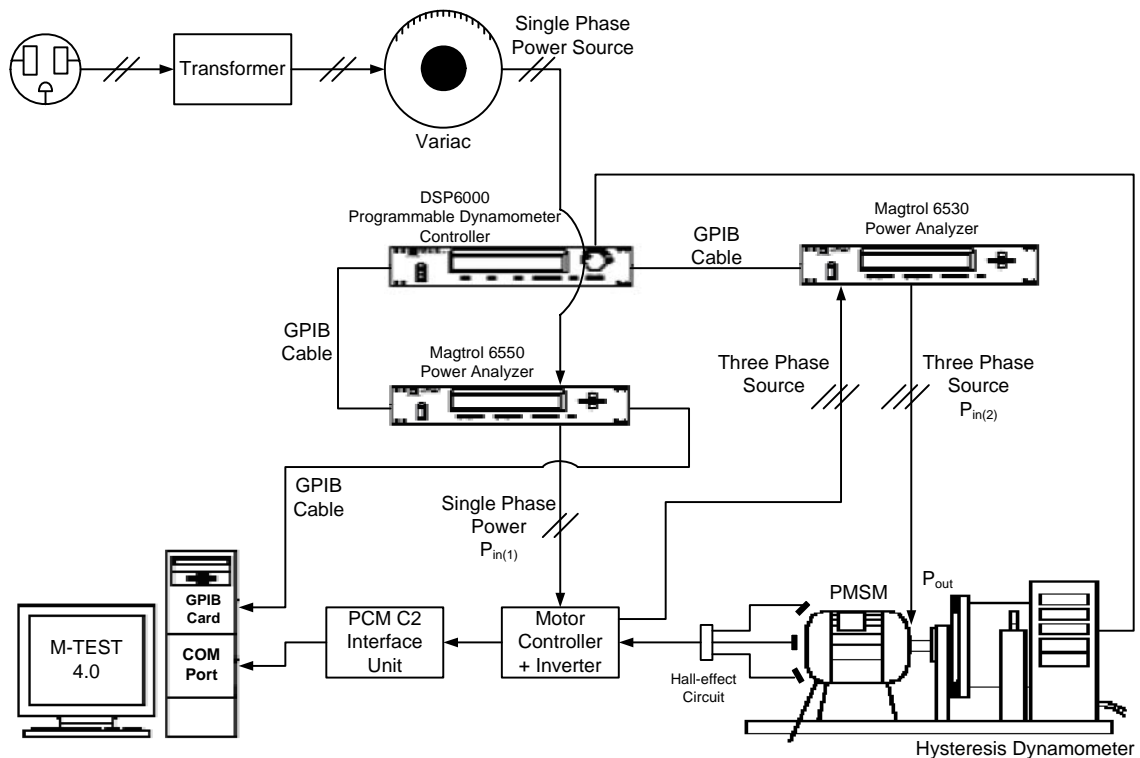


Fig. 8.7. Overall system configuration.

8.1.4. The M-Test 4.0 Software

Magtrol's M-TEST 4.0[®] software is a state-of-the-art motor testing program for Windows[®]-based data acquisition. Used in conjunction with Magtrol's Motor Testing Equipment, M-TEST 4.0[®] provides testing and data options to help determine the performance and characteristics of a motor under test.

The data generated by the program can then be stored, displayed and printed in tabular or graphic formats, and easily imported into a spreadsheet (Microsoft[®] Excel). M-TEST 4.0[®] is ideal for tasks such as simulating loads, cycling the unit under test and motor ramping.

In our tests, M-TEST 4.0[®] is equipped to work in conjunction with the following Magtrol motor testing instruments:

- Dynamometer Controller (DSP6000)
- Hysteresis Dynamometer
- Power Analyzer (Model 6530 and 6550)

8.1.5. Curve Testing

M-TEST 4.0[®] can be used in a way that simulates complex load profiles. This may be for a heat run or endurance testing, simulating a real life usage, or just for checking a few specific data points.

Loading may be accomplished by closing a control loop on Speed, Torque, or Output Watts, plus Amps or Input Watts if a power analyzer is incorporated into the system. Because closed loop speed and torque are internal functions of the dynamometer controller, the control loops are very fast and highly controllable. The remaining functions use a routine in M-TEST 4.0[®] to close the loop and provide control. These will not provide as tight a control as the internal functions, but they are quite satisfactory for most applications.

Loading can be accomplished by either stepping or ramping to the desired point. If a load point is wanted to be stepped up suddenly, then a time of “0” (zero) should be entered for that point. If a ramp to a load point is desired, then the number of seconds should be entered (or minutes, depending on the timebase setting) for the controller to ramp from the starting point to the ending point. To remain at a fixed load for a period of time, the same value for "From" and "To" is used. Any values entered in the “From” and “To” columns will be in the units specified by the control parameter.

To obtain the desired electrical parameters, such as power factor, efficiency, and etc. in open-loop control, the following torque curve test is performed depicted as a table in Fig. 8.8:

Sequence	From	To	Time	Description
1	0	0	10	Dwell at 0 N.m. for 10 seconds
2	0	10	10	Ramp the torque from zero to 10 in 10 seconds
3	10	10	10	Dwell at 10 N.m. for 10 seconds
4	10	0	30	Ramp down to zero in 30 seconds
5	0	0	10	Dwell at 0 N.m. for 10 seconds

Fig. 8.8. Sample curve test.

And the graphical representation of the above torque curve test is given in Fig. 8.9.

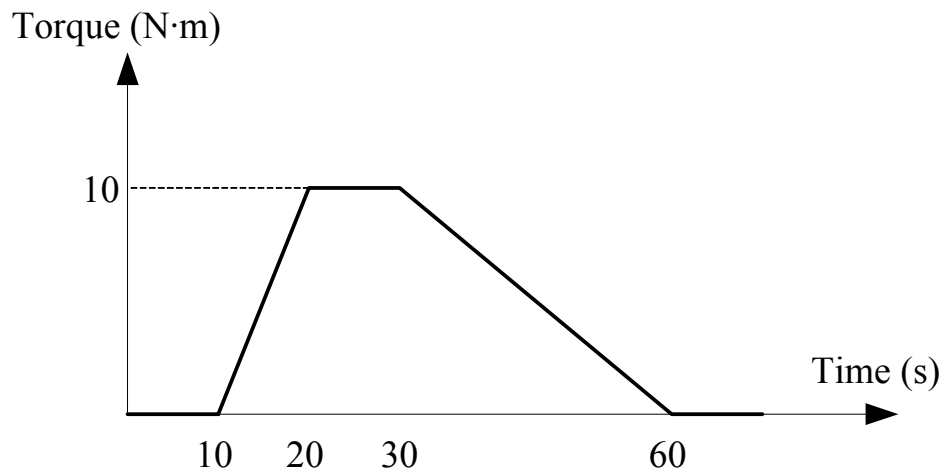


Fig. 8.9. Graphical representation of the sample curve test.

8.2. Experimental vs. Simulation Results (Commercial Agitation Control)

In this section of Chapter VIII, the simulation and experimental results of the commercialized agitation cycle speed control are given and those results are discussed and compared. Several important motor parameters, such as efficiency and power factor as well as line current, motor phase currents, DC-link voltage and motor speeds, are obtained both in simulation and in experimentation and they are compared.

8.2.1. Complete Agitation Speed Control Analysis (Steady-State)

First, to compare with the experimental steady-state results, a steady state simulation model is built in SIMPLORER[®]. Validation is achieved by comparing several parameters such as line current observed in the single phase rectifier as depicted in Fig. 8.10, overall efficiency (input real power is measured in the experiment and calculated in the simulation from a single phase supply source, and power factor. The input line current obtained from the simulation under 10 N·m of load torque at steady state (100 rpm) closely resembles the real-time line current. This concludes one section of the validation process between the SIMPLORER[®] agitation steady-state model and the real-time agitation system.

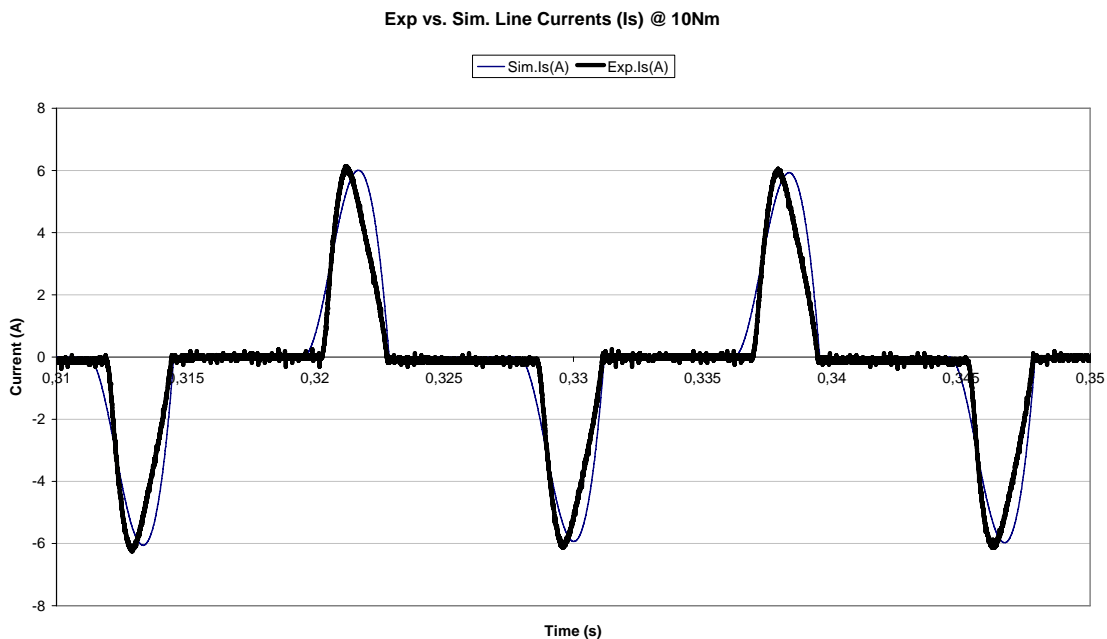


Fig. 8.10. Input current of the single phase diode rectifier at 10 N·m of load torque.

Fig. 8.10 represents the input currents (simulation and experiment) of the single phase diode rectifier fed by input voltage source from the wall plug. It is captured using a LeCroy Digital Oscilloscope at 10 N·m of load torque when the motor runs at 100 rpm. The experimental input currents in Figs. 8.10 and 8.11 are identical, but the currents

shown in Fig. 8.10 are exported from SIMPLORER[®] and from the LeCroy DSO to Microsoft[®] Excel for a better comparison of the simulated and experimental input currents.

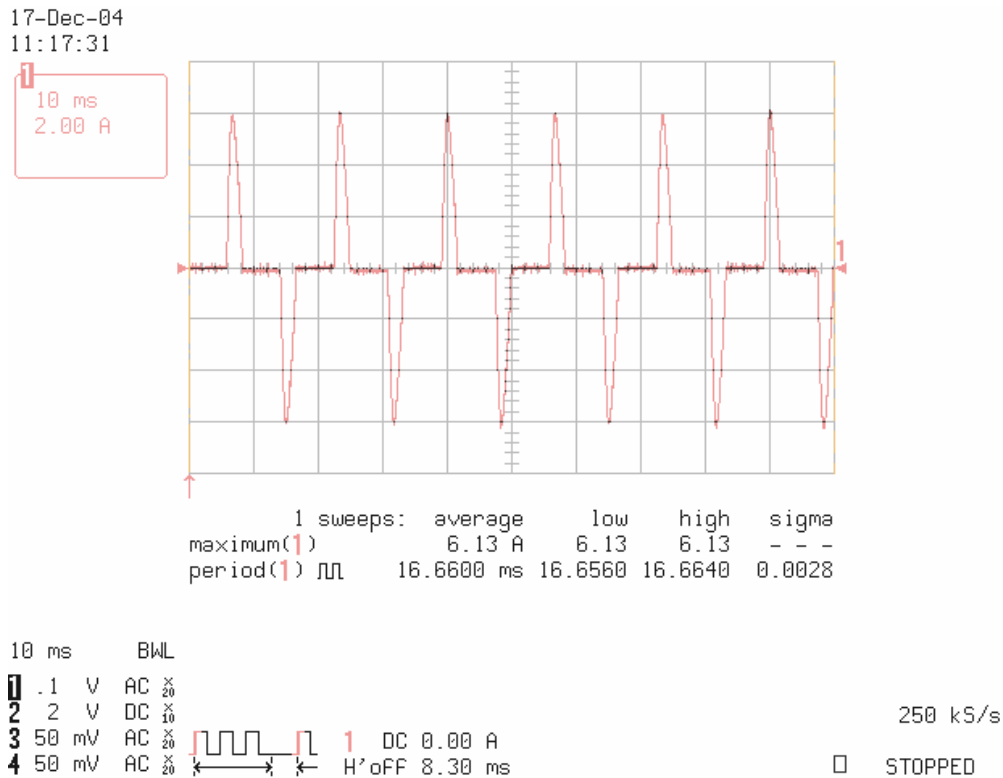


Fig. 8.11. Input current to the single phase diode rectifier (experiment) at 10 N·m of load torque (100 rpm).

The voltage source feeding the single phase diode rectifier is obtained from the wall plug which is measured as 122.1 Vrms. This value is used in the simulations as shown in Fig. 8.12.

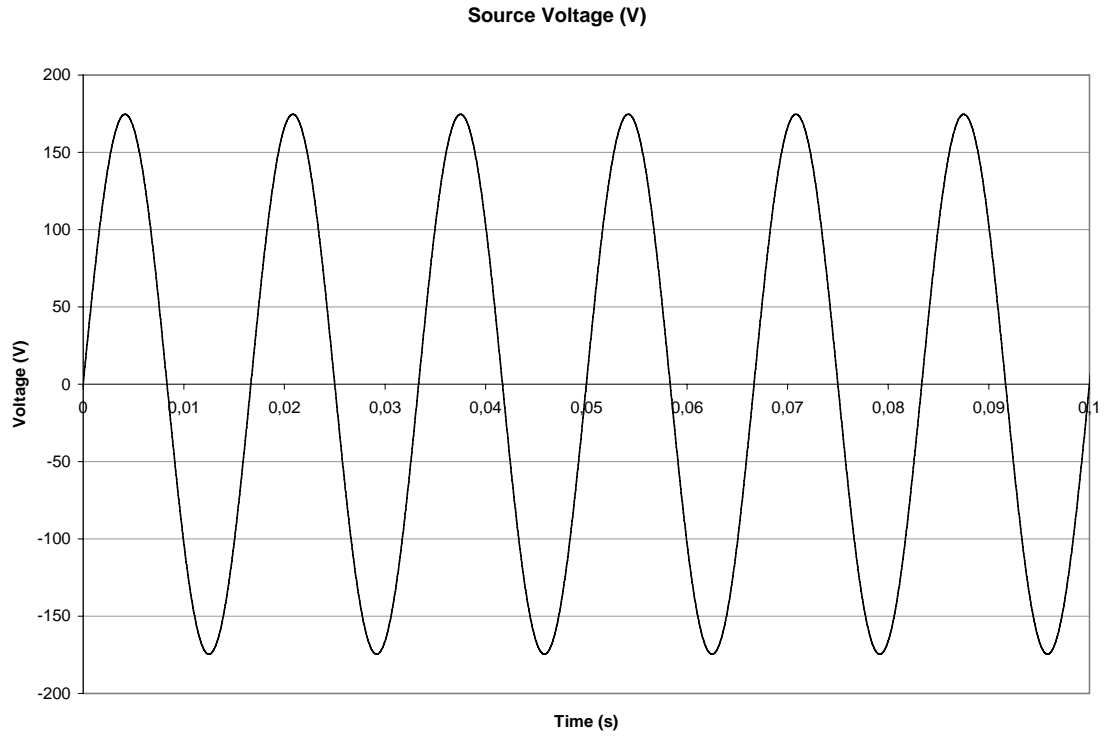


Fig. 8.12. Voltage source obtained from the wall plug.

Fig. 8.13 shows the DC-link voltage of the three-phase inverter when the 122.1 Vrms sinusoidal input voltage is applied to the single phase diode rectifier.

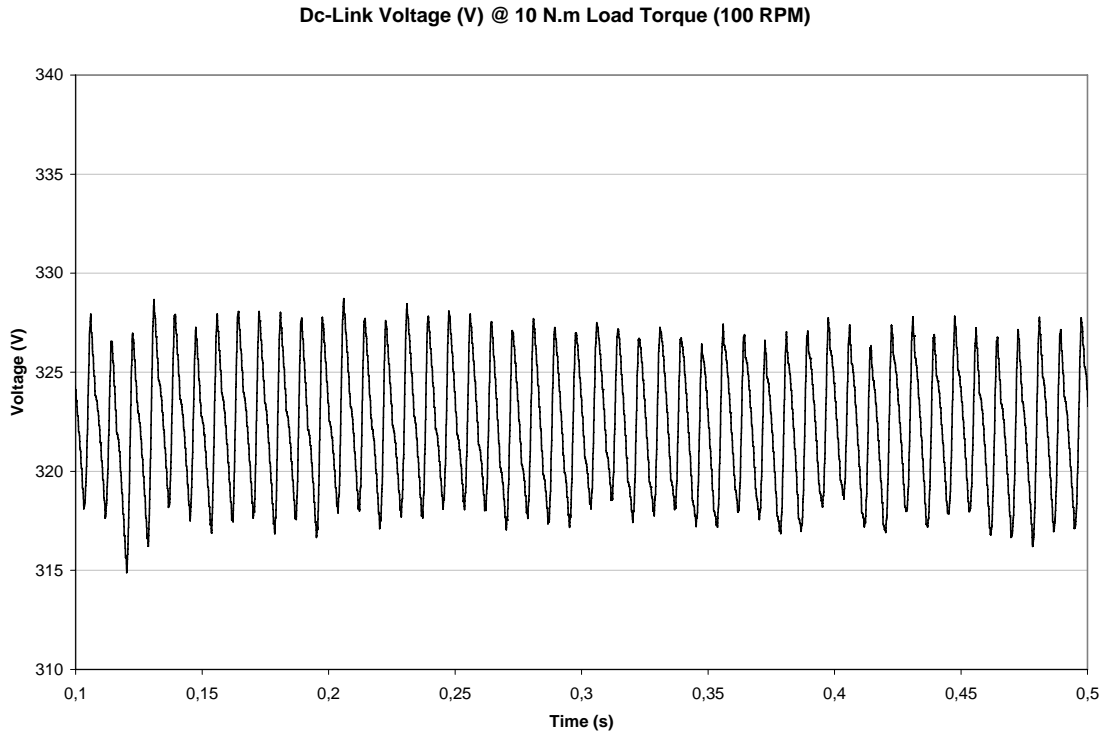


Fig. 8.13. DC-link voltage of the VSI at 10 N·m of load torque (100 rpm).

Fig. 8.14. indicates the simulated steady-state speed and experimental speed at 10 N·m of load torque. It can be seen that the speed responses are very similar. Due to the large sampling time provided by the dynamometer controller, (0.1 second in the curve test; more detail about curve testing will be discussed later in this chapter) the real-time speed fluctuates more than the simulated one. Additionally, the dynamometer has a 60-bit encoder inside which only has a resolution of 0.5 rpm for the speed calculation. For example, if the actual speed is 100.3 rpm, the dynamometer velocity sensor rounds it up to 100.5 rpm, therefore the real-time speed observed is almost constant all the time except when there is a step change in the speed that is greater than 0.5 rpm. On the other hand the simulation speed result has a higher resolution so it shows more speed ripples.

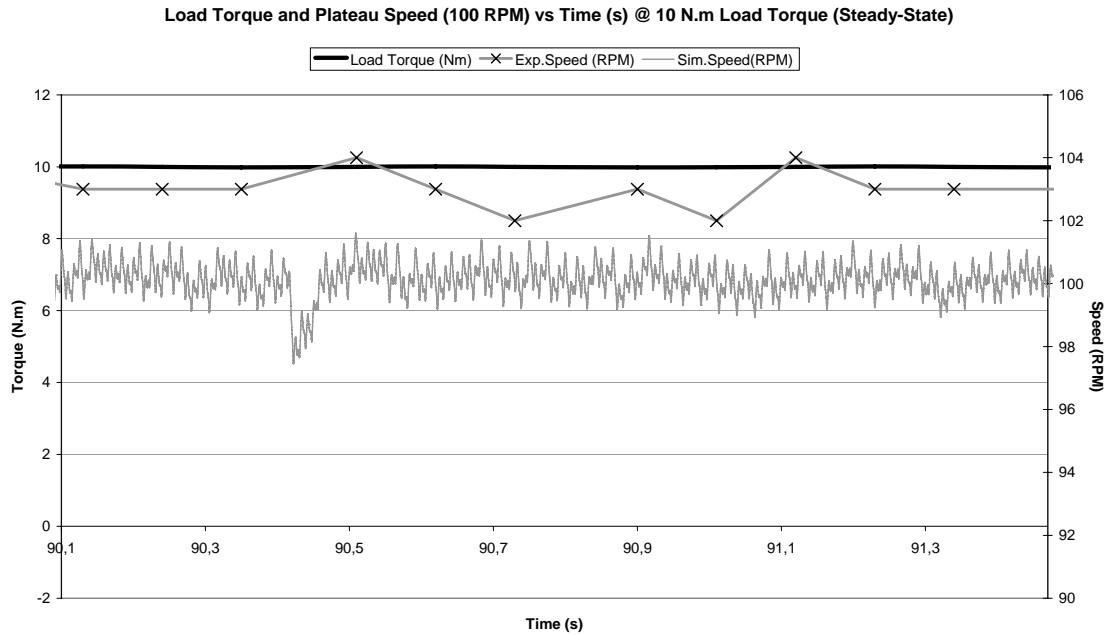


Fig. 8.14. Steady-state load torque and plateau speeds (experiment and simulation) at 10 N·m of load torque (100 rpm).

The motor is assumed to be rotating at a constant speed, which is chosen as 100 rpm in our test, therefore in steady-state simulation, the transient is ignored by setting the initial motor speed to 100 rpm in the motor parameters part of the SIMPLORER[®] built-in PMSM model. The reason that 100 rpm is chosen is because it is the average agitation control steady-state speed used in many commercial top-loaded washing machine drives; therefore in all simulations 100 rpm is chosen as a reference speed value.

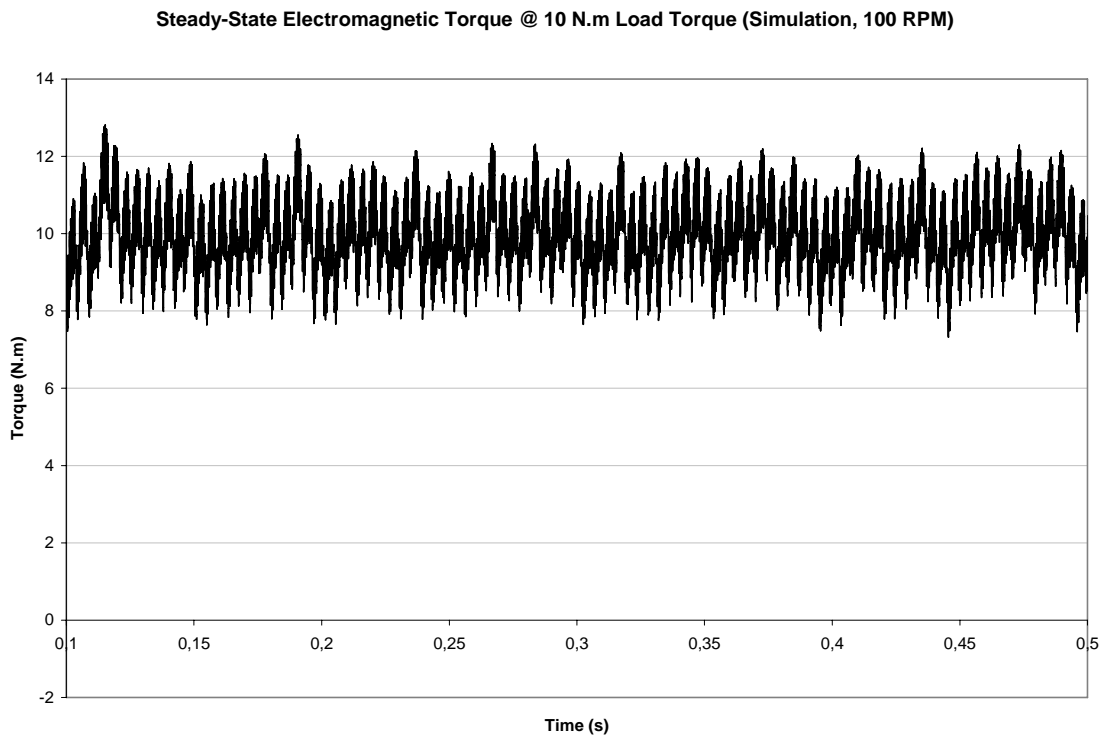


Fig. 8.15. Steady-state electromagnetic torque (simulation) at 10 N·m of load torque (100 rpm).

In steady-state, the electromagnetic torque produced by the motor is obtained as shown in Fig. 8.15. If other effective torque components are ignored in the electromagnetic torque equation of the motor, such as viscous damping coefficients and etc., then the average torque is almost equal to the load torque, which is 10 N·m in this case. When the time scale of Fig. 8.15 is increased, the resultant torque has excessive pulsation mainly due to the shape of the excitation currents and the back-EMF waveform of the motor. Since this motor has a sinusoidal back-EMF, if the excitation is provided with square wave currents then the multiplication of these signals, which is the resultant electromagnetic torque, will generate more torque pulsation than that of the sinusoidal current excitation. If less torque pulsation is desired then it is better to energize this motor with sinusoidal currents. That is why sinusoidal excitation under the DTC scheme

is proposed in Chapter VI. The results of the proposed method are given in Section 8.2.2 of this chapter and those results are discussed.

Overall efficiency is obtained in a way that input power is calculated (in simulation) from the input single phase supply source and the output power is calculated (in simulation) from the known electromagnetic torque of the motor as illustrated in Fig. 8.16. Obtaining the overall efficiency for real-time is performed by using several pieces of equipment such as the Magtrol power analyzer model 6530, the dynamometer controller model DSP 6000, and the hysteresis dynamometer model HD-800-6N.

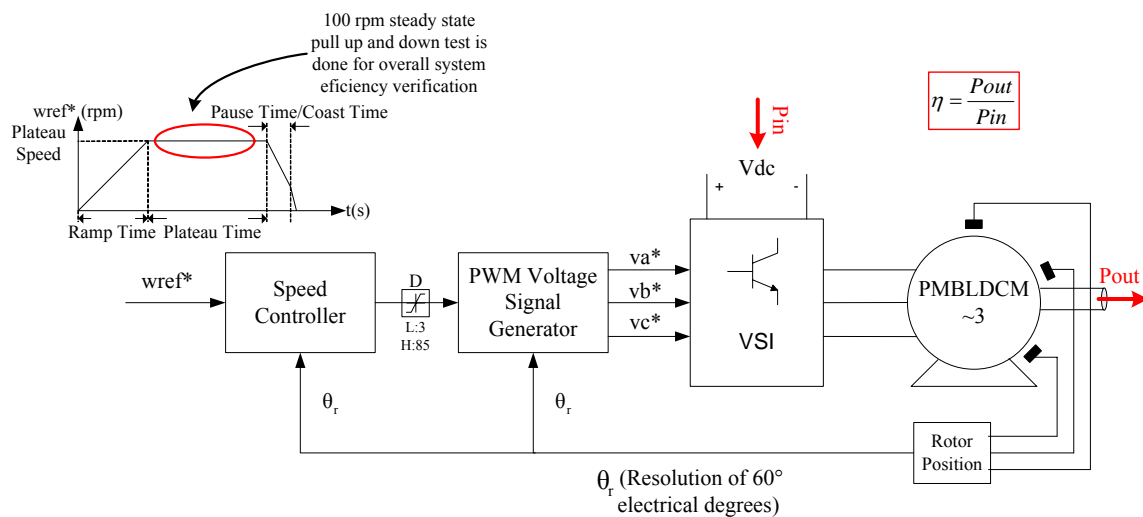


Fig. 8.16. Block diagram of the overall commercialized agitation washer control with the trapezoidal voltage waveform and efficiency calculation and measurement.

Experimental and simulated three phase excitation currents are shown in Figs. 8.17 and 8.18, respectively. The simulated three phase square wave motor currents resemble the experimental currents and their amplitudes are quite similar to each other. This validates the preciseness of the simulated model when compared with the real control system.

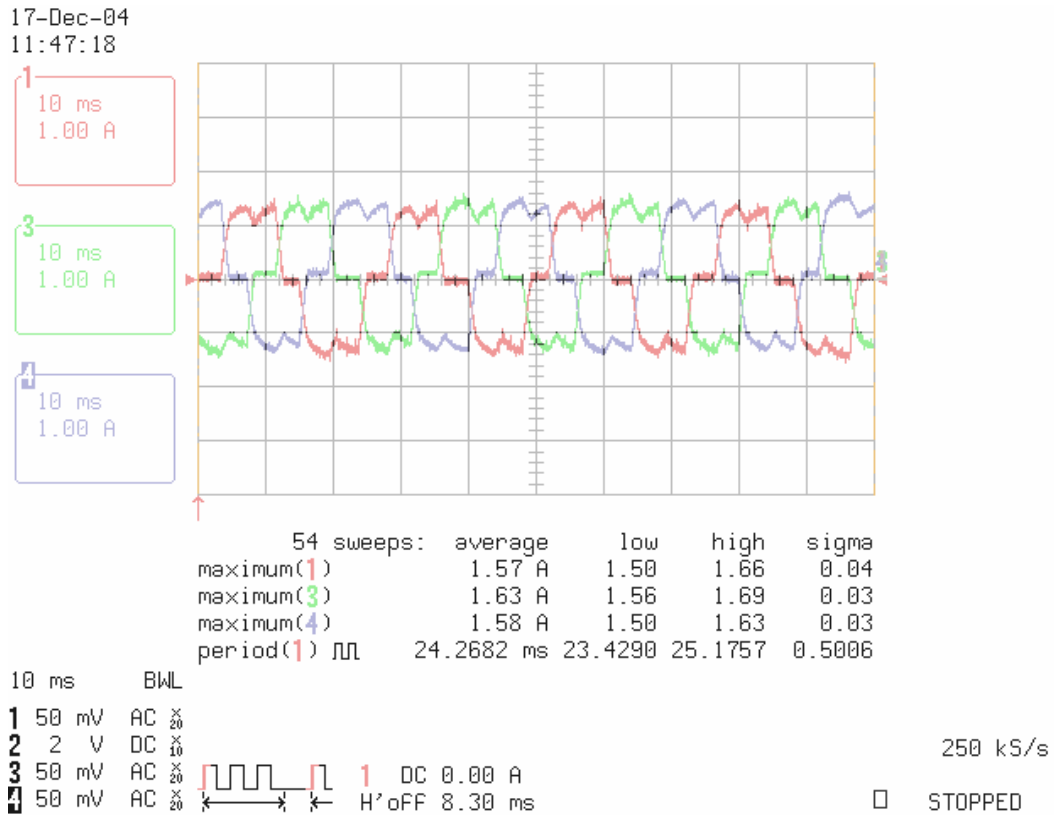


Fig. 8.17. Experimental three-phase motor phase currents at 10 N·m of load torque (100 rpm).

Fig 8.19 shows a comparison of the simulation and experimental results of the efficiency and power factor in a commercialized overall agitation speed controller. As expected, the power factor and efficiency of the simulation are greater than the experimental results.

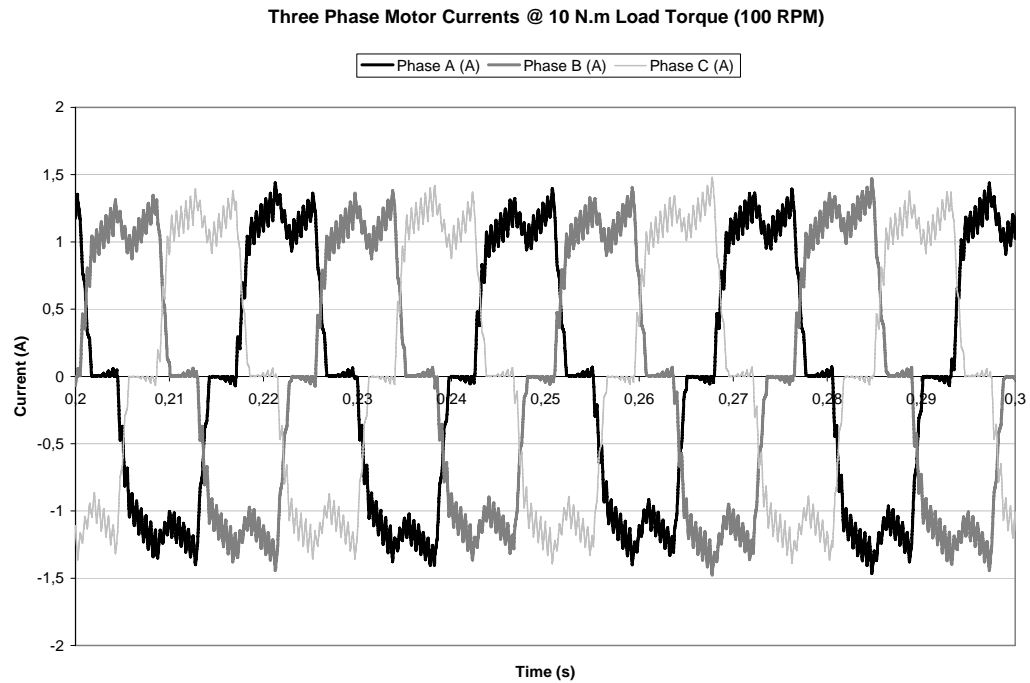


Fig. 8.18. Simulated three-phase motor currents at 10 N·m of load torque (100 rpm).

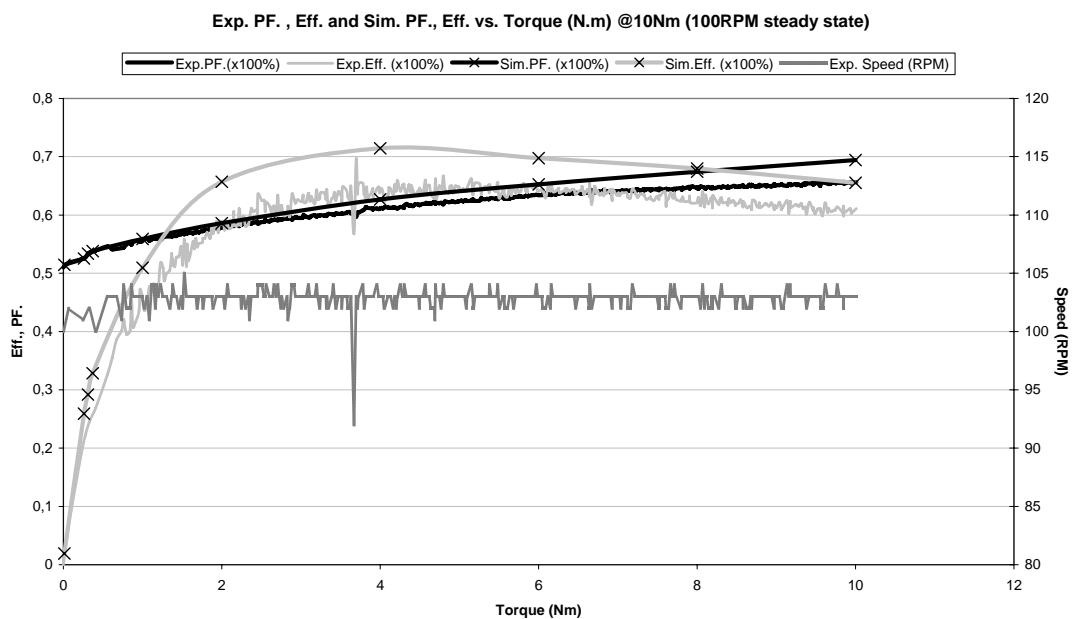


Fig. 8.19. Exp. PF., eff., and sim. PF., eff. vs. torque at 10 N·m (100 rpm).

Second, to compare with the experimental transient results, a transient model (ramp up) is built again in SIMPLORER[®] and added to the steady state model such that complete agitation model is achieved. A simplified block diagram of the overall commercialized agitation washer control is displayed in Fig. 8.20. The speed controller block, shown in Fig. 8.20, is not the typical PI or PID type compensator. It acts as a P controller or what you might call a hysteresis controller. Speed regulation is achieved by the help of three hall-effect sensors. The time difference between two consecutive hall-effect signals is the key of speed sensing in this simple agitation speed controller. Depending on the difference in the measured speed (in some sense the estimated speed) and the reference speed, the PWM duty cycle value is adjusted (either increased or decreased) accordingly, but it is kept lower than the maximum allowable PWM value, PWM_{max} , by using saturation block as shown in Fig. 8.20. This scenario would occur mainly during the steady-state region. In the event of ramping, in this case from zero speed till steady-state speed, (plateau speed) the PWM duty cycle value (starting from a certain value such that under light load the motor can start up easily) is constantly increased until ramp time is over. At that moment the motor speed is measured for the first time and it will be continuously checked as long as the plateau region is active. The speed is checked through the end of the stroke time until the beginning of the next stroke.

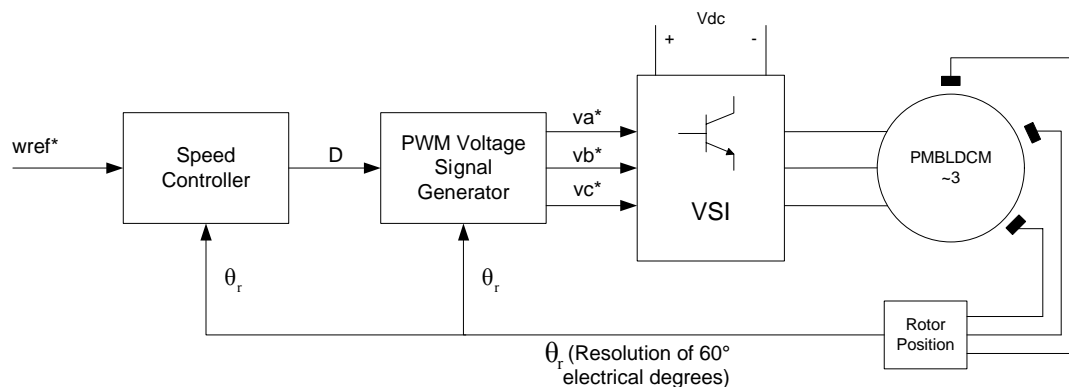


Fig. 8.20. Block diagram of the overall commercialized agitation washer control with trapezoidal voltage waveform.

8.2.2. Complete Agitation Speed Control Analysis (Transient and Steady-States)

Calculations of some electrical parameters of the control system, such as power factor and overall efficiency, are done by using the steady-state model. To implement the agitation algorithm in SIMPLORER[®], a ‘state graph’ method is considered to be very suitable for the simple logical based agitation algorithm. State graphs are used in conjunction with transition state blocks which determine whether the state should active or inactive depending on the logic of the transition blocks. Efficiency and power factor calculations are performed in two different ways and same results are obtained. First, SIMPLORER[®]'s own rms and mean value measurement blocks are used to calculate the efficiency and power factor in a similar manner to the open-loop MATLAB/SIMULINK[®] model. The second way of obtaining those parameters is by using SIMPLORER[®]'s DAY Post Processor. After the simulation is run and finished, in the DAY Post Processor's main menu, when the <<Power>> option is selected in SIMULATION>Analysis then the active power, apparent power, reactive power, power factor, Total Harmonic Distortion (THD), and FFT of the selected currents or voltages can be gathered. By knowing the active power of the input signal and output power of the motor, efficiency can be easily calculated.

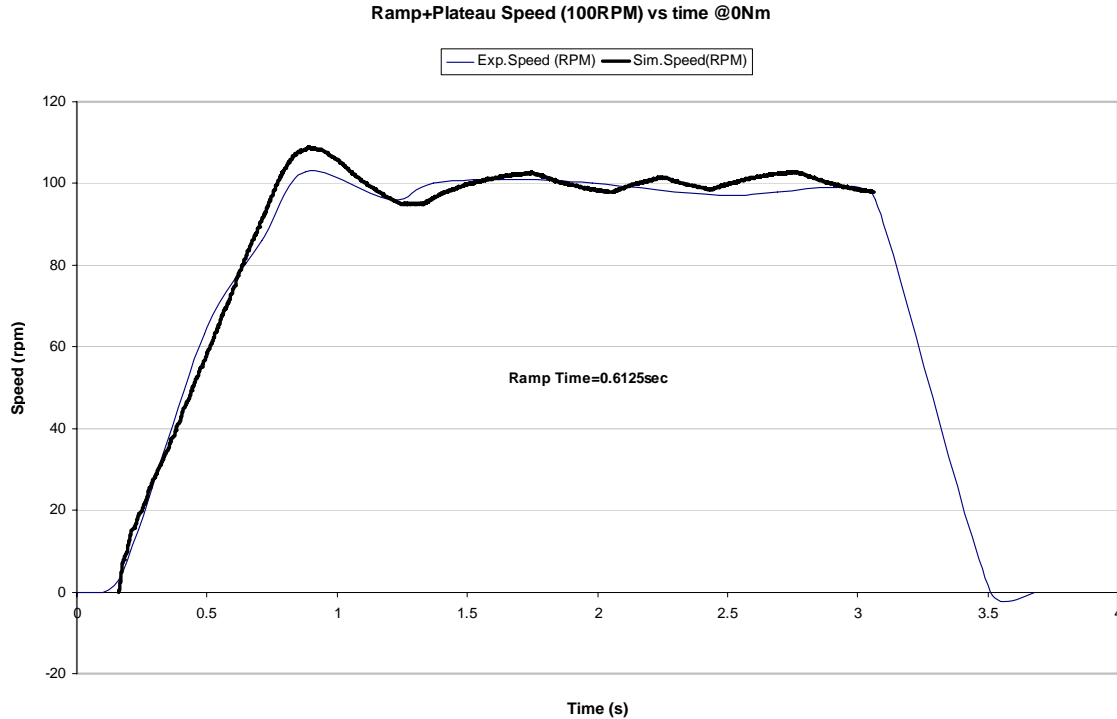


Fig. 8.21. Experimental and simulation speed response (transient and steady-state) at no-load.

The transient and steady state performance are illustrated in Figs. 8.21 through 24. Those figures display the simulation and experimental ramp up and steady state conditions at the 100 rpm plateau speed under no-load with a 612.5 ms ramp time, under no-load with a 700 ms ramp time and at under 5 N·m of load torque with a 200 ms ramp time, respectively. The simulation and experimental results are plotted in one xy-axis to compare and validate the results easily. The results which were obtained from the simulation closely resemble the speed response of the experimental tests. Since the speed control is sluggish, the results are not satisfied. The transient speed response of the simulations at no-load generate a slightly larger overshoot and settling time as compared with the experimental ones. The reason for this could be the neglect of some side effects in the simulation model, such as windage torque, friction on couplings, the dynamometer's inertia, etc. These problems were not observed when the motor was initially loaded and ran at 5 N·m, as shown in Fig. 8.22. The main reason of not

observing the oscillation effect on the speed result when 5 N·m load torque was applied is that 5 N·m of load torque is much larger than the other effective torques, such as windage torque and friction. On every occasion once the transient state passes, the steady state results are observed to be much closer to the experiments.

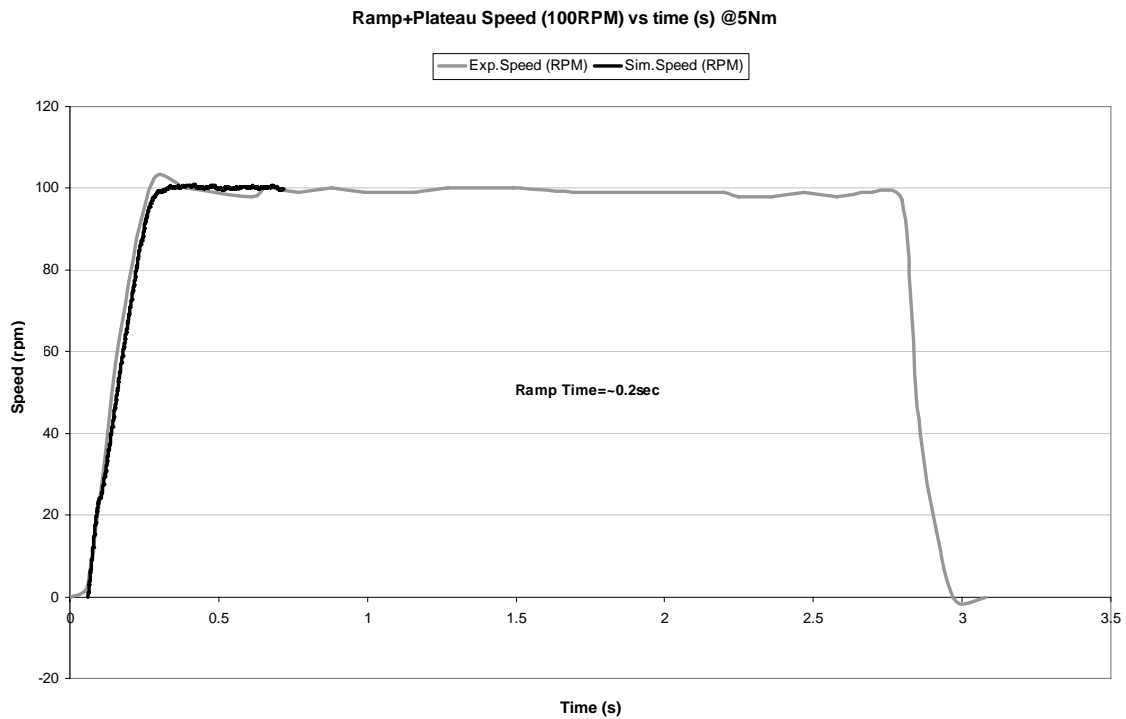


Fig. 8.22. Experimental and simulation speed response (transient and steady-state) at 5 N·m of load torque.

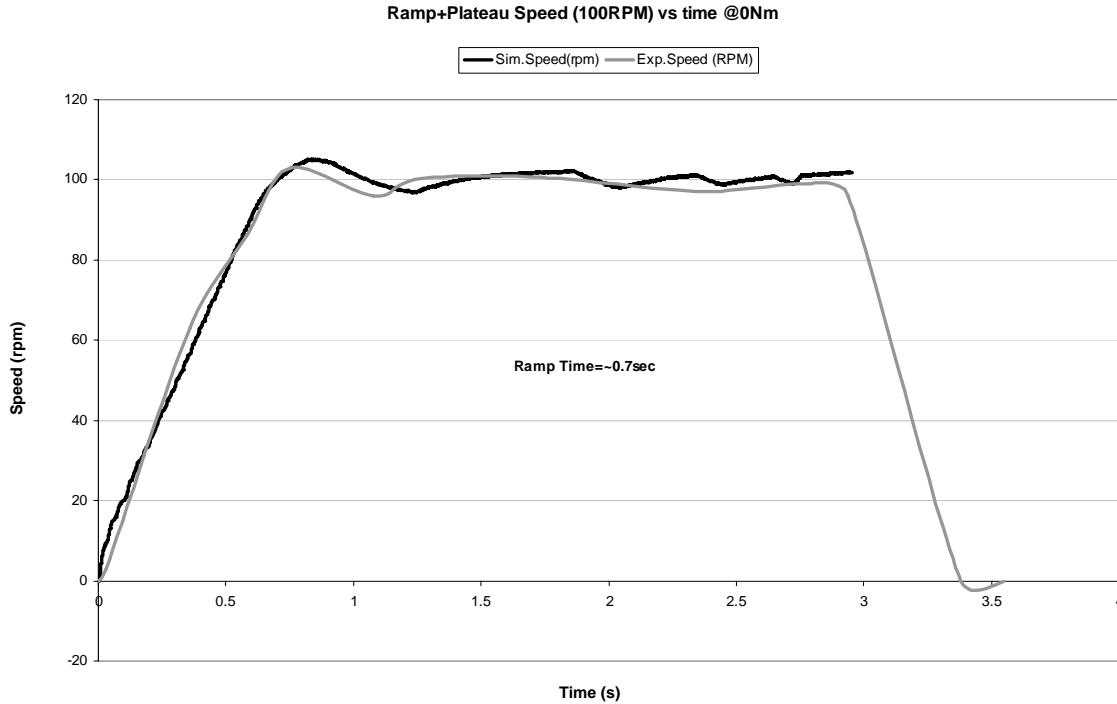


Fig. 8.23. Experimental and simulation speed response (transient and steady-state) at no-load (0.7 second ramp time).

Fig. 8.24 shows the simulation of the rotor position from the beginning of the transient state when the ramp time is chosen as 660 ms and the plateau speed as 100 rpm under no-load. It can be seen that when the time and rotor speed increases the sawtooth periods become more narrow until the steady-state is reached at 0.66 second shown in Fig. 8.24. Once the steady-state speed is achieved, as seen in Figs. 8.21 through 8.23, then the sawtooth periods become more identical which means that the speed of the rotor is constant.

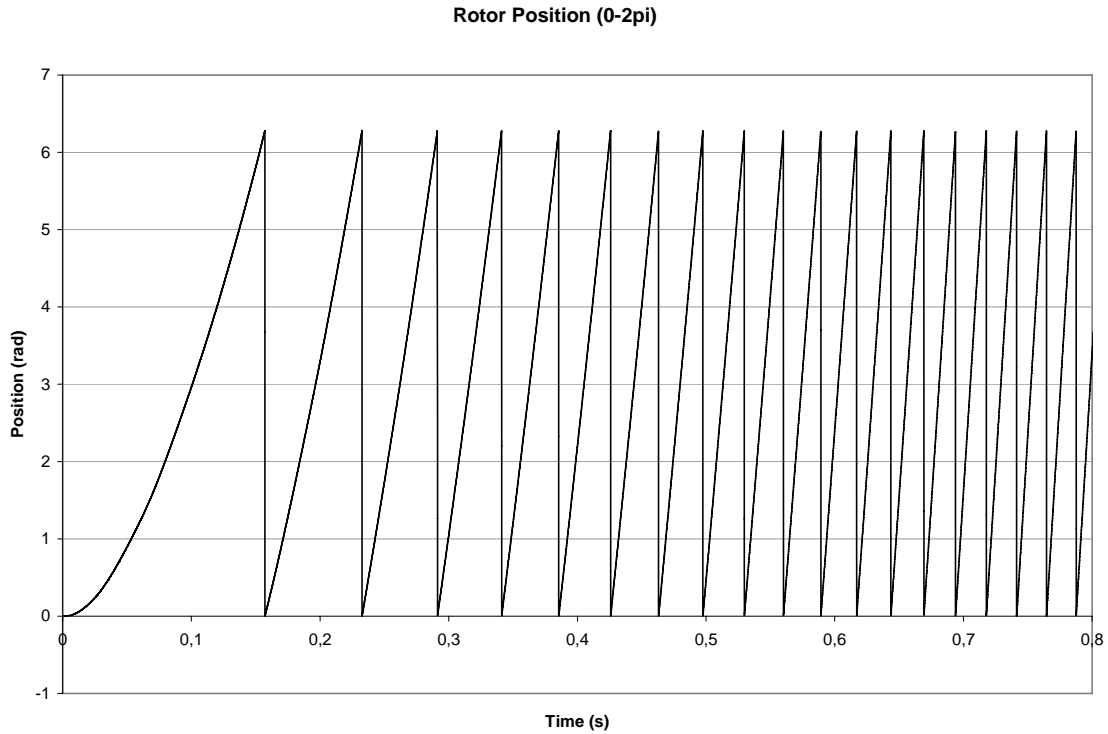


Fig. 8.24. Rotor position obtained in simulation.

Figs. 8.25 and 8.26 indicate the steady-state and the combined transient - steady-state SIMPLORER[®] models of the commercialized agitation washer controller, respectively.

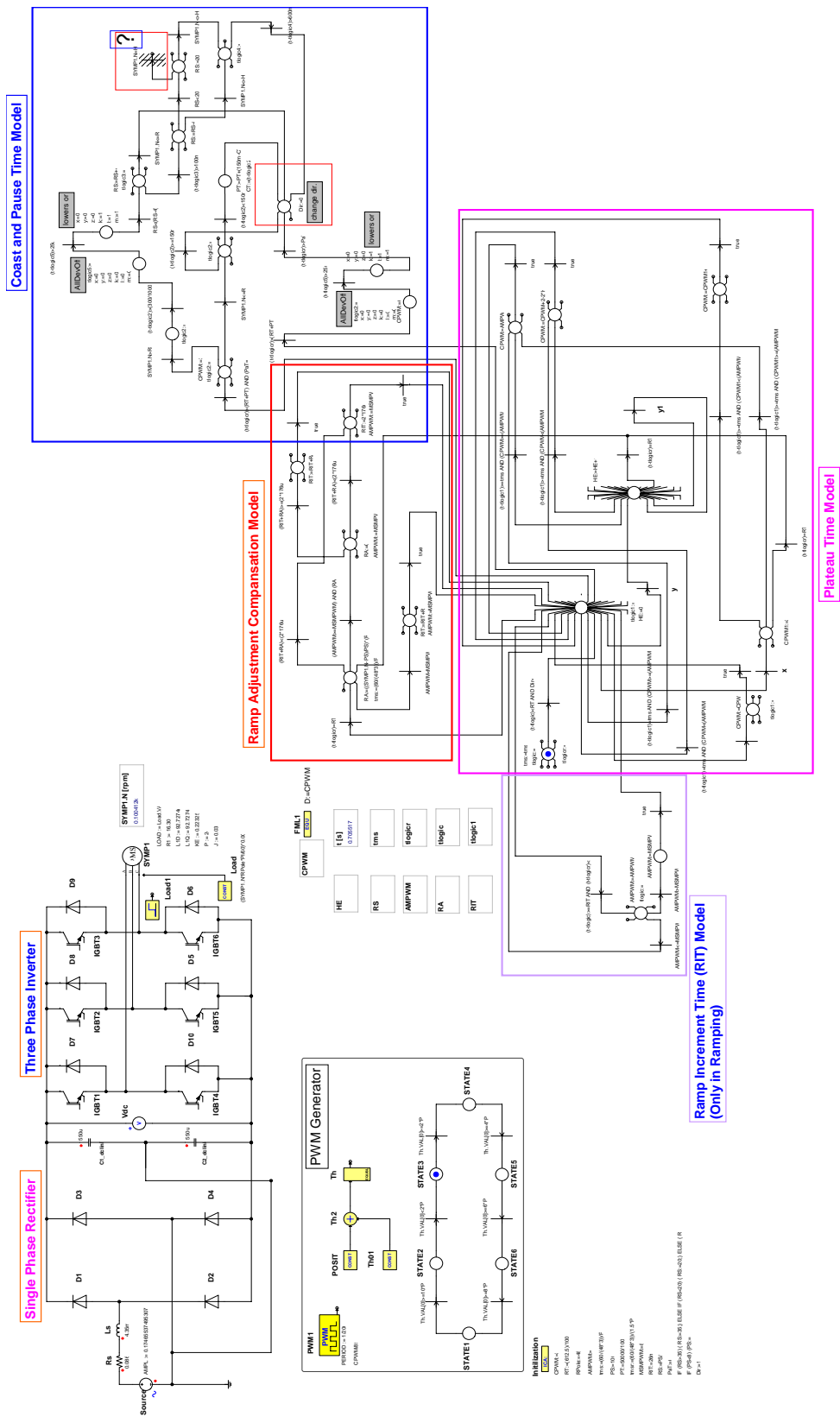


Fig. 8.26. SIMPLORER® model of commercialized overall agitation speed control system (transient+steady-state).



Fig. 8.27. Agitation speed control test-bed.

Fig. 8.27 shows the complete experimental setup including pancake motor, hysteresis dynamometer, power analyzer, dynamometer controller and microcontroller used for agitation speed control tests.

8.2.3. Simulation Results of the Proposed DTC Method Used in Agitation Cycle Speed Control

The proposed DTC scheme is simulated to validate its superiority over the commercialized simple agitation speed control of a laundry washing machine. Several simulation results are obtained and discussed. These include: real and estimated rotor position, stator, transient and steady-state speed response under 7 N·m of initial load to 10 N·m of load torque during the acceleration period, stator flux linkage trajectories,

amplitude of the stator flux linkage, amplitude of the electromagnetic torque, three phase motor currents and voltages, and errors in the real and estimated positions.

Although the commercialized simple agitation speed controller simulation is built and tested in SIMPLORER[®], to validate the proposed speed control the complete proposed DTC scheme has been implemented in MATLAB/SIMULINK[®]. The reason for using MATLAB/SIMULINK[®] is because of the edge of flexibility, speed, superiority in control and diversity in system tools and components over SIMPLORER[®]. The simulations presented in this section are the results of the proposed DTC algorithm as discussed in Chapter VI. The operating points of the motor speed and load torque are chosen as 100 rpm steady-state plateau speed, and a 7 N·m to 10 N·m ramp up load characteristic used during the acceleration period, respectively. The 7 N·m to 10 N·m load behavior represents the heavy loads for a washing machine. A similar test can be done for medium and light loads also. One might consider the Light Load range as being 0 N·m-4 N·m, the Medium Load range as 4 N·m-7 N·m, and the Heavy Load range as 7 N·m-10 N·m or up. Depending on the size of the washing machine, these values can be modified. In the proposed DTC scheme, the ramp up time period is set to 0.35 second, the plateau region starts from 0.35 second and ends at 1 second and the coast time starts at 1 second and continues till 1.25 seconds. These values are changeable depending on the washing profile. You might agree that when the delicate washing cycle is preferred, then longer ramp up, plateau region and coast times are chosen. For rough washing those times should be shorter. All parameters are assumed to be known exactly and no parameter change effect is added to the simulations. The sampling time of the overall control system is chosen as 25 μs and the hysteresis bandwidths are 0.005 for torque control and 0.001 for flux control. Decreasing the sampling time and narrowing the bandwidths of the hysteresis controllers may mitigate the torque, flux and current ripples which are common issues of the conventional DTC scheme. The stator flux path will also become more circular, but the effect of these variations are not included in this thesis, only a constant sampling time and constant hysteresis bands are assumed in all simulations.

The conventional DTC scheme is simulated again in MATLAB/SIMULINK[®] to compare to the proposed method when the conventional scheme has some discrepancies in stator flux estimation due to stator resistance variations caused by low speed and/or high temperature, offset errors in voltage and currents sensing generating drift in the back-EMF integration because of the wrong initial flux values and/or measurement errors in voltage and currents.

The stator resistance change effect will be simulated and compared. The resistance value will be intentionally altered during the ramp up and at steady state to observe the effect of change on speed and torque response. The amount of deviation might occur in the stator flux linkage trajectory will also be noted when the change in resistance affects the speed and torque response. At high load and high temperature, the resistance may change in the range of 1.3 to 1.75 times of its nominal value. In the simulations of the conventional DTC of PMSM, the stator resistance value will be changed to 1.5 times of its nominal value during ramp up and at steady state, especially under transient loads such as a 7 N·m to 10 N·m incremental load characteristic which is proportional to speed during the transient state. The drift effect will also be performed by applying a constant DC value to the measurement of the voltages and currents. Additionally, the simulation of the initial flux linkage error will be carried out. The results of those simulations are given in this section and are discussed.

Since the load torque cannot be known initially unless a weight measurement system is used in the washing machine, starting the motor with a preferred ramp rate rather than a step speed profile will be a huge turning point in the proposed DTC scheme. To solve the starting problem, one method which looks at the washing load capacity chosen by customer, and estimates the load torque so that smoother starting can be achieved. The method uses the load information to adjust the initial integral value of the PI controller. In our tests, load torque (heavy load) value in real washing machine increases from 7 N·m (assumed initial load on the machine) to 10 N·m during the ramp up period (load torque is proportional to the speed) and settles to 10 N·m during the steady state. The plateau speed is selected as 100 rpm. Since there is a constant initial

torque, T_{em_0} , due to ramp up, this can be used in the integrator (PI) as: $J_{eq} * (100 * 2 * \pi / 60 * P / 2) / 0.35$ if the inertia (J_{eq}) of the overall system is roughly known, therefore the final value of the initial integrator value, ($T_{em_0} + 8.5$), will be the initial torque, in which 8.5 is an example of the estimated initial load torque by looking at the customer's choice of load capacity of the laundry cloths. There will be no position or speed information from the system start up till the first hall-effect sensor information is read. From this point till the end of ramp time the estimated speed and the reference speed will be subtracted from each other as given by:

$$\omega_{ref} - \omega_{est} > 40 \text{ rad/s}$$

If the value of this subtraction is higher than a predetermined value like 40 rad/s then at the next stroke the initial integrator value of the PI controller will be decreased by a reasonable amount. In these tests, 1 N·m is used to be as close to the initial load torque value (7 N·m is used in the tests) as possible and to minimize the oscillations in speed and to get more smooth starting. These constant values are based on the ramp up rate, how fast and smooth the speed profile is desired to be, etc. Since there is no rotor position or any other sensor information used until the first hall-effect sensor signal the system starts in open-loop. Regular open-loop starting requires PWM voltage generation to speed up the motor at a predetermined frequency range or closed-loop starting with BLDC type of quasi square current control, however, this method does not need a PWM block to start the motor appropriately without any oscillation. This will eliminate the disadvantage of using extra code in the proposed control. This is quite beneficial for the industrial applications such that microcontrollers with less memory can be used.

The simulation results show that the acceleration which is used in the speed estimation during the complete transient state (ramp up) and in the steady-state degrades the performance of the speed control. Therefore, the speed estimation information including the acceleration is obtained only at starting before the rotor position completes the full cycle. Acceleration due to the ramp rate is never ignored in the speed and position estimations. For example, when the initial rotor flux linkage is located in the Sector 1 the following procedures are conducted to estimate the speed:

- In Sector 1 ($11\pi/6-\pi/6$), in Sector 2 ($\pi/6-\pi/2$), and in Sector 3 ($\pi/2-5\pi/6$) acceleration is included in the speed estimation algorithm. This is done to sense the actual acceleration of the motor more precisely during the transient state to find a better initial integrator value for PI controller.
- The coast region is simulated without any acceleration in speed which provided a better speed response than when the acceleration was included to the speed estimation (acceleration information is still used for position estimation).

At the start up, the rotor flux linkage which might be located in other sectors rather than the first sector the rotor speed can be obtained in a similar manner such that the acceleration is included in the speed estimation in only three consecutive sectors. For the other hall-effect sensor position ranges, the average speed information is preferred rather than the one with the acceleration and better results are obtained. If a load disturbance occurs at any point between the two hall-effect sensor signals, the rate of change of speed will be assumed very wrong looking at the previous acceleration information for estimating the speed. It has been observed that the proportional coefficient value should be chosen very low so instability will not occur during the ramp up. To overcome these problems, the acceleration information is only used in the estimation at the very beginning of the start up. The acceleration information is required during transient (ramp up) because the initial ramp rate has to be used in the speed estimation to determine the speed estimation error when the first few hall-effect sensors results are read. Once this is known, the initial PI integrator value can be modified starting from the very next agitation stroke for better starting.

8.2.3.1. Transient and Steady-State Response Under Load Condition

The torque characteristics of the PMSM when a 7 N·m to 10 N·m transient load torque is applied during the 0.35 second ramp up period are shown in Fig. 8.28. In the same figure the initial integrator value of the PI controller is chosen as 7 N·m with an additional ramp rate formula. Since there is an initial load on the machine due to the laundry, the motor should reach the same torque level to start up. If the initial torque value is small and tries to be incremented for a long time period then desired certain ramp rate can be deviated so that initial torque value should be as close as load torque value. As it can be seen from Fig. 8.28 the actual and estimated electromagnetic torque closely resemble the reference electromagnetic torque generated by PI controller (used for speed control). After 1 second the plateau region is over and the coast time starts. In this case the coast time is selected as 0.25 second. It can be observed that the transient electromagnetic torque during the ramp time is tracking the load torque quite well. During the steady state, a very pure and constant torque response is achieved. After the plateau region is over (steady-state), the coast time starts (0.25 second long). During the coast region, the motor tries to reach zero speed at 0.25 second. Because less attention is put on the coast time control, the torque response is imperfect but reasonable.

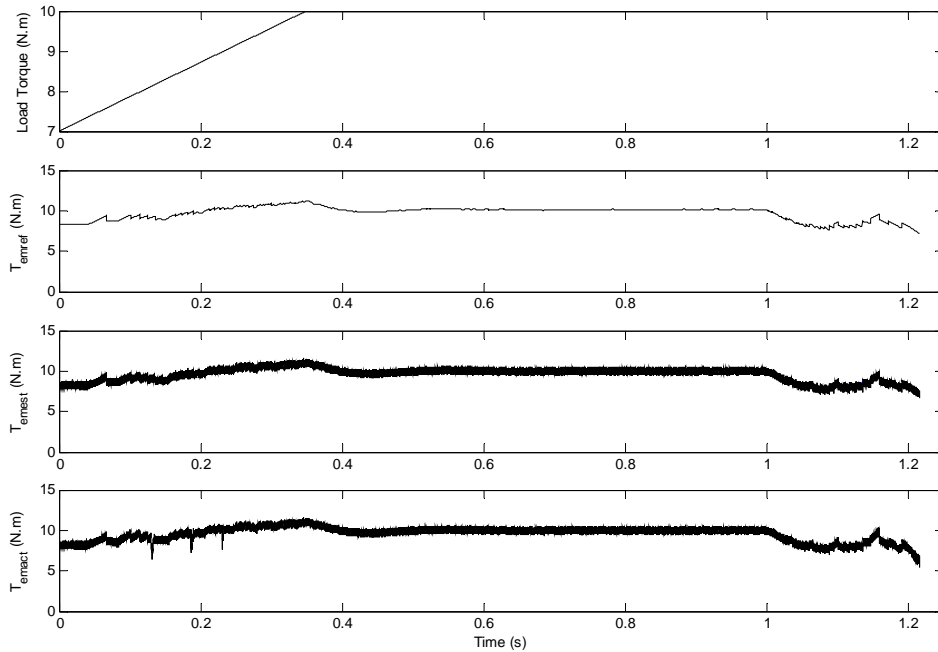


Fig. 8.28. Load torque (T_L), T_{emref} , T_{emest} , and T_{emact} at a 0.35 second ramp time when the PI integrator initial value is 7 N·m.

Fig. 8.29 shows the stator flux linkage reference value, λ_s^* , (0.223256 Wb which is equal to the rotor flux linkage amplitude) estimated stator flux linkage, λ_{s_est} , and actual stator flux linkage, λ_{s_act} , respectively at a 0.35 second ramp up time when the initial integrator value of the PI controller is selected as 7 N·m. Three small pikes in the estimation of the stator flux amplitude are seen in Fig. 8.29 due to small dips that occurred in the actual torque around 0.2 second. At the end of the plateau time and starting from the middle of the coast time the actual stator flux amplitude deviates due to corrupted torque when less attention is put on the speed control during the coast time. On the other hand, the steady state stator flux linkage values (both estimated and actual) track the commanded value quite well. The λ_{sD} and λ_{sQ} circular trajectory is shown in Fig. 8.30. The three small spikes occurred in the stator flux linkage estimation can be also observed in the circular trajectory.

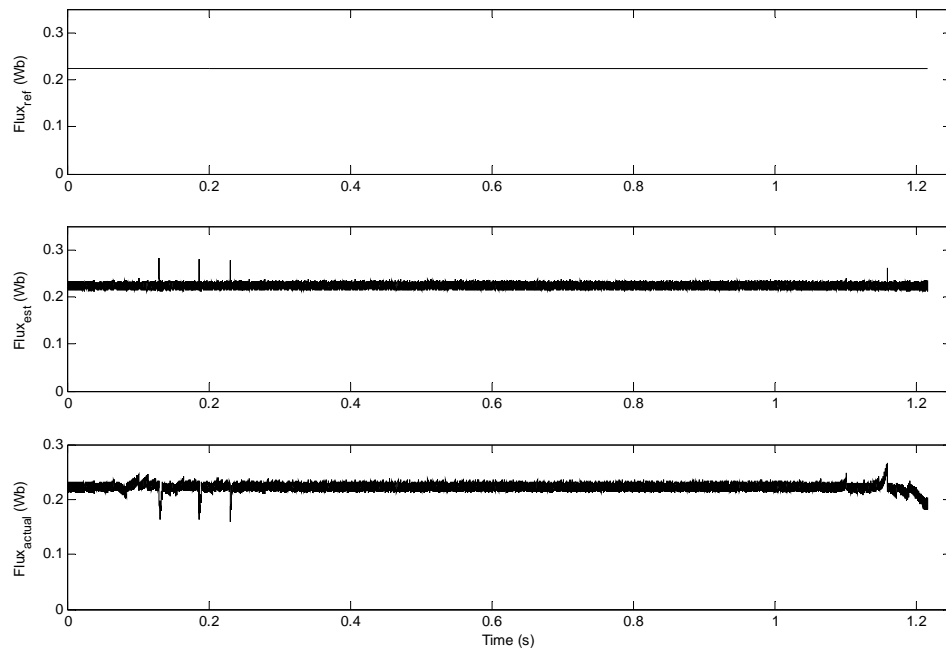


Fig. 8.29. λ_s^* (reference stator flux), λ_{s_est} and λ_{s_act} at a 0.35 second ramp time when the PI integrator initial value is 7 N·m.

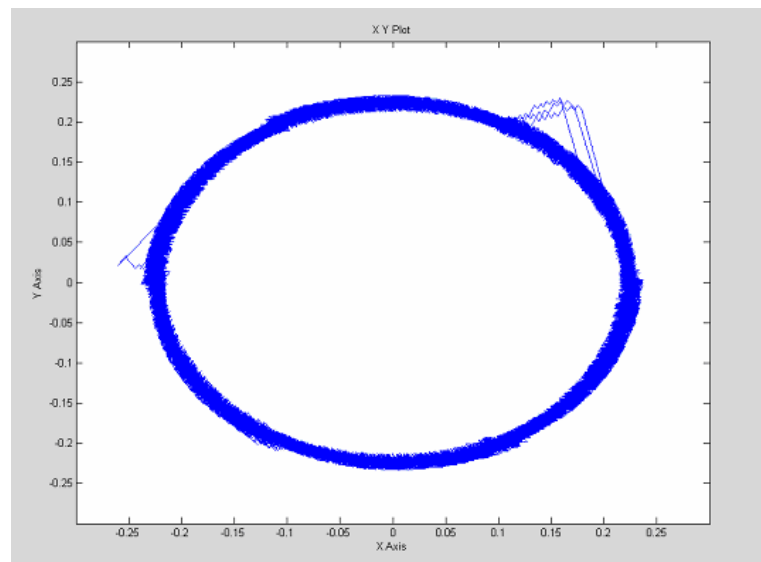


Fig. 8.30. λ_{sD} and λ_{sQ} circular trajectory at a 0.35 second ramp time when the PI integrator initial value is 7 N·m.

Almost the same behavior is observed when the initial integrator value of the PI controller is chosen as 8.5 N·m which is higher than the initial load torque value. The result of this is that in the beginning of the ramp up speed torque oscillations are inevitable, as shown in Fig. 8.31. In the same figure one third of the ramp up period torque drops from 10 N·m (8.5 N·m plus the initial ramp rate causes an almost 2 N·m initial torque) to around 7 N·m to level out with load torque value.

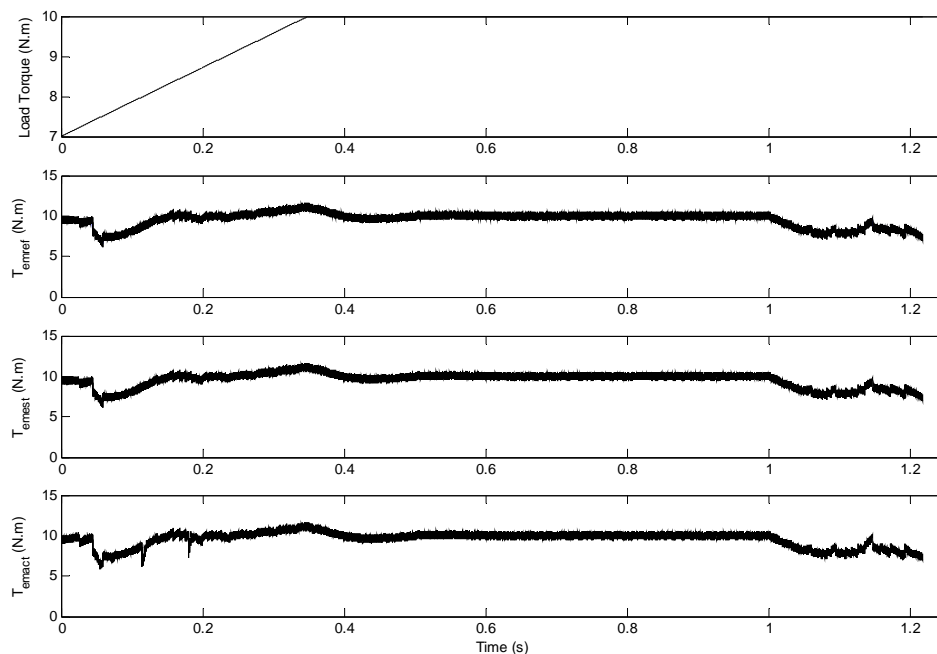


Fig. 8.31. Load torque (T_L), T_{emref} , T_{emest} , and T_{emact} at a 0.35 second ramp time when the PI integrator initial value is 8.5 N·m.

The stator flux linkage values are represented in Fig. 8.32 when the initial integrator value of the PI controller is 8.5 N·m. Due to the higher initial torque value over the load torque in first few milliseconds, the actual stator flux linkage is observed as higher than what is necessary. It converges to the reference value, however, less than 0.1 second later. That increase in the actual stator flux linkage causes two small pikes in the estimation of the stator flux linkage as can be seen in Fig. 8.32. After the torque converges to the reference value, the dips in the actual torque cause the stator flux

linkage to reflect the same behavior with two small dips in the ramp. Those two small dips generate two small pikes in the estimation of the stator flux linkage. Overall the stator flux linkage results are quite reasonable, especially at steady state. The λ_{sD} and λ_{sQ} circular trajectory is shown in Fig. 8.33. Five small pikes that occurred in stator flux linkage estimation can be also observed in the circular trajectory.

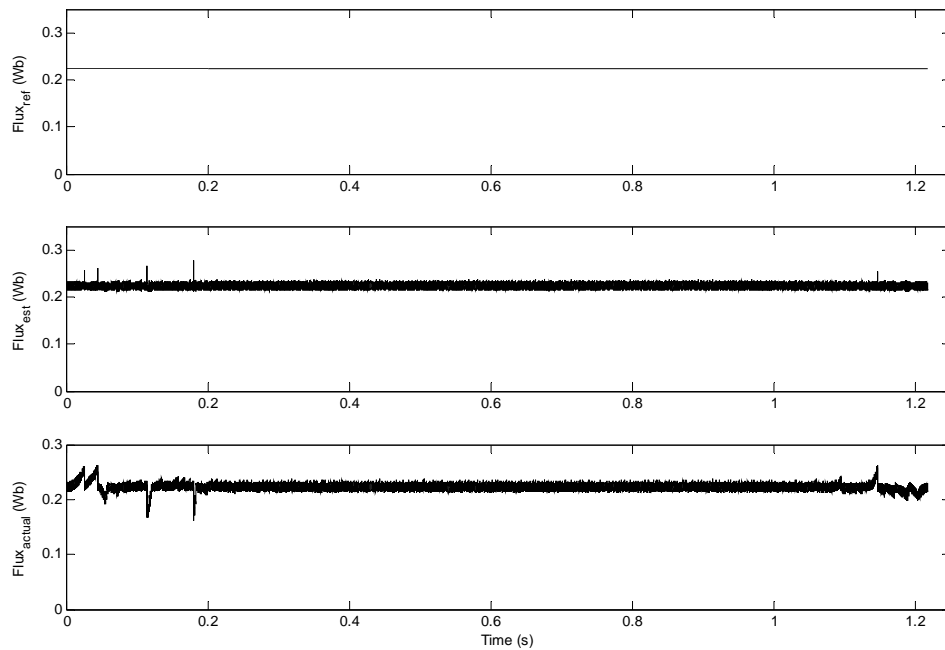


Fig. 8.32. λ_s^* (reference stator flux), λ_{s_est} and λ_{s_act} at a 0.35 second ramp time when the PI integrator initial value is 8.5 N·m.

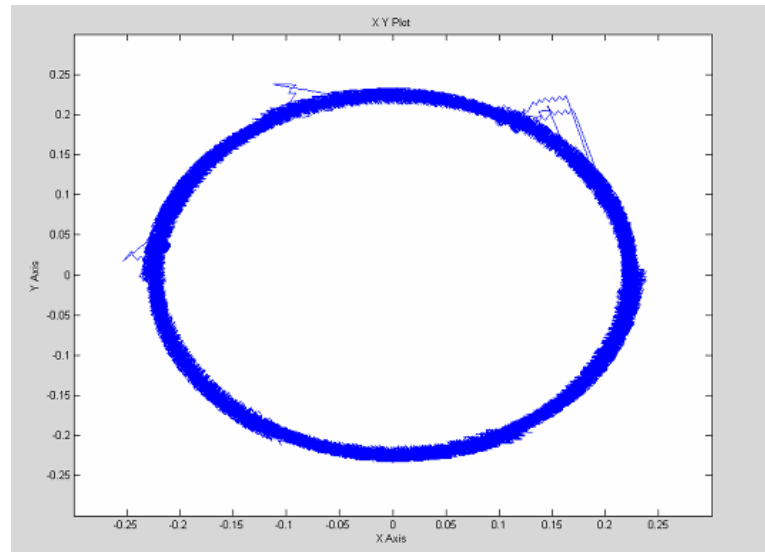


Fig. 8.33. λ_{sD} and λ_{sQ} circular trajectory at a 0.35 second ramp time when the PI integrator initial value is 8.5 N·m.

Figs. 8.34 and 8.35 illustrate the motor's Phase A, d and q axes currents in the rotor reference frame when initial integrator of the PI controller is 7 N·m and 8.5 N·m, respectively. In both cases, the q-axis current in rotor reference frame increases to reflect the load variation. The d-axis current remains close to zero so that the maximum torque/current ratio is achieved even in the dynamic response. The q-axis current wave outlines the wave of the Phase A current which shows that the d- and q-axes currents are decoupled just like in vector control. As a consequence, even though the DTC scheme does not directly control the currents (rotor frame d and q axes) when the topology is investigated in the rotor reference frame similarities with the vector control scheme can be observed.

The dynamic response of the d- and q-axes currents in the RRF and the Phase A current under a 7 N·m to 10 N·m transient load during the ramp up when the initial integrator value of the PI controller is chosen as 7 N·m are shown in Fig. 8.34. Three hall-effect sensors are used to assist the control algorithm for continuous rotor position estimation. With the gradual increase of speed, a smooth change in the stator current and the q-axis current in the RRF are observed during the dynamic state. Fig. 8.34 shows the

actual q-axis and d-axis currents in the rotor reference frame obtained by the encoder and the estimated currents from the position observer method assisted by the three hall-effect sensors. At steady state, the amplitude of the stator current is essentially unchanged.

During the steady state, the d-axis current stays close to zero during constant torque control. The q-axis current varies according to the load (it increases gradually with the load torque and remains constant when the load torque is constant). All the figures prove the validity of the proposed DTC method.

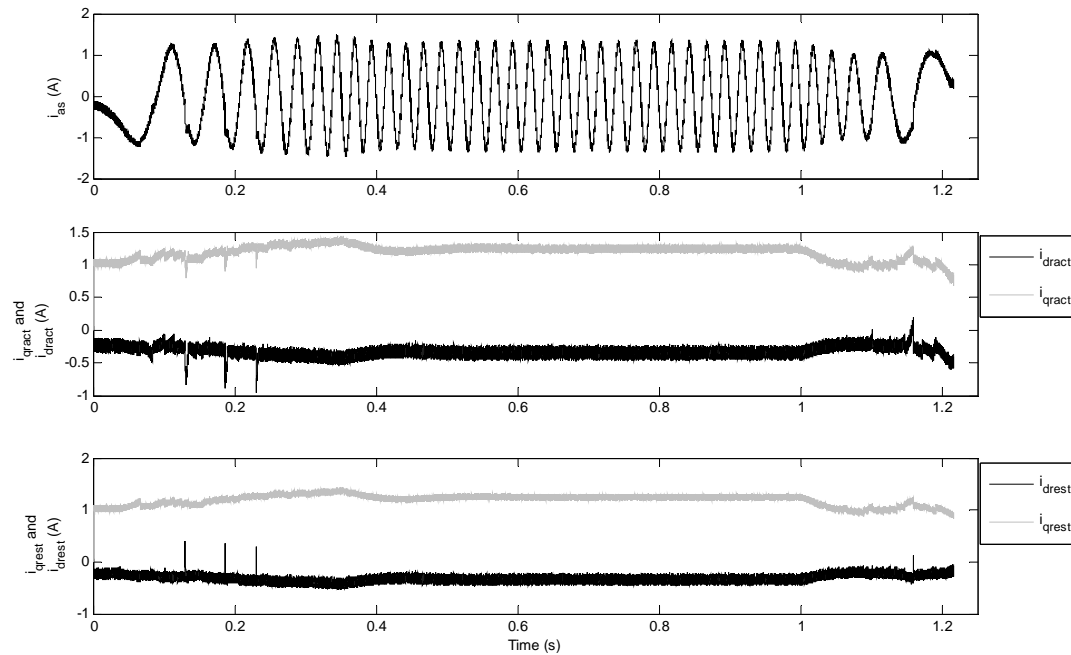


Fig. 8.34. Phase-A current (i_{as}), i_{dqract} , and i_{dqrest} when a 0.35 second ramp time is used when the PI integrator initial value is 7 N·m.

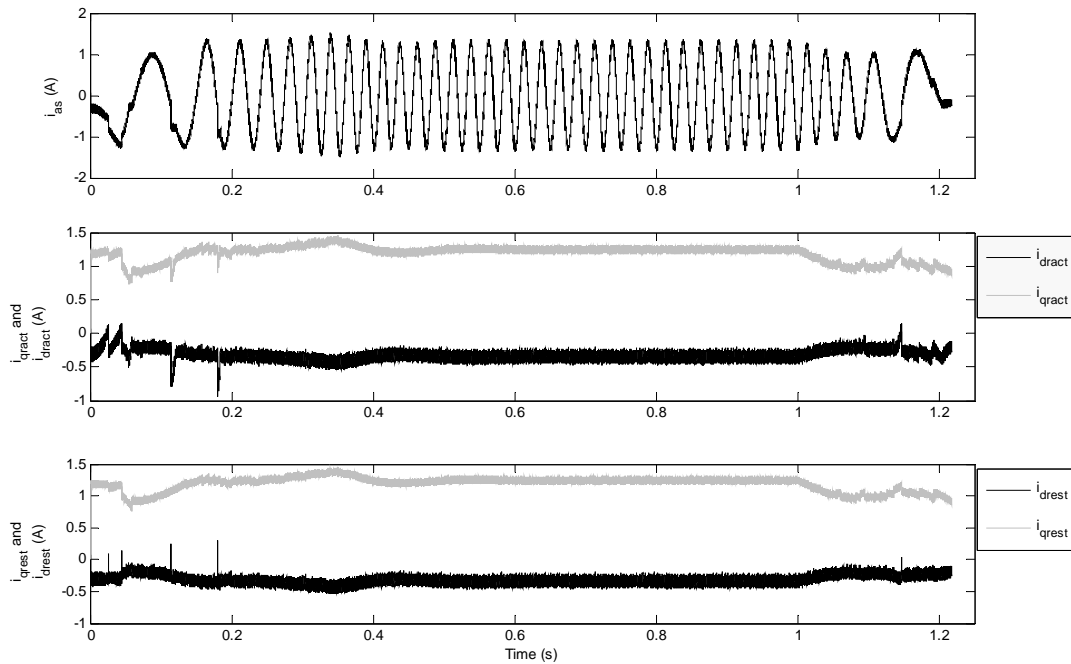


Fig. 8.35. Phase-A current (i_{as}), i_{dqract} , and i_{dqrest} when a 0.35 second ramp time is used when the PI integrator initial value is 8.5 N·m.

The dynamic response of speed when the initial integrator value of the PI controller is 7 N·m is illustrated in Fig. 8.36. Clearly, the actual speed is capable of following the reference speed accurately from zero speed to 100 rpm, and also from 100 rpm to zero speed in the coast region. Based on this observation, the estimated rotor position is displayed in Fig. 8.36. It can be seen that the proposed rotor position estimation by the help of three cost-effective hall-effect sensors tracks the actual position quite well.

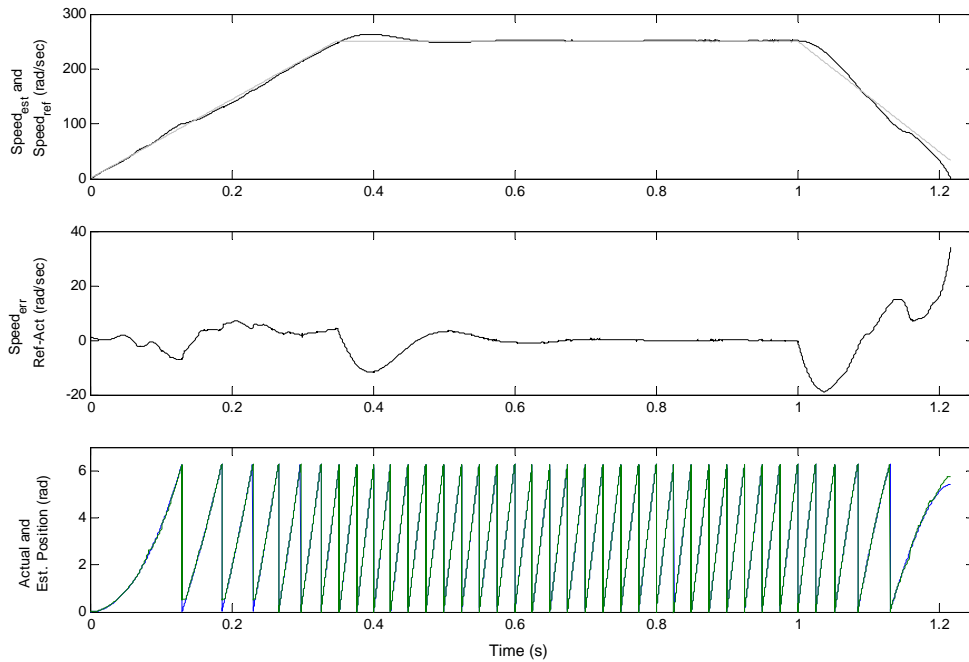


Fig. 8.36. Reference and actual speed, speed error (ref-act), actual and estimated position when a 0.35 second ramp time is used when the PI integrator initial value is 7 N·m.

In Fig. 8.37, the dynamic response of motor speed is represented when the initial integrator value of the PI controller is 8.5 N·m. Since the initial torque is higher than the load torque, more overshoot is observed than when the initial integrator value is 7 N·m. It takes less than 0.2 second for the speed to converge to the reference value, however, from now on the actual speed is capable of following the reference speed very well. Based on this observation, the estimated rotor position is displayed in the same figure. It can be seen that the proposed rotor position estimation by the help of three cost-effective hall-effect sensors tracks the actual position quite well.

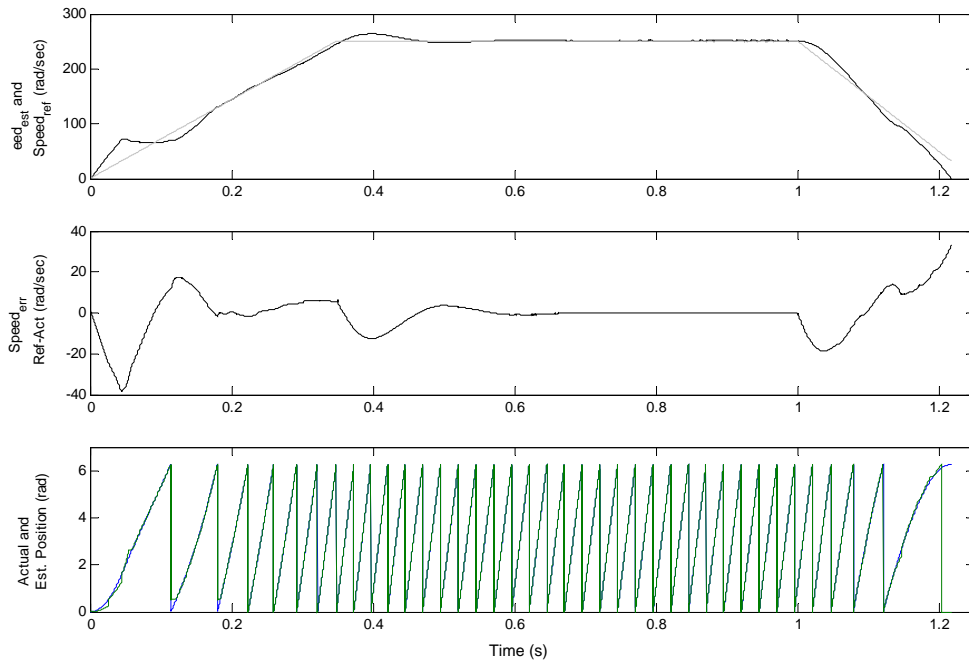


Fig. 8.37. Reference and actual speed, speed error (ref-act), actual and estimated position when a 0.35 second ramp time is used when the PI integrator initial value is 8.5 N·m.

The torque characteristics of the PMSM when a 7 N·m. to 10 N·m. transient load torque is applied during a 0.6125 second ramp up period are shown in Fig. 8.38. In the same figure the initial integrator value of the PI controller is chosen as 7 N·m with an additional ramp rate formula. Since there is an initial load on the machine due to the laundry, the motor should reach the same torque level to start up. As it can be seen from Fig. 8.39, the actual and estimated electromagnetic torque resemble the reference electromagnetic torque generated by the PI controller (used for speed control). After the 1.2 seconds plateau region is over the coast time starts. In this case the coast time is selected as 0.25 second (total stroke time is 1.45 seconds). It can be observed that the transient electromagnetic torque during ramp time is tracking the reference torque quite well. During the steady-state a very pure and constant torque response is achieved. After the plateau region is over (steady-state) the coast time starts (0.25 second long). During the coast region the motor tries to reach zero speed at 0.25 second.

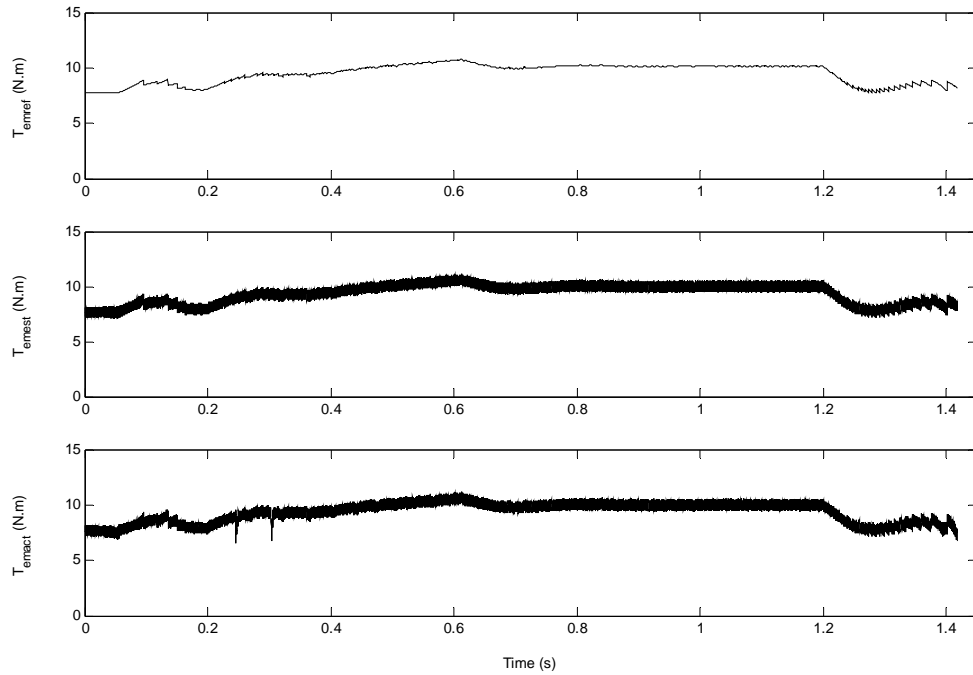


Fig. 8.38. T_{emref} , T_{emest} , and T_{emact} at a 0.6125 second ramp time when the PI integrator initial value is 7 N·m.

Fig. 8.39 shows the stator flux linkage reference value, λ_s^* , (0.223256 Wb which is equal to the rotor flux linkage amplitude), the estimated stator flux linkage, λ_{s_est} , and the actual stator flux linkage, λ_{s_act} , respectively at a 0.6125 second ramp up time when the initial integrator value of the PI controller is selected as 7 N·m.

For the next simulation the ramp time increases to imitate the delicate washing cycle. It will give us a good validation opportunity with the conventional agitation control because most of the time the conventional agitation control is tested under a 0.6125 second ramp up time.

Three small pikes in the estimation of the stator flux amplitude are seen in Fig. 8.39 due to the small dips in the actual torque at approximately 0.2 second. At the end of the plateau time and starting from the middle of the coast time the actual stator flux amplitude deviates due to corrupted torque because less attention is put on the speed

control during the coast time. On the other hand, the steady state stator flux linkage values (both estimated and actual) track the commanded value quite well. The λ_{sD} and λ_{sQ} circular trajectory is shown in Fig. 8.40. Three small pikes that occurred in stator flux linkage estimation can also be observed in the circular trajectory.

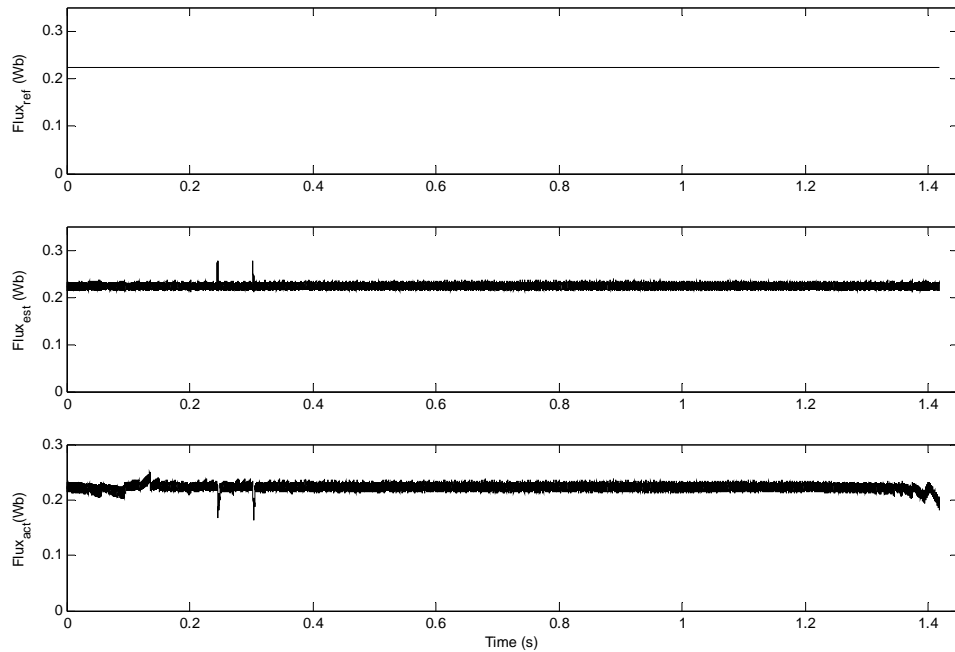


Fig. 8.39. λ_s^* (reference stator flux), λ_{s_est} and λ_{s_act} at a 0.6125 second ramp time when the PI integrator initial value is 7 N·m.

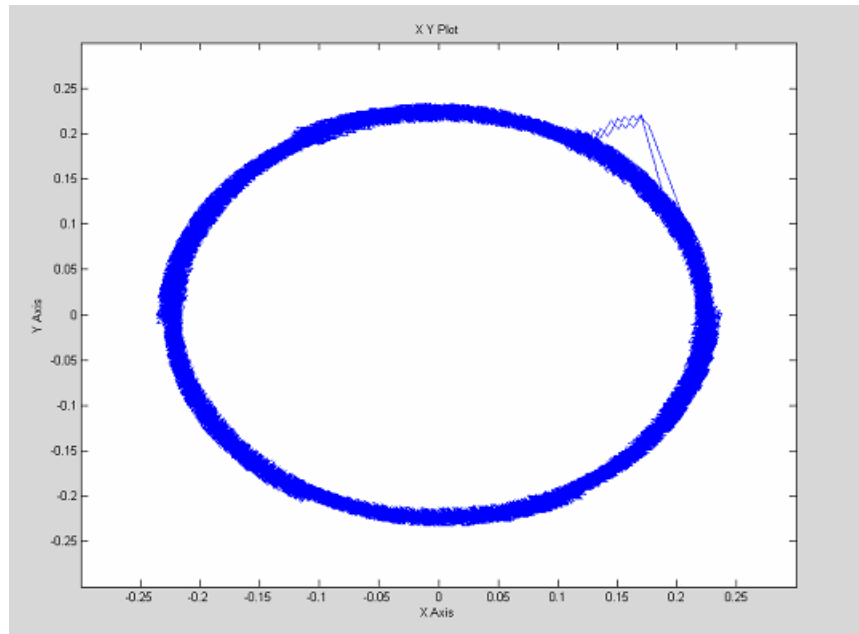


Fig. 8.40. λ_{sD} (X axis) and λ_{sQ} (Y axis) circular trajectory at a 0.6125 second ramp time when the PI integrator initial value is 7 N·m.

The dynamic response of the d and q-axes currents in the RRF and the Phase A current at a 0.6125 second ramp up time under a 7 N·m to 10 N·m transient load during the ramp up when the initial integrator value of the PI controller is chosen as 7 N·m are shown in Fig. 8.41. Three hall-effect sensors assist to the control algorithm for continuous rotor position estimation. With the gradual increase of speed, a smooth change in the stator current and q-axis current in the RRF are observed during the dynamic state. Fig. 8.41 shows the actual q-axis and d-axis currents in the rotor reference frame obtained by the encoder and the estimated currents from the position observer method assisted by the three hall-effect sensors. During steady state, the amplitude of the stator current is essentially unchanged.

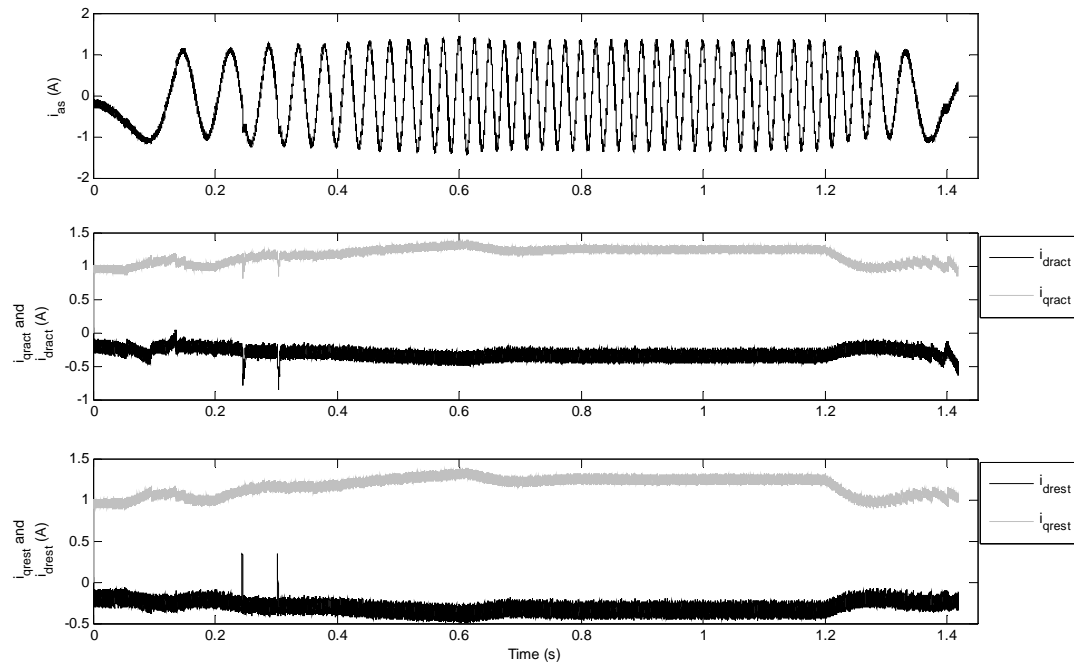


Fig. 8.41. Phase-A current (i_{as}), i_{dqract} , and i_{dqrest} when a 0.6125 second ramp time is used when the PI integrator initial value is 7 N·m.

The dynamic response of the speed at a 0.6125 second ramp up time when the initial integrator value of the PI controller is 7 N·m is represented in Fig. 8.42. Since the initial torque is almost as close as load torque minus the overshoot in the speed response is observed. Based on the observer, the estimated rotor position is displayed in the same figure. It can be seen that the proposed rotor position estimation with the help of three cost-effective hall-effect sensors tracks the actual position quite well.

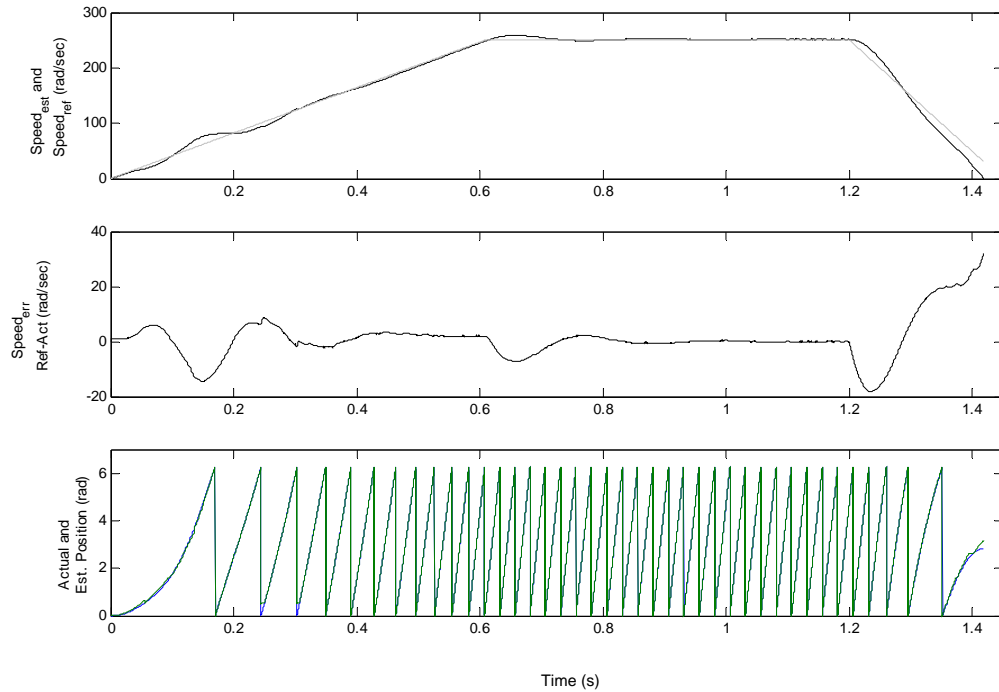


Fig. 8.42. Reference and actual speeds, speed error (ref-act), and actual and estimated positions when a 0.6125 second ramp time is used when the PI integrator initial value is $7 \text{ N}\cdot\text{m}$.

8.2.3.2. Effects of Stator Resistance Variation in Conventional DTC with Encoder

In order to examine the effects of the R_s variations of a PM synchronous machine, a MATLAB/SIMULINK[®] conventional DTC model was developed. The DC-link voltage is set at 370 volts. The R_s value in the motor model is varied by certain amount, such as 1.5 times of the nominal value (steady-state, transient and starting etc.). It should be noted that in all the work related to the resistance change presented here, the transient load torque is assumed to ramp from $7 \text{ N}\cdot\text{m}$ to $10 \text{ N}\cdot\text{m}$ to mimic the real washing machine load characteristics.

First, a conventional DTC is simulated without the stator resistance change. Figs. 8.43 and 8.44 show the reference and actual speeds, actual position, and the three

phase currents, the reference and estimated electromagnetic torques and the estimated stator flux linkage when a 0.35 second ramp up time is selected and the stator resistance is not varied, respectively. Since no resistance change effect is applied and an encoder is used for speed control, good results are achieved.

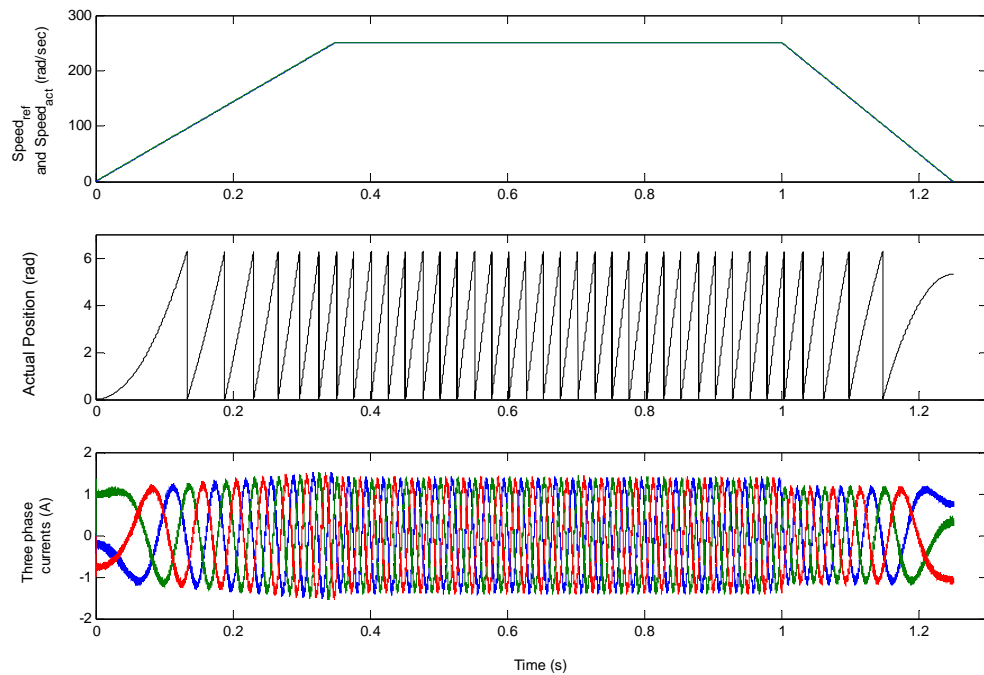


Fig. 8.43. Reference and actual speeds, actual position, and three phase currents when a 0.35 second ramp time is used (no initial torque, just ramp rate is added). Stator resistance change effect is not applied.

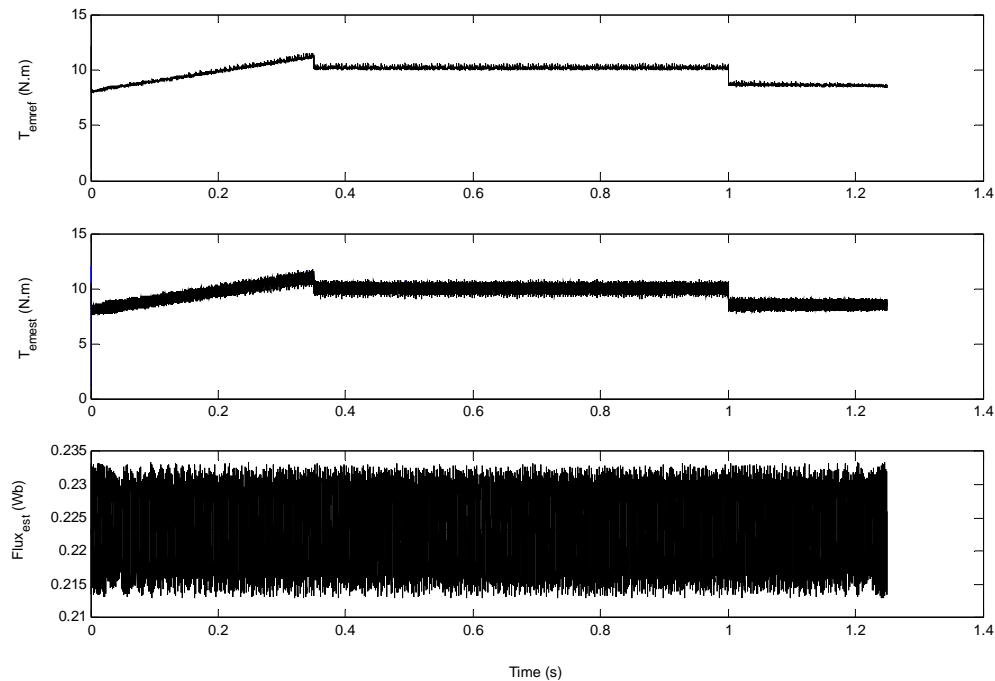


Fig. 8.44. T_{emref} , T_{emest} , and $Flux_{est}$ at a 0.35 second ramp time. Stator resistance change effect is not applied.

A mismatch between the controller set stator resistance and its actual value in the machine can create instability as shown in Fig. 8.45. This figure shows the simulation results for a step stator resistance change from 100% to 150% of its nominal value at 0 second and a torque command (7 N·m to 10 N·m) is applied at the start up. The drive system becomes unstable if controller instrumented stator resistance is lower than its actual value in the motor. This may be explained as follows: As the motor resistance increases in the machine, then its current decreases for the same applied voltages, which decreases the flux and electromagnetic torque. The controller has the opposite effect in that the decreased currents, which are inputs to the system, cause decreased stator resistance voltage drops in the calculator resulting in higher flux linkages and electromagnetic torque estimation. They are compared with their command values giving larger torque and flux linkages errors resulting in commanding larger voltages and hence in larger currents leading to a run off condition. The instability result under a

step change is questionable as the stator resistance does not change in a step manner in practice. From the earlier work a linearly decreasing stator resistance provided the same result. Even for such a gradual change of stator resistance, note that the system becomes unstable. The controller calculated electromagnetic torque and stator flux linkages are equal to set values and contrary to the real situation in the machine. Therefore, any scheme using these values for parameter compensation would not be effective. For example, the airgap power feedback control for parameter compensation in an indirect vector controlled drive system is successful but it will not work in the DTC drive system.

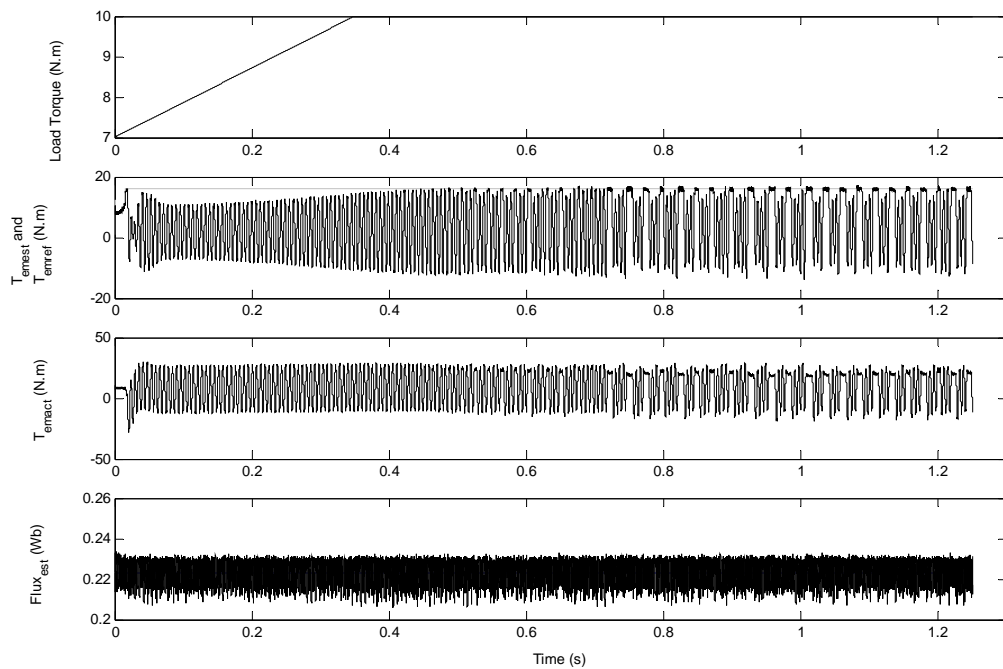


Fig. 8.45. Load torque (TL), T_{emref} , T_{emest} , T_{emact} , and estimated stator flux linkage under step stator resistance change ($1.5 \times R_s$) at 0 second when ramp time is 0.35 second when the initial integrator value of the PI is chosen as 7 N·m.

Fig. 8.46 illustrates the actual and reference speeds, actual position, and three phase motor currents. It can be seen from Fig. 8.45 that due to the lack of control of the

torque caused by the stator resistance mismatch, the speed control becomes unstable after a few milliseconds of running. If the mismatch in R_s is larger, the instability occurs earlier and vice versa.

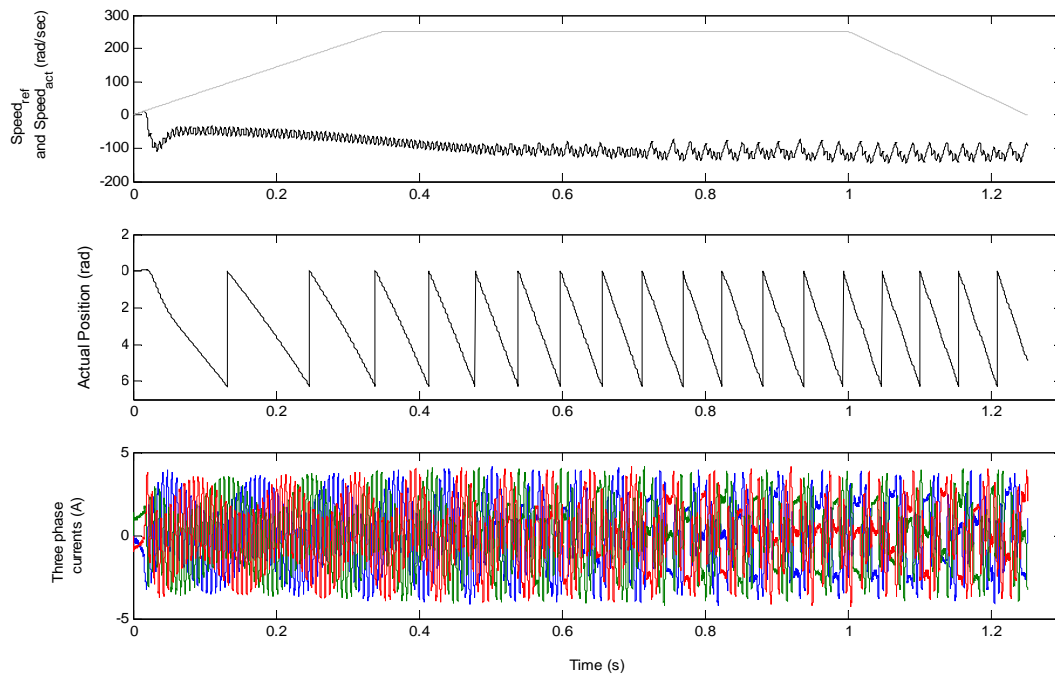


Fig. 8.46. Reference and actual speeds, actual position, and three phase currents when a 0.35 second ramp time is used (no initial torque, just ramp rate is added). Stator resistance is increased by $1.5x R_s$ at 0 second ($V_{dc} = 370$ V).

When the stator resistance with a %50 mismatch in R_s happens during the steady-state, as shown in Fig. 8.47, the speed tracks the commanded value very well. The problem with this, however, is that the actual motor current increases.

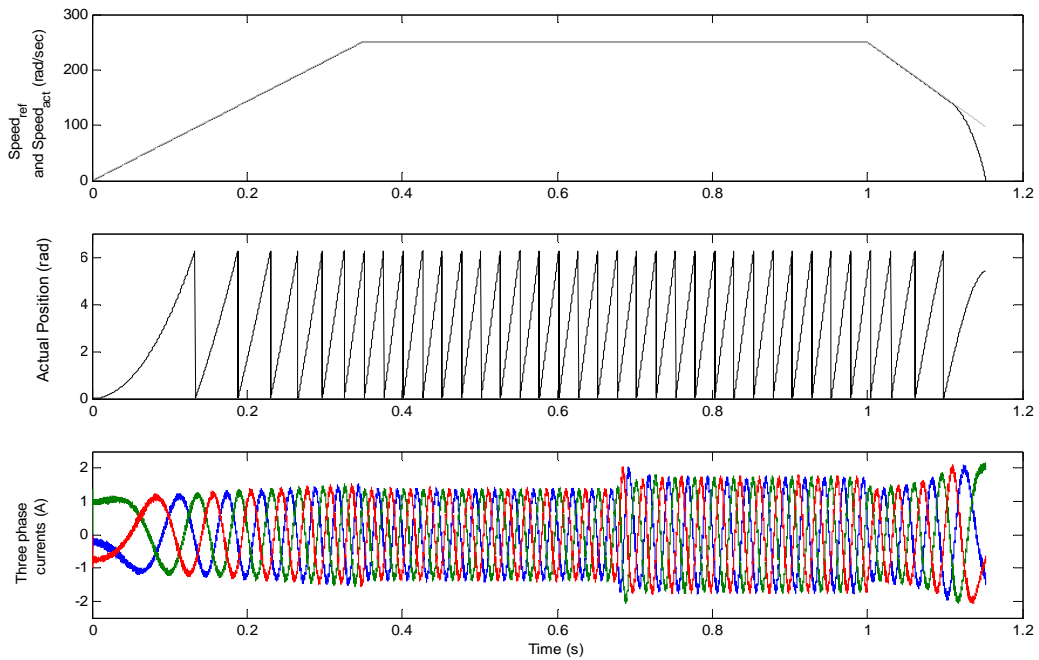


Fig. 8.47. Reference and actual speeds, actual position, and three phase currents when a 0.35 second ramp time is used (no initial torque, just ramp rate is added). Stator resistance is increased by $1.5x R_s$ at 0.675 second ($V_{dc} = 370$ V).

When the stator resistance is increased, the estimated and reference electromagnetic torque values also increase while the stator flux linkage estimation remains constant, as depicted in Fig. 8.48.

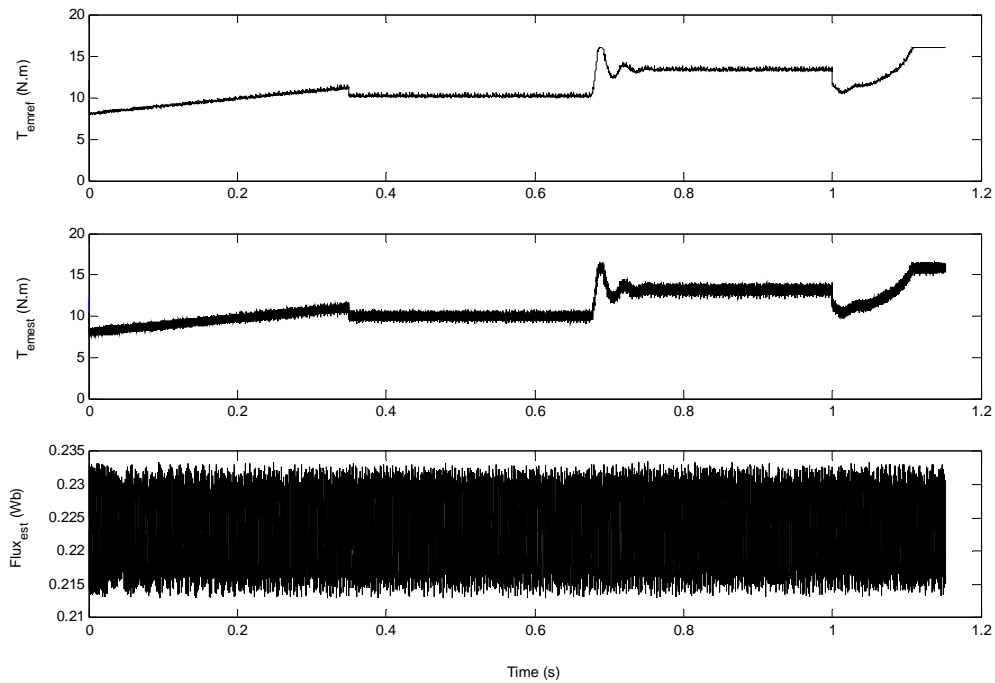


Fig. 8.48. T_{emref} , T_{emest} , and $Flux_{est}$ at a 0.35 second ramp time. Stator resistance is increased by $1.5x R_s$ at 0.675 second ($V_{dc} = 370$ V).

Fig. 8.49 illustrates a good comparison between the estimated electromagnetic torque, the estimated stator flux linkage value, the actual electromagnetic torque and the actual stator flux linkage value, respectively. When the resistance increases during steady-state, the actual value of the electromagnetic torque increases but the actual stator flux linkage value decreases.

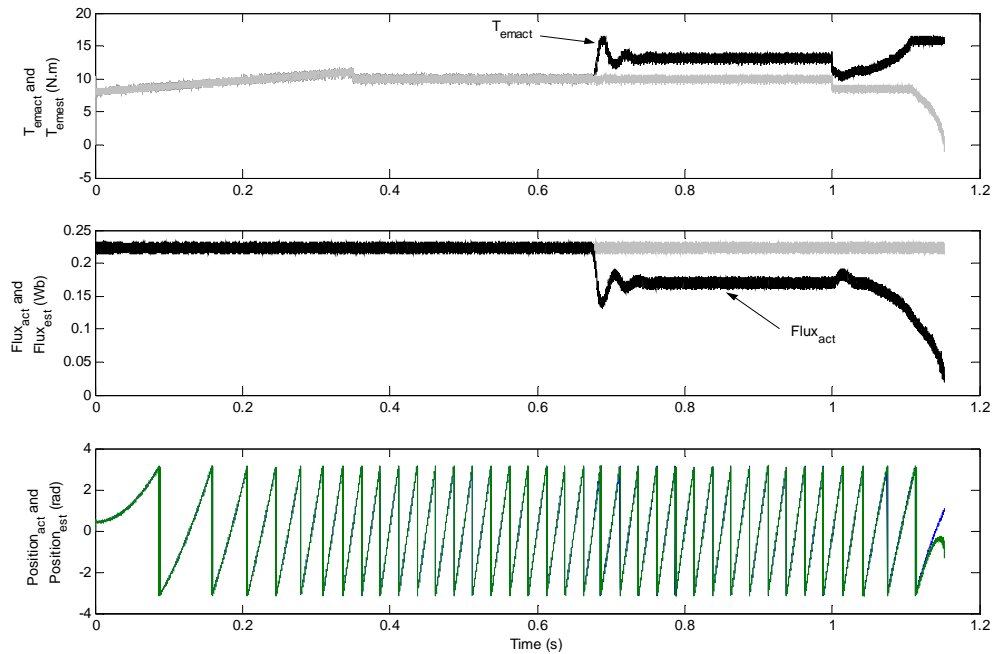


Fig. 8.49. T_{emest} , T_{emact} , $Flux_{est}$, $Flux_{act}$, estimated and real rotor positions with a 0.35 second ramp time. Stator resistance is increased by $1.5x R_s$ at 0.675 second ($V_{dc} = 370$ V).

Since washing machine agitation speed control needs to work back and forth between zero and the plateau speed quickly, the resistance change effect will also be observed in the transient as well as in the start up, even though the change happens in steady-state. The simulation results show that the change in the stator resistance during the transient state causes more devastating results in the closed loop speed control, even with an encoder. Fig. 8.50 shows the electromagnetic torque and the stator flux linkage behavior of the motor when resistance is incremented by 50% of its nominal value at $0.35/2$ second. After a few milliseconds the motor torque becomes unstable which makes the flux linkage and speed control go unstable. As soon as the step change in the stator resistance occurs at the transient state the speed goes unstable as shown in Fig. 8.51. As discussed earlier in this section, in reality the resistance will not change as a step change, it changes gradually. Recent simulation tests conducted by some authors claim that the

gradual change in resistance will only prolong the period of time before instability occurs.

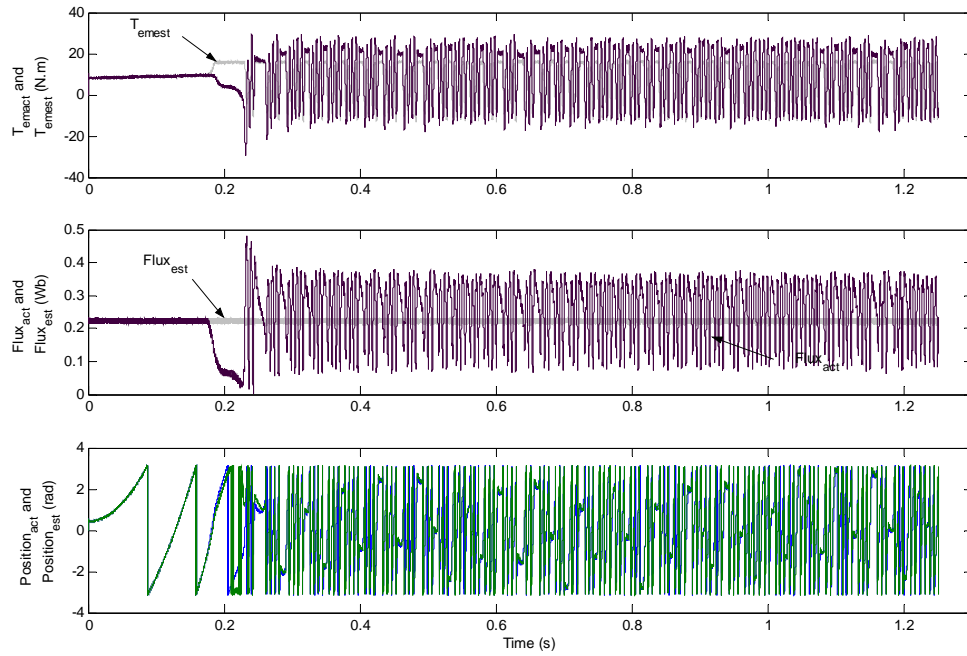


Fig. 8.50. T_{emest} , T_{emact} , $Flux_{est}$, $Flux_{act}$, estimated and real rotor positions with a 0.35 second ramp time. Stator resistance is increased by $1.5x R_s$ at 0.35/2 second

$$(V_{dc} = 370 \text{ V}).$$

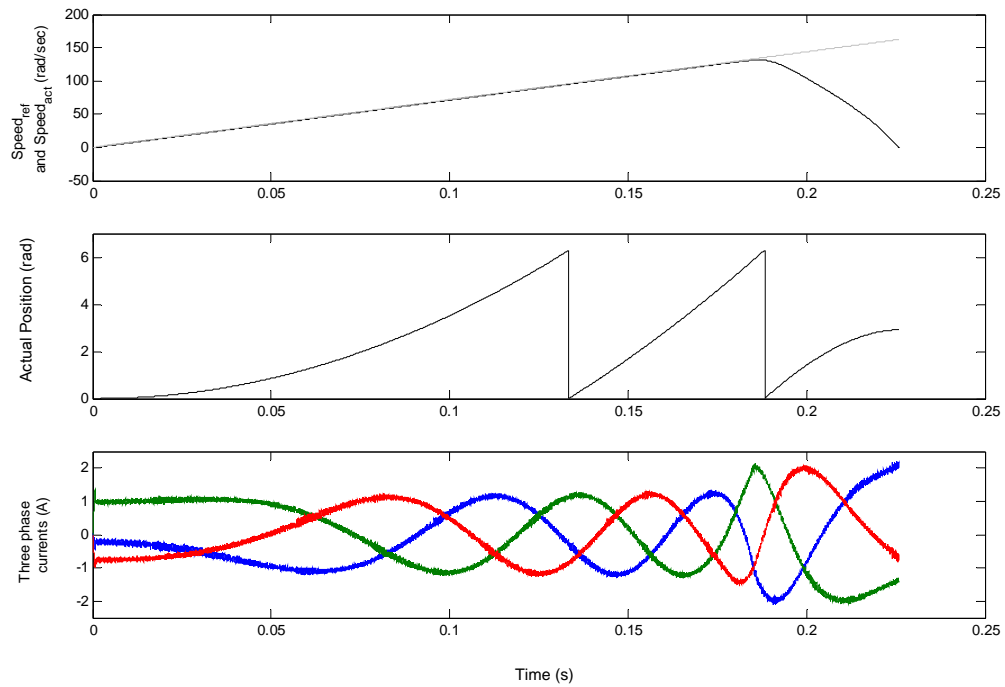


Fig. 8.51. Reference and actual speeds, actual position, and three phase currents when a 0.35 second ramp time is used (no initial torque, just ramp rate is added). Stator resistance is increased by $1.5 \times R_s$ at 0.35/2 second ($V_{dc} = 370$ V).

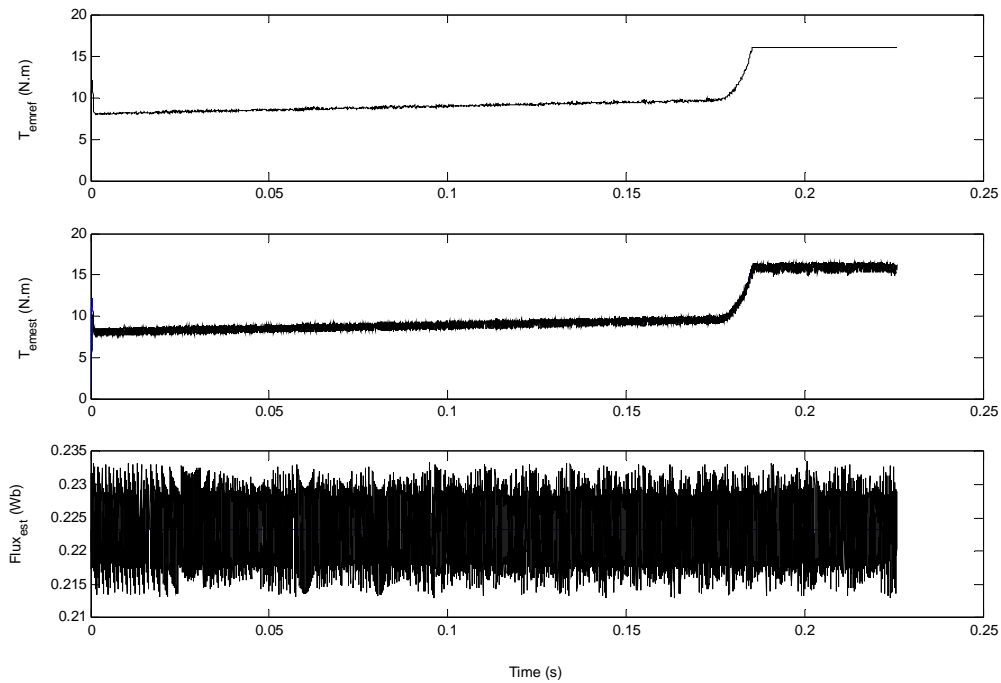


Fig. 8.52. T_{emref} , T_{emest} , and $Flux_{est}$ with a 0.35 second ramp time. Stator resistance is increased by $1.5x R_s$ at 0.35/2 second ($V_{dc} = 370$ V).

Fig. 8.53 illustrates the estimated stator flux linkage circular trajectory when the stator resistance is increased by 50% of its nominal value at steady state. The proportional coefficient of the speed in PI controller is chosen as 9 and the integral coefficient as 3 for all the simulation that are run.

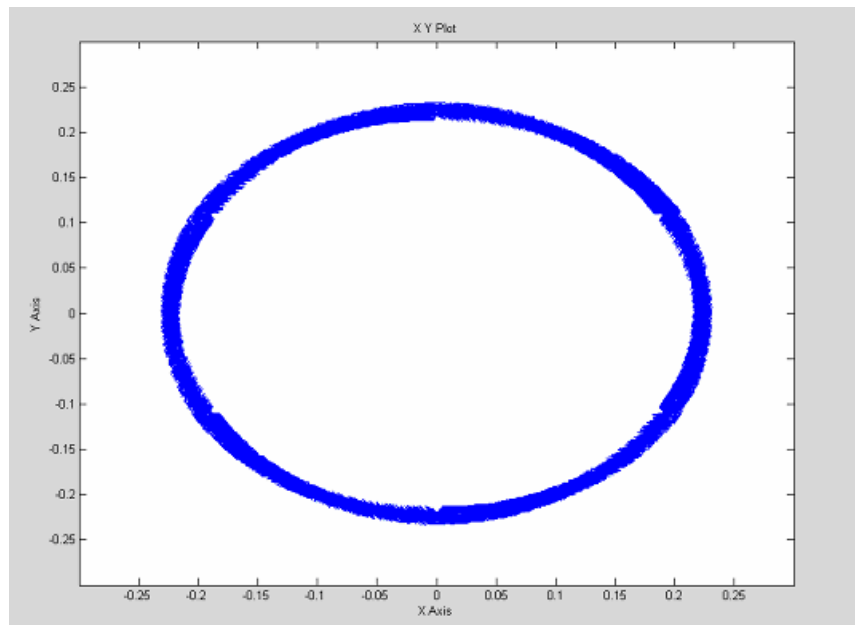


Fig. 8.53. Estimated λ_{sD} (X axis) and λ_{sQ} (Y axis) circular trajectory with a 0.35 second ramp time. Stator resistance is increased by $1.5 \times R_s$ at 0.675 second ($k_p=9$, $k_i=3$).

The estimated stator flux linkage trajectory when the stator resistance value is step changed at 0.35/2 second is given in Fig. 8.54. It can clearly be seen that the resistance value changed in the transient state causes the stator flux linkage locus to be less smooth than the change occurring at steady-state depicted in Fig. 8.53.

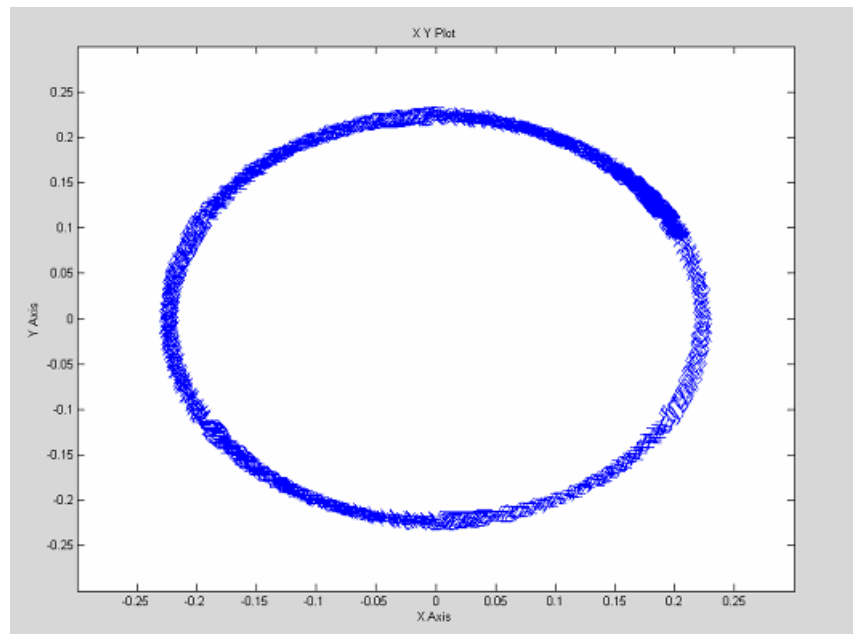


Fig. 8.54. Estimated λ_{sD} (X axis) and λ_{sQ} (Y axis) circular trajectory with a 0.35 second ramp time. Stator resistance is increased by $1.5x R_s$ at 0.35/2 second ($k_p=9$, $k_i=3$).

The actual stator flux linkage locus when resistance is varied at the transient state (0.35/2 second) is shown in Fig. 8.55. Unlike the estimated flux linkage, the actual value of the stator flux linkage is out of the circular trajectory limit. In this case, the simulation is stopped at 0.28 second to let the deviation in the flux linkage locus be seen clearly.

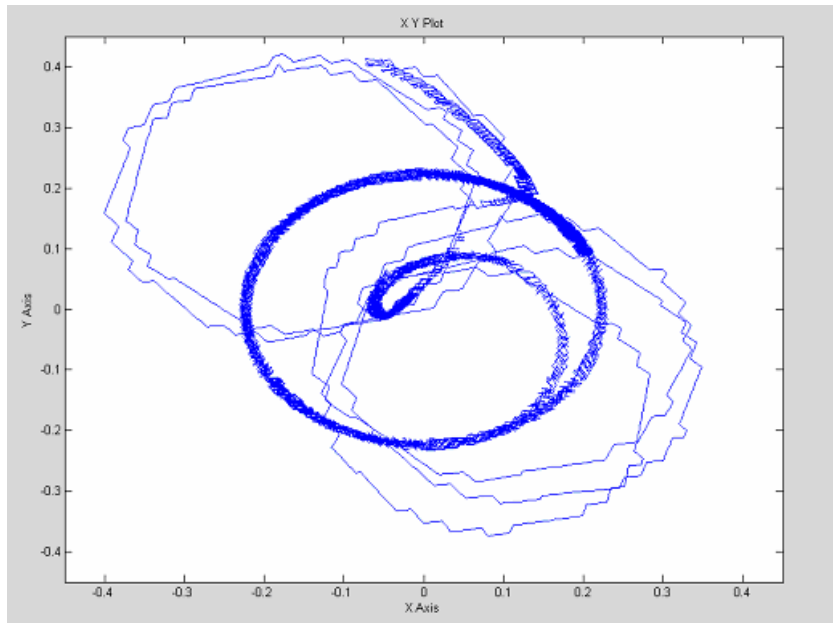


Fig. 8.55. Actual λ_{sD} (X axis) and λ_{sQ} (Y axis) circular trajectory with a 0.35 second ramp time. Stator resistance is increased by $1.5 \times R_s$ at $0.35/2$ second (stopped at 0.28 s.).

When the stator resistance is changed at steady-state, the circular trajectory becomes smaller as shown in Fig. 8.56. This occurs when the stator resistance is increased during the transient state. It has been observed that much quick instability occurs in the speed control when the stator resistance varies during the transient state compared to stator resistance varies during steady-state. If the application lets the motor start once and runs at steady-state then most of the time less instability may be observed because of the stator resistance change effect. On the other hand, in the washing machine speed control, the speed has zero, transient, and steady-state conditions such that the change in stator resistance can occur at any time. This is so that worse case (transient state) scenario can be considered.

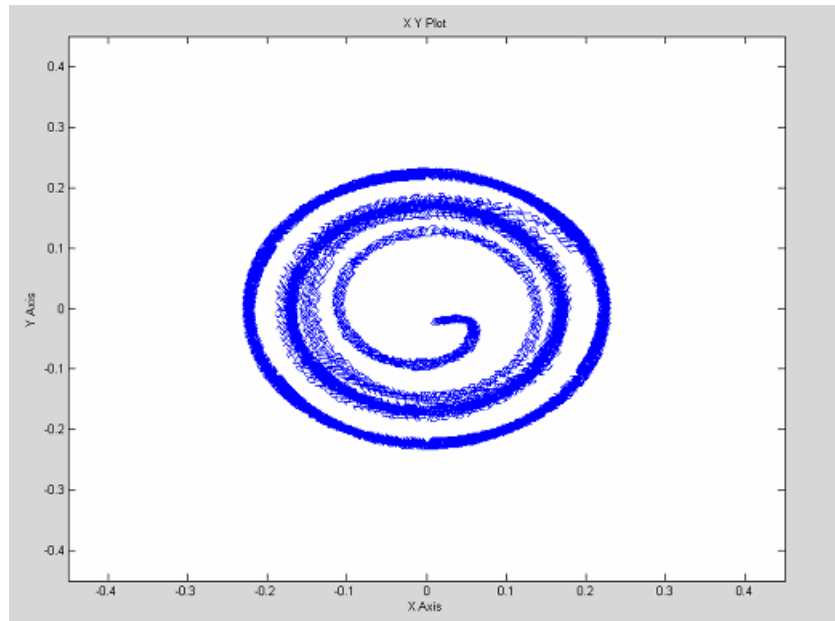


Fig. 8.56. Actual λ_{sD} (X axis) and λ_{sQ} (Y axis) circular trajectory with a 0.35 second ramp time. Stator resistance is increased by $1.5x R_s$ at 0.675 second (stopped at 0.28 s.)

8.2.3.3. Drift Problem Occurs in Conventional DTC Scheme

The stator flux is estimated in DTC by integrating the difference between the input voltage and the voltage drop across the stator resistance. When the stator flux is indirectly estimated from the integration of the back-EMF, any DC-offset is also integrated and would eventually lead to large drifts in the stator flux linkage. Operational amplifiers are normally used to amplify the signal from the current and voltage sensors. These sensors have a temperature dependent DC-offset. Since the current measurement path contains many analog devices, DC-offset is an inevitable problem. The error in the stator flux estimation also causes an error in the torque estimation, so the drive system may become unstable [35].

The scaling error is another type of current measurement error. Stator currents are transformed to the voltage signal by current sensors and are transformed into digital values via low pass filters and A/D converters. The output of a current sensor must be

scaled to fit the input range of an A/D converter to get the real value of a current. During this process, some scaling error may be introduced. Obviously, drift compensation is an important factor in a practical implementation of the integration, since drift can cause a large error in the estimated flux linkage. The error in the estimated flux linkage can cause error in the estimated torque and speed [35].

Figs. 8.57 through 8.59 show the experimental results when a 0.1 A (~ 4% of the rated current) offset is introduced. Figure 8.57 shows the reference and actual speeds and the actual position and three phase motor currents with an offset added. It is seen that the speed quickly goes unstable at start up and the accumulation of the offset error causes the estimated stator flux to drift from its origin as shown in Fig. 8.59. Fig. 8.58 shows the load torque, the reference and actual electromagnetic torque and also the reference and actual stator flux linkages. Starting at 0.4 second, the stator flux linkage oscillates too much and its amplitude increases greatly and from around 0.5 second the actual developed torque oscillates and in a short time goes unstable (not shown in the figure).

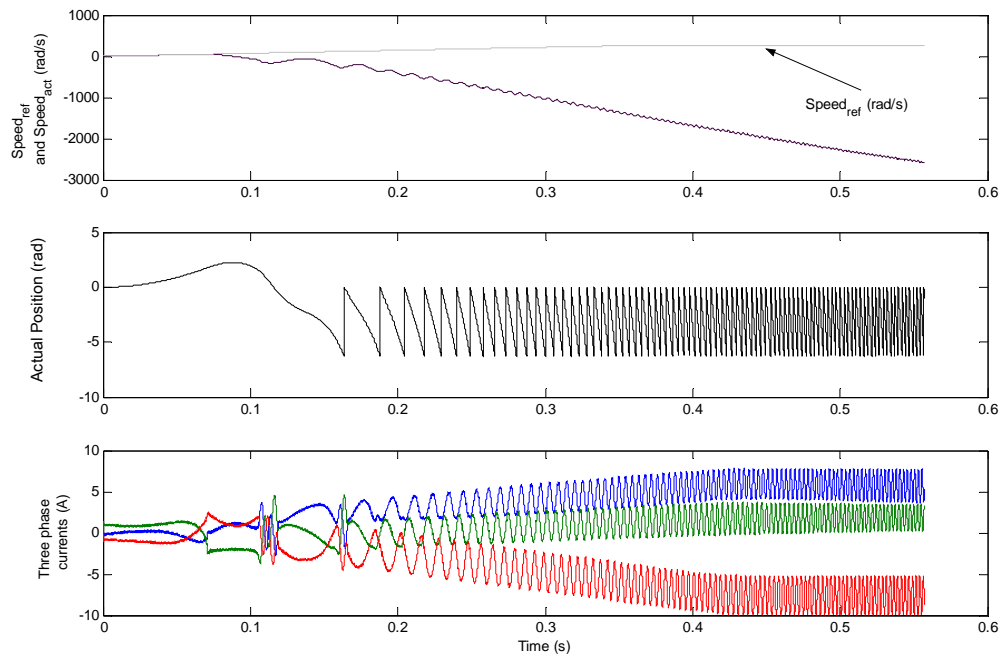


Fig. 8.57. Reference and actual speeds, actual position, and three phase currents when a 0.35 second ramp time is used (no initial torque, just ramp rate is added). A 0.1 A current offset is added to the D- and Q-axes currents in the SRF ($V_{dc} = 370$ V).

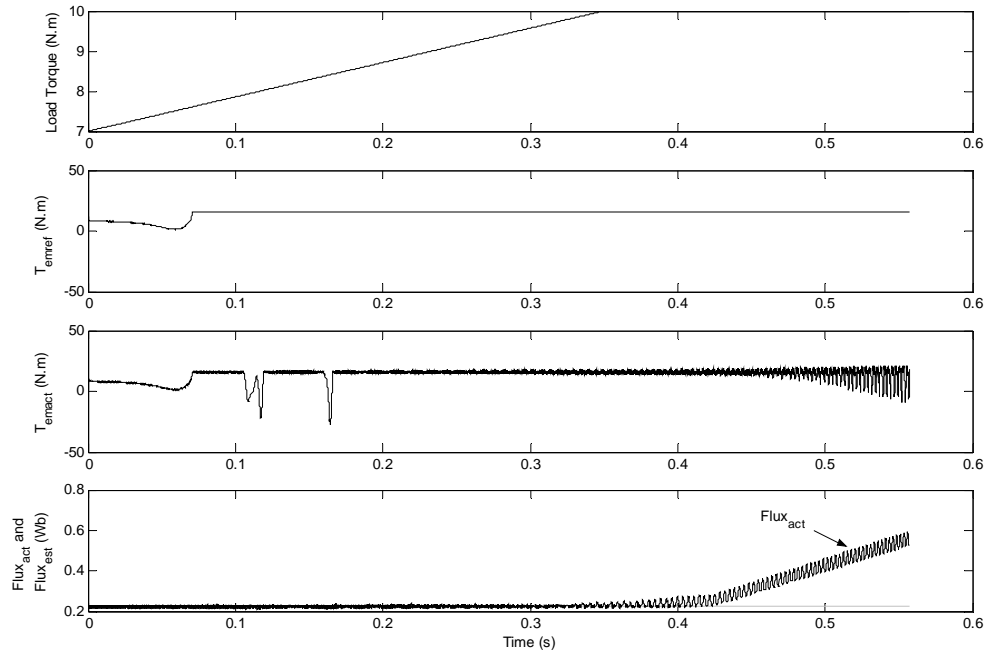


Fig. 8.58. Load torque (TL), T_{emref} , T_{emact} , $Flux_{est}$, and actual stator flux linkage.

A 0.1 A offset occurs on the D- and Q-axes currents in the SRF when the ramp time is 0.35 second.

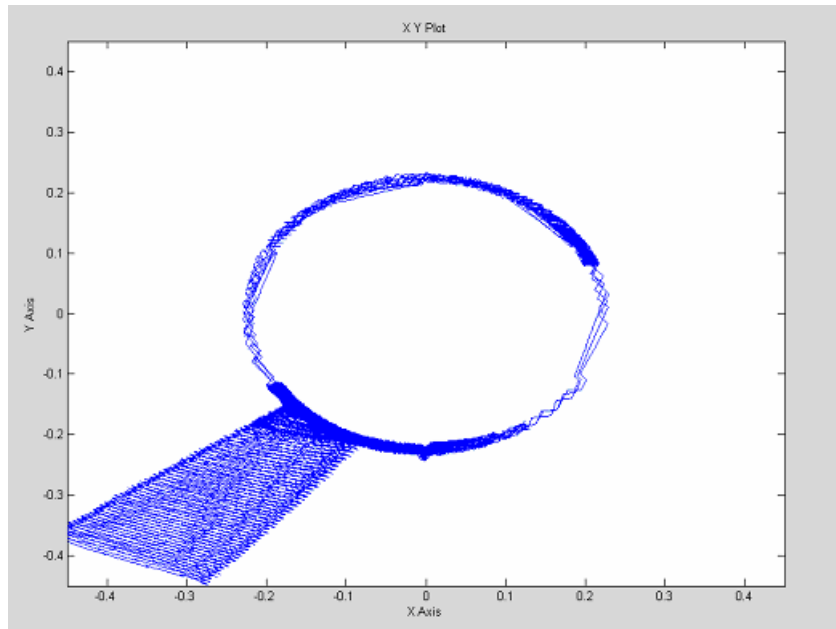


Fig. 8.59. Estimated λ_{sD} (X axis) and λ_{sQ} (Y axis) circular trajectory with a 0.35 second ramp time. A 0.1 A offset is included in the D- and Q-axes currents in the SRF ($V_{dc} = 370$ V). ($k_p=9$, $k_i=3$).

8.2.3.4. Overview of the Offset Error Occurred in the Proposed DTC Scheme

Unlike the conventional DTC scheme, the test results shown below prove that around a 4% offset in the d- and q-axes currents in the RRF does not affect the closed-loop speed control of the proposed DTC scheme. When there is an initial 7 N·m load torque in the washing machine which gradually increases to a 10 N·m steady-state limit proportional to the speed (choosing 7.5 N·m. initial integrator value in the speed PI controller) results in smooth starting in the case of an offset added to the currents. If a 7 N·m initial value is selected, a lower smoothness in the speed response is observed. Since the adaptive initial value correction algorithm (discussed earlier in this section) is used, after a few strokes the right value would be reached even if there is an offset in the measurement systems.

Figs. 8.60 to 8.64 display several simulation results when a 0.1 A offset error is included to the d- and q-axes currents in the RRF. Similar behaviors are observed in the results without the offset error discussed earlier in this section.

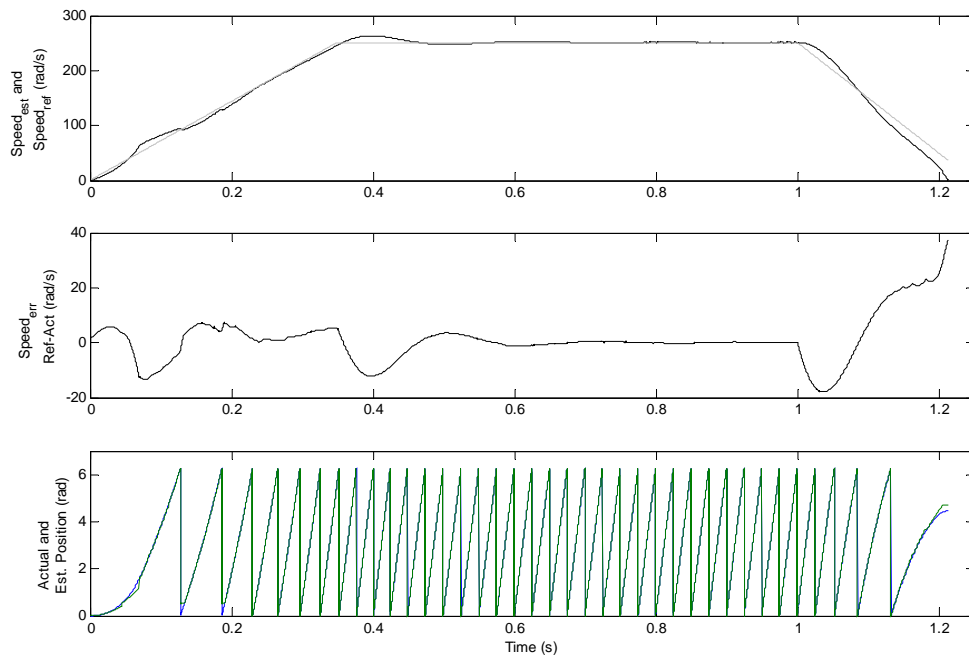


Fig. 8.60. Reference and actual speeds, speed error (ref-act), estimated and actual positions when a 0.35 second ramp time is used (7.5 N·m initial torque is used in the PI's integrator with appropriate ramp rate). A 0.1 A offset is included in the d- and q-axes currents in the RRF ($V_{dc} = 370$ V).

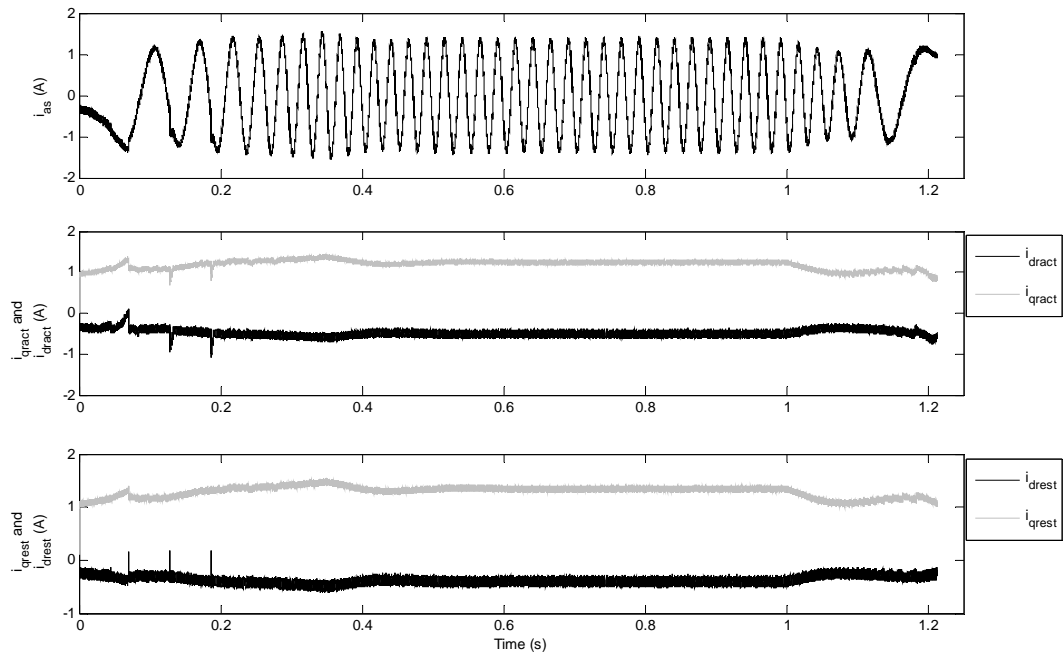


Fig. 8.61. Phase-A current (i_{as}), $i_{dq_{ract}}$, and $i_{dq_{rest}}$ when a 0.35 second ramp time is used with a PI integrator initial value of 7.5 N·m. A 0.1 A offset is included in the d- and q-axes current in the RRF ($V_{dc} = 370$ V).

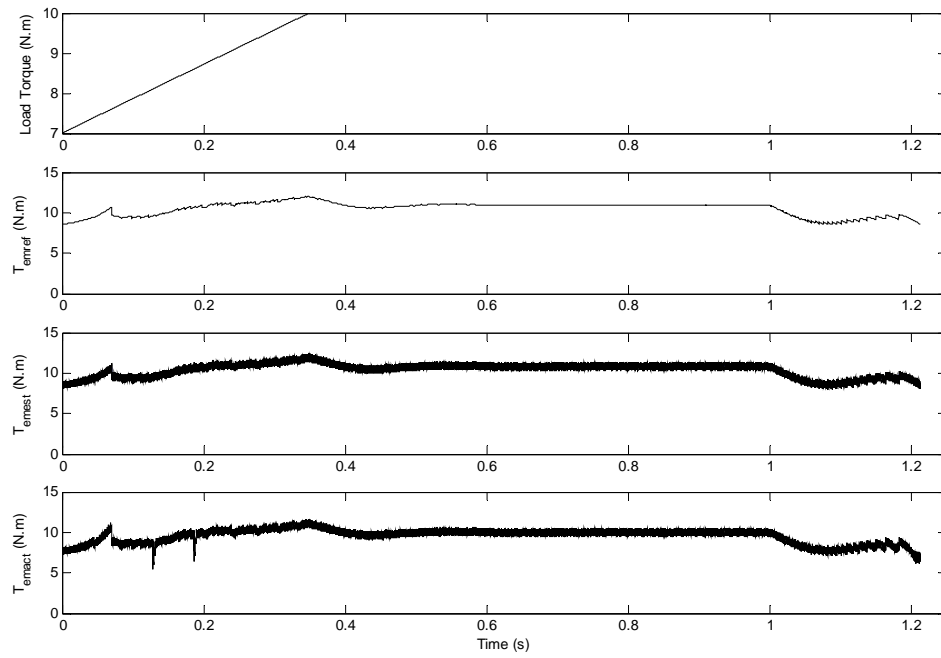


Fig. 8.62. Load torque (TL), T_{emref} , T_{emest} , and T_{emact} . A 0.1 A offset occurs on d- and q-axes currents in the RRF when ramp time is 0.35 second ($V_{dc} = 370$ V).

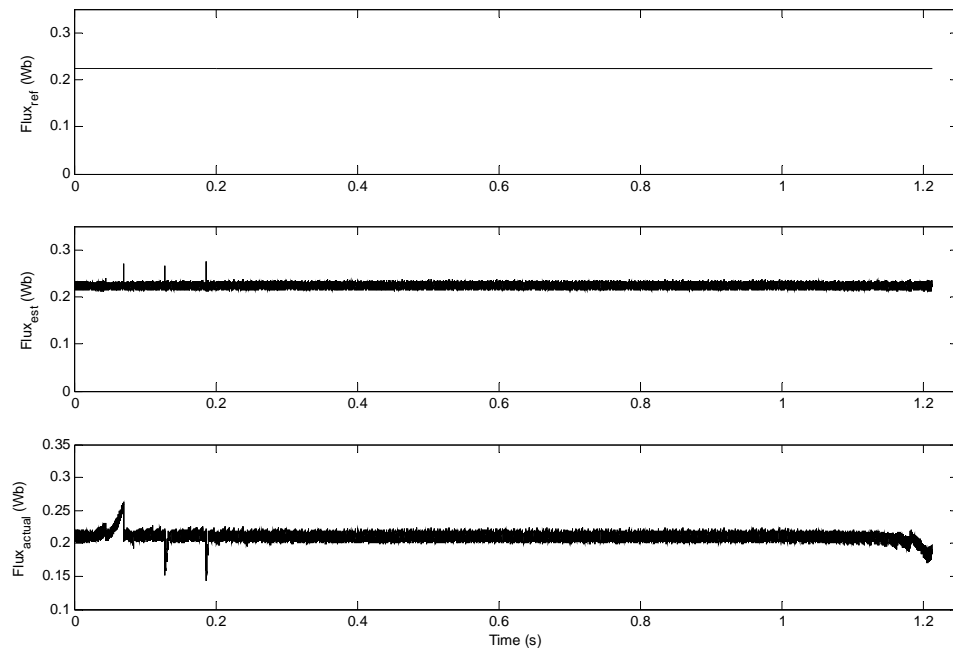


Fig. 8.63. $Flux_{ref}$, $Flux_{est}$, $Flux_{actual}$ when a 0.35 second ramp time is used with a PI integrator initial value of 7.5 N·m. A 0.1 A offset is included to the d- and q-axes currents in the RRF ($V_{dc} = 370$ V).

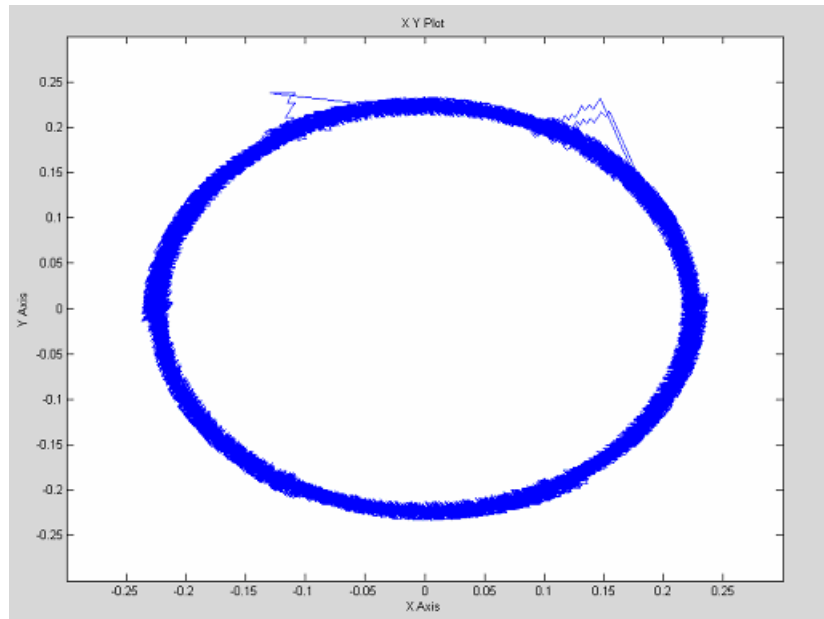


Fig. 8.64. Estimated λ_{sD} (X axis) and λ_{sQ} (Y axis) circular trajectory at a 0.35 second ramp time with a PI integrator initial value of 7.5 N·m. A 0.1 A offset is included in the d- and q-axes currents in the RRF ($V_{dc} = 370$ V). ($k_p=9$, $k_i=3$).

8.2.3.5. Overview of the Rotor Flux Linkage Error Occurred in the Proposed DTC Scheme

Similar to conventional the DTC scheme having R_s variations due to temperature change and low the speed effect, in the proposed scheme the rotor flux linkage value is considered as constant in most of the cases. The exception to this is in high temperature conditions. Some experiments show that amplitude of the rotor flux linkage can vary up to 20-30 percent of its nominal value at around 100 C° on the motor stator windings. The value of the rotor flux linkage amplitude decreases when temperature rises. Several simulations are conducted to examine the effect of the rotor flux linkage change effect when the motor heats up on the closed-loop control of the proposed DTC scheme. The rotor flux linkage amplitude is step changed when the motor speeds up (at 0.35/2 second) proportional to the load torque. This is considered the worse case

situation. The results, however, prove that the 30% decrease in the rotor flux linkage amplitude does not have a large impact on the closed-loop speed control.

Some of the simulation results when the rotor flux linkage value is changed by 70% of its nominal value are given from Figs. 8.65 through 8.69.

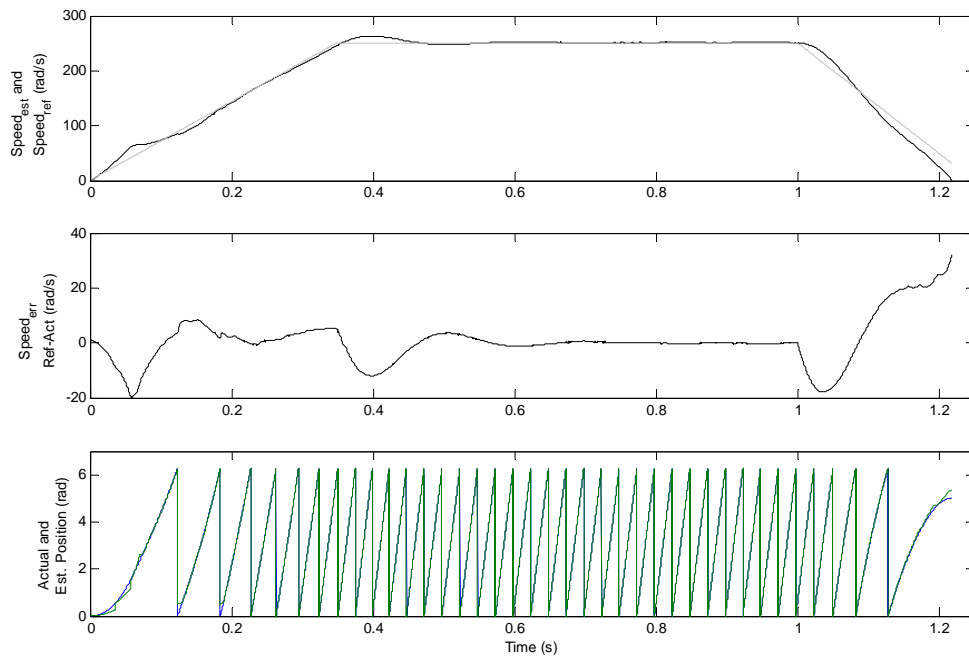


Fig. 8.65. Reference and actual speeds, speed error (ref-act), estimated and actual positions when a 0.35 second ramp time is used (7 N·m. initial torque is used in the PI's integrator with appropriate ramp rate). $0.7 \times \lambda_r$ is used at 0.35/2 second in the motor

model ($V_{dc} = 370$ V). ($k_p=9$, $k_i=3$).

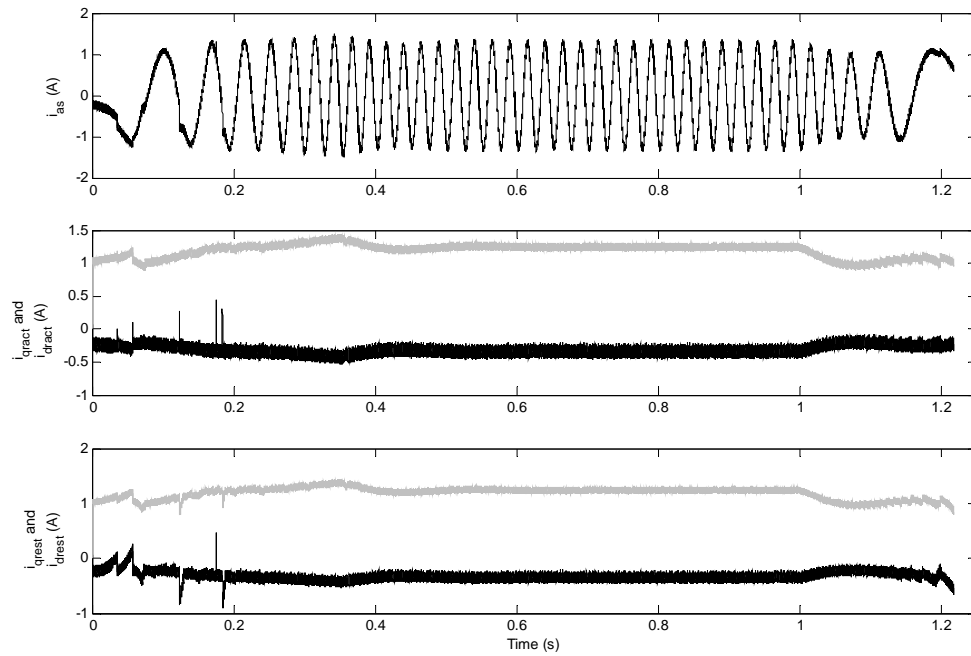


Fig. 8.66. Phase-A current (i_{as}), i_{dqract} , and i_{dqrest} when a 0.35 second ramp time is used with a PI integrator initial value of 7 N·m. $0.7 \times \lambda_r$ is used at 0.35/2 second in the motor model ($V_{dc} = 370$ V). ($k_p=9$, $k_i=3$).

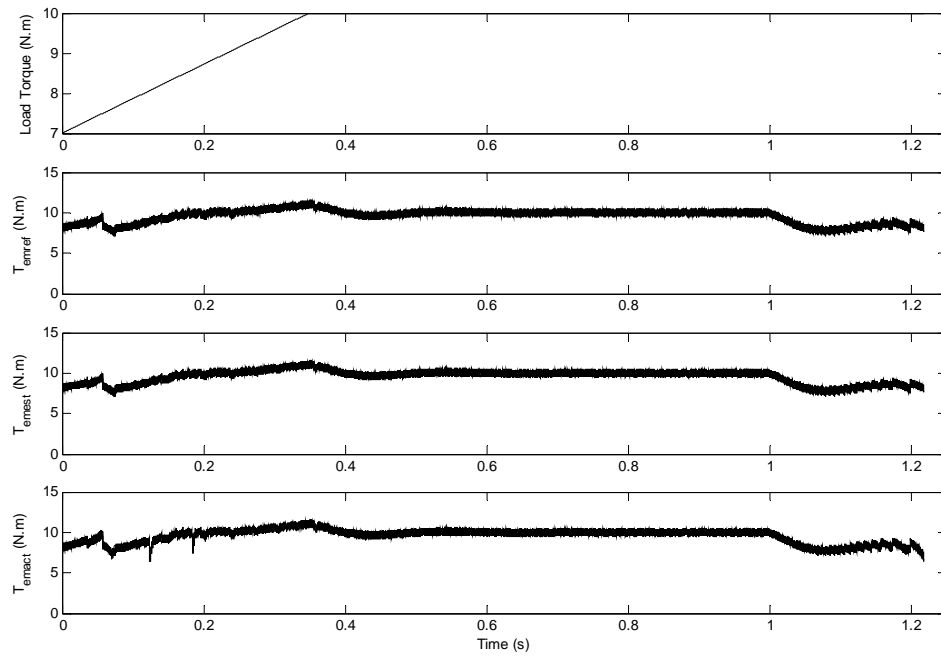


Fig. 8.67. Load torque (TL), T_{emref} , T_{emest} , and $T_{emact} \cdot 0.7 \times \lambda_r$ is used at 0.35/2 second in the motor model ($V_{dc} = 370$ V). ($k_p=9$, $k_i=3$).

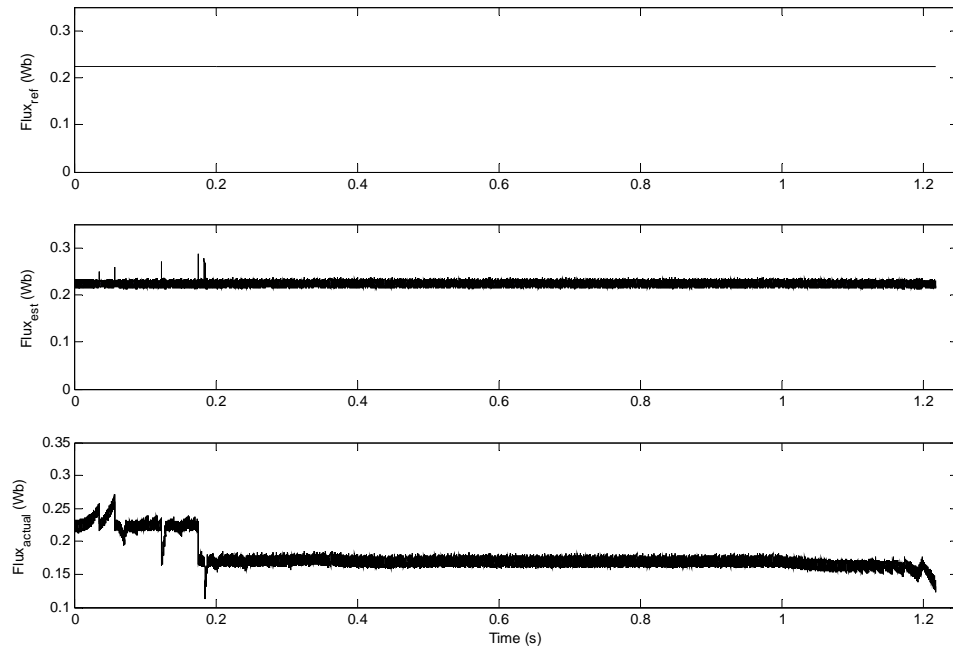


Fig. 8.68. $Flux_{ref}$, $Flux_{est}$, $Flux_{actual}$ when a 0.35 second ramp time is used with a PI integrator initial value of 7 N·m. $0.7 \times \lambda_r$ is used at 0.35/2 second in the motor model ($V_{dc} = 370$ V). ($k_p=9$, $k_i=3$).

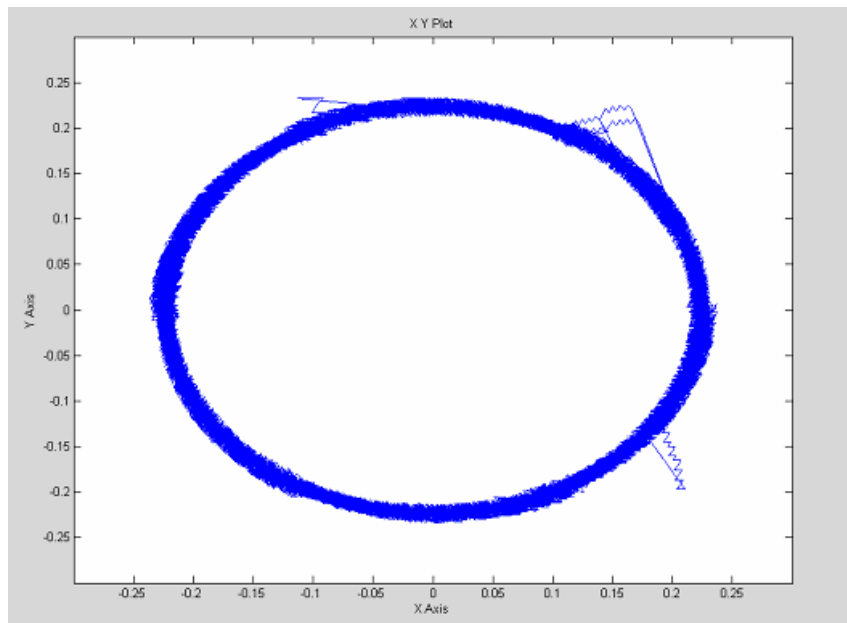


Fig. 8.69. Estimated λ_{sD} (X axis) and λ_{sQ} (Y axis) circular trajectory at a 0.35 second ramp time with a PI integrator initial value of 7 N·m. $0.7 \times \lambda_r$ is used at 0.35/2 second in the motor model ($V_{dc} = 370$ V). ($k_p=9$, $k_i=3$).

CHAPTER IX

SUMMARY AND FUTURE WORK

9.1. Summary of the Work and Conclusion

The primary contribution of this thesis work is the development, analysis and simulation verification of DTC of PMSM algorithm using three hall-effect sensors that is based on rotor reference frame topology for the improvement of the commercial top-loaded laundry washing machine agitation speed control system.

Since DTC scheme is often categorized as a sensorless torque control technique because stator flux linkage and electromagnetic torque can easily be estimated without a mechanical position or speed sensor at all but very low speeds. At very low and zero speeds, the technique suffers the same performance degradation as any sensorless method that is based on back-EMF integration. At very low speeds the back-EMF information is very weak and quietly comparable with the supply voltage in addition of resistance variation in conjunction with current and voltage sensing errors (offset errors causing a drift in integration). On the other hand, since proposed method does not use any integration (back-EMF integration), and uses the rotor position information which is updated at every 60 electrical degrees by the help of three cost-effective hall-effect sensors very low speed control is performed without any problem unlike basic DTC scheme.

Observer based type of position estimation techniques have problem of accumulating the position errors. Hall-effect sensor correction method gives a solution for these problems. By correcting the estimated position every cycle, no compensation algorithm is required and accumulating error is also eliminated.

This method eliminates the need of back-EMF integration to estimate the stator flux linkage; instead, rotor reference frame solution which relies only on the parameters of rotor flux linkage amplitude and dq-axis synchronous inductances rather than more sensitive stator resistance used in basic DTC scheme, is proposed for the same purpose. First, the mathematical basis of the developed method is derived and explained in detail then simulation model is built in MATLAB/SIMULINK[®] to verify the proposed method both in transient and steady-state condition with transient load starting from 7 N·m at start up and increase up to 10 N·m proportional to speed and the results are given and are discussed. As it can be seen in Section 8.2.3 of Chapter VIII, results of the simulations verify the feasibility of the proposed control scheme over the commercialized one. One conclusion can be drawn from the results is that the proposed method shows superior speed and torque responds when compare with the commercial agitate speed control system. Comparing to conventional DTC scheme when it has resistance variations and offset error causing drift in the stator flux linkage and eventually the instability in closed-loop speed control, those effects are included to the proposed DTC scheme also but no speed or torque instability are noted. Instead of resistance variation, rotor flux linkage amplitude is varied in the proposed DTC topology because only two motor parameters (rotor flux linkage amplitude and synchronous inductance) are used in the scheme.

9.2. Future Work

More work could be done in the future to improve the DTC of PMSM drive in both quality and economical manner. Some of those possible works are listed below:

- Current sensorless technique can be considered.
- Parameter change effect and their compensation can be included.

- Current model used in this thesis can be combined with voltage model to improve the performance of the speed control.
- One of the efficient ways of sensorless control techniques, high frequency injection, can be implemented.
- One and/or two hall-effect sensors instead of three can be used.
- Saturation effect on the synchronous inductance can be included.
- Temperature arise impacting on rotor flux linkage amplitude can be studied.

REFERENCES

- [1] A. Khurram, "Position and speed sensorless control of permanent magnet synchronous motors." Ph.D. dissertation, Michigan State University, East Lansing, MI, 2001.
- [2] P. Vas. *Vector Control of AC Machines*. London, U.K.: Oxford Univ. Press, 1990.
- [3] R.V. Khopkar, "DC-DC converter current source fed naturally commutated brushless DC motor drive." M.S. thesis, Texas A&M University, College Station, TX, 2003.
- [4] V. Valkenburg and Nooger & Neville, Inc. *Basic Electricity*, Revised ed. Indianapolis, IN: PROMPT Pub., 1992.
- [5] G. Rizzoni. *Principles and Application of Electrical Engineering*, Revised 4th ed. New York, NY: McGraw-Hill Publishing Company, 2004.
- [6] J. Luukko, "Direct torque control of permanent magnet synchronous machines - analysis and implementation." Ph.D. dissertation, Lappeenranta University of Technology, Lappeenranta, Finland, 2000.
- [7] T. Kim, "Sensorless control of the BLDC motors from near-zero to full speed." Ph.D. dissertation, Texas A&M University, College Station, TX, 2001.
- [8] L. Hao, "Permanent magnet AC motor full speed range operation using hybrid sliding mode observer." Ph.D. dissertation, Texas A&M University, College Station, TX, 2002.
- [9] D.Y. Ohm, "Dynamic model of PM synchronous motors," Drivetech, Inc., Blacksburg, Virginia. www.drivetech.com.
- [10] C.M. Ong. *Dynamic Simulation of Electric Machinery Using MATLAB / SIMULINK*. Upper Saddle River, NJ: Prentice Hall PTR, 1998.
- [11] P. Yedamale, "Brushless DC (BLDC) Motor Fundamentals," Application Note 885, Microchip Technology Inc., Chandler, AZ, 2003.
- [12] P. Pillay, "Modeling simulation and analysis of permanent magnet synchronous and brushless DC motor drives." Ph.D. dissertation, Virginia Polytechnic Institute and State University, Blacksburg, VI, 1987.

- [13] S.P.Waikar, "A low-cost low-loss brushless permanent magnet motor drive." Ph.D. dissertation, Texas A&M University, College Station, TX, 2001.
- [14] D. Y. Ohm and J. H. Park, "About commutation and current control methods for brushless motors," *28th Annual Symposium on Incremental Motion Control Systems and Devices*, San Jose, CA. July 26-29, 1999.
- [15] B.K. Bose. *Power Electronics and Variable Frequency Drives - Technology and Application*. Piscataway, NJ: IEEE Press, 1997.
- [16] P. Vas, *Sensorless Vector and Direct Torque Control*. London, U.K.: Oxford Univ. Press, 1998.
- [17] J.R. Hendershot Jr and T.J.E. Miller. *Design of Brushless Permanent-Magnet Motors*. Oxford, U.K.: Magna Physics/Clarendon, 1994.
- [18] K. Hasse, "Drehzahlverfahren für schnelle umkehrantriebe mit stromrichtergespeisten asynchron-kurzschlusslaufer-motoren," *Regelungstechnik*, vol. 20, pp. 60–66, 1972.
- [19] I. Takahashi and T. Noguchi, "A new quick-response and high efficiency control strategy of an induction machine," *IEEE Trans. Ind. Appl.*, vol. IA-22, pp. 820–827, Sept./Oct. 1986.
- [20] U. Baader, M. Depenbrock, and G. Gierse, "Direct self control (DSC) of inverter-fed-induction machine—A basis for speed control without speed measurement," *IEEE Trans. Ind. Appl.*, vol. 28, pp. 581–588, May/June 1992.
- [21] M. Depenbrock, "Direct self control of inverter-fed induction machines," *IEEE Trans. Power Electron.*, vol. 3, pp. 420–429, Oct. 1988.
- [22] M. Depenbrock, "Direct self-control of the flux and rotary moment of a rotary-field machine," U.S. Patent 4 678 248, July 7, 1987.
- [23] C. French and P. Acarnley, "Direct torque control of permanent magnet drives," *IEEE Trans. Ind. Appl.*, vol. IA-32, pp. 1080–1088, Sept./Oct. 1996.
- [24] L. Zhong, M. F. Rahman, W. Y. Hu, and K. W. Lim, "Analysis of direct torque control in permanent magnet synchronous motor drives," *IEEE Trans. Power Electron.*, vol. 12, pp. 528–536, May 1997.
- [25] I. Takahashi and T. Noguchi, "Take a look back upon the past decade of direct torque control," in *Proc. IEEE-IECON'97 23rd Int. Conf.*, vol. 2, 1997, pp. 546–551.

- [26] D. Casadei, G. Serra, and A. Tani, "Implementation of a direct torque control algorithm for induction motors based on discrete space vector modulation," *IEEE Trans. Power Electron.*, vol. 15, pp. 769–777, July 2000.
- [27] C. G. Mei, S. K. Panda, J. X. Xu, and K. W. Lim, "Direct torque control of induction motor-variable switching sectors," in *Proc. IEEE-PEDS Conf.*, Hong Kong, July 1999, pp. 80–85.
- [28] A. Tripathi, A. M. Khambadkone, and S. K. Panda, "Space-vector based, constant frequency, direct torque control and dead beat stator flux control of AC machines," in *Proc. IEEE-IECON'01 Conf.*, Nov. 2001, pp. 1219–1224.
- [29] C. Lascu, I. Boldea, and F. Blaabjerg, "A modified direct torque control for induction motor sensorless drive," *IEEE Trans. Ind. Appl.*, vol. 36, pp. 122–130, Jan./Feb. 2000.
- [30] D. Swierczynski, M. Kazmierkowski, and F. Blaabjerg, "DSP based direct torque control of permanent magnet synchronous motor (PMSM) using space vector modulation (DTC-SVM)," in *Proc. IEEE Int. Symp. Ind. Electron.*, vol. 3, May 2002, pp. 723–727.
- [31] L. Tang, L. Zhong, M. F. Rahman, and Y. Hu "A novel direct torque control for interior permanent-magnet synchronous machine drive with low ripple in torque and flux—a speed-sensorless approach," in *Proc. IEEE Trans. Ind. Appl.*, vol. 39, pp. 1748–1756, Nov/Dec 2003.
- [32] C. Martins, X. Roboam, T. A. Meynard, and A. S. Caryalho, "Switching frequency imposition and ripple reduction in DTC drives by using a multilevel converter," *IEEE Trans. Power Electron.*, vol. 17, pp. 286–297, Mar. 2002.
- [33] Y. A. Chapuis, D. Roye, and J. Davoine, "Principles and implementation of direct torque control by stator flux orientation of an induction motor," in *Conf. Rec. IEEE-IAS Annu. Meeting*, vol. 1, 1995, pp. 185–191.
- [34] B. K. B. And and N. R. Patel, "A programmable cascaded low-pass filter-based flux synthesis for a stator flux-oriented vector-controlled induction motor drive," *IEEE Trans. Ind. Electron.*, vol. 44, pp. 140–143, Feb. 1997.
- [35] M. R. Zolghadri and D. Roye, "A fully digital sensorless direct torque control system for synchronous machine," *Elect. Mach. Power Syst.*, vol. 26, pp. 709–721, 1998.

- [36] M.F. Rahman, Md. E. Haque, L. Tang, and L. Zhong, "Problems associated with the direct torque control of an interior permanent-magnet synchronous motor drive and their remedies," *IEEE Trans. Ind. Electronics.*, vol. 51, pp. 799–809, August 2004.
- [37] S. Mir, M. E. Elbuluk, and D. S. Zinger, "PI and fuzzy estimators for tuning the stator resistance in direct torque control of induction machines," *IEEE Trans. Power Electron.*, vol. 13, pp. 279–287, Mar. 1998.
- [38] L. Zhong, M. F. Rahman, K. W. Lim, Y. Hu, and Y. Xu, "A fuzzy observer for induction motor stator resistance for application in direct torque control," in *Conf. Rec. IEEE Power Electronics and Drive Systems Conf.*, 1997, pp. 91–96.
- [39] B. S. Lee and R. Krishnan, "Adaptive stator resistance compensator for high performance direct torque controlled induction motor drive," in *Conf. Rec. IEEE-IAS Annu. Meeting*, St. Louis, MO, 1998, pp. 423–423.
- [40] M. E. Haque and M. F. Rahman, "Influence of stator resistance variation on direct torque controlled interior permanent magnet synchronous motor drive performance and its compensation," in *Conf. Rec. IEEE-IAS Annu. Meeting*, 2001, pp. 2563–2569.
- [41] R. Dhaouadi, N. Mohan, and L. Norum, "Design and implementation of an extended Kalman filter for the state estimation of a permanent magnet synchronous motor," *IEEE Trans. Power Electron.*, vol. 6, no. 3, pp. 491–497, 1991.
- [42] M. Schroedl, "Sensorless control of AC machines at low speed and standstill based on the "INFORM" method," in *Conf. Rec. IEEE-IAS Annu. Meeting*, San Diego, CA, Oct. 6–10, 1996, pp. 270–277.
- [43] M. Schroedl, "Sensorless control of permanent magnet synchronous motors," *Elect. Mach. Power Syst.*, vol. 22, no. 2, pp. 173–185, Mar./Apr. 1994.
- [44] R. B. Sepe and J. H. Lang, "Real-Time observer-based (adaptive) control of a permanent-magnet synchronous motor without mechanical sensors," *IEEE Trans. Ind. Appl.*, vol. 28, pp. 1345–1352, Nov./Dec. 1992.
- [45] A. B. Kulkarni and M. Ehsani, "A novel position sensor elimination technique for the interior permanent magnet synchronous motor drive," *IEEE Trans. Ind. Appl.*, vol. 28, pp. 144–150, Jan./Feb. 1992.
- [46] S. Ogasawara and H. Akagi, "An approach to real time position estimation at zero and low speed for a PM motor based on saliency," in *Conf. Rec. IEEE-IAS Annu. Meeting*, San Diego, CA, Oct. 6–10, 1996, pp. 29–35.

- [47] S. Ostlund and M. Brokemper, "Sensorless rotor-position detection from zero to rated speed for an integrated PM synchronous motor drive," *IEEE Trans. Ind. Appl.*, vol. 32, pp. 1158–1165, Sept./Oct. 1996.
- [48] P. B. Schmidt, M. L. Gasperi, G. Ray, and A. H. Wijenayake, "Initial rotor angle detection of a nonsalient pole permanent magnet synchronous machine," in *Conf. Rec. IEEE-IAS Annu. Meeting*, New Orleans, LA, Oct. 5–9, 1997, pp. 549–463.
- [49] T. Noguchi, K. Yamada, S. Kondo, and I. Takahashi, "Initial rotor position estimation method of sensorless PM motor with no sensitivity to armature resistance," *IEEE Trans. Ind. Electron.*, vol. 45, pp. 118–125, Feb. 1998.
- [50] M. W. Degner and R. D. Lorenz, "Using multiple saliencies for the estimation of flux, position, and velocity in AC machines," in *Conf. Rec. IEEE-IAS Annu. Meeting*, New Orleans, LA, Oct. 5–9, 1997, pp. 760–767.
- [51] M. J. Corley and R. D. Lorenz, "Rotor position and velocity estimation for a salient-pole permanent magnet synchronous machine at standstill and high speeds," *IEEE Trans. Ind. Appl.*, vol. 34, pp. 784–789, July/Aug. 1998.
- [52] A. Consoli, G. Scarcella, and A. Testa, "Sensorless control of AC motors at zero speed," in *Proc. IEEE ISIE*, vol. 1, Bled, Slovenia, July 1999, pp. 373–379.
- [53] B.K. Bose. *Modern Power Electronics and AC Drives*. Upper Saddle River, NJ: Prentice Hall PTR., 2002.
- [54] S. Morimoto, M. Sanada and Y. Takeda, "High performance current-sensorless drive for PMSM and SynRM with only low resolution position sensor," *IEEE Trans. Ind. Appl.*, vol. 39, no. 3, pp. 792-801 May/June 2003.
- [55] J. Bu, L. Xu, T. Sebastian and B. Liu, "Near-zero speed performance enhancement of PM synchronous machines assisted by low cost hall effect sensors," in *Proc. IEEE APEC'98*, 1998, pp. 68-74.
- [56] D.J. Ensor, "Acceleration controller for laundry machine motor." U.S. Patent 5,398,298, March 14, 1995.
- [57] G.D. Duncan, "Electronic motor controls, laundry machines including such controls and/or methods of operating such controls." U. S. Patent RE37,360E, September 11, 2001.
- [58] J.D. Harwood, "Agitation period control of laundry machine Motor." U.S. Patent 5,726,546, March 10, 1998.

APPENDIX A

MB90460/5 Series

(Continued)

- Low-power consumption mode :
 - Sleep mode
 - Stop mode
 - CPU intermittent operation mode
- Package :
 - LQFP-64 (FPT-64P-M09 : 0.65 mm pitch)
 - QFP-64 (FPT-64P-M06 : 1.00 mm pitch)
 - SDIP-64 (DIP-64P-M01 : 1.78 mm pitch)
- CMOS technology

■ PRODUCT LINEUP

Part number	MB90V460	MB90F462	MB90F462A	MB90F463A	MB90462	MB90467
Item						
Classification	Development / evaluation product	Mass-produced products (Flash ROM with flash security)			Mass-produced products (Mask ROM)	
ROM size	—	64K Bytes		128K Bytes	64K Bytes	
RAM size	8K Bytes	2K Bytes				
CPU function	Number of instruction : 351 Minimum execution time : 62.5 ns / 4 MHz (PLL x 4) Addressing mode : 23 Data bit length : 1, 8, 16 bits Maximum memory space : 16 MBytes					
I/O port	I/O port (CMOS) : 51					
PWC	Pulse width counter timer : 2 channels					1 channel
	Timer function (select the counter timer from three internal clocks) Various pulse width measuring function (H pulse width, L pulse width, rising edge to falling edge period, falling edge to rising edge period, rising edge to rising edge period and falling edge to falling edge period)					
UART	UART : 2 channels With full-duplex double buffer (8-bit length) Clock asynchronous or clock synchronized transmission (with start and stop bits) can be selectively used Transmission can be one-to-one (bidirectional communication) or one-to-n (master-slave communication)					
16-bit reload timer	Reload timer : 2 channels Reload mode, single-shot mode or event count mode selectable Can be worked with multi-pulse generator or individually (MB90460 series only)					
16-bit PPG timer	PPG timer : 3 channels					2 channels
	PWM mode or single-shot mode selectable Can be worked with multi-functional timer, multi-pulse generator (MB90460 series only) or individually					

Fig. A-1. Specifications of the Fujitsu MB907462A microcontroller.

MB90460/5 Series

Part number	MB90V460	MB90F462	MB90F462A	MB90F463A	MB90462	MB90467
Item						
Multi-functional timer (for AC/DC motor control)	16-bit free-running timer with up or up-down mode selection and buffer: 1 channel 16-bit output compare : 6 channels 16-bit input capture : 4 channels 16-bit PPG timer : 1 channel Waveform generator (16-bit timer: 3 channels, 3-phase waveform or dead time)					
Multi-pulse generator (for DC motor control)	16-bit PPG timer : 1 channel Waveform sequencer (includes 16-bit timer with buffer and compare clear function) 16-bit reload timer operation (toggle output, one-shot output selectable) Event counter function : 1 channel built-in					Not present
8/10-bit A/D converter	8/10-bit resolution (8 channels) Conversion time : Min. 6.13 μ s (16 MHz internal clock)					
DTP/External interrupt	8 independent channels Selectable causes : Rising edge, falling edge, "L" level or "H" level					
Low-power consumption	Stop mode / Sleep mode / CPU intermittent operation mode					
Package	PGA256	LQFP-64 (FPT-64P-M09 : 0.65 mm pitch) QFP-64 (FPT-64P-M06 : 1.00 mm pitch) SDIP-64 (DIP-64P-M01 : 1.78 mm pitch)				
Power supply voltage for operation*	4.5 V to 5.5 V*					
Process	CMOS					

* : Varies with conditions such as the operating frequency (See section "■ ELECTRICAL CHARACTERISTICS"). Assurance for the MB90V460 is given only for operation with a tool at a power supply voltage of 4.5 V to 5.5 V, an operating temperature of 0 to +25 °C, and an operating frequency of 1 MHz to 16 MHz.

Fig A-1. (continued).

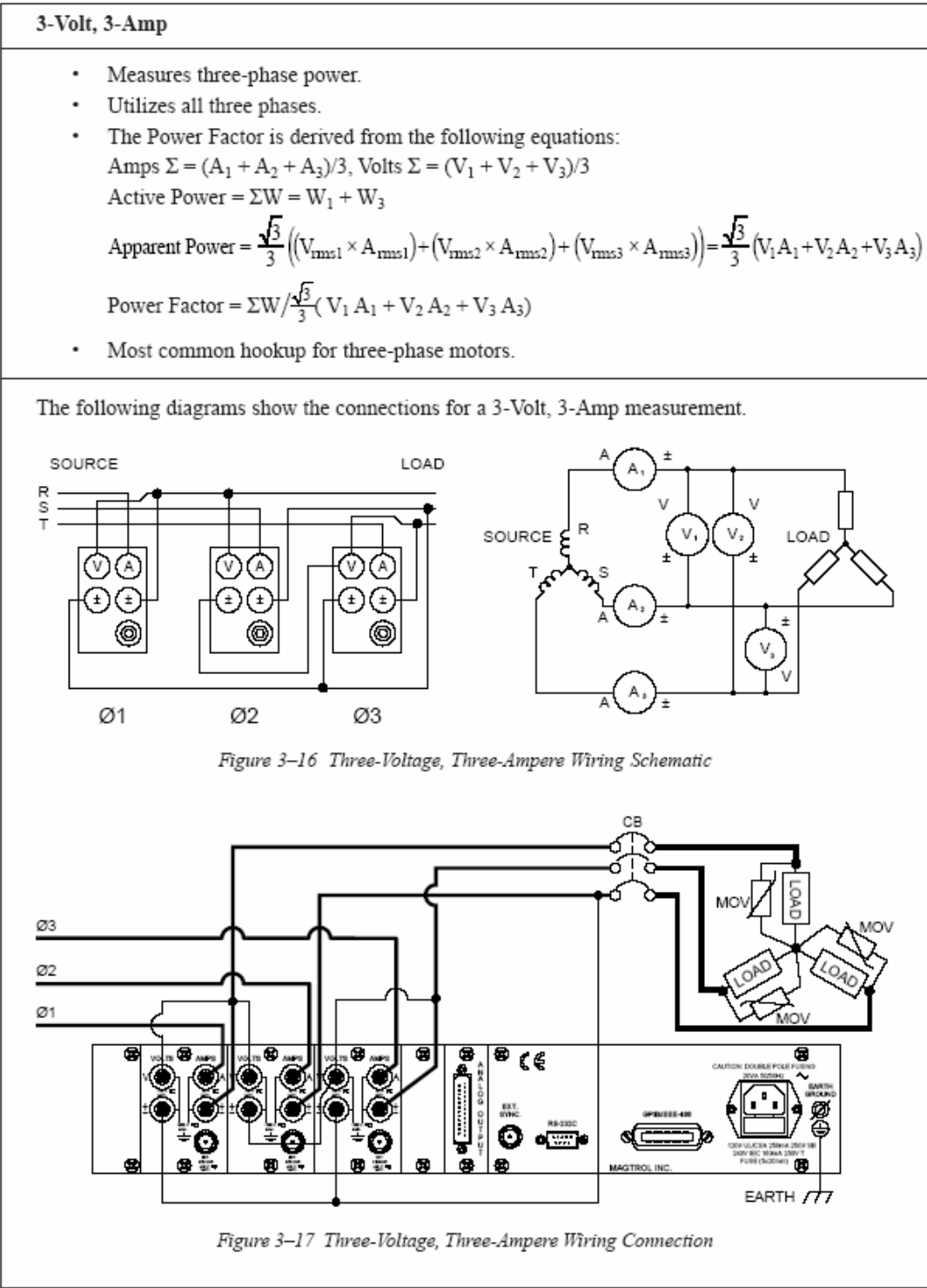


Fig. A-2. Theoretical background of active power, apparent power, power factor and connection of the power analyzer to the load (motor).

MOTOR PARAMETERS

p (number of poles) : 48

V_{rated} : 325 V

I_{peak} : 3.5 A

$\lambda_r = \sqrt{2}k_e$ (rotor flux linkage): 0.223256 Vs/rad

R_s : 16.30983 Ω

L_s : 61.8183 mH

$L_d = L_q$: 92.72745 mH

T_{peak} : 30 N·m

VITA

Salih Baris Ozturk received his Bachelor of Science degree from Istanbul Technical University, Istanbul, Turkey, in June 2000. He worked in the Electrical Machines and Power Electronics Laboratory, in the Department of Electrical Engineering at Texas A&M University, College Station, Texas, with Dr. Hamid A. Toliyat as his advisor, and he obtained a M.S. degree in December 2005. He is currently pursuing a Ph.D. degree in the same university.

Salih Baris Ozturk is a student member of the IEEE.

He can be reached in care of:

Dr. Hamid A. Toliyat
Electrical Machines & Power Electronics Laboratory
Department of Electrical Engineering
TAMU 3128
Texas A&M University
College Station, Texas 77843-3128